Semiconductors, Vol. 35, No. 10, 2001, pp. 1117–1119. Translated from Fizika i Tekhnika Poluprovodnikov, Vol. 35, No. 10, 2001, pp. 1169–1171.

ATOMIC STRUCTURE AND NONELECTRONIC PROPERTIES OF SEMICONDUCTORS

Some Aspects of SiC CVD Epitaxy

V. V. Zelenin, M. L. Korogodskiĭ, and A. A. Lebedev

Ioffe Physicotechnical Institute, Russian Academy of Sciences, Politekhnicheskaya ul. 26, St. Petersburg, 194021 Russia

Submitted February 5, 2001; accepted for publication February 7, 2001

Abstract—A brief comparative analysis of techniques for the CVD epitaxy of SiC is made. Two tendencies in the use of inner reactor equipment are distinguished. Irrespective of the design features and the active gases used, chemical reactions of hydrogen with the interior of the reactor occur concurrently with the epitaxial growth. These reactions control the actual [C]/[Si] ratio in the gas phase and in part determine the background impurity concentration in pure epilayers. © *2001 MAIK "Nauka/Interperiodica".*

Owing to its electrical properties and the well-developed technology of the substrate material, silicon carbide (SiC) occupies a prominent position in semiconductor studies. A constantly increasing number of reports concerned with the CVD epitaxial growth of silicon carbide with a wide variety of reactor designs, gas-phase systems, and epitaxial growth modes are being published. The system propane–silane–hydrogen (C_3H_8–SiH_4–H_2) has found the widest application for epitaxial growth of SiC [1]; other systems have been studied to a much lesser extent [2–6]. For any gas-phase system used in SiC epitaxy with independent sources, one of the main parameters is the [C]/[Si] ratio between the active gas phase components delivered into the reactor. This ratio determines the carrier concentration in SiC and, in some varieties of CVD technology, also the type of conduction in the grown layers. The numerical values of this ratio and the corresponding concentrations of uncompensated donors (acceptors) may differ fundamentally between different reactors, even those ensuring, at first glance, similar growth conditions. Therefore, it is important to analyze the growth conditions and distinguish the key factors to gain an understanding of the wide variety of technological solutions. This issue is the subject of the present communication.

The wide variety of reactors for the gas-phase epitaxy of SiC can be divided into modifications based on two concepts: (1) the cold wall method in which the gas mixture is delivered into a water-cooled reactor and chemical reactions occur in the zone closely adjacent to a heated substrate [7] and (2) the hot wall technique in which the gas mixture is fed into a heated volume where a substrate is placed [8]. The second approach is more favorable thermodynamically; however, industrial reactors have a simpler design in the former case [9]. By virtue of the fact that the epitaxial growth of SiC occurs at a high temperature, the number of construction materials working under these conditions is limited. Commonly, graphite is used in heaters and other inner components. Analysis of published data and the results of our own experiments on the technology of epitaxial SiC growth from the gas phase reveal two tendencies. The first consists in using graphite components with a SiC coating to preclude the egress of impurities (in particular, boron) from graphite into an epilayer [8]. The second consists in that purer and denser carbon materials, e.g., glassy carbon and pyrolytic graphite, are used without coatings [6, 10]. The complete or partial replacement of carbon by high-melting metals, such as molybdenum, tungsten [2], and tantalum [1], is also possible; it is preferable to carbidize the metallic members, as was done in [11].

A coating of the carbon components must guarantee the layer continuity. The best coatings are obtained on porous brands of graphite [12]. The occurrence of cracks is equivalent to the absence of a coating. The porosity has, however, a negative aspect, namely, that the more developed the surface, the stronger the adsorption and the more pronounced the "memory" of the preceding processes. In this context, special measures should be taken to evacuate the reactor when in a hot state.

Epitaxial growth is commonly performed in an atmosphere of hydrogen at temperatures $T > 1500$°C. As a result, hydrogen reacts with reactor components, both coated and not. Therefore, after the reactor is brought into a prescribed temperature state, it already contains an atmosphere enriched in silicon and/or carbon even before the introduction of the main components. In the case of a SiC coating, the characteristic chemical reaction between the coating and hydrogen can be written for the temperature intervals T = 1200–1500 and $\gtrsim$1500°C in the form

$$\begin{aligned} SiC + 2H_2 &\longrightarrow Si + CH_4, \\ SiC + (1/2)H_2 &\longrightarrow Si + (1/2)C_2H_2. \end{aligned} \qquad (1)$$

In a variant without a coating, the interaction with the reactor components can be characterized in the same temperature interval by the reactions

$$C + 2H_2 \longrightarrow CH_4, \quad 2C + H_2 \longrightarrow C_2H_2. \qquad (2)$$

The thermodynamic aspects of chemical reactions between carbon and silicon carbide were considered in great detail in [13, 14].

On introducing into the reactor the crystal-forming gases (silane, propane), reactions (1) and (2) proceed concurrently with the reactions of SiC formation, with the [C]/[Si] ratio in the reactor changing. In the case of a SiC coating, reactions (1) lead to the formation of silicon drops in the epilayers obtained in the [C]/[Si] range corresponding to enrichment with silicon. In the absence of a coating, there is no free silicon in the gas phase, according to (2); however, in this case, SiC that formed on reactor components as a result of parasitic deposition in preceding processes may act as a source of silicon drops. The negative phenomenon of silicon drop formation is eliminated by using clean carbon reactor components. Another way to eliminate drops is to introduce carbon-containing molecules into the reactor, with the result that the equilibrium of reaction (1) is shifted to the left, with free silicon formation suppressed [15, 16]. Nevertheless, our results [17] and data of [18] demonstrated that an excess of carbon favors the incorporation of background aluminum into an epilayer, with a high-resistivity region formed at the substrate–layer interface. Presumably, a more radical way to suppress silicon drop formation is to introduce hydrogen chloride into the reactor in the preepitaxial stage and to terminate the growth process in an inert gas [19]. Hydrogen chloride binds free silicon into chlorosilane molecules, and the termination of the process in an inert atmosphere prevents the occurrence of reaction (1). With the low-pressure CVD variant used, drop formation is also not observed [20].

One more negative aspect in epitaxy with SiC coating is the virtually complete etching-off of the coating under the substrate in the course of growth. Therefore, it was necessary to protect the coating. In [21], this problem was solved by placing a substrate on a plate of pure polycrystalline silicon carbide. It should be noted that, in a higher temperature variant of epitaxy ($T \gtrsim 1800$°C), the interaction of hydrogen with the reactor components is so strong that there is no need to deliver carbon-containing gases into the reactor during epilayer growth [22]. This interaction can be suppressed by introducing helium as the carrier gas [21]; however, in this case, the process becomes too expensive (the use of lower cost argon is undesirable because of its low heat conductivity). In processes with helium, reactions (1) and (2) also occur, since hydrogen is liberated in the reaction of SiH_4 decomposition and, in addition, most of the hydrogen is in a more chemically active atomic state at these temperatures.

The analysis performed shows that, irrespective of the design features of the reactors and the active gases used, the reaction of hydrogen with reactor components proceeds concurrently with epitaxial growth: a reaction of type (1) in the first case and that of type (2) in the second. These reactions control the actual [C]/[Si] ratio in the gas phase and, in part, the background impurity concentration in pure epilayers. The extent of this interaction is evaluated experimentally by the minimum concentration of the background impurity: for each reactor and growth conditions, there exists a certain [C]/[Si] ratio at which the background concentration in an undoped material is the lowest [17]. Comparison of growth data shows that the achievable level of background concentration in epilayers grown in a reactor with coated and uncoated components may be rather low (10^{13}–10^{14} cm^{-3}). Undoped epilayers grown in reactors with a SiC coating are, as a rule, *n*-type [8, 23]. At the same time, epitaxial SiC layers grown in reactors having no coatings may exhibit, depending on the [C]/[Si] ratio, both *n*- and *p*-type conduction. The minimum concentration corresponds to a region in which the type of conduction changes [1, 10, 11, 24].

The aforesaid can be illustrated by the results presented in the table for undoped epilayers grown by various technologies. The order of magnitude of the minimum achieved background concentrations of carriers (uncompensated impurities $N_D - N_A$ or $N_A - N_D$), obtained at virtually the same temperatures and related to [C]/[Si] values, were compared. As can be seen from the table, the [C]/[Si] ratios at which the minimum concentration is achieved may differ substantially for variants with and without coating.

Thus, the analysis of the experimental data on CVD epitaxial growth of SiC with low background concentration in various reactors and gas media shows that there are two tendencies in SiC technology, as regards the use of inner reactor components. With the materials

Growth conditions and parameters of SiC layers

T, °C	N_D–N_A (N_A–N_D), cm^{-3}	[C]/[Si]	Type of conduction	Technique	Heater material	Gas system	Source
~1600	~10^{15}	1.2	*n*	c.w.	Graphite with SiC coating	C_3H_8–SiH_4–H_2	[23]
~1600	~10^{14}	3	*n*	h.w.	Graphite with SiC coating	"	[8]
~1550	~10^{13}	0.8	*p*, *n*	c.w.	Graphite	"	[10]*
~1600	~10^{15}	0.3	*p*, *n*	h.w.	Graphite + tantalum	"	[11]
~1600	~10^{15}	0.45	*p*, *n*	h.w.	Vitreous carbon	CH_4–SiH_4–H_2	[24]

* Working pressure in the system 350 Torr; c.w. stands for cold wall technique, and h.w. stands for hot wall technique.

used as above, reactions with reactor components proceed in the reactor concurrently with epitaxial growth, irrespective of the reactor design and the gas mixtures employed. These reactions control the actual [C]/[Si] ratio in the gas phase. A characteristic distinction between the reactors with SiC coating of reactor components and without it consists in that the [C]/[Si] ratios of the active gases fed into the reactor, ensuring the minimum concentration, differ manyfold. It also follows from the analysis performed that using the variants with coated inner reactor components makes the cost of the epitaxial process higher for about the same final result. Therefore, the high-cost procedure of reactor component coating in most cases can be excluded in mass production, which makes the second tendency promising.

ACKNOWLEDGMENTS

This study was supported by the Russian Foundation for Basic Research (grant no. 00-02-16688).

REFERENCES

1. S. Minagva and H. C. Gatos, Jpn. J. Appl. Phys. **10** (12), 1680 (1971).
2. M. S. Saidov, Kh. Shamuratov, and M. A. Kadyrov, J. Cryst. Growth **87**, 519 (1988).
3. V. V. Zelenin, V. A. Solov'ev, S. M. Starobinets, *et al.*, Fiz. Tekh. Poluprovodn. (St. Petersburg) **29** (6), 1122 (1995) [Semiconductors **29**, 581 (1995)].
4. H. Matsunami, S. Nishino, M. Odaka, and T. Tanaka, J. Cryst. Growth **31**, 72 (1975).
5. C. Hallin, I. G. Ivanov, T. Eglisson, *et al.*, J. Cryst. Growth **183**, 163 (1998).
6. V. V. Zelenin, A. A. Lebedev, S. M. Starobinets, and V. E. Chelnokov, Mater. Sci. Eng. B **46**, 300 (1997).
7. M. Fatemi and P. E. R. Nordquist, J. Appl. Phys. **61**, 1883 (1987).
8. E. Janzen and O. Kordina, Inst. Phys. Conf. Ser. **142**, 653 (1996).
9. A. A. Burk, M. J. O'Loughlin, and S. S. Mani, Mater. Sci. Forum **264–268**, 83 (1998).
10. R. Rupp, P. Langing, J. Volki, and D. Stephani, J. Cryst. Growth **146**, 37 (1995).
11. L. B. Rowland, G. T. Dunne, and J. A. Freitas, Mater. Sci. Forum **338–342**, 161 (2000).
12. S. Nishino, A. Powell, and H. A. Will, Appl. Phys. Lett. **42** (5), 460 (1983).
13. B. V. Spitsyn, Tekh. Sredstv Svyazi, Ser. Tekhnol. Proizvod. Oborud., No. 4, 7 (1991).
14. M. D. Alendorf and R. J. Kee, J. Electrochem. Soc. **138** (3), 841 (1991).
15. J. A. Powell and L. G. Matus, Springer Proc. Phys. **43**, 14 (1989).
16. C. Hallin, F. Owman, P. Martenson, *et al.*, J. Cryst. Growth **181**, 241 (1997).
17. V. V. Zelenin, A. A. Lebedev, and M. L. Korogodskiĭ, in *Abstracts of the 3rd International Seminar on Silicon Carbide and Related Materials, Novgorod, 2000*, p. 49.
18. A. A. Bark, Jr. and L. B. Rowland, Appl. Phys. Lett. **68** (3), 382 (1996).
19. J. A. Powell, D. J. Larkin, and P. B. Abel, J. Electron. Mater. **24**, 295 (1995).
20. B. E. Landini and G. R. Brandes, Appl. Phys. Lett. **74** (18), 2632 (1999).
21. O. Kordina, A. Henry, E. Janzen, and C. H. Carter, Mater. Sci. Forum **264–268**, 97 (1998).
22. J. T. Kendall, J. Chem. Phys. **21** (5), 821 (1953).
23. S. Karmann, C. Haberstrob, F. Engelbrecht, *et al.*, Physica B (Amsterdam) **185**, 75 (1993).
24. V. V. Zelenin, A. A. Lebedev, M. G. Rastegaeva, *et al.*, Mater. Sci. Eng. B **61–62**, 183 (1999).

Translated by M. Tagirdzhanov

Semiconductors, Vol. 35, No. 10, 2001, pp. 1120–1122. Translated from Fizika i Tekhnika Poluprovodnikov, Vol. 35, No. 10, 2001, pp. 1172–1174.

ATOMIC STRUCTURE AND NONELECTRONIC PROPERTIES OF SEMICONDUCTORS

The Effect of CVD Growth Conditions of 6*H*-SiC Epilayers on Al Incorporation

V. V. Zelenin, M. L. Korogodskiĭ, and A. A. Lebedev

Ioffe Physicotechnical Institute, Russian Academy of Sciences, Politekhnicheskaya ul. 26, St. Petersburg, 194021 Russia

Submitted February 5, 2001; accepted for publication February 7, 2001

Abstract—Results obtained in studying CVD-grown *p*-type undoped epitaxial 6*H*-SiC layers by secondary-ion mass spectrometry are reported. The possible sources of background impurity, the mechanism of its incorporation into a layer, and the relationship between stoichiometry and adsorption, on the one hand, and the "site competition" effect, on the other, are discussed. The accumulation of aluminum in the adsorption layer of SiC is attributed to its surface activity. The increase in Al concentration with growing carbon concentration is related to the formation of silicon vacancies occupied by aluminum atoms. © *2001 MAIK "Nauka/Interperiodica".*

INTRODUCTION

It was shown in our previous study [1] that, in the CVD growth of 6*H*-SiC layers in the system methane–silane–hydrogen in the absence of intentional doping, both *n*- and *p*-type layers can be obtained, depending on the [C]/[Si] ratio in the gas phase. The range of conduction type changeover in the [C]/[Si] scale depends on the process temperature. The logarithm of the concentration of uncompensated donors, $\ln(N_D - N_A)$, [acceptors, $\ln(N_A - N_D)$] is a linear function of [C]/[Si] at concentrations $\lesssim 10^{18}$ cm^{-3}. The effect manifests itself in that the impurity incorporation depends on the [C]/[Si] ratio and was named in the literature on epitaxial SiC growth as the "site competition" effect consisting in a competitive occupation of crystal matrix sites by impurities [2]. We report on a study of nominally undoped *p*-type epitaxial 6*H*-SiC layers by secondary-ion mass spectrometry (SIMS) and discuss the possible sources of the background impurity, the mechanism of its incorporation into the layer, and the relationship between the stoichiometry and adsorption, on the one hand, and the "site competition" effect, on the other.

EXPERIMENT

The key factor in the incorporation of an impurity into a crystal is impurity adsorption on the crystal surface. The most frequently occurring acceptor impurity in SiC is Al. To find out whether Al is present and to reveal its possible sources and incorporation mechanism, we performed experiments on epitaxial growth and "freezing" of the adsorption layer. Epitaxial SiC layers were grown at $T = 1600$°C in the system CH_4–SiH_4–H_2 on *p*-type CREE (USA) substrates with an (0001)Si surface misoriented by 3° ($11\bar{2}0$). Since it was found that *p*-type conduction is achieved under growth conditions with increased carbon concentration in the gas phase, the adsorption layer was frozen by interrupting the growth process and cooling the reactor to room temperature in an atmosphere of hydrogen with methane. The experimental conditions and the results obtained in studying layers by SIMS are presented in Table 1 and in the figure. An analysis demonstrated the presence of aluminum in the epilayers, and the instants of interruption and cooling correspond to the appearance of Al peaks in the SIMS spectrum (sample no. 2, termination of the process; sample no. 3, the middle of the process).

DISCUSSION

As seen from Table 1 and the figure, the most favorable conditions for the growth of pure layers are those in sample no. 1. The concentration of Al (N_{Al}) in this layer is below the sensitivity limit of the employed SIMS installation. An important factor for obtaining low $N_A - N_D$ concentration is *in situ* substrate etching of the substrate in hydrogen, prior to epitaxial growth, with the result that the concentrations of electrically active carriers may differ by an order of magnitude for close [C]/[Si] values (Table 1, samples nos. 1 and 2) [1]. Raising the [C]/[Si] value leads to higher Al concentration in a layer (sample no. 3). Presumably, the source of Al is glassy carbon containing 10^{-4} at. % Al (Al enters the gas phase through the reaction of hydrogen with the glassy carbon reactor members). The thermodynamic analysis of the reaction of hydrogen with carbon materials (graphite, diamond) shows that C_2H_2 molecules predominate in the gas phase at $T \gtrsim 1500$°C [3]:

$$2C + H_2 \longrightarrow C_2H_2. \quad (1)$$

The next possible source of Al is the SiC layer on the glassy carbon reactor members, which "memorize" preceding experiments; Al comes into the gas phase through a reaction of this SiC layer with hydrogen:

$$SiC + 2H_2 \longrightarrow CH_4 + Si \quad (2)$$

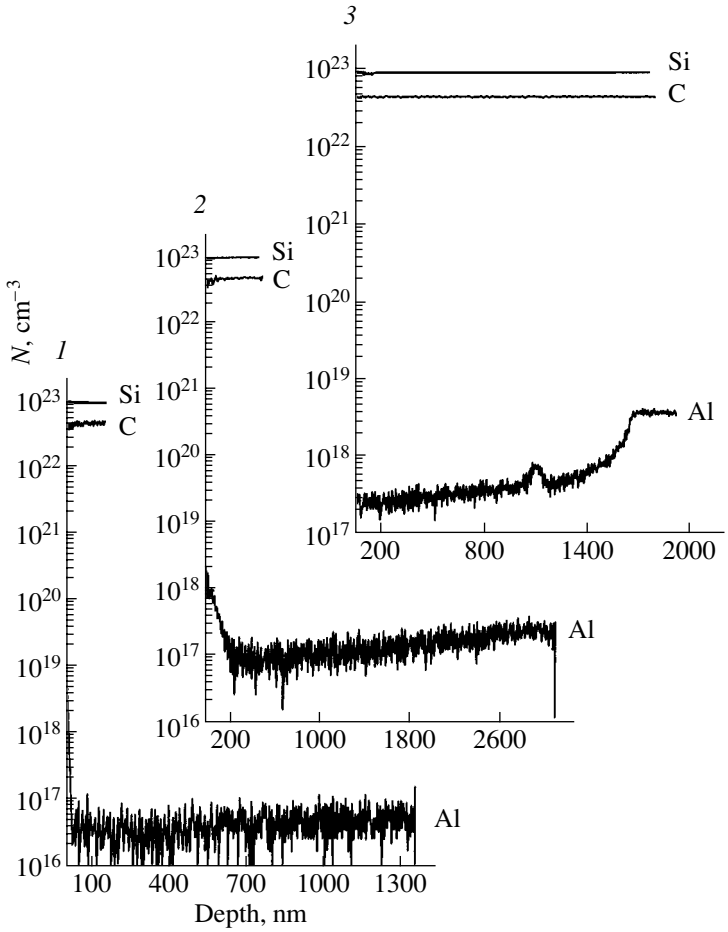

Al distribution across the epilayers: (*1–3*) correspond to sample numbers in Table 1. (*N*) Atomic concentration.

and/or

$$2SiC + H_2 \longrightarrow C_2H_2 + 2Si. \quad (3)$$

One more possible source of Al is the *p*-SiC : Al substrate, with Al coming into the gas phase in a way similar to reactions (2) and (3). As for the mechanism of autodoping with Al through its diffusion from the *p*-type substrate into the layer, it may be stated that, according to [4], the diffusion coefficient of aluminum in SiC at the temperatures mentioned is low ($D \sim 10^{-15}$ cm^2/s), which is attributed to the formation of low-mobility complexes involving vacancies [4]. The presented results are in good agreement with the data obtained in the system propane–silane–hydrogen [5].

The process in which an impurity passes into a crystal can be divided into three stages: (i) diffusion through the diffusion layer of the gas phase, (ii) adsorption of impurity atoms on the crystal surface, and (iii) incorporation of the impurity into the crystal in the

Table 1. Conditions of technological experiments and SiC layer parameters

Sample no.	N_A–N_D, cm^{-3}	N_{Al}, cm^{-3}	[C]/[Si]	Conditions of experiment
1	5.2×10^{15}	3×10^{16} (Background)	0.5	*In situ* substrate etching in H_2; growth, termination of growth, and cooling in H_2.
2	2.6×10^{16}	9×10^{16}	0.47	No pregrowth *in situ* etching of the substrate in H_2; termination of growth and cooling in $H_2 + CH_4$.
3	2.5×10^{17}	3×10^{17}	4	*In situ* etching of the substrate in H_2; growth, suspension of growth, cooling to room temperature in $H_2 + CH_4$, resumption of growth.

Note: The N_A–N_D concentration was found in capacitance–voltage measurements.

course of layer growth. Since the different positions in the crystal lattice are in a certain relationship with one another, it is impossible to add a structural unit to the lattice without altering simultaneously a number of other structural units [6]. For example, the introduction of a Si atom into the SiC compound inevitably gives rise to a carbon vacancy (V_C). Thus, during the growth of epitaxial SiC layers with deviation from stoichiometry, a deficiency of Si or C atoms on the surface of a growing film can be compensated for either by atoms coming to the surface from the interior of the crystal and leaving vacancies behind or by foreign atoms, if these are present and dissolve in the crystal matrix; finally, both these mechanisms may be operative simultaneously. In this case, the atoms from the surface pass into the bulk and the number of sites on the surface remains unchanged.

The adsorption is considered positive if the solute concentration at the surface exceeds that in the solution, otherwise it is negative. Substances in the surface layer, whose presence reduces the surface tension (positive adsorption), are called surface-active. Those substances whose presence makes the surface tension higher (negative adsorption) are called surface-inactive [7]. These substances tend to leave the surface layer. As seen from the figure, it should be considered that the appearance of Al peaks is due to the accumulation of the metal at the phase boundary; i.e., Al is a surface-active impurity for SiC. The generalized moment introduced and substantiated in [8],

$$m = eZ/r,$$

where e is the electron charge, Z is the valence, and r is the radius of ion by Goldschmidt, may serve as a numerical criterion of whether an impurity is surface-active or inactive. An impurity is surface-active if its generalized moment is higher than the generalized moments of solvent atoms, and is called surface-inactive otherwise.

Table 2 lists the momenta of C, Si, Al, and B atoms. It can be seen that the generalized momentum of Al is lower than those of carbon and silicon, and, therefore, Al is a surface-active impurity. Thus, the criterion presented is in agreement with our experiment. Al is accumulated at the phase boundary and is incorporated into the lattice only in the presence of a silicon vacancy, i.e., in the case of a silicon-depleted gas phase.

The amount of vacancies in SiC also depends on the degree of hexagonality [9]. In this context, the closest to stoichiometry is the 4*H*-SiC polytype characterized by the highest hexagonality. Consequently, under the conditions when the [C]/[Si] ratio in the adsorption layer is nearly stoichiometric and the growth rates are nearly equilibrium, aluminum must not be incorporated into a growing layer. Indeed, spectra of low-temperature photoluminescence from epitaxial 4*H*-SiC layers grown in the gas system under study at certain [C]/[Si] ratios contain no Al-related bands [10]. As for boron, it has a generalized moment higher than that of silicon and lower than that of carbon. Thus, boron is a surface-inactive impurity with respect to silicon and a surface-active impurity with respect to carbon. Therefore, boron would be expected to accumulate on the (0001)C face, but not on the (0001)Si face.

Table 2. Radii and generalized moments of ions

Ion	Ionic radius, 10^{-10} m	m, 10^{-9} C m^{-1}
C^{4+}	0.2	32
Si^{4+}	0.39	16.4
B^{3+}	0.2	24
Al^{3+}	0.57	8.4

CONCLUSION

Glassy carbon reactor members are the source of background aluminum in the layers grown. The accumulation of Al at the phase boundary is accounted for by its surface activity. The increase in Al concentration in the epitaxial SiC layer with increasing carbon concentration is due to Al incorporation into silicon vacancies appearing because of the presence of superstoichiometric carbon in the adsorption layer; i.e., the concentration of Al depends on the [C]/[Si] ratio.

ACKNOWLEDGMENTS

This study was supported by the Russian Foundation for Basic Research (project no. 00-02-16688).

REFERENCES

1. V. V. Zelenin, A. A. Lebedev, M. G. Rastegaeva, *et al.*, Mater. Sci. Eng. B **61–62**, 183 (1999).
2. D. J. Larkin, MRS Bull. **22** (3), 36 (1997).
3. B. V. Spitsyn, Tekh. Sredstv Svyazi, Ser. Tekhnol. Proizvod. Oborud., No. 4, 7 (1991).
4. E. N. Mokhov, Author's Abstracts of Doctoral Dissertation (Fiz.-Tekh. Inst. im. A. F. Ioffe Ross. Akad. Nauk, St. Petersburg, 1998).
5. A. A. Burk, Jr. and L. B. Rowland, Appl. Phys. Lett. **68** (3), 382 (1996).
6. F. A. Kröger, *The Chemistry of Imperfect Crystals* (Wiley, New York, 1964; Mir, Moscow, 1969).
7. I. P. Bazarov, *Thermodynamics* (Fizmatgiz, Moscow, 1961).
8. V. K. Semechenko, *Surface Phenomena in Metals and Alloys* (Gosizdat, Moscow, 1957).
9. N. D. Sorokin, Yu. M. Tairov, V. F. Tsvetkov, and M. A. Chernov, Kristallografiya **28**, 910 (1983) [Sov. Phys. Crystallogr. **28**, 539 (1983)].
10. C. Hallin, I. G. Ivanov, T. Egilsson, *et al.*, J. Cryst. Growth **183**, 163 (1998).

Translated by M. Tagirdzhanov

Semiconductors, Vol. 35, No. 10, 2001, pp. 1123–1125. Translated from Fizika i Tekhnika Poluprovodnikov, Vol. 35, No. 10, 2001, pp. 1175–1177.

ELECTRONIC AND OPTICAL PROPERTIES OF SEMICONDUCTORS

Analysis of the Temperature Dependence of Electron Concentration in $CdGeAs_2$ Single Crystals

S. I. Borisenko

Siberian Physicotechnical Institute, Tomsk, 634050 Russia

Submitted October 30, 2001; accepted for publication January 31, 2001

Abstract—The temperature dependence of electron concentration in $CdGeAs_2$ single crystals grown by a new method is analyzed. The concentration of native defects and the activation energy are calculated. It is shown that the activation energy has a resonance character, and the concentration of native defects in the temperature range studied (10–500 K) far exceeds the electron concentration. © *2001 MAIK "Nauka/Interperiodica".*

INTRODUCTION

In [1], the temperature dependence of an unprecedentedly high electron mobility in $GdGeAs_2$ single crystals grown by a new method of low-temperature crystallization from nonstoichiometric melts [2] was studied. Scattering by singly charged native defects with a screened Coulomb-type potential, as well as by the polar optical phonons and by the plasma oscillations of a free-electron gas, was considered as the dominant mechanisms of scattering. This scattering mechanism enabled a good agreement between the experimental and calculated data on Hall mobility to be reached [2]. However, the nature of the native defects which supply electrons to the conduction band in these single crystals and their concentration and activation energy remained unclear. In order to partially resolve this problem, a numerical analysis of the experimental data on the temperature dependence of the Hall coefficient in $CdGeAs_2$ single crystals with degenerate electron gas was carried out. Assuming that the native defects that can each supply a single electron to the conduction band are of the donor type in the model of singly and doubly charged centers, we calculated the concentration and the activation energy of these defects, taking into account the tail of the density of states in the conduction band.

BASIC FORMULAS

The temperature dependence of electron concentration in the conduction band was analyzed by numerically solving the equation of electroneutrality

$$n = n_0 + n_L = p_D, \tag{1}$$

where n_0 is the concentration of free electrons responsible for conductivity, n_L is the concentration of electrons localized due to the fluctuations in the electrostatic potential of ionized defects,

$$p_D = \frac{N_D}{\sqrt{\pi}V_0}\int_{-\infty}^{+\infty}\frac{\exp(-V/\sqrt{2}V_0)}{g\exp\left(\dfrac{\xi-\varepsilon_D-V}{k_0T}\right)+1}dV \tag{2}$$

is the hole concentration at the native defects, N_D is the total concentration of native defects which supply electrons to the conduction band, ε_D is the ionization energy of the defects, g is the effective degeneracy factor, ξ is the Fermi level measured from the bottom of an "unperturbed" conduction band,

$$V_0 = \frac{e^2}{4\pi\varepsilon_0\varepsilon}(2\pi p_D L_D)^{1/2} \tag{3}$$

is the root-mean-square (rms) fluctuation of electron potential energy [3],

$$L_D = \left(\frac{e^2}{\varepsilon_0\varepsilon_s}\frac{\partial n_0}{\partial\xi}\right)^{-1/2} \tag{4}$$

is the Debye screening length, and ε_0 in (3) and (4) is the dielectric constant of free space. Within the approximation of a highly degenerate electron gas and assuming the nonparabolicity of the energy spectrum at the conduction-band bottom, the total electron concentration in the conduction band was calculated by the formula

$$n = \frac{1}{3\pi^2}\left(\frac{2m^*(\xi)}{\hbar^2}\xi\right)^{3/2}, \tag{5}$$

where

$$m^*(\xi) = \frac{\hbar^2}{2P^2} \times \frac{(\xi+\varepsilon_0)\left[\left(\xi+\varepsilon_0+\frac{2}{3}\Delta_{so}\right)\left(\xi+\varepsilon_0+\frac{1}{3}\Delta_{so}-\Delta_{cr}\right)-\frac{2}{9}\Delta_{so}^2\right]}{(\xi+\varepsilon_0)\left(\xi+\varepsilon_0+\frac{2}{3}\Delta_{so}\right)-\frac{2}{3}\Delta_{cr}\left(\xi+\varepsilon_0+\frac{1}{3}\Delta_{so}\right)} \tag{6}$$

1063-7826/01/3510-1123$21.00 © 2001 MAIK "Nauka/Interperiodica"

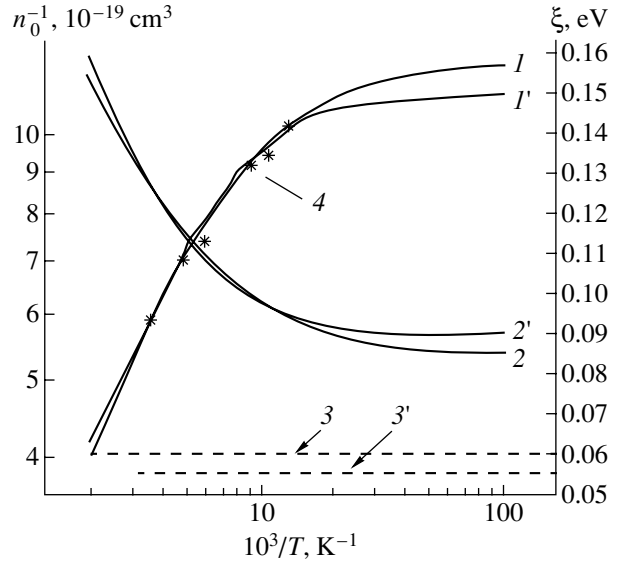

Fig. 1. Temperature dependences (*1*, *1*') of concentration n_0 of nonlocalized electrons, (*2*, *2*') of the Fermi level ξ, and (*3*, *3*') of the ionization energy ε_D in *n*-$CdGeAs_2$; (*4*) are the experimental data [2]. Calculations are carried out for the degeneracy factors (*1*–*3*) $g = 0.5$ and (*1*'–*3*') $g = 2$.

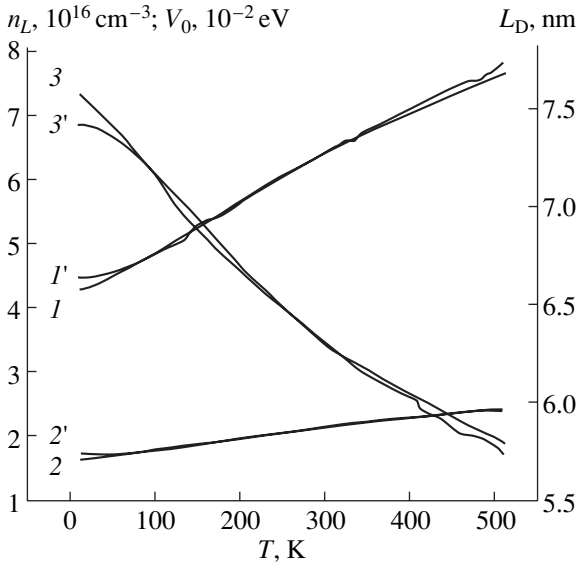

Fig. 2. Temperature dependences (*1*, *1*') of the concentration n_L of localized electrons, (*2*, *2*') of the rms fluctuation of the energy V_0, and (*3*, *3*') of the Debye screening length. Calculations are made for the degeneracy factors (*1*–*3*) $g = 0.5$ and (*1*'–*3*') $g = 2$.

is the effective mass in the four-band approximation for a direct gap diamond-like isotropic semiconductor with a chalcopyrite lattice [3] and P, ε_0, Δ_{so}, and Δ_{cr} are the parameters of the energy spectrum of electrons and holes in the vicinity of the conduction-band bottom and top [4]. The anisotropy can be neglected because its magnitude is small for the electrons in $CdGeAs_2$ [4]. The concentration of localized electrons in a parabolic approximation for the energy spectrum was calculated by the formula

$$n_L = \int_{-\infty}^{0} f_0(E)\rho(E)dE = \frac{4CV_0^{3/2}(m_0^*)^{3/2}}{\pi^2\hbar^3}, \qquad (7)$$

where $m_0^* = m^*(0)$, $\rho(E)$ is the density of states in the tail region of the band [3], and

$$C = \frac{1}{\sqrt{\pi}}\int_{-\infty}^{0} dy \int_{-y}^{\infty} \exp(-x^2)\sqrt{y+x}\,dx = 0.17046. \qquad (8)$$

Parameters of native defects in *n*-$GdGeAs_2$

g	N_D, 10^{19} cm^{-3}	N_D^*, 10^{19} cm^{-3}	ε_D, meV	ε_D^*, meV
0.5	1.2	0.9	60	73
2	5.0	2.9	55	74

Note: N_D^* and ε_D^* are obtained in the absence of tails in the density of states.

In this study, it was assumed that the concentration of free electrons for the degenerate electron gas is related to the Hall coefficient by the well-known expression $n_0 = 1/eR$.

ANALYSIS OF CALCULATIONS

The unknown quantities N_D and ε_D were calculated by the self-consistent method taking account of the expressions (1)–(7) for a given value of g and two values of the electron concentration obtained from the Hall coefficient measured at room and liquid-nitrogen temperatures [2]. For a singly charged defect, the parameter g was assumed to be equal to 2, for a doubly charged defect in the first charged state $g = 0.5$. For the calculation of energy spectrum in the vicinity of the conduction-band bottom, the following parameters were used: $P = 0.92$ eV nm, $\varepsilon_0 = 0.74$ eV, $\Delta_{so} = 0.33$ eV, and $\Delta_{cr} = 0.21$ eV [4]. According to Eq. (6), such parameters corresponded to the value $0.034m_0$ of the angle-averaged effective mass at the bottom of the band.

The obtained values of N_D and ε_D best fitted to the experiment (Fig. 1) are given in the table. According to the calculations, the donor level of a native defect is a resonance one. The concentration of defects heavily depends on the model chosen for a defect (on the parameter g). The concentration of electrons is found to be much lower than the concentration of defects which are predominantly in the neutral state at the temperatures used in the experiment. The estimation of the localization region of electrons at neutral defects from

the Heisenberg uncertainty relation shows that the size of this region is close to the average distance between defects (3–4 nm). This suggests that there is a slight quantum splitting of a donor level and allows one to assume that no impurity band is formed. The broadening of the level is of a purely classical origin and is determined by the rms fluctuation of the electron energy, which, like the screening length, is a function of temperature (Fig. 2). It should be mentioned that according to a more accurate theory of tails in the density of states [5], in which the parameter V_0 is less important than in Kane's theory [3] and serves as a fitting parameter, the calculated value of ionization energy turns out to be too low, and the concentration of defects, too high. This means that the values listed in the table with regard to and regardless of the tails in the densities of states can be considered as the extreme values for N_D and ε_D.

The lack of experimental data makes it impossible to choose a particular model for a defect and to refine its charge state. According to the calculation, the concentration of electrons varies only slightly following a drop in temperature to 10 K and remains at a level of 10^{18} cm^{-3}, which can be verified in this temperature range by measuring the parameter g (Fig. 1).

REFERENCES

1. S. I. Borisenko, V. Yu. Rud', Yu. V. Rud', and V. G. Tyuterev, Fiz. Tekh. Poluprovodn. (St. Petersburg) **35** (6), 720 (2001) [Semiconductors **35**, 690 (2001)].
2. I. K. Polushina, V. Yu. Rud', Yu. V. Rud', and T. N. Ushakova, Fiz. Tverd. Tela (St. Petersburg) **41**, 1190 (1999) [Phys. Solid State **41**, 1084 (1999)].
3. T. N. Morgan, Phys. Rev. A **139**, 343 (1965).
4. S. I. Borisenko and G. F. Karavaev, Izv. Vyssh. Uchebn. Zaved., Fiz., No. 4, 101 (1988).
5. H. C. Casey, Jr. and F. Stern, J. Appl. Phys. **47**, 631 (1976).

Translated by A. Zalesskiĭ

Semiconductors, Vol. 35, No. 10, 2001, pp. 1126–1131. Translated from Fizika i Tekhnika Poluprovodnikov, Vol. 35, No. 10, 2001, pp. 1178–1183.

ELECTRONIC AND OPTICAL PROPERTIES OF SEMICONDUCTORS

Nonlinear and Dynamic Properties of Charge Transport in Polycrystalline Silicon under Optical Illumination

K. M. Doshchanov

Physicotechnical Institute, Fizika–Solntse Research and Production Enterprise, Academy of Sciences of Uzbekistan, Uzbekistan, 700084 Tashkent

Submitted June 8, 2001; accepted for publication February 8, 2001

Abstract—Nonlinear and dynamic properties of the photocurrent in polycrystalline silicon (polysilicon) are studied theoretically. The admittance of the photoexcited polysilicon is calculated as a function of frequency, DC bias, and illumination level. Application of the theory to the spectroscopy of interface states at grain boundaries is considered. The possibility of determining the recombination current density at grain boundaries by measuring the nonlinear photocurrent and photoadmittance is demonstrated. © *2001 MAIK "Nauka/Interperiodica".*

INTRODUCTION

As is well known, the photoelectric properties of polycrystalline silicon (polysilicon) are determined to a large extent by nonequilibrium electronic processes at grain boundaries [1–4]. A study of the static and dynamic characteristics of the electrical conductivity of polysilicon under optical illumination presumably gives the most comprehensive insight into these processes. Up to now, studies in this field have been confined to the steady-state linear photocurrent. In this study, nonlinear and dynamic properties of the photocurrent are analyzed theoretically.

The theory of the dynamic electrical conductivity of polycrystalline semiconductors in the dark was developed in [5–8]. An application of the theory to the spectroscopy of interface states (ISs) at grain boundaries was considered in [7, 8]. In the same studies, relations between the density of IS near the quasi-Fermi level for electrons localized at the grain boundaries and measurable static and dynamic characteristics of the dark electrical conductivity in polycrystals were derived.

It is known that the illumination of a polycrystal fundamentally changes the electron distribution over the IS energy levels [1, 3, 9]. Therefore, it would be expected that additional information on the IS spectrum can be obtained by analyzing the experimental data obtained in measuring the steady-state photocurrent and photoadmittance (admittance of a photoexcited polycrystal). It should also be noted that these measurements can be carried out at rather low temperatures, thereby improving the accuracy of determining the IS density. In this context, we also consider an application of the theory to IS spectroscopy.

1. STEADY-STATE PHOTOCURRENT

Let us consider, as in [1–4], a polycrystal composed of similar cubic grains doped with a shallow donor impurity with concentration N_d. Acceptor type IS exist at the grain boundaries, distributed over energy E with density $\rho_s(E)$. The capture of electrons to the ISs energy levels gives rise to depletion layers and the related intercrystallite potential barriers at grain boundaries. In what follows, a coarse-grained polycrystal with grain size $d \gg W$ (where W is the depletion layer width at the grain boundary) will be considered.

Following [1–4], we assume that illumination of a polycrystal causes uniform photogeneration of electron–hole pairs in the grain bulk. The photoexcitation level is limited by the condition $p_0 \ll p \ll N_d$, where p_0 is the equilibrium hole density and p is the hole density in the photoexcited crystal.

Let a dc voltage U_0 be applied to the photoexcited crystal. The grain boundaries are oriented either parallel or normal to the field direction. It was shown in [3] that in this case the photoelectric characteristics of the polycrystal can be determined using a 1D model: a chain of identical bicrystals with an effective photoexcitation level $g^* = g - 2j_R/ed$, where g is the rate of electron–hole pair photogeneration in the 3D polycrystal, j_R is the recombination current density at grain boundaries oriented parallel to the field direction, and e is the absolute value of the electron charge.

Let us consider one bicrystal from the chain. The electronic processes at the grain boundary are described by the equations

$$j_{n1,2} = j_n^* \pm [e\nu_n S_n(N_s - n_s)n_{1,2} - eI_n], \quad (1)$$

$$j_{p1,2} = j_p^* \mp [e\nu_p S_p n_s p_{1,2} - eI_p], \quad (2)$$

where j_{n1} and j_{p1} are, respectively, the electron and hole currents immediately to the right of the grain boundary; j_{n2} and j_{p2} the same to the left of the grain boundary; j_n^* (j_p^*) is the density of the tunnel current of electrons (holes) across the grain boundary; $v_n(v_p)$ is the mean thermal velocity of electrons (holes); $S_n(S_p)$ is the cross section of electron (hole) capture to the IS energy levels; N_s is the total IS density;

$$n_s = \int_{E_V}^{E_C} \rho_s(E) f(E) dE \tag{3}$$

is the density of electrons localized at the grain boundary; n_1 and p_1 are, respectively, the free electron and hole densities immediately to the right of the grain boundary; n_2 and p_2 are the same to the left of the boundary;

$$I_n = v_n N_C S_n \int_{E_V}^{E_C} \rho_s(E) f(E) \exp\left(\frac{E - E_C}{kT}\right) dE, \tag{4}$$

$$I_p = v_p N_V S_p \int_{E_V}^{E_C} \rho_s(E)[1 - f(E)] \exp\left(\frac{E_V - E}{kT}\right) dE, \tag{5}$$

are the electron and hole emission currents from the grain boundary into the grain bulk; and $f(E)$ is the electron distribution over the IS energy levels. The rest of the notations are standard.

The steady-state current density in the polycrystal, $j_{dc} = j_n + j_p$, where $j_n = (j_{n1} + j_{n2})/2$ and $j_p = (j_{p1} + j_{p2})/2$ are, respectively, the densities of the electron and hole current across the grain boundary. The charge transfer across the grain boundary is due to the asymmetry of the intercrystallite barrier in an external electric field. The barrier heights to the right and to the left of the grain boundary are, respectively, $V_1 = V(1 - \beta)^2$ and $V_2 = V(1 + \beta)^2$, where

$$V = e^2 n_s^2 / 8\varepsilon_0 \varepsilon N_d, \quad \beta = eU_b / 4V,$$

$$U_b = (U_0/D - j_{dc}/e\mu_n N_d) d$$

is the voltage drop across the intercrystallite barrier, D is the polycrystal length, μ_n is the electron mobility in the grain bulk, and $\varepsilon_0\varepsilon$ is the permittivity of the grain material.

The function $f(E)$ is determined from the equation $j_{n1} - j_{n2} = j_{p1} - j_{p2}$. Calculations yield the following expressions:

$$f(E) = f(E - F_n)\Phi(E) + f(E - F_p)[1 - \Phi(E)], \tag{6}$$

$$\Phi(E) = \frac{\Phi_n[1 - f(E - F_p)]}{\Phi_n[1 - f(E - F_p)] + \gamma\Phi_p f(E - F_n)}, \tag{7}$$

where $f(E - F_{n,p})$ is the Fermi–Dirac distribution;

$$F_n = E_C + kT \ln \Phi_n, \quad F_p = E_V - kT \ln \Phi_p$$

are the quasi-Fermi levels for, respectively, electrons and holes at the grain boundary;

$$\Phi_n = (n_1 + n_2)/2N_C; \quad \Phi_p = (p_1 + p_2)/2N_V;$$

$$\gamma = v_p S_p N_V / v_n S_n N_C.$$

By using the explicit form of $f(E)$ in (2), we obtain the relation

$$j_{p2} - j_{p1} = eS(0) N_V \Phi_p,$$

where

$$S(0) = 2v_p S_p \left[1 - \exp\left(\frac{F_p - F_n}{kT}\right)\right] \times \int_{E_V}^{E_C} \rho_s(E) f(E - F_n) \Phi(E) dE \tag{8}$$

is the hole recombination rate at the grain boundary [9].

We now show that the following condition is satisfied in the coarse-grained polysilicon:

$$\frac{D_p}{S(0) L_p \tanh\xi} \exp\left(1 - \frac{V_1}{kT}\right) \ll 1, \tag{9}$$

where D_p and L_p are, respectively, the hole diffusion coefficient and diffusion length in the grain bulk and $\xi = d/2L_p$. It follows from our calculations that in this case

$$j_{p2} = -j_{p1} = eg^* L_p \tanh\xi.$$

It is important to note that j_{p1} and j_{p2} are independent of V_1 and V_2 and, consequently, of the external field. Therefore, the recombination current density is the same at all grain boundaries, irrespective of their orientation with respect to the field direction. Taking into account the relation $g^* = g - 2j_R/ed$, we obtain

$$j_{p2} - j_{p1} = j_R = 2egL,$$

where

$$L = L_p \xi \tanh\xi / (\xi + 2\tanh\xi).$$

Since $j_p = 0$ when (9) is satisfied, the current density in the polycrystal is determined by the electron current across the grain boundary:

$$j_{dc} = e v_n \theta_n (n_1 - n_2),$$

where

$$\theta_n = D_n^* + S_n(N_s - n_s)/2,$$

D_n^* is the integral transparency of the grain boundary for electrons [4]. At

$$v_n \theta_n \ll \mu_n \sqrt{2N_d V_1 / \varepsilon_0 \varepsilon}$$

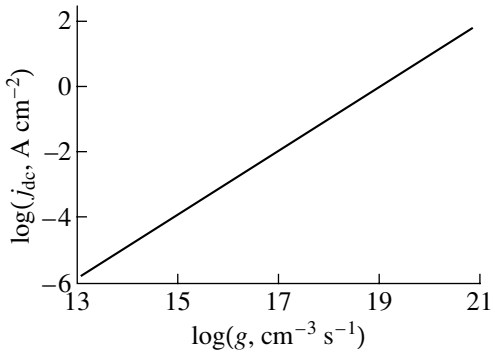

Fig. 1. Photocurrent density j_{dc} vs. photoexcitation level g at constant bias $U_b = 0.25$ V.

it suffices to define the densities n_1 and n_2 by relations $n_{1,2} = N_d \exp(-Z_{1,2})$, where $Z_{1,2} = V_{1,2}/kT$ [7]. Then for j_{dc} and Φ_n, we have

$$j_{dc} = e\nu_n \theta_n N_d [\exp(-Z_1) - \exp(-Z_2)], \quad (10)$$

$$\Phi_n = \frac{N_d}{2N_C}[\exp(-Z_1) + \exp(-Z_2)]. \quad (11)$$

It follows from the above relations that the function $\Phi(E)$ depends on n_s, $S(0)$, g, and U_b parametrically. Therefore, expressions (3) and (8) constitute a set of integral equations, whose solution gives n_s and $S(0)$ as functions of g and U_b. Calculations can be essentially simplified at $F_n - F_p \gg kT$ if the approximation $f(E - F_{n,p}) = \theta(F_{n,p} - E)$ is used, where $\theta(F_{n,p} - E)$ is the step function. Then instead of (3) and (8), we have

$$e[N_s(F_n) - n_s]\Phi_n = j_R \tau_0, \quad (12)$$

$$S(0) = 2\nu_p S_p [n_s - N_s(F_p)], \quad (13)$$

where

$$N_s(E) = \int_{E_V}^{E} \rho_s(E')dE'$$

is the integral IS density, and $\tau_0 = (2\nu_n S_n N_C)^{-1}$. For the density of the steady-state photocurrent, we obtain from expressions (10)–(13)

$$j_{dc} = \frac{\theta_n j_R}{S_n[N_s(F_n) - n_s]} \tanh\left(\frac{eU_b}{2kT}\right). \quad (14)$$

A linear dependence of the photocurrent density on the mean electric field strength in the polycrystal ($U_0 D$) corresponds to $eU_b \ll kT$ [3, 4]. At $eU_b \gtrsim kT$, the linear dependence becomes sublinear. At $eU_b \gg kT$, a weak rise in j_{dc} occurs owing to a decrease in the denominator of (14). The decrease in $N_s(E) - n_s$ takes place because the lowering of the intercrystallite barriers by the electric field is accompanied by additional capture of electrons to the IS energy levels.

Let us determine the applicability range of expression (14) for polysilicon with the following parameters: $T = 200$ K, $\varepsilon = 11.8$, $E_g = 1.12$ eV, $N_C = 1.5 \times 10^{19}$ cm^{-3}, $N_V = 5.5 \times 10^{18}$ cm^{-3}, $\nu_n = \nu_p = 10^7$ cm/s, $N_d = 5 \times 10^{15}$ cm^{-3}, $D_p = 20$ cm^2/s, $L = 10^{-2}$ cm, $D_n^* = 10^{-2}$, $S_n = 10^{-15}$ cm^2, $S_p = 2 \times 10^{-14}$ cm^2, $N_s = 10^{12}$ cm^{-2}, $E_s = E_V + 0.66$ eV, and $\Gamma = 0.3$ eV [1–4] (E_s and Γ are the parameters of the IS density Gaussian distribution). The condition $p \ll N_d$ is equivalent to $g \ll S(0)N_d/2L$, where the right-hand side is on the order of ~10^{22} cm^{-3} s^{-1}. At $g = 10^{21}$ cm^{-3} s^{-1}, the left-hand side of (9) is on the order of ~10^{-2} (being even less at lower excitation levels). At $g \geq 10^{13}$ cm^{-3} s^{-1}, the difference $F_n - F_p > 10\,kT$.

Thus, for the parameters presented above, expression (14) is valid at 10^{13} cm^{-3} s$^{-1} \leq g \leq 10^{21}$ cm^{-3} s^{-1}. Figure 1 presents the results of calculation of the photocurrent density as a function of the photoexcitation level. The logarithmic derivative $d\log j_{dc}/d\log g < 1$; i.e., we have a sublinear dependence of j_{dc} on g, which is due to an increase in $N_s(F_n) - n_s$ with growing photoexcitation level.

2. PHOTOADMITTANCE

Let us now consider the fundamental aspects of charge transport in a photoexcited polycrystal upon application of an AC voltage $U(t) + U_0 + \tilde{U}\exp i\omega t$, where $\tilde{U}$ and ω are the amplitude and the frequency of the small signal ($e\tilde{U}d/D \ll kT$, $\omega\tau_M \ll 1$, and $\tau_M = \varepsilon_0\varepsilon/e\mu_n N_d$ is the Maxwellian relaxation time in the quasi-neutral part of a grain). The AC current density reads $j(t) = j_{dc} + \tilde{j}\exp i\omega t$, where $\tilde{j}$ is the complex amplitude of current density oscillations.

When condition (9) is satisfied, the time-dependent density $n_s(t)$ of electrons localized at grain boundaries is determined from the equation

$$\tau_0 \frac{dn_s(t)}{dt} = [N_s - n_s(t)]\Phi_n(t) - 2\tau_0[I_n(t) + gL], \quad (15)$$

where $I_n(t)$ is the AC current of electron emission from the grain boundary into each neighboring grain; the function $\Phi_n(t)$ has the form of (11) but with time-dependent Z_1 and Z_2:

$$Z_{1,2}(t) = V(t)[1 \mp eU_b(t)/4V(t)]^2/kT,$$

$$V(t) = e^2 n_s^2(t)/8\varepsilon_0\varepsilon N_d;$$

$$U_b(t) = [U(t)/D - j(t)/e\mu_n N_d]d$$

is the voltage drop across the intercrystallite barrier. Since $n_s(t)$ and $I_n(t)$ can be expressed in terms of the

time-dependent distribution function of electrons over IS energy levels $f(E, t)$, (15) is just the equation for this function. In the case under consideration, $f(E, t) = f(E) + \tilde{f}(E)\exp i\omega t$, where $f(E)$ is defined by (6) and (7). The time-dependent density of electrons at IS energy levels reads $n_s(t) = n_s + \tilde{n}_s \exp i\omega t$. Calculations in many respects similar to those performed in [7] lead to the following expressions:

$$\tilde{n}_s = \frac{n_s \alpha B}{1 + 2\alpha(1-\beta^2)Z} \frac{e\tilde{U}_b}{2kT}, \quad (16)$$

$$\alpha = \frac{1}{n_s} \int_{E_V}^{E_C} \frac{\rho_s(E) f(E-F_n)[1-f(E)]dE}{1 + i\omega\tau_1 f(E-F_n)}, \quad (17)$$

where

$$B = \tanh(eU_b/2kT) - \beta, \quad Z = V/kT,$$

$$\tilde{U}_b = (\tilde{U}/D - \tilde{j}/e\mu_n N_d)d, \quad \tau_1 = \tau_0/\Phi_n.$$

At moderate temperatures, the integral in (17) can be calculated using the approximations

$$f(E-F_{n,p}) = \theta(F_{n,p} - E),$$

$$f(E-F_n)[1-f(E-F_n)] = kT\delta(E-F_n).$$

As a result, α is determined as a sum of two terms. The first of these does not vanish after the photoexcitation is terminated and describes the recharging of IS energy levels near the quasi-Fermi level F_n. By contrast, the second term is entirely determined by the polycrystal photoexcitation and describes the recharging of IS energy levels within the range $F_p < E < F_n$. At $F_n - F_p \gg kT$ the first term is much smaller than the second and can be neglected. Then, we obtain for $\tilde{n}_s$ at $F_n - F_p \gg kT$

$$\tilde{n}_s = \frac{[N_s(F_n - F_p)]B}{(1 + i\omega\tau)(1 + A)} \frac{e\tilde{U}_b}{kT}, \quad (18)$$

where

$$\tau = \tau_0/\Phi_n(1 + A), \quad A = 2Z(1-\beta^2)[N_s(F_n) - n_s]/n_s.$$

Since, with condition (9) fulfilled, the charge transport across the grain boundary is only effected by electrons, the results of [7] can be used to determine $\tilde{j}$. Neglecting small terms in the corresponding formula in [7] and taking into account (18), we obtain for the grain boundary admittance $Y_b = \tilde{j}/\tilde{U}_b$

$$Y_b = G_{HF} + i\omega C_{HF} - \frac{G_1}{1 + i\omega\tau}, \quad (19)$$

$$G_{HF} = \frac{ej_{dc}}{2kT}\left[\coth\left(\frac{eU_b}{2kT}\right) - \beta\right], \quad (20)$$

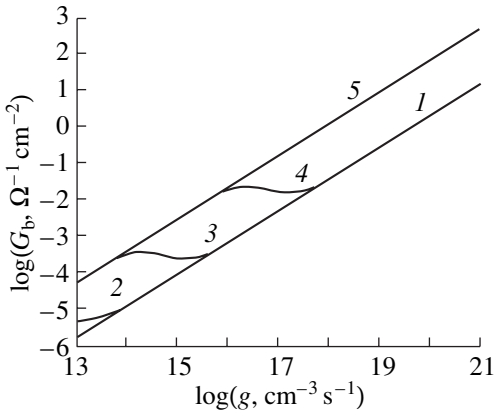

Fig. 2. Grain boundary conductance G_b vs. photoexcitation level g at U_b = 0.25 V and various frequencies ω. (*1*) $G_{dc}(\omega = 0)$; ω, s^{-1}: (*2*) 2π, (*3*) 200π, (*4*) $2 \times 10^4\pi$, and (*5*) G_{HF}.

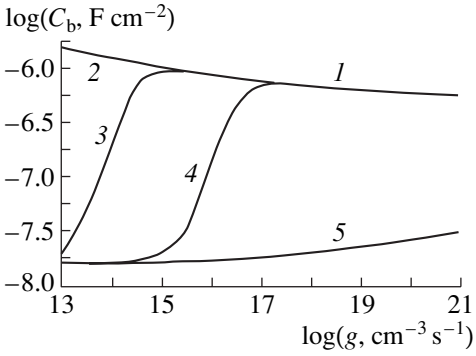

Fig. 3. Grain boundary capacitance vs. photoexcitation level g at U_b = 0.25 V and various frequencies ω. (1) C_b (ω = 0); ω, s^{-1}: (*2*) 2π, (*3*) 200π, (*4*) $2 \times 10^4\pi$, and (*5*) C_{HF}. Curves *1* and *2* merge.

where G_{HF}, $C_{HF} = \varepsilon_0\varepsilon N_d/n_s$ are the high-frequency ($\omega\tau \gg 1$) conductance and capacitance of the grain boundary, and the following designation is introduced:

$$G_1 = ej_{dc}AB/2kT(1 + A).$$

The last term in (19) determines the contribution from IS recharging to the grain boundary photoadmittance.

The photoadmittance of a polycrystal, calculated per unit sample cross-section area, reads

$$Y = \left(\frac{D}{Y_b d} + \frac{D}{e\mu_n N_d}\right)^{-1}. \quad (21)$$

Expressions for the grain boundary conductance ($G_b = \mathrm{Re}\, Y_b$) and capacitance ($C_b = \mathrm{Im}\, Y_b/\omega$) can easily be obtained from (19). Numerical calculations of G_b and C_b in polysilicon with parameters presented above

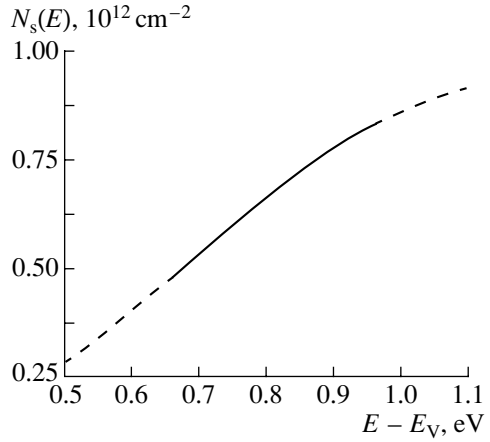

Fig. 4. Integral IS density N_s(E) calculated using (22) and (23) (solid line). Dashed line represents the preset integral IS density used in numerical calculation of j_{dc}, G_b, and C_b (Figs. 1–3).

show that at $eU_b \gg kT$ the grain boundary conductance and capacitance depend on U_b only slightly. This is due to the weak dependence of j_{dc} and τ on U_b. The results of the calculation of G_b and C_b as a function of the photoexcitation level at fixed U_b and ω are presented in Figs. 2 and 3. The rather strong dependence of τ on g leads to a distinctive dependence of G_b and C_b on g in the frequency range 10^3 s$^{-1} \le w \le 10^8$ s^{-1}. At low excitation levels, $\omega\tau \gg 1$ and

$$G_b = G_{HF}, \quad C_b = C_{HF};$$

τ decreases with increasing photoexcitation level. At $\omega\tau \approx 1$, a changeover from the high-frequency conductance and capacitance to low-frequency values occurs. At high excitation levels, $\omega\tau \ll 1$ and

$$G_b = G_{dc}, \quad C_b = C_{dc},$$

where

$$G_{dc} = G_{HF} - G_1, \quad C_{dc} = C_{HF} + G_1\tau,$$

are the low-frequency grain boundary conductance and capacitance. At $\omega\tau \ll 1$, the contribution from IS recharging to the grain boundary conductance and capacitance is the highest.

It should be noted that at low temperatures the dark admittance of the grain boundary is also determined by an expression of the type (19) with, however, $A = \rho_s(F_n)V(1 - \beta^2)/n_s$ [7].

3. SPECTROSCOPY OF INTERFACE STATES

Let us find relations that make it possible to determine $N_s(E)$ from measured static and dynamic characteristics of the electrical conductivity of a photoexcited polycrystal. In doing so, we assume that the parameters d, N_d, and μ_n are known. Then, we can easily calculate the grain boundary conductance and capacitance from measured ReY and ImY values, using (21). Therefore, it suffices to determine relations defining the explicit dependence of $N_s(E)$ on G_b, C_b, j_{dc}, and U_b; $U_b = (U_0/D - j_{dc}/e\mu_n N_d)d$.

With the use of (20), β can be expressed in terms of experimentally measurable quantities:

$$\beta = \coth(eU_b/2kT) - p_{HF},$$

where

$$p_{HF} = 2kTG_{HF}/ej_{dc}.$$

It is noteworthy that V, n_s, and F_n can be expressed in terms of β:

$$V = eU_b/4\beta, \quad n_s = \sqrt{2\varepsilon_0\varepsilon N_d U_b/e\beta},$$
$$F_n = E_C - \frac{eU_b(1+\beta^2)}{4\beta} + kT\ln\left[\frac{N_d}{N_C}\cosh\left(\frac{eU_b}{2kT}\right)\right]. \quad (22)$$

The following relation can be obtained from (19):

$$N_s(F_n) = n_s + \frac{n_s(p_{HF} - p_{dc})}{2(1-\beta^2)Z(B - p_{HF} + p_{dc})}, \quad (23)$$

where $p_{dc} = 2kTG_{dc}/ej_{dc}$.

Apparently, (22) and (23) are the sought-for relations. With p_{HF} and p_{dc} determined from measured j_{dc}, ReY, and ImY of a polysilicon sample at different optical radiation intensities incident on the sample, we can calculate, using the relations (22) and (23), $N_s(E)$ in the range $E_1 \le E \le E_2$, where E_1 corresponds to the lowest photoexcitation level and E_2, to the highest. This statement can be illustrated as follows: let us conditionally take the results of numerical calculations, presented in Figs. 1–3, to be experimental data and use them to calculate $N_s(E)$ by means of (22) and (23). The results obtained in this calculation are presented in Fig. 4, where the IS density is determined in the range E_V + 0.668 eV $\le E \le E_V$ + 0.961 eV. The photoexcitation level $g_1 = 10^{13}$ cm^{-3} s^{-1} corresponds to the lower limit, and the photoexcitation level $g_2 = 10^{21}$ cm^{-3} s^{-1} to the upper.

Expression (19) can also be applied to obtain the following useful relations, valid at $eU_b \gg kT$:

$$\frac{S_n}{\theta_n} = \frac{e^2(p_{HF} - p_{dc})p_{dc}}{2kTp_{HF}(C_{dc} - C_{HF})}, \quad (24)$$

$$j_R = \frac{2j_{dc}(p_{HF} - p_{dc})^2 C_{HF}}{(1-\beta^2)p_{HF}(C_{dc} - C_{HF})}. \quad (25)$$

The numerical value of the parameter θ_n can be found by comparing (22) with the expression

$$F_n = E_C + kT\ln(j_{dc}/2e\nu_n N_C\theta_n),$$

valid at $eU_b \gg kT$. Therefore, (24) allows us to determine S_n from experimental data. Relation (25) makes it possible to determine the dependence of j_R on the incident optical radiation intensity. Using the data presented in Figs. 1–3, we can readily make certain that, at any g, relation (24) gives a constant value of 10^{-13} cm^2 (i.e., $S_n = 10^{-15}$ cm^2 at $\theta_n = 0.01$), while relation (25) reproduces the linear dependence $j_R = 2egL$.

CONCLUSION

Thus, relations (22)–(23) can serve as a theoretical basis of an experimental technique for determining the integral IS density, electron capture cross section to IS energy levels, and recombination current at grain boundaries from the measured nonlinear photocurrent and photoadmittance in polysilicon.

REFERENCES

1. D. P. Joshi and D. P. Bhatt, IEEE Trans. Electron Devices **37**, 237 (1990).
2. D. P. Bhatt and D. P. Joshi, J. Appl. Phys. **68**, 2338 (1990).
3. K. M. Doshchanov, Fiz. Tekh. Poluprovodn. (St. Petersburg) **30**, 558 (1996) [Semiconductors **30**, 305 (1996)].
4. K. M. Doshchanov, Fiz. Tekh. Poluprovodn. (St. Petersburg) **31**, 954 (1997) [Semiconductors **31**, 813 (1997)].
5. G. E. Pike, Phys. Rev. B **30**, 795 (1984).
6. G. Blatter and F. Greuter, Phys. Rev. B **33**, 3952 (1986).
7. K. M. Doshchanov, Fiz. Tekh. Poluprovodn. (St. Petersburg) **28**, 1645 (1994) [Semiconductors **28**, 917 (1994)].
8. K. M. Doshchanov, Fiz. Tekh. Poluprovodn. (St. Petersburg) **32**, 690 (1998) [Semiconductors **32**, 619 (1998)].
9. K. M. Doshchanov, Geliotekhnika, No. 1, 69 (1999).

Translated by S. Ktitorov

Semiconductors, Vol. 35, No. 10, 2001, pp. 1132–1134. Translated from Fizika i Tekhnika Poluprovodnikov, Vol. 35, No. 10, 2001, pp. 1184–1187.

ELECTRONIC AND OPTICAL PROPERTIES OF SEMICONDUCTORS

Specific Features of the Liquid-Phase Epitaxial Growth of SiC Epilayers in Vacuum

D. A. Bauman[1], A. V. Gavrilin[2], V. A. Ivantsov[3], A. M. Morozov[2,4], and N. I. Kuznetsov[2,3]

[1] *Institute for High-Performance Computing and Databases, St. Petersburg, 198005 Russia*
e-mail: bauman@mail.ru
[2] *Crystal Growth Research Center, St. Petersburg, 194021 Russia*
[3] *Ioffe Physicotechnical Institute, Russian Academy of Sciences, Politekhnicheskaya ul. 26, St. Petersburg, 194021 Russia*
[4] *TDI Inc., 8660 Dakota, Gaithersburg MD 20877, USA*

Submitted February 12, 2001; accepted for publication February 13, 2001

Abstract—4*H*-SiC epilayers were grown by a liquid-phase epitaxy in vacuum. It was found that the seed layer with steps characteristic of liquid-phase epitaxy should be preliminary deposited on the substrate. It is demonstrated that growth in a vacuum leads to a decrease in the concentration of uncompensated carriers $N_d - N_a$ to the level of 2×10^{16} cm^{-3}. © *2001 MAIK "Nauka/Interperiodica".*

INTRODUCTION

In the last few decades, the progress in the field of semiconductor electronics stimulated the development of new methods for fabricating semiconductor structures and obtaining new semiconductor materials. Silicon carbide is one of the compounds widely used in this field due to its unique properties [1]. In this study, liquid-phase epitaxy (LPE) of SiC is investigated. This technique has a number of obvious advantages compared to other methods for obtaining structures with SiC layers. First, in a series of studies (see, for example, [2, 3]), it was suggested to use LPE to grow a covering layer over macrodefects (micropipes) on the substrate surface. This made it possible to grow high-uniformity epilayers with a low defect content. Another advantage is the possibility of growing the LPE layers on large-size substrates (as large as 50 mm in diameter) [4], which allows the fabrication of large-area semiconductor devices. In addition, LPE makes it possible to grow SiC layers with a rather large diffusion length and a low concentration of deep-level centers [5]. The aforesaid determines the prospects of LPE application for the fabrication of high-power semiconductor devices.

The major disadvantage of the container LPE technique is the high concentration of residual impurities. Impurity sources include, for example, residual gases in the growth chamber, or graphite components. The main purpose of these investigations was the development of the LPE of undoped 4*H*-SiC epilayers from the solution–melt in a graphite crucible. The concentration of the residual impurity in the layer in the range of $(1–5) \times 10^{16}$ cm^{-3} should be provided.

To solve this problem, a series of experiments was carried out in 99.9997%-pure argon with the crucible and thermal shielding made from graphite of extra-purity grade. This led to the growth of polytype-free *n*-4*H*-SiC epilayers with a residual impurity concentration of about 10^{17} cm^{-3}. The average normal growth rate measured was approximately 0.27 μm/h. To exclude uncontrollable impurity entering the layers from a gas atmosphere and further lowering the impurity concentration in the 4*H*-SiC layers, it was suggested to grow them in vacuum.

EXPERIMENTAL

For LPE of SiC, a Nika-S setup, which was adapted for this purpose, was used. A description of the setup may be found in [3]. Graphite components, including the crucible, were made of graphite of extra-purity grade. Single-crystal Si with a resistivity of ~400 Ω cm was used as the active component of the melt.

In all experiments carried out in a vacuum chamber with residual pressure of $(4–5) \times 10^{-4}$ Pa, the growth temperature was 1250°C and the growth duration was 2–5 h.

The CREE *n*-4*H*-SiC substrates misoriented by 3.5° and 8.0° to the $[1\bar{2}10]$ direction with respect to the basal face Si(0001) were used in growth. Some substrates had a mirrorlike polished surface. Other substrates had an *n*-type seed layer 1.0–1.5 μm thick with a residual impurity concentration of 10^{18} cm^{-3} and growth steps typical of LPE. The seed layer was preliminary deposited on the polished surface by LPE in Ar.

RESULTS

The LPE 4*H*-SiC monotypic epilayers 3 μm thick were grown on the substrates with a seed layer. The normal growth rate was 0.8 μm/h. Figure 1 demon-

strates a scanning electron microscopy (SEM) micrograph of the cleavage of one of these structures. The surface of the layer grown in vacuum has a step structure characteristic of LPE on misoriented substrates (Fig. 2). The preferential step arrangement along the $[1\bar{1}00]$ direction on the largest part of the substrate surface is clearly observed. The results of capacitance–voltage (*C–V*) measurements of the concentration of an uncompensated impurity are shown in Fig. 3. It can be seen that the impurity concentration is $(2–3) \times 10^{16}$ cm^{-3}, which is almost an order of magnitude lower than the value characteristic of the layers grown in Ar.

No growth steps were found on the surface of the layers grown on mirrorlike substrates without the preliminarily deposited epilayer, and the sample surfaces remained smooth. Even at the largest SEM magnification, the layers were indistinguishable on the cleavages of these structures. The *C–V* measurements revealed the concentration profile shown in Fig. 3. The profile depth (of about 0.2 μm) and its shape were independent of the duration of the substrate immersion into the melt. A sharp profile rise at 5×10^{18} cm^{-3} corresponds to the residual impurity level in the substrate. The shape of remaining part of the concentration profile, namely, the plateau at the level of 10^{17} cm^{-3}, can be explained as follows. The melt evaporation leads to the vapor condensation on the substrate after its separation from the melt. The vapor pressure of C at about 1250°C is about 10^{-15} Torr, which is negligibly small compared to the vapor pressure of Si at the same temperature. Thus, the melt deposited on the substrate is strongly depleted in C, which leads to a partial dissolution of the substrate in the layer of the condensed substance. During the subsequent cooling, the inverse solidification proceeds, which leads to the formation of the defect-rich layer with a concentration of about 10^{17} cm^{-3}. Under the conditions described above, growth from the melt was not observed on the mirrorlike substrate surfaces in vacuum.

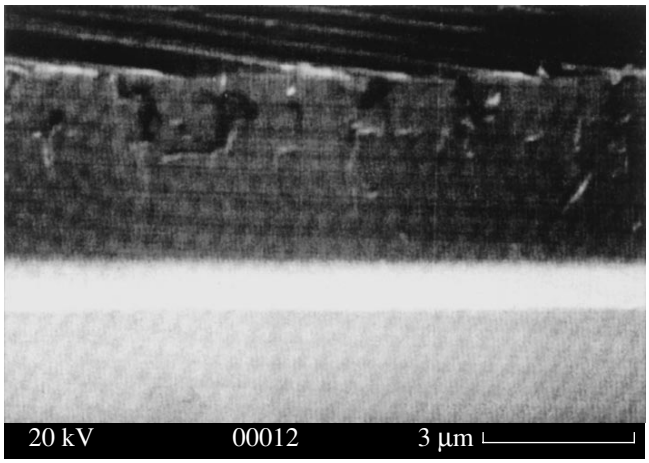

Fig. 1. Scanning electron micrograph of the cross-section cleavage of the structure grown in vacuum on the 4*H*-SiC substrate with a seed layer. The thickness of the upper epilayer is 3 μm. The thickness of a seed layer is 1 μm.

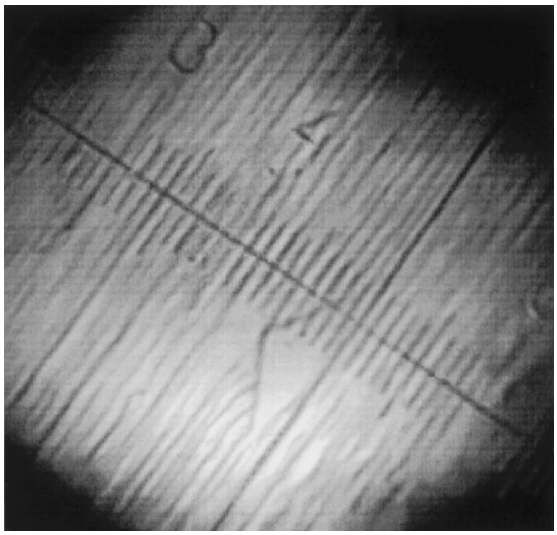

Fig. 2. Surface of 4*H*-SiC epilayer grown on the substrate with the preliminarily deposited seed layer. The growth time is 2 h, the layer thickness is 3 μm, and the growth temperature T = 1250°C. One scale division corresponds to 4 μm.

DISCUSSION

One of specific features of LPE in vacuum is a rather intense melt evaporation at above 1400°C. This leads, firstly, to a substantial variation in LPE conditions. Secondly, this restricts the growth time and, consequently, the epilayer thickness. Stable growth in a vacuum calls for a substantial decrease in the growth temperature. However, decreasing the temperature, in our case by 150°C compared to the growth in Ar, causes the carbon solubility in the melt to decrease. Accordingly, the rate of diffusion saturation of the melt with C at the interface with the surface of a graphite crucible decreases. In turn, it is well known that the onset of film solidification on the solid substrate calls for melt supersaturation above a certain critical value [6]. In the general case, this value depends on the temperature, the melt composition, the state of the surface, and some other factors. A decrease in the degree of melt supersaturation can be one possible factor inhibiting growth. In order to verify this assumption, we carried out an experiment in a vacuum with the melt which was preliminarily saturated in Ar at a higher temperature over the time interval exceeding the saturation time in the vacuum. This melt was preliminarily used for the LPE of SiC in Ar for 6 h at a higher temperature. As a result, only the defect-rich layer was found on the mirrorlike postgrowth substrate, whereas the epilayer was grown on the substrate with seed steps. Thus, we may assume that either the melt supersaturation in the vacuum under these conditions does not play a significant role in the onset of crystalli-

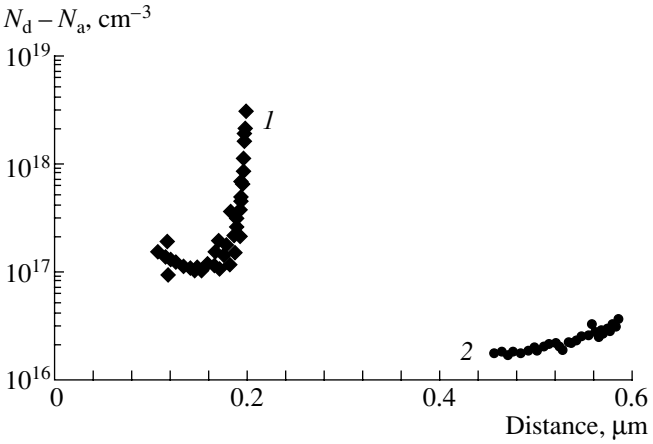

Fig. 3. Concentration of uncompensated impurity N_d–N_a in the 4*H*-SiC epilayer grown on (*1*) the mirrorlike substrate and (*2*) a substrate with the preliminarily deposited seed layer. The doping level of starting 4*H*-SiC substrates was 5×10^{18} cm^{-3}.

zation or its critical value is independent of the C content in the melt.

Another specific feature of the SiC epilayers grown by LPE in a vacuum is the low temperature gradient in the growth region of the melt compared to the gradient in Ar. This is apparently related to a weaker heat removal from the upper substrate surface and graphite components. The temperature gradient in the near-substrate part of the melt affects the flux of material to the substrate and the rate of the convective replenishment of the depleted near-substrate region, and determines the kinetics of epilayer nucleation and growth [7, 8]. A decrease in the temperature gradient may inhibit the growth under the aforementioned conditions.

Thus, it is demonstrated experimentally that a stable LPE in vacuum at sufficiently low temperatures (≤1250°C) calls for the deposition of the seed layer with characteristic growth steps on the substrate. However, the eventual establishment of the exact cause of inhibiting the growth on smooth substrates calls for additional investigations.

CONCLUSION

Based on the investigations carried out, LPE in a vacuum was suggested for obtaining SiC layers with a low concentration of residual impurities. The necessity of preliminary growth of the seed SiC layer was demonstrated. The growth in vacuum has its own special features. Specifically, intense melt evaporation may lead to a certain growth instability. In order to solve this problem, it seems appropriate to carry out the growth at a reduced pressure exceeding the pressure characteristic of a vacuum chamber. It was noted that the graphite components might serve as the impurity source in addition to the neutral atmosphere. For this reason, it is probable that the use of graphite covered with the SiC layer may further reduce the concentration. This will be the subject of further investigations.

ACKNOWLEDGMENTS

We thank V. A. Dmitriev for helpful comments during his participation in discussions. This study was supported in part by grants STP-971879 and INTAS no. 97-2141.

REFERENCES

1. B. J. Baliga, in *Proceedings of the 6th International Conference on Silicon Carbide and Related Materials, Kyoto, Japan, 1995*, p. 1.
2. S. V. Rendakova, I. P. Nikitina, A. S. Tregubova, and V. A. Dmitriev, J. Electron. Mater. **27**, 292 (1998).
3. S. V. Rendakova, V. Ivantsov, and V. A. Dmitriev, Mater. Sci. Forum **264–268**, 163 (1998).
4. V. E. Chelnokov, A. L. Syrkin, and V. A. Dmitriev, Diamond Relat. Mater. **6**, 1480 (1997).
5. N. I. Kuznetsov, A. M. Morozov, D. A. Bauman, *et al.*, Mater. Sci. Forum **338–342**, 229 (2000).
6. G. Sears, J. Chem. Phys. **25**, 154 (1956).
7. M. N. Kahn, S. Nishizawa, W. Bahng, and K. Arai, Mater. Sci. Forum **338–342**, 233 (2000).
8. S. A. Kukushkin and V. V. Slezov, *Disperse Systems on Solid Surfaces* (Nauka, St. Petersburg, 1996).

Translated by N. Korovin

Semiconductors, Vol. 35, No. 10, 2001, pp. 1135–1138. Translated from Fizika i Tekhnika Poluprovodnikov, Vol. 35, No. 10, 2001, pp. 1188–1191.

ELECTRONIC AND OPTICAL PROPERTIES OF SEMICONDUCTORS

Nonadditive Photoconductivity and Induced States in Zinc Selenide Crystals

V. P. Migal'

Zhukovsky National Aerospace University, Kharkiv, 61070 Ukraine

Submitted January 10, 2001; accepted for publication February 15, 2001

Abstract—The distribution of growth defects of various types arising in zinc selenide crystals grown from the melt under highly nonequilibrium conditions determines different, but interrelated metastable states of samples cut from different parts of the same ingot. The characteristic features of the dielectric response of these states, as well as of the states induced by an external action, are established. © *2001 MAIK "Nauka/Interperiodica".*

Bulk crystalline zinc selenide ingots (more than 50 mm in diameter) grown from the melt under highly nonequilibrium conditions involve various types of growth defects generating residual stresses. They form a complicated stressed–strained state of the crystal, whose specific attribute is the spectrum of elastic eigenmodes [1]. They also lead to the initiation of new degrees of freedom in the crystal (as in a vibratory system) owing to which the number of low-frequency elastic eigenmodes in the spectrum increases with the density of growth defects in a sample [2]. These features of the mechanical properties of these crystals make it possible to assign them to dissipative structures, which can be found in various metastable states [3]. On the other hand, identical frequencies of certain vibratory modes and other general attributes were revealed in the spectra of eigenmodes for samples of the same shape cut from the same ingot. Thus, we may assume that the samples cut from different parts of an ingot are in different, but interrelated metastable states. However, as a rule, anomalies of physical properties are discovered in individual samples of the ingot. These anomalies include the optical sensitization of new bands in the spectrum of steady-state photoconductivity under monochromatic illumination from the region of excitation or emission of photoluminescence, which is of scientific and practical interest [4].

The majority of II–VI crystals are high-resistivity piezoelectrics which are sensitive to various external factors; in particular, elastic fields of growth defects induce the dispersion region of the complex permittivity ε^* of the relaxation type [5] in these crystals. Further investigations along this line showed that ε^* measured at the frequency f_0, which is inversely proportional to the most probable relaxation time, is very sensitive to external factors. Thus, its variations during photoexcitation (at a wavelength of λ) or heating (a temperature of T) plotted on the phase plane in the form of $\varepsilon^*(\lambda)$ and $\varepsilon^*(T)$ diagrams integrally represent the self-consistent variations in internal elastic and electric fields of the II–VI crystals [6–8]. This makes it possible to consider such a crystal as a system in which the character of interrelations between the electric, elastic, and electronic subsystems is determined by the conditions of the growth and the postcrystallization cooling. In this case, the variations in ε^* at the phase plane under a certain external factor F can be considered as the consequence of the induced states through which a crystal passes in the course of adapting to these factors. It is evident that the $\varepsilon^*(F)$ diagrams contain much information about the "actual crystal" system, whose extraction requires a systematic approach to the analysis of the dielectric response of these crystals. In the context of such an approach, it is of interest to determine what attributes of dielectric response integrally represent the metastable state of various zinc selenide crystals, which is the main purpose of this study.

We investigated samples from nominally undoped zinc selenide crystals cut from ingots, whose diameter exceeded 50 mm, grown from the melt under high pressure in argon. The growth defects were investigated by the etch-pattern method and also by the shadow and polarization-optical methods. On the opposite faces of the samples of $10 \times 10 \times 3$ and $6 \times 6 \times 2$ mm in size, the indium–gallium contacts were deposited. The real (ε') and imaginary (ε'') parts of the complex permittivity (ε^*) of the samples were measured in the frequency range of 10^2–10^7 Hz using the capacitance method. A set of samples cut from the same ingot was divided into two groups. An attribute of a small number of samples in the first group was the initiation of new bands in the spectrum of steady-state photoluminescence under monochromatic illumination.

Typical growth defects, which generate residual stresses in all the samples, include planar defects and lamels of various nature. They can be seen in the crossed Nicol prisms for all the samples as the bands of alternating birefringence. The elastic fields of these defects generate a spatially nonuniform electric field in the piezoelectric crystal. This field determines the new

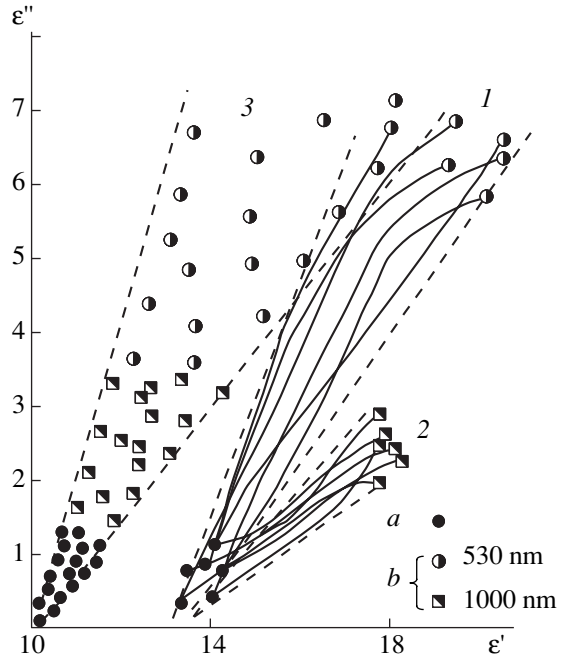

Fig. 1. Families of $\varepsilon^*(\Phi_0)$ diagrams for (*1*, *2*) the samples of the first group and also (*3*) the distribution of $\varepsilon^*(\Phi_0)$ points for the samples of the second group on the phase plane. T = 293 K. (*a*) ε_D^* and (*b*) ε_λ^* at 530 and 1000 nm.

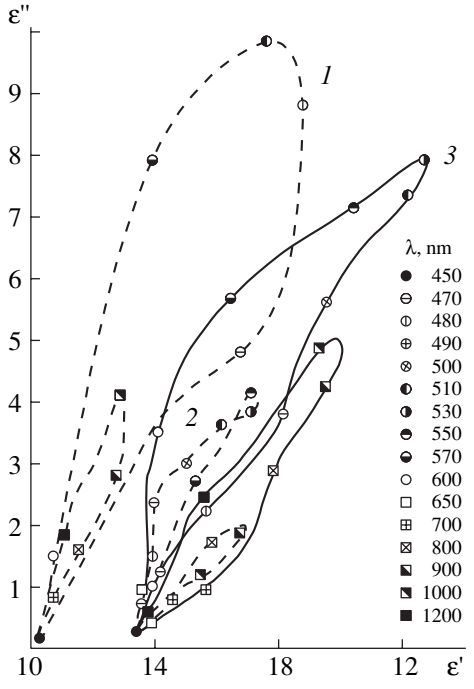

Fig. 2. Characteristic diagrams $\varepsilon^*(\lambda)$ for (*1*) the samples of the second group and (*2*, *3*) the samples of the first group.

character of interrelations between the subsystems in the perfect crystal. For this reason, it is not surprising that the correlation analysis of dielectric parameters for all the samples cut from different parts of an ingot showed that the permittivity ε'_D and dielectric-loss factor ε''_D measured in the dark for the second group of the samples at a frequency f_0 = 1 kHz correlate well with the growth-defect density. Thus, in spite of a spread in these parameters for the samples, the mapping points ε_D^* corresponding to their values on the phase plane are distributed within the sector *3* bounded by the dashed lines in Fig. 1. As a rule, in the samples of the second group, the growth-defect density correlates with the values of the ε_D^* modulus. It turns out that the set of the ε_λ^* points representing the sample states induced by the monochromatic illumination was also arranged within this sector. It is established that the metastable state for every sample represented by the point ε_D^* in the phase-plane sector is also characterized by the $\varepsilon^*(\lambda)$ and $\varepsilon^*(\Phi_0)$ diagrams, where Φ_0 is the intensity of the monochromatic light from the region of the highest extrinsic photosensitivity. For the samples of the given group, these diagrams are similar. A typical $\varepsilon^*(\lambda)$ diagram is shown in Fig. 2 (curve *1*). In these diagrams, the relationship between the lengths of arcwise sections and the relationship between the areas enveloped by two parts of the $\varepsilon^*(\lambda)$ diagram and corresponding to two spectral bands of photosensitivity are similar. It is remarkable that one part of the diagram appears to envelop another. If the photoexcitation intensity increases or if there is additional monochromatic illumination, no significant changes are observed in the shape of the $\varepsilon^*(\lambda)$ diagrams. Thus, in the phase-plane sector, each ε_D^* point represents a reasonably steady metastable state, and their set can be assigned to the same class of metastable states to which all the second-group samples belong.

At first glance, the ε_D^* phase-plane points, which correspond to samples of the first group, are arranged less regularly. However, the family of the $\varepsilon^*(\Phi_0)$ diagrams obtained for the photoexcitation of the samples from the region of the maxima of extrinsic photosensitivity (0.53 and 1.0 μm) forms two sectors (see Fig. 1, curves *1*, *2*). We emphasize that the character of these $\varepsilon^*(\Phi_0)$ diagrams is similar only provided that Φ_0 is less than a certain critical intensity Φ_{cr}, which is an individual characteristic of the sample. An attribute of the $\varepsilon^*(\lambda)$ diagrams for these samples, whose form is shown in Fig. 2 (curve *2*), is the separation of the diagram in the phase plane into two parts corresponding to different photosensitivity bands. The most important feature of the metastable states of the samples of the first group is a change in the character of the interrelations between the crystal subsystems for the excitation intensity exceeding a certain critical value Φ_{cr} that manifests itself in the dependence of the shape of the $\varepsilon^*(\lambda)$ diagrams on the excitation level Φ_0. For example, the $\varepsilon^*(\lambda)$ diagrams obtained for an intensity lower and higher than the critical one are radically different (see Fig. 2,

curves *2*, *3*). It should also be noted that, at high excitation intensities, the $\varepsilon^*(\lambda)$ diagram acquires elements of similarity characteristic of samples of the first group. Furthermore, at a high excitation intensity, the $\varepsilon^*(\lambda)$ diagrams for the samples of both groups have an overlapping region, which indicates that identical states can be induced in the samples of different groups (see Figs. 1, 2). It was established that the shape of the $\varepsilon^*(\lambda)$ diagrams also changes if the samples of the first group were subjected to an external biasing electric field or to a uniaxial compression $P = 25$ kgf/cm^2 along the [111] axis. Thus, the $\varepsilon^*(\lambda)_F$ diagrams obtained under additional F factors can also serve as attributes for the metastable states of the crystal. The metastable states formed in the samples of the first group likely represent the states with the interrelations between certain subsystems "frozen" in the course of postcrystallization cooling. In this case, the tendency of the samples of the first group to transfer from one class of states into another, which is observed when the photoexcitation intensity increases, can be considered as the recovery of these interrelations; this takes place because the samples of the first group have certain attributes of the metastable states of the samples of the second group in the induced state.

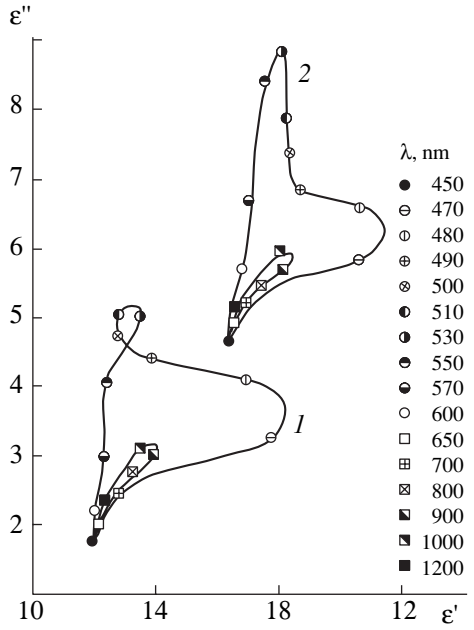

Fig. 3. $\varepsilon^*(\lambda)$ diagrams for the samples of the first group under illumination with a wavelength of (*1*) 650 and (*2*) 530 nm.

In the context of these concepts, the influence of an intense additional monochromatic illumination from the region of emission or excitation of the luminescence (0.65 and 0.53 μm) of the crystal, whose intensity $\Phi_\lambda > \Phi_{cr}$ can be considered as the transition of the samples of the first group into new induced states. Their attribute is the pronounced dependence of the $\varepsilon^*(\lambda)$ diagrams on a wavelength of intense illumination (see Fig. 3, curves *1*, *2*). We note that these states are characterized by new bands appearing in the photosensitivity spectrum.

It is evident that, owing to the influence of highly nonequilibrium growth conditions in certain regions of a zinc selenide crystal, specific structural formations are generated by multifactor nonequilibrium growth conditions. Therefore, we may assume that the metastable-state classes for the samples of the first and second groups differ in the distribution character of the complex centers responsible for photosensitivity. In the crystals of the first group, they are distributed nonuniformly over the regions that differ radically in their stressed–strained state; as a result, the character of interrelations between crystal subsystems changes with a self-consistent modification of internal fields under the influence of an external factor. In particular, certain interrelations between the subsystems are evidently "frozen," and there is a specific hierarchy of interrelations between the crystal subsystems. In this case, the nonequilibrium charge carriers screening the internal electric field reestablish the character of interrelations between the natural subsystems for the majority of zinc selenide crystals. In our opinion, this indicates that the relaxation processes are not completed during crystal growth under highly nonequilibrium conditions and verifies the individual character of the formation of interrelations between the crystal subsystems in the samples of the first group.

The above assumptions are corroborated partially by the results of investigating the influence of pressure and electric field bias on the bands of the alternating birefringence. It turns out that only in the samples of the first group does the reconstruction take place in the complicated pattern of bands under the uniaxial compression of the crystal to 25 kgf/cm^2 along the [111] axis. In this case, we observed the following: (a) the appearance of new bands, (b) the merging or splitting of the bands, and (c) a decrease in the intensity of certain bands down to their disappearance with increasing level of compression. Using the Rayleigh compensator, we found that certain interlayers rotate the polarization plane; i.e., they are optically active. Using nematic liquid crystals, we found that individual interlayers differ in their resistivity. This and the $\varepsilon^*(\lambda)$ and $\varepsilon^*(\Phi_0)$ diagrams make it possible to consider the crystals of the first group as heterogeneous systems for which a nonadditive photoconductivity is inherent.

Under a combined selective effect on various subsystems of the crystal, it also turned out to be possible to induce other states, whose attributes are similar to those observed in the samples having other photoelectric anomalies. In this case, the most efficient method for forming radically new metastable states is to treat a sample acoustically using an ac electric quadrupole field [9] in combination with intense additional illumination and heating.

Thus, the types, the density, and the distribution of growth defects inherited during crystal growth form two sets of interrelated metastable states in the ingot. These states differ in the character of dielectric response to an external effect. It is for this reason that the attributes suggested in this study for the states of an “actual crystal” system make it possible to establish the character of interrelations between the subsystems of the crystal and to choose optimal treatment methods.

ACKNOWLEDGMENTS

This study was supported by the Foundation for Basic Research of the Ministry of Education and Science of Ukraine.

REFERENCES

1. V. K. Komar’, V. P. Migal’, and O. N. Chugaĭ, Neorg. Mater. **34**, 800 (1998).
2. A. S. Gerasimenko, V. K. Komar, V. P. Migal, and O. N. Chugai, Funct. Mater. **4**, 392 (1997).
3. A. V. Gurevich and R. G. Mints, Usp. Fiz. Nauk **142**, 161 (1984) [Sov. Phys. Usp. **27**, 19 (1984)].
4. J. G. Gavrikova, V. P. Migal, and A. L. Rvachev, Phys. Status Solidi A **37**, K21–K24 (1976).
5. V. P. Migal’, A. L. Rvachev, and O. N. Chugaĭ, Fiz. Tekh. Poluprovodn. (Leningrad) **19**, 1517 (1985) [Sov. Phys. Semicond. **19**, 935 (1985)].
6. Yu. A. Zagoruĭko, V. K. Komar’, V. P. Migal’, and O. N. Chugaĭ, Funkts. Mater. **1**, 135 (1994).
7. Yu. A. Zagoruĭko, V. K. Komar’, V. P. Migal’, and O. N. Chugaĭ, Fiz. Tekh. Poluprovodn. (St. Petersburg) **29**, 1065 (1995) [Semiconductors **29**, 552 (1995)].
8. Yu. A. Zagoruĭko, V. K. Komar’, V. P. Migal’, and O. N. Chugaĭ, Fiz. Tekh. Poluprovodn. (St. Petersburg) **30**, 1046 (1996) [Semiconductors **30**, 556 (1996)].
9. I. A. Klimenko and V. P. Migal’, Pis’ma Zh. Tekh. Fiz. **25** (24), 24 (1999) [Tech. Phys. Lett. **25**, 980 (1999)].

Translated by V. Bukhanov

Semiconductors, Vol. 35, No. 10, 2001, pp. 1139–1143. Translated from Fizika i Tekhnika Poluprovodnikov, Vol. 35, No. 10, 2001, pp. 1192–1196.

ELECTRONIC AND OPTICAL PROPERTIES OF SEMICONDUCTORS

Electrical and Photoelectric Properties of Polycrystalline Textured CdTe

Yu. V. Klevkov, S. A. Kolosov, S. A. Medvedev, and A. F. Plotnikov

Lebedev Physical Institute, Russian Academy of Sciences, Leninskiĭ pr. 53, Moscow, 117924 Russia

Submitted January 22, 2001; accepted for publication February 15, 2001

Abstract—The temperature dependences of the resistivity and photoconductivity spectra of polycrystalline coarse-grained stoichiometric CdTe purified in the process of repeated recrystallization at temperatures two times lower than melting point were studied; CdTe ingots were synthesized from starting components subjected profound purification. It is shown that the main characteristics of polycrystals (resistivity, and the lifetime and mobility of carriers) are determined by composite complexes formed as a result of interaction between extended and point defects. The values of the product of mobility multiplied by lifetime are determined. © *2001 MAIK "Nauka/Interperiodica".*

1. INTRODUCTION

The application of cadmium telluride to detect ionized radiation is only worthwhile if the leakage currents in the devices do not exceed 10^{-7} A in electric fields of ~1000–3000 V/cm. This means that the crystal resistivity for such devices has to be ~10^8–10^9 Ω cm.

Up to now, CdTe single crystals doped with chlorine and obtained by the method of the traveling heater are considered as the best material for a high-quality detector. The compensated crystals possess a high resistivity ($\rho \approx 10^8$–10^9 Ω cm) and values of lifetimes of electrons (τ_e) and holes (τ_p) unsurpassed at the present time. One shortcoming of the method is the variation of the resistivity along the ingot.

Theoretical calculations show that CdTe can be obtained with the resistivity $\rho \approx 10^9$ Ω cm without doping with donor impurities if a structurally perfect crystal free of residual chemical impurities is grown. However, in practice, the resistivity of real nominally undoped crystals, irrespective of how they were fabricated, does not exceed 10^5–10^6 Ω cm [1].

Recently, the melt-growth methods for the preparation of undoped CdTe crystals with a stoichiometric composition and $\rho \approx 10^9$–10^{10} Ω cm [2, 3] using high-purity starting components have been developed. However, such crystals have structural imperfections and contain background impurities at the level of 10^{16} cm^{-3} (at best) and have a high level of compensation. Usually a set of deep electron states is present in the band gap which actually determines the main properties of the material (resistivity, and carrier mobilities and lifetimes).

The extended defects (dislocations, subgrain boundaries, twins, and grain boundaries), combined with point defects (impurity-related and native), play an important role in the formation of structurally complex defects and, as a consequence, produce deep electron states in the band gap of undoped crystals. At present, it is difficult to determine the role of all these defects.

We have attempted to obtain CdTe stoichiometric crystals with the lowest possible content of background impurities at lower temperatures. To this end, we developed methods for low-temperature synthesis with the subsequent profound purification of the compound and the rendering of its composition to that corresponding to minimum pressure (the composition close to stoichiometric at crystallization temperatures of 600–620°C) [4].

Despite the textured structure of the polycrystals obtained, it is possible, in our opinion, to separate the role of the grain boundaries in the formation of adjacent defects against the background of low amount of the main residual impurities ($\lesssim 10^{14}$ cm^{-3}) and minimum concentrations of the native point defects.

Previously, the role of extended defects in textured polycrystalline CdTe was studied by optical methods [5, 6]. In this study, the efforts along this line are continued using some electrical methods, in particular, by measuring the conductivity and photoconductivity temperature dependences.

2. EXPERIMENTAL

The high-purity *p*-CdTe samples ($\rho \approx 10^5$–10^6 Ω cm) of stoichiometric composition with a textured structure in the growth direction of the [111] single-crystal grain were used in measurements of electrical properties. The mean size of the single-crystal grain was no smaller than 1.5–2.0 mm in diameter. The samples were selected from polycrystalline ingots grown at temperatures of 600–620°C in the course of the finishing purification of CdTe [7]. Samples $5 \times 5 \times 1.5$ mm in size were prepared by mechanical grinding and lapping perpendicular to the growth direction in the {111} plane.

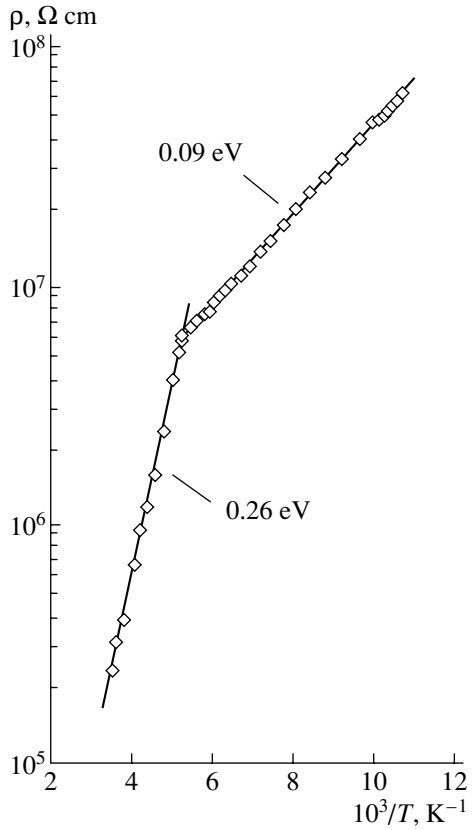

Fig. 1. Temperature dependence of *p*-CdTe resistivity.

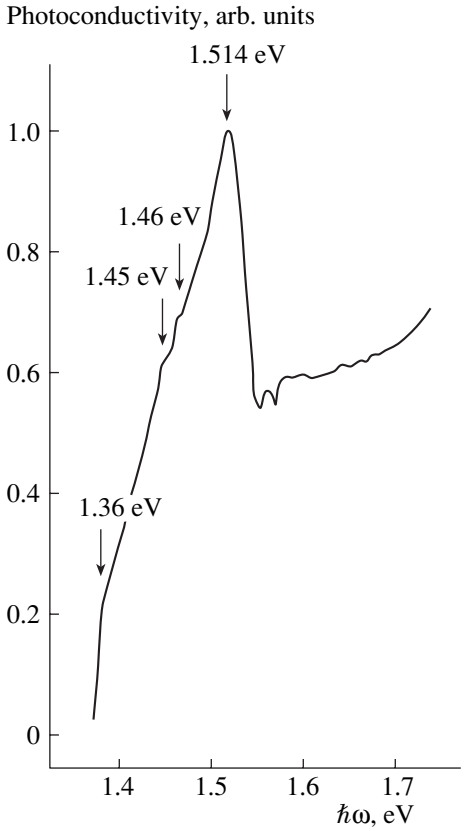

Fig. 2. *p*-CdTe photoconductivity spectrum.

The contacts on the {111} surfaces were formed after etching in a bromine–methanol solution by the gold deposition method from a gold chloride solution.

The photoconductivity was measured at the temperature T = 65 K in the region of intrinsic absorption (photon energies $\hbar\omega$ = 1.3–1.6 eV).

The temperature dependence of the resistivity was measured in the range T = 65–293 K.

3. RESULTS AND DISCUSSION

The temperature dependence of the resistivity of the *p*-CdTe sample cut along the growth direction of the monograin [111] is shown in Fig. 1. The resistivity of the sample at room temperature was $\rho \approx 3 \times 10^5$ Ω cm, which corresponds to the concentration of free holes $p \approx 2.9 \times 10^{11}$ cm^{-3} (for the hole mobility μ_p = 70 cm^2 V^{-1} s^{-1} [8]). As can be seen from Fig. 1, two types of centers are present in this sample with the energy levels E_v + 0.09 eV and E_v + 0.26 eV.

For this set of energy levels and the total concentration of electrically active impurities of $<10^{13}$ cm^{-3}, it is difficult to bring these parameters into agreement with each other, since neither the calculations according to the formulas of classical statistics [9] nor according to the formulas of heavily compensated semiconductors [10] yield such values of free carrier concentrations if only point defects are believed to be present in the sample.

To a certain extent, the contradictions can be eliminated if one assumes that the material parameters are determined by composite defects (complexes) appearing as a result of the interaction of extended defects with point ones (impurity-related and native) due to their segregation. The main extended defects in our materials are the grain boundaries and to a lesser extent the twins, since the dislocation density measured in the single-crystal grain does not exceed 10^2 cm^{-2}.

The energy levels we observed were found as far back as 1989 [11] both in compensated and uncompensated CdTe crystals obtained by the traveling-heater method. Up to 20 types of defects forming the energy levels in the band gap were reported by Samimi *et al.* [11]. It was concluded that most of these defects are not simple point defects or impurities but composite complexes including both extended and point defects.

Actually, other centers with shallower energy levels may be present in our samples. The spectral dependence of the photoconductivity presented in Fig. 2 confirms this assumption. The long-wavelength threshold of the photoconductivity corresponds to the electron transition from the energy level E_v + (0.26 ± 0.02) eV

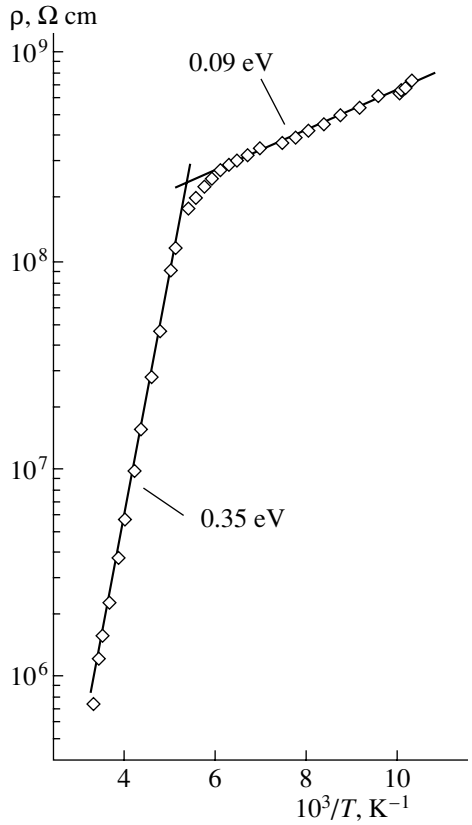

Fig. 3. Temperature dependence of *p*-CdTe resistivity after annealing in Cd vapor

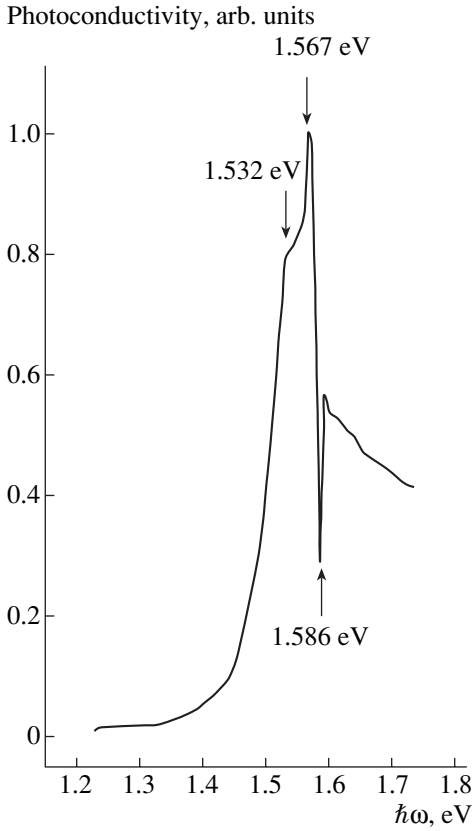

Fig. 4. Photoconductivity spectrum of CdTe annealed in Cd vapor.

to the conduction band (the photoconductivity in *p*-CdTe is effected by free electrons [12]). The rise of the photoconductivity signal in the region of shorter wavelengths is indicative of the presence of shallower levels, which apparently make an insignificant contribution to the free carrier concentration. Both the isolated impurity centers and the clusters of impurity centers in the vicinity of the extended defects may be responsible for the position of the levels in this energy region.

A sharp decrease in the photoconductivity signal for the photon energies $\hbar\omega > 1.514$ eV is caused either by the high surface-recombination rate or by a strong excitonic absorption in this energy region.

It is worthwhile noting that the estimations of the product of the lifetime of electrons (τ_e) by the value of their mobility (μ_e) on the basis of the steady-state photoconductivity signal yield the value of 2×10^{-3} cm^2 V^{-1}. This value of $\mu_e\tau_e$ is usually characteristic of CdTe:Cl crystals of the detector quality [13].

The temperature dependence of the resistivity of this sample after its annealing in the saturated Cd vapor at a temperature of ~650°C for 72 h is presented in Fig. 3. The inversion of the conductivity type was not observed. As a result of annealing, the resistivity increased only by two times at room temperature. The energy level E_v + 0.26 eV transformed into the level E_v + 0.35 eV. No significant changes in the free hole concentration occurred.

This fact indicates that the redistribution of charges over the defect, which already exists, occurred, e.g., owing to the change of the distances between the dangling bonds at the boundaries or to a partial redistribution of impurities close to them. These changes are more pronounced in the spectrum in Fig. 4. The long-wavelength threshold of the photoconductivity signal in the annealed sample shifted to shorter wavelengths and corresponds to the electron transition from the levels ~E_v + 0.35 eV and E_v + 0.09 eV to the conduction band. The energy levels observed at the rise edge of the photoconductivity signal (Fig. 2) are not distinguishable in the annealed sample.

The dip in the photoconductivity spectrum in the region of $\hbar\omega \approx 1.58$ eV is apparently associated with strong excitonic absorption. Similar photoconductivity spectra have previously been observed at nearly liquid-helium temperatures [14]. The photoconductivity in this spectral region was not observed at higher temperatures [14], which can be associated with short electron lifetimes.

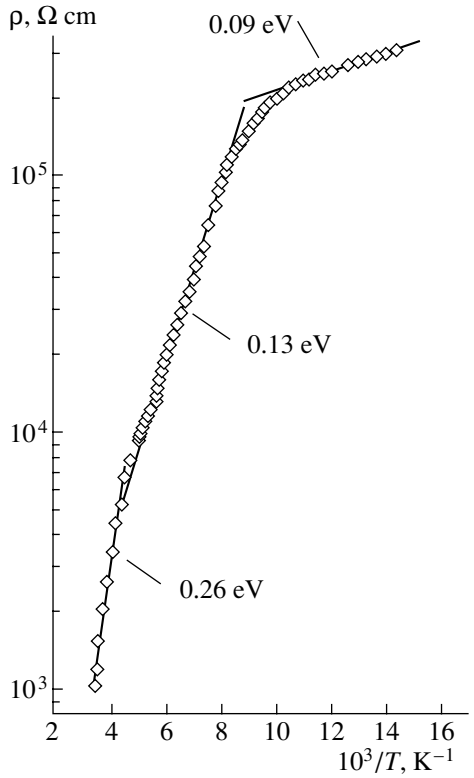

Fig. 5. Resistivity temperature dependence of CdTe crystallized at low temperatures.

We should note that, according to the signals of the steady-state photoconductivity, the lifetime of free electrons in the annealed samples increases by nearly two times (~4 μs).

The electron lifetime values obtained in the purified CdTe polycrystals indicate that the defects introducing the levels $E_v + 0.09$ eV, $E_v + 0.26$ eV, and $E_v + 0.35$ eV only slightly affect the transport properties of electrons.

The resistivity temperature dependence for the polycrystalline CdTe sample cut from the ingot part crystallized at lower temperatures is shown in Fig. 5. As can be seen from Fig. 5, the sample resistivity at room temperature is as low as ~10^3 Ω cm. In addition to defects with the local levels $E_v + 0.09$ eV and $E_v + 0.26$ eV, a previously unobserved defect makes itself evident in this sample (it was possibly not seen due to a low concentration of such defects in the samples with higher resistivity), with the state $E_v + (0.13 \pm 0.02)$ eV being related to this defect. The concentration of such defects is ~10^{13} cm^{-3} and is comparable with the concentration of centers related to the level $E_v + 0.26$ eV. We believe that this is one of the possible centers, which actually determines the free-electron lifetime, since we failed to measure the photoconductivity in this sample owing to a low signal amplitude (the lifetime being too short). At the same time, these are the centers which cause an intense line of radiative recombination to appear near the grain boundaries; this line was observed in the photoluminescence spectrum at 100 K [6]. We should note that these centers made themselves evident in the samples with higher resistivity in the form of a poorly resolved line ($\hbar\omega = 1.46$ eV) in the photoconductivity spectra (Fig. 2). We believe that such a center also has a complicated structure and is formed with the participation of an extended defect and uncontrollable impurity likely of donor type.

4. CONCLUSION

At the present time, the nature of many deep electronic states in CdTe associated with the various point defects is established rather reliably. Unfortunately, despite intense studies over a number of years in this field, the electronic properties of extended defects in II–VI compounds (dislocations, twins, and grain boundaries) remain insufficiently studied.

Schroter *et al.* [15] attempted to clarify the situation using the behavior of dislocations in silicon as an example. The extended defects are the source of stresses and long-range electric fields; they interact with point defects thus introducing deep electronic states and, consequently, substantially affect the concentration, mobilities, and lifetimes of carriers [15]. The nature of such defects [15], is determined both by the atomic structure of the extended defect and by the mechanism of interaction with the point defects.

The results of our study are completely consistent with this opinion. The energy levels observed with activation energies of 0.13 and 0.26 eV are consistent within the limits of experimental accuracy with the emission bands *Y* (1.47 eV) and *Z* (1.36 eV), which were recorded in the photoluminescence measurements [6] in CdTe polycrystals of stoichiometric composition. However, the results obtained do not allow us to judge unambiguously either the electronic structure of the extended defects, or the nature of their interaction with the point defects. Therefore, the role of composite defects in the formation of crystals with a high resistivity and long lifetime of mobile carriers still remains unclear. For its clarification, more sophisticated research methods must be used (local-structural, polarization, etc.). We plan to continue our studies along these lines.

ACKNOWLEDGMENTS

We are grateful to Professor V.S. Bagaev for valuable comments.

This study was supported by the Russian Foundation for Basic Research, project no. 99-02-18161.

REFERENCES

1. M. Hage-Ali and P. Siffert, Nucl. Instrum. Methods Phys. Res. A **322**, 313 (1992).

2. P. Rudolph, S. Kawasaki, S. Yamashita, *et al.*, J. Cryst. Growth **149**, 201 (1995).
3. P. Rudolph, S. Kawasaki, S. Yamashita, *et al.*, J. Cryst. Growth **161**, 28 (1996).
4. S. A. Medvedev, Yu. V. Klevkov, V. S. Bagaev, and A. F. Plotnikov, Nauka–Proizvod. **6** (31), 16 (2000).
5. A. Gukasyan, A. Kvit, Y. Klevkov, and S. Oktyabrsky, Solid State Commun. **97** (10), 897 (1996).
6. A. Gukasyan, A. Kvit, Y. Klevkov, and S. Kazaryan, Mater. Sci. Eng. B **B47**, 87 (1997).
7. S. A. Medvedev and Yu. V. Klevkov, RF Patent No. 243014 (1999).
8. S. Devlin, *Physics and Chemistry of II–VI Compounds*, Ed. by M. Aven and J. Prener (North-Holland, Amsterdam, 1967; Mir, Moscow, 1970).
9. K. Seeger, *Semiconductor Physics* (Springer-Verlag, New York, 1973; Mir, Moscow, 1977).
10. G. F. Neumark, Phys. Rev. B **26** (21), 2250 (1982).
11. M. Samimi, B. Biglary, M. Haga-Ali, *et al.*, Nucl. Instrum. Methods Phys. Res. A **289**, 243 (1989).
12. V. E. Lashkarev, M. K. Sheĭnkman, and A. V. Lyubchenko, *Nonequilibrium Processes in Photoconductors* (Naukova Dumka, Kiev, 1981).
13. Y. Eisen and A. Shor, J. Cryst. Growth **184/185**, 1302 (1998).
14. R. E. Kremer and W. B. Leigh, J. Cryst. Growth **86**, 490 (1988).
15. W. Schroter, J. Kronewitz, U. Gnauert, *et al.*, Phys. Rev. B **52** (19), 13726 (1995).

Translated by T. Galkina

Semiconductors, Vol. 35, No. 10, 2001, pp. 1144–1146. Translated from Fizika i Tekhnika Poluprovodnikov, Vol. 35, No. 10, 2001, pp. 1197–1199.

ELECTRONIC AND OPTICAL PROPERTIES OF SEMICONDUCTORS

Density of Localized States in $(Pb_{0.78}Sn_{0.22})_{0.95}In_{0.05}Te$ Solid Solutions

S. A. Nemov*, D. A. Potapova, Yu. I. Ravich*, and S. D. Khanin****

** St. Petersburg State Technical University, Politekhnicheskaya ul. 29, St. Petersburg, 195251 Russia*

*** Hertzen Russian State Pedagogical University, St. Petersburg, 191186 Russia*

Submitted February 15, 2001; accepted for publication February 16, 2001

Abstract—The hopping conductivity and the Seebeck coefficient have been measured in $Pb_{0.78}Sn_{0.22}Te$ with 5 at. % In and supplementary donor doping with Cl. The experimental data obtained are compared with similar results for supplementary acceptor doping with Tl. At temperatures of 150 K and higher, the thermoelectric power changes its sign from positive to negative on the introduction in sufficient amounts of either donors or acceptors. An analysis of the dependence of the thermoelectric power on the content of supplementary donors and acceptors yields the density of localized indium states as a function of energy. The function is essentially nonmonotonic, exhibiting both a density-of-states peak and a minimum between this peak and the conduction band. © *2001 MAIK "Nauka/Interperiodica".*

In indium-doped $Pb_{1-x}Sn_xTe$ solid solutions, hopping conduction is observed at unusually high temperatures and impurity densities [1–4], with the transport occurring by hopping between nearest neighbors in the temperature range T = 100–400 K. The activation energy of hopping conductivity can be determined from the temperature dependence of conductivity σ [1, 2], and an analysis of the thermoelectric power under supplementary donor and acceptor doping yields the density of localized states as a function of energy ε [3, 4]. Supplementary doping with impurities forming no localized states near the chemical potential level makes it possible to shift the chemical potential μ with respect to electronic energy states and thereby to scan the energy spectrum of localized states.

The thermoelectric power S is used to determine the density g of localized states using the relation obtained by means of the effective medium theory [5],

$$S = -\frac{5}{6}\frac{k}{e}\left(\frac{\varepsilon_h^2}{2kT} + \frac{2}{3}\pi^2 kT\right)\left(\frac{d\ln g}{d\varepsilon}\right)_{\varepsilon=\mu}, \qquad (1)$$

where ε_h is the activation energy of hopping conductivity. With ε_h determined from the temperature dependence of conductivity, the thermoelectric power can be used to find the quantity

$$f = \left(\frac{d\ln g}{d\varepsilon}\right)_{\varepsilon=\mu} \qquad (2)$$

as a function of the electron concentration n equal to the difference of the donor and acceptor densities (if each electrically active atom generates or absorbs an electron, which is the case for all of the dopants used: In, Tl, and Cl). Numerical integration over n yields the density of states g and the chemical potential μ as functions of n; i.e., it gives the dependence $g(\mu)$ in parametric form [4].

Previous studies [3, 4] have shown that, at an In content of 3 at. %, the thermoelectric power is negative at any temperature and concentration of supplementary dopants, and therefore, the density of states determined by the method of supplementary donor and acceptor doping grows steadily with increasing energy. In contrast, at an In content as high as 5 at. %, the thermoelectric power reversed its sign both with increasing temperature [2] and upon addition of a Tl acceptor impurity [4]. An analysis of the experimental curves obtained revealed a peak of the density of localized states [4]. It would be expected that there is a minimum in the density of states (soft gap) between this peak and the conduction band.

To reveal the $g(\mu)$ minimum, we measured and analyzed the conductivity and the thermoelectric power in a solid solution with 5 at. % indium and supplementary doping with Cl, the latter impurity being a singly charged donor in IV–VI compounds. The obtained experimental results are analyzed together with data on supplementary doping with thallium [4].

The activation energy ε_h determined from the slope of the straight lines representing the $\ln\sigma(T^{-1})$ dependence was nearly the same for all the samples [(45 ± 5) meV] for both Cl and Tl. Therefore, supplementary donor or acceptor doping at a fixed In content

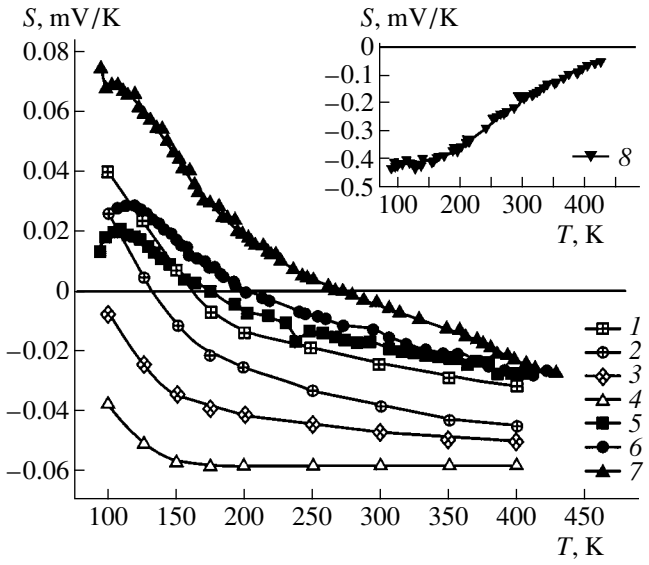

Fig. 1. Thermoelectric power vs. temperature for $(Pb_{0.78}Sn_{0.22})_{0.95}In_{0.05}Te$ samples with supplementary doping with Cl or Tl. N_{Tl}: (*1*) 0, (*2*) 1, (*3*) 1.5, and (*4*) 2 at. %; N_{Cl}: (*5*) (0.6–1), (*6*) 1, (*7*) 2, and (*8*) 2.5 at. %.

has virtually no effect on the scatter of energy levels, determining the activation energy of hopping conduction.

Figure 1 shows temperature dependences of the thermoelectric power under supplementary doping with chlorine or thallium (up to concentrations of N_{Cl} = 2.5 at. % and N_{Tl} = 2 at. %). It is noteworthy that at relatively low temperatures (150 K and lower), where the thermoelectric power is positive without supplementary doping, its sign is reversed to negative upon doping with sufficient amounts of either acceptors or donors. For example, at a Cl content of 2.5 at. %, the thermoelectric power is negative over the entire temperature range under study.

The density of localized states was calculated as a function of energy (at 150 K) by the method mentioned above and described in detail in [4]. The f values calculated using the experimental thermoelectric power S and the activation energy ε_h obtained from the temperature dependence of conductivity are given in the table in relation to the electron concentration n. The density of states $g(\mu)$ is presented in Fig. 2. This dependence shows not only a maximum, but also a minimum lying ~100 meV higher. The result obtained confirms the earlier assumptions of nonmonotonic energy dependence of the density of localized states.

The data on the density of localized states at an In content of 3 and 5 at. %, obtained in this study and in [4], show that the region of localized states extends into the band gap as deep as at least ~100 meV, this value noticeably exceeding the activation energy of hopping conductivity, equal to 35–45 meV. This difference can

Experimental values of thermoelectric power S at T = 150 K and the $f(n)$ function for $(Pb_{0.78}Sn_{0.22})_{0.95}In_{0.05}Te$ with supplementary doping with Tl and Cl

Sample no.	N_{Tl}, at. %	N_{Cl}, at. %	S, μV/K	n, cm^{-3}	f, eV^{-1}
*C*6		2.5	–400	11.25	34.08
*C*5		2	44	10.50	–3.749
*C*3		1	17	9.00	–1.448
*C*1		0	7	7.50	–0.596
*T*1	0		7	7.50	–0.596
*T*2	0.5		7	6.80	–0.596
*T*3	1		–12	6.00	1.022
*T*4	1.5		–35	5.30	2.982
*T*5	2		–58	4.50	4.941

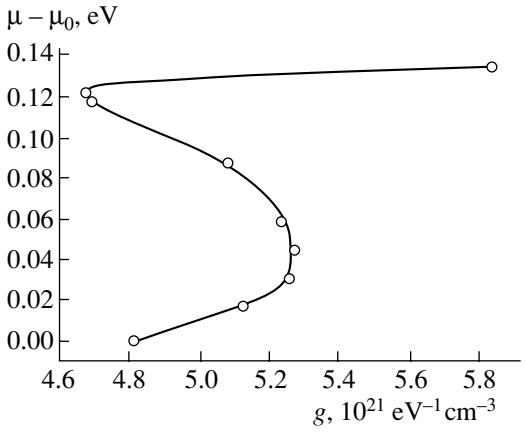

Fig. 2. Density of electronic localized states in $(Pb_{0.78}Sn_{0.22})_{0.95}In_{0.05}Te$ solid solution.

be accounted for by taking into account that the activation energy of hopping conductivity is the mean energy distance between neighboring impurity centers, whereas the width of the localized states region can be enhanced by large-scale heterogeneities. The assumption that there exists a large-scale random potential was used earlier [1] to account for the dependence of the activation energy on the content of In impurity giving rise to the localized states under study.

REFERENCES

1. Yu. I. Ravich, S. A. Nemov, and V. I. Proshin, Fiz. Tekh. Poluprovodn. (St. Petersburg) **29**, 1448 (1995) [Semiconductors **29**, 754 (1995)].
2. S. A. Nemov, V. I. Proshin, and Yu. I. Ravich, Fiz. Tekh. Poluprovodn. (St. Petersburg) **30**, 2165 (1996) [Semiconductors **30**, 1128 (1996)].
3. T. G. Abaĭdulina, S. A. Nemov, V. I. Proshin, and Yu. I. Ravich, Fiz. Tekh. Poluprovodn. (St. Petersburg) **30**, 2173 (1996) [Semiconductors **30**, 1133 (1996)].
4. Yu. I. Ravich and S. A. Nemov, Fiz. Tekh. Poluprovodn. (St. Petersburg) **35** (2), 164 (2001) [Semiconductors **35**, 158 (2001)].
5. T. E. Whall, J. Phys. C **14**, L887 (1981).

Translated by D. Mashovets

Semiconductors, Vol. 35, No. 10, 2001, pp. 1147–1150. Translated from Fizika i Tekhnika Poluprovodnikov, Vol. 35, No. 10, 2001, pp. 1200–1203.

ELECTRONIC AND OPTICAL PROPERTIES OF SEMICONDUCTORS

Interference of Polarized Beams near the Isotropic Point of the CdS Crystal

I. V. Brovchenko, V. I. Romanenko*, and V. I. Tovstenko

Institute of Physics, National Academy of Sciences of Ukraine, Kiev, 03028 Ukraine

** e-mail: vr@iop.kiev.ua*

Submitted January 17, 2001; accepted for publication March 5, 2001

Abstract—The interference of polarized beams in thin CdS crystals placed between crossed polarizers is considered. It is shown that in the case of incomplete polarization of the interfering beams the spectral position of the transmission minimum near the isotropic point depends on the crystal thickness. © *2001 MAIK "Nauka/Interperiodica".*

A certain time ago, an analysis of the transmission spectra of thin CdS crystals in polarized beams (a shift of the transmission minimum was observed on samples placed between crossed polarizers whose principal transmission axes were oriented at an angle of 45° to the crystal optical axis **C**) led to the conclusion that the refractive index depends on the crystal thickness [1–5]. The effect was so strong that possible changes in the refractive index due to structural defects, the deformation of very thin samples, the deformation associated with optical contact between the crystal and substrate, etc., could be disregarded and the dependence of the refractive index on the sample thickness as a purely geometrical factor could be considered the principal reason for the shift of the minimum.

The thickness dependence of the spectral position of the transmission intensity maximum was observed in [6] with a collinear configuration of polarizers. This effect was attributed to a change in $|\Delta n| = |n_\perp - n_\parallel|$, resulting from the dissimilarity of structural defects in crystals with different thicknesses ($n_\perp$ and $n_\parallel$ are the refractive indices for light polarized, respectively, perpendicularly and parallel to the optical axis of the crystal).

On the other hand, no dependence of the refractive index on sample thickness was observed in [7–11]. For instance, the resonance positions under quantum confinement conditions were in good agreement with the refractive indices in thick crystals [7], and the direct measurements of $n(\lambda)$ in [8–11] for thicknesses of 0.2–1 μm did not reveal any differences (λ is the wavelength of light in free space).

The aim of this study was to demonstrate that the interpretation of the interference pattern presented in [1–6] is not unambiguous: the unusually high sensitivity of the spectral position of extrema near the isotropic point can be accounted for by specific features of interference, manifested with incomplete polarization of the interfering beams, which, in our opinion, is always the case in real optical systems.

Let us consider this issue in more detail. We denote the ratio of intensities of the maximum and minimum transmissions of the input polarizer by y_p and the ratio of the same quantities for the analyzer by y_a. Futhermore, let the crossing angle of the input and output polarizers be Θ, and let the angular deviation of the optical axis of the wafer from the direction of the maximum transmission of the input polarizer be β.

Using the results obtained in [12–15], we can demonstrate that, at normal incidence onto the crystal surface, the ratio of intensities of the incident and transmitted light is

$$I = 0.5k_pk_a[|T_1|^2S_1^2F_1 + |T_2|^2S_2^2F_2 - |T_1||T_2|S_1S_2(1-y_a)\sin 2(\Theta-\beta)\cos(\alpha_1-\alpha_2)], \quad (1)$$

where k_p and k_a are the squared amplitudes of the maximum transmission for, respectively, the input and output polarizers;

$$S_1 = \sin\beta - \sqrt{y_p}\cos\beta; \quad (2)$$

$$S_2 = \cos\beta + \sqrt{y_p}\sin\beta; \quad (3)$$

$$F_1 = \sin^2(\Theta-\beta) + y_a\cos^2(\Theta-\beta); \quad (4)$$

$$F_2 = \cos^2(\Theta-\beta) + y_a\sin^2(\Theta-\beta); \quad (5)$$

$$T_j = \frac{1-R_j}{\sqrt{(1-R_j)^2 + 4R_j\sin^2 k_j}}; \quad (6)$$

$$\alpha_j = k_j + \phi_j; \quad (7)$$

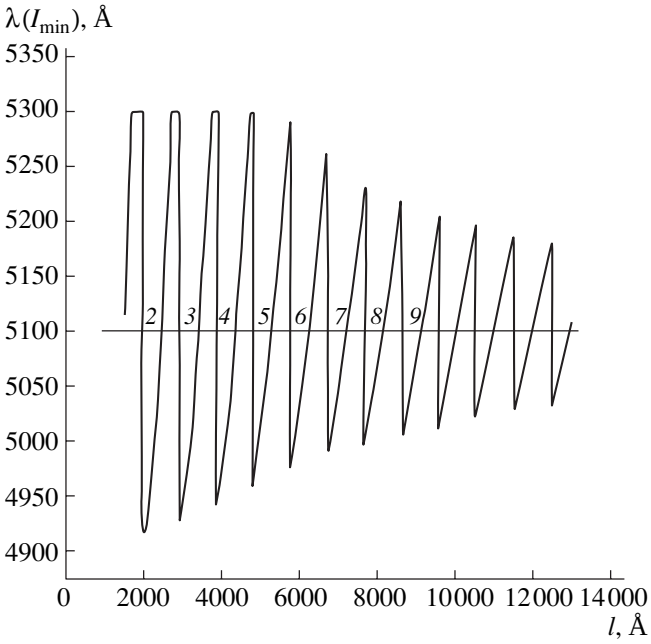

Fig. 1. Spectral position of the transmission minimum as a function of the crystal thickness near the inversion point for the CdS crystal (4950 Å ≤ λ ≤ 5250 Å) at incomplete polarization of the interfering beams.

$$\phi_j = \arctan\frac{R_j \sin k_j}{1 - R_j \cos 2k_j}; \quad (8)$$

$$R_j = \left(\frac{n_j - 1}{n_j + 1}\right)^2; \quad (9)$$

$$k_j = 2\pi n_j \frac{l}{\lambda}; \quad (10)$$

and l is the sample thickness.

We denote by subscript $j = 1$ the field amplitudes, phases, and refractive indices for the polarization perpendicular to the crystal optical axis **C**, whereas $j = 2$ stands for the parallel polarization.

The tabulated values of the index n_1 in the range λ = 4950–5250 Å [9] were used for numerical calculation with formula (1). The following expression was obtained using these values:

$$n_1 = n_\perp = 2.31452 + \frac{5.344}{\lambda - 4855} + \frac{225.244}{\lambda - 4406.23}. \quad (11)$$

At the points λ = 4950, 5100, and 5250 Å, formula (11) is in agreement with the experimental data to within $\pm 1 \times 10^{-6}$; the maximum deviation at other points of the interval does not exceed $\pm 3.7 \times 10^{-3}$. In plotting the dependence of n_2 on wavelength λ, we used the tabulated values of $|n_\perp - n_\parallel|$ from [16] for the points $\lambda = \lambda_i +$ 150 Å and $\lambda = \lambda_i - 100$ Å, where λ_i is the inversion point:

$$n_2 = n_\parallel = 2.38342 + \frac{4.5424}{\lambda - 4827} + \frac{177.7}{\lambda - 4419}. \quad (12)$$

According to [9], $n_\perp(\lambda_i) = n_\parallel(\lambda_i) = 2.661$.

Let us now consider formula (10) in more detail. In thick samples, when the interference peaks with amplitudes T_1 and T_2 are not resolved and the amplitudes themselves are smooth functions of the optical thickness nl of a crystal, the spectral position of the transmission peaks is independent of the depolarization of interfering beams, with the principal minimum coinciding with the inversion point λ_i and corresponding to the zero order $m = 0$ of interference

$$(n_\perp - n_\parallel) l = m\lambda. \quad (13)$$

Formula (13) is not valid for thicknesses at which, according to [13], the interference minima (maxima) T_j are resolved. Indeed, near the inversion point, at distances of about 100–150 Å, the difference $|n_\perp - n_\parallel|$ changes by about 0.01–0.03. In this case, $|T_1|^2$ and $|T_2|^2$ differ from each other by only several percent. Setting $n_\perp = n_\parallel$ in (1) and, therefore, $T_1 = T_2 = T$, $\alpha_1 = \alpha_2 = \alpha$, we obtain in the approximation under consideration

$$I(\lambda) \approx |T|^2 P(\Theta), \quad (14)$$

where the function

$$P(\Theta) = 0.5 k_p k_a \times \cos^2\Theta[(1 + \sqrt{y_p}\tan\Theta)^2 + y_a(\tan\Theta - \sqrt{y_p})^2] \quad (15)$$

describes the intensity of light transmitted through the system of two polarizers crossed at an angle Θ in the absence of a crystal.

It can readily be shown that this function has a maximum at $\Theta = \Delta$ and a minimum at $\Theta = \Delta + \pi/2$, where

$$\Delta = \arctan\sqrt{y_p}. \quad (16)$$

At the transmission minimum

$$P_{\min}(\Theta = \Delta + \pi/2) = 0.5 k_p k_a y_a (1 + y_p) < P(\Theta = \pi/2) = 0.5 k_p k_a (y_a + y_p). \quad (17)$$

Thus, at $P(\Theta) \neq 0$, the position of the transmission minimum will be determined by a condition more complicated than (13), with account taken of the amplitudes T_j in the vicinity of λ_i. For this reason, the position of the minimum will, generally speaking, depend on the crystal thickness and coincide with λ_i only for those l which satisfy the condition for either a Fabry–Perot interference minimum for the amplitudes $T(\lambda_i)$

$$4 n_i l = (2m + 1)\lambda_i \quad (18)$$

or a maximum

$$2 n_i l = m\lambda_i. \quad (19)$$

Condition (13) is valid without corrections only in the ideal case of $y_p = y_a = 0$, $\Theta = \pi/2$, $\beta = \pi/4$.

The spectral position of the transmission minimum $\lambda(I_{min})$, calculated using (1) for different l values, is presented in Fig. 1. To simplify the calculations, the polarizers were assumed to be homogeneous; i.e., $y_p = y_a = y$, $k_p = k_a = k$, and k was set equal to unity. We also assumed that, in the adjustment of the system in the absence of a crystal, the crossing angle of the polarizers was set to the minimum transmission ($\Theta = \Delta + \pi/2$), and the angle between the optical axis of the crystal and the direction of maximum transmission of the input polarizer was considered to be $\pi/4$. With account taken of the depolarizing properties of the cryostat windows, the effective minimum to maximum transmission ratio was taken equal to 5×10^{-3}.

The interference minima coinciding with λ_i and satisfying the condition (18) are enumerated in the figure in correspondence with their order. The minima $\lambda(I_{min}, l)$, for which the condition (19) is fulfilled, alternate with the minimum points determined by (18). The periodicity of interference in l for both types of extrema is $\lambda_i/2n_i \approx 958.3$ Å. As seen from Fig. 1, the function $\lambda(I_{min}, l)$ changes much faster near the thicknesses, satisfying the condition (19), and both the rate of $\lambda(I_{min}, l)$ variation and the total swing of wavelengths from $\lambda_{min}(I_{min}, l)$ to $\lambda_{max}(I_{min}, l)$ grow with decreasing thickness. In a real experimental situation, this may lead to strongly dissimilar optical properties of different parts of a crystal because of the presence on the sample surface of growth steps one or several lattice constants high.

A calculation of the function (1) for other parameters of the optical system—y, Θ, and β—demonstrated that at the same thicknesses, except those satisfying the condition (18), the deviation of the intensity minimum position from the inversion point λ_i increases (decreases) with increasing (decreasing) y. The position of the minimum can also be controlled by varying the angles Θ and β.

The table compares the results of our calculation with experimental data [1, 2, 4]. The first column presents the experimental positions of the transmission minima for sample thicknesses from the second column, and the third column gives l values calculated using formula (1) for the experimental $\lambda(I_{min})$ from the first column.

A discrepancy of 6–10% between the experimental and calculated thicknesses for the last three samples is due, in our opinion, to the following factors: inaccuracy in determining $\lambda(I_{min})$ from plots in [1, 2, 4]; a substantial experimental error in determining the minimum position because of the large band width in very thin crystals [1]; and the higher relative error compared with that in thick crystals in measuring the thicknesses of thin samples. The last circumstance is related to a contribution from the additional phase ϕ (8) to the optical thickness of a sample. The undesirable effect can be eliminated by means of methods described in [17] but not employed in [1–5].

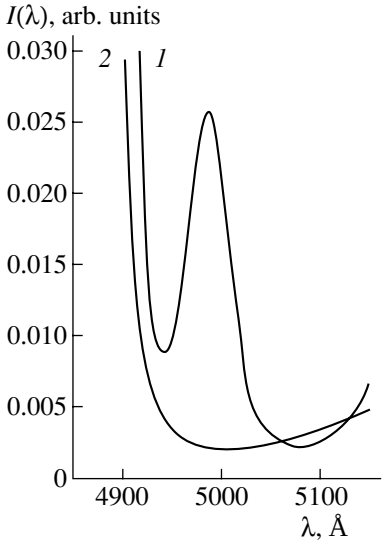

Fig. 2. Transmission intensity vs. wavelength near the isotropic point of the CdS crystal at incomplete polarization of interfering beams: (*1*) l = 12800 Å and (*2*) l = 5020 Å.

The wavelength dependence of the transmission intensity for crystals with l = 5020 and 12800 Å, presented in Fig. 2, is in qualitative agreement with the shape of the curves in [2, 3]. An inverse proportionality of the band width to the optical thickness of the crystal, characteristic of the extrema of the Fabry–Perot interference [13], is clearly seen.

The analysis made in this study demonstrated that, in the case of a refractive index independent of the crystal thickness [7–11], the spectral position of the transmission minimum near the isotropic point in an experiment with incompletely polarized beams in thin CdS crystals placed between crossed polarizers will depend on the crystal thickness. Therefore, the results obtained in [1–5] can be accounted for not only by the thickness dependence of the refractive index but also by incom-

Table

$\lambda(I_{min})$, Å (experiment)	l, Å, of the crystal (experiment)	l, Å, of the crystal (calculation)
5080	12900	12800
5042	8000	7880
5034	6000	6000
5015	5000	5020
4975	3600	3980
4932	2700	2940
4922	1800	1920

plete polarization of the interfering beams, resulting from imperfections of the optical system elements.

With collinear polarizers, the transmission maximum will exhibit a similar dependence on the crystal thickness near the isotropic point.

REFERENCES

1. M. I. Strashnikova, V. Ya. Reznichenko, V. V. Cherny, and V. N. Myasnikov, Solid State Commun. **47**, 375 (1983).
2. M. I. Strashnikova, V. Ya. Reznichenko, and V. V. Cherny, Phys. Status Solidi B **141**, K153 (1987).
3. M. I. Strashnikova, V. Ya. Reznichenko, and V. V. Chernyĭ, Ukr. Fiz. Zh. **32**, 187 (1987).
4. V. Ya. Reznichenko, M. I. Strashnikova, and V. V. Chernyĭ, Ukr. Fiz. Zh. **33**, 535 (1988).
5. V. Ya. Reznichenko, M. I. Strashnikova, and V. V. Cherny, Phys. Status Solidi B **152**, 675 (1989).
6. S. A. Abagyan, G. A. Ivanov, Yu. A. Lomov, and Yu. E. Shandrin, Fiz. Tekh. Poluprovodn. (Leningrad) **4**, 2379 (1970) [Sov. Phys. Semicond. **4**, 2049 (1970)].
7. V. A. Kiselev, I. V. Makarenko, B. S. Razbirin, and I. N. Ural'tsev, Fiz. Tverd. Tela (Leningrad) **19**, 1348 (1977) [Sov. Phys. Solid State **19**, 1374 (1977)].
8. I. V. Makarenko, I. N. Uraltsev, and V. A. Kiselev, Phys. Status Solidi B **98**, 773 (1980).
9. M. P. Lisitsa, S. F. Terekhova, and N. A. Onishenko, Phys. Status Solidi B **115**, 187 (1983).
10. M. P. Lisitsa, S. A. Boĭko, S. F. Terekhova, and Z. L. Denisova, Zh. Prikl. Spektrosk. **36**, 100 (1982).
11. V. A. Kiselev, I. N. Uraltsev, and I. V. Makarenko, Solid State Commun. **59**, 591 (1985).
12. B. I. Stepanov and V. P. Gribkovskiĭ, *An Introduction to the Theory of Luminescence* (Akad. Nauk BSSR, Minsk, 1963).
13. N. I. Kaliteevskiĭ, *Wave Optics* (Vysshaya Shkola, Moscow, 1978).
14. W. A. Shurcliff, *Polarized Light: Production and Use* (Harvard Univ. Press, Cambridge, 1962; Mir, Moscow, 1965).
15. V. I. Tovstenko, Ukr. Fiz. Zh. **22**, 1897 (1977).
16. J. M. Bieniewski and S. J. Czyrak, J. Opt. Soc. Am. **53**, 496 (1963).
17. M. P. Lisitsa and N. T. Tsvelykh, Zavod. Lab. **22**, 1072 (1956).

Translated by S. Ktitorov

Semiconductors, Vol. 35, No. 10, 2001, pp. 1151–1154. Translated from Fizika i Tekhnika Poluprovodnikov, Vol. 35, No. 10, 2001, pp. 1204–1207.

ELECTRONIC AND OPTICAL PROPERTIES OF SEMICONDUCTORS

Random Potential Relief and Extrinsic Photoconductivity of Compensated Germanium

Yu. P. Druzhinin and E. G. Chirkova*

Institute of Radio Engineering and Electronics, Russian Academy of Sciences, Moscow, 101999 Russia

** e-mail: chi@cplire.ru*

Received April 19, 2001; accepted for publication April 24, 2001

Abstract—A photoconductivity spectrum normalized to the optical absorption of compensated germanium is simulated at low temperatures $kT \ll W$ (where W denotes the energy scale of the random potential that stems from impurity Coulomb interaction). By fitting the simulated spectrum to the experimental data, the value of W and the occupancy of the shallow-donor impurity band are estimated. A weak energy dependence of the mean free path of electrons in the random potential relief is inferred. *© 2001 MAIK "Nauka/Interperiodica".*

The photoconductivity spectrum of compensated germanium is known to differ radically from the impurity-absorption spectrum [1]. This difference is particularly pronounced at low temperatures, $kT \ll W$, where W is the energy scale of the random potential that is due to the impurity Coulomb interaction.

The objective of this study is to analyze the specific features of conductivity over the random potential relief by comparing the simulated and experimental photoconductivity spectra normalized to the optical absorption. The numerical simulation of the $\sigma(h\nu)$ spectrum was carried out under the following assumptions.

1. The random potential is described by Gaussian statistics [2]:

$$P(U) = \frac{1}{(2\pi)^{1/2}W}\exp\left(-\frac{U^2}{2W^2}\right), \qquad (1)$$

where U is the potential energy, $P(U)$ is the probability density of the random potential U, and W is the energy scale of the random potential.

2. As a result of exposure to photons with energy $h\nu$, electrons are excited from the energy level E_F, where E_F is the Fermi level whose position depends on the occupancy of the shallow-level donor N_0/N_d (N_0 is the concentration of the neutral shallow impurity and N_d is the total concentration of the shallow impurity). Since the total energy E is reckoned from the average potential energy in the conduction band, the Fermi energy is negative, $E_F < 0$. According to (1), we obtain

$$N_0/N_d = 0.5\left(1 + \mathrm{erf}\frac{E_F + E_i}{W}\right),$$

where E_i is the shallow-impurity ionization energy; for antimony, E_i amounts to 10 meV.

3. Following [3], the photoconductivity spectrum $\sigma(h\nu)$ can be written as

$$\sigma(h\nu) = \int_{-\infty}^{E_g}[S_0(E) + \sigma(E_p)\delta(E - E_p)]dE, \qquad (2)$$

where E is the total energy of an electron, E_p is the mobility-threshold energy (we assume that it coincides with the percolation level), and E_g is the energy level to which electrons are excited by the signal irradiation with photon energy $h\nu$: $h\nu = E_g - E_F$. In accordance with (2), the photoconductivity $\sigma(h\nu)$ vanishes when $E_g < E_p$ and shows a stepwise increase to $\sigma(E_p)$ when $E_g > E_p$ [2]. Further growth under this condition depends on the carrier contribution $S_0(E)$ to conductivity. Let us assume that $S_0(E)$ is proportional to the crystal volume fraction $V(E)$ available for classical motion. This assumption evidently becomes invalid for the energies close to the percolation level; however, these energies correspond to relatively small volume fractions available in the three-dimensional case. In particular, for the normally distributed random potential, $V(E_p) \approx 0.17$ and $E_p \approx -W$ [2]. Then, $S_0(E)$ can be written as

$$S_0(E) = 0.5\left(1 + \mathrm{erf}\frac{E}{W}\right).$$

Assuming that $\sigma(E_p) = 0$ and $E_p = -\infty$ (the validity of these assumptions will be discussed below), we obtain a photoconductivity spectrum in the following form:

$$\sigma(h\nu) = (h\nu + E_F)S_0(h\nu + E_F) + W^2P(h\nu + E_F).$$

Simulated spectra, together with the experimental data they are fitted to, are shown in Figs. 1 and 2 for two samples with different doping levels and compensation degrees. Sample I contains copper in doubly and triply charged states with respective concentrations N_2 and

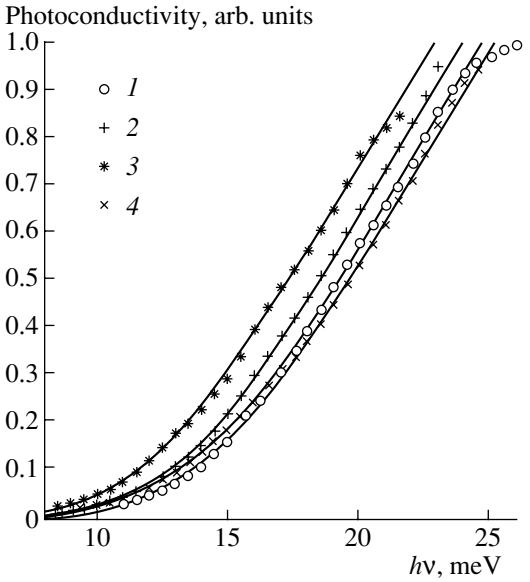

Fig. 1. (*1–4*) Experimental and (solid curves) simulated photoconductivity spectra of Ge:(Cu,Sb): (*1–3*) for sample I at different illumination intensities, $N_d \approx 1.5 \times 10^{15}$ cm^{-3}, $N_{Cu} \approx 6 \times 10^{14}$ cm^{-3}; (*4*) for sample II, $N_d \approx 1.5 \times 10^{15}$ cm^{-3}, $N_{Cu} \approx 4.3 \times 10^{14}$ cm^{-3}.

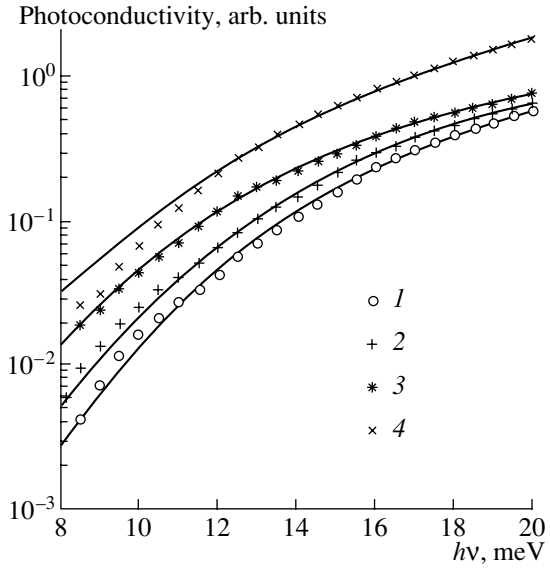

Fig. 2. The same as in Fig. 1 but on a semilog scale.

N_3, which are roughly equal (at high temperatures). At low temperatures, $T = 4.2$ K, under illumination, a partial neutralization of the shallow donor occurs due to the electrons leaving the triply charged level of copper for the conduction band. The neutralization degree can be varied to some extent by changing the intensity of the external illumination (see table). Sample II contains copper atoms in the triply charged state only, and the occupancy of the shallow donor N_0/N_d at low temperature is approximately 0.14. Numerical values of the adjustable parameters W and N_0/N_d employed are listed in the table. We note that a change in the parameter N_0/N_d shifts the linear portion of the photoconductivity spectrum (Fig. 1, $h\nu - E_i > W$), while W affects the superlinear portion of the spectrum (Fig. 2, $-W < h\nu - E_i < W$).

For the samples in question, the energy scale of the random potential W can be estimated as follows. In [4], the quantities E_p and V_p were evaluated for a compensated semiconductor with singly charged impurities. For $N_0/N_d < 0.2$, V_p varied within the range of 0.16–0.18, which is close to the value it takes in the case of the Gaussian potential [2], for which we have $E_p \approx -W$. This result can be applied to our study if the multiply charged copper atoms are accounted for. For this purpose, while estimating the extent of large-scale relief in the asymptotic approximation $N_0/N_d \ll 1$, one should use $N_{eff} = N_d + Z^2 N_{Cu}$ [2], where $Z = 2$ for sample I and $Z = 3$ for sample II (for singly charged impurities, $Z = 1$ and, therefore, $N_{eff} = 2N_d$). Taking into consideration that, in the asymptotic limit, W is a power-law function of N_{eff} with the exponent 2/3 and using the fact that, for a low concentration of screening centers, the results obtained in [2] and [4] should coincide, we obtain the following correction coefficients that account for the multiple charge A_Z ($W_Z = A_Z W$): $A_2 = 1.2$ and $A_3 = 1.6$ for samples I and II, respectively. It is evident that the multiple charge of an impurity significantly increases the energy scale of the random potential (as well as its spatial scale). As a result, calculated values of W proved to be in good agreement with those obtained by fitting (see table). Another point to emphasize is the independence of the large-scale relief from the illumination intensity in the asymptotic limit. This is due to the fact that the total concentration of the screening centers remains constant ($N_3 + N_0 = \text{const}$), which is also confirmed by the results of fitting (or, vice versa, the conclusion drawn from the asymptotic consideration is supported by the experiment). As can be seen from the table, the calculated occupancy N_0/N_d is close to the results of optical measurements.

It is worth noting that, for sample I, a good fit of the spectra to the experiment is observed within the entire spectral range, whereas for sample II, the fitting deviates from the experiment at $h\nu \approx 10$ meV. It is reasonable to associate this deviation with the influence of the mobility threshold E_p. However, the mobility threshold does not manifest itself in full measure in the experiment (a fall proportional to $\exp(1/kT)$ is not observed in the photoconductivity spectrum normalized to absorption). This may be caused by two experimental circumstances. (i) The measurements were carried out in a fairly high electric field that distorts the "fieldless" percolation process. (ii) Due to the optical charge exchange, the electron distribution over the shallow

impurity level located above E_F differs from the Fermi law. The amazingly close fit to experimental spectra attained for sample I in a low-energy range should be considered as accidental. It is evidently a consequence of inadequately describing the "tails" of the probability density of the random potential as Gaussian. For example, within the context of the quasi-classical approach, the highly excited states of the shallow impurity induce the asymptotic decrease in the density of electronic states proportional to $E^{-5/2}$ [5], which yields a considerably steeper fall than the normal (Gaussian) potential does with the same variance (defined as an average square of potential energy for a random-quantity distribution). Due to a larger compensation degree and to a multiple charge of the relief-forming impurities, the large-scale components of the random potential are more important in sample II than in sample I; therefore, the normal distribution more adequately describes sample II, yet it leads to a discrepancy between the fitting and experiment near the mobility threshold. The discrepancy, however, follows from the approximate character of the conductivity simulation rather than from the static properties of the relief.

The conductivity of a nonuniform material where the scale of nonuniformity is less than or on the order of the free path can be calculated by the Kubo–Greenwood formula [6]. After being applied to photoconductivity spectrum (2), it yields $S_0(E)$ and $\sigma(E_p)$ in the following form:

$$S_0(E) = \frac{d(g^2L)}{dE} f(E),$$

$$\sigma(E_p) = g^2(E_p)L(E_p)f(E_p),$$

where $g = g(E)$ is the average density of electronic states in the conduction band; $f(E)$ is the electron distribution function determined for $kT \ll W$ for instance in [5]; and $L = L(E)$ varies as an average square of velocity operator, which at high energies (i.e., outside the potential relief) is in turn proportional to the free path [6]. Within the relief ($-W < E < W$), the $L(E)$ function remains unknown. In the range below E_p, $L(E)$ vanishes. In the classical potential, this vanishing is considered to occur continuously within a narrow energy range near the percolation level (in our case, it coincides with the mobility threshold) [2]. Beyond the relief, when momentum is scattered by a charged impurity, $S_0(E)$ is energy-independent [3]. This gives rise to the linear dependence of photoconductivity on the energy of signal irradiation $h\nu$, which is confirmed by experimental results. Within the relief, the $L(E)$ function may be assumed to be nearly constant. Bearing in mind that the density of states and the distribution function depend on energy mainly in terms of the available volume fraction $V(E)$ [2, 5] and presuming the conductivity at the mobility threshold $\sigma(E_p)$ to be negligibly small (the fitting procedure even disregards the existence of this threshold), we may define $S_0(E)$ as a quantity proportional to $V(E)$.

Taking into account the finiteness of E_p and $\sigma(E_p)$ would give rise to additional terms in the expression for the photoconductivity spectrum $\sigma(h\nu)$. These terms would change the energy of the linear portion cutoff, which is equivalent to an error in determining the occupancy of the shallow impurity level, and would also distort the photoconductivity spectrum in the range of photon energies corresponding to the charge carrier excitation to almost the mobility threshold E_p. In this spectral range, however, the assumption that $S_0(E)$ is proportional to the available volume fraction is obviously invalid. In view of this, we did not carry out the fitting in the spectral range specified. One more comment should be made concerning the error caused by finiteness of $\sigma(E_p)$ and E_p in determining the occupancy of the shallow impurity. The close coincidence of the ratio N_0/N_d obtained by fitting with the results of optical measurements validates the approach within which the mobility threshold E_p is taken as $-\infty$ and $\sigma(E_p) = 0$.

In our opinion, a good agreement between the value obtained for the parameter W by fitting and that derived from calculation implies only a slight dependence of the average squared operator of velocity in the relief on the carrier energy. On the other hand, slightly different scales of the potential relief obtained for sample II where, as was mentioned above, the large-scale component of the relief is of greater importance than the medium-scale component are indicative of a stronger energy dependence of the average squared operator of velocity. The observed shift of the linear portion of $\sigma(h\nu)$ curve with the intensity of short-wavelength illumination (see Fig. 1) suggests that, under the spectroscopic experimental conditions, recharging of the shal-

Adjustable parameters of the samples under study: experimental, calculated, and fitted values

Sample no.	N_d, cm^{-3}	N_{Cu}, cm^{-3}	N_0/N_d	N_0/N_d	W, meV	W, meV
			optics	fitting	theory	fitting
1	1.5×10^{15}	6×10^{14}	0.13 0.2 0.3	0.11 0.16 0.28	2.9	3.0
2	1.5×10^{15}	4.3×10^{14}	0.14	0.14	4.5	4.1

low impurity is unimportant and the carrier distribution over the shallow donor closely obeys the Fermi statistics.

To summarize the aforesaid, a photoconductivity spectrum normalized to the optical absorption is simulated in compensated germanium at low temperature. Fitting the adjustable parameters of the model yields values that closely coincide with those obtained from the experiment or are independently calculated. This enabled us to conclude that the average squared operator of the velocity (or free path) within the relief depends only slightly on energy. Also of interest is the reverse problem: with the given average squared operator of the velocity, to refine the characteristics of the relief, for instance, its energy scale, by comparing simulated and experimental photoconductivity spectra normalized to absorption.

ACKNOWLEDGMENTS

We are grateful to V.N. Gubankov for his encouragement and participation in the discussion of the results.

REFERENCES

1. Yu. P. Druzhinin and E. G. Chirkova, Fiz. Tekh. Poluprovodn. (St. Petersburg) **29**, 1575 (1995) [Semiconductors **29**, 820 (1995)].
2. B. I. Shklovskiĭ and A. L. Efros, *Electronic Properties of Doped Semiconductors* (Nauka, Moscow, 1979; Springer-Verlag, New York, 1984).
3. Sh. M. Kogan, Fiz. Tekh. Poluprovodn. (Leningrad) **11**, 1979 (1977) [Sov. Phys. Semicond. **11**, 1176 (1977)].
4. Nguen van Lien and B. I. Shklovskiĭ, Fiz. Tekh. Poluprovodn. (Leningrad) **13**, 1763 (1979) [Sov. Phys. Semicond. **13**, 1025 (1979)].
5. V. Karpus and V. I. Perel', Fiz. Tekh. Poluprovodn. (Leningrad) **16**, 2129 (1982) [Sov. Phys. Semicond. **16**, 1373 (1982)].
6. N. F. Mott and E. A. Davis, *Electronic Processes in Non-Crystalline Materials* (Clarendon, Oxford, 1979; Mir, Moscow, 1982).

Translated by A. Sidorova-Biryukova

Semiconductors, Vol. 35, No. 10, 2001, pp. 1155–1160. Translated from Fizika i Tekhnika Poluprovodnikov, Vol. 35, No. 10, 2001, pp. 1208–1213.

SEMICONDUCTOR STRUCTURES, INTERFACES, AND SURFACES

Photocapacitance Effect at Low Temperatures in a Unipolar MIS Capacitor with a Semiconductor Electrode Doped with Two Different Acceptor Impurities

N. A. Penin

Lebedev Physical Institute, Russian Academy of Sciences, Leninskiĭ pr. 53, Moscow, 119991 Russia

Submitted December 13, 2000; accepted for publication February 5, 2001

Abstract—The photocapacitance effect at low temperatures in a unipolar MIS capacitor with a semiconductor electrode doped with two types of acceptor impurities characterized by different ionization energies E_{ia} (deep-level acceptor) and E_{ib} (shallow-level acceptor) is examined theoretically. It is shown that the photocapacitance response of such a capacitor arises in a relatively narrow range of bias voltages. The maximum of the response at a constant bias depends on the temperature as $\exp(E_{ia}/kT)$. An infinite increase in the photocapacitance response is related to the singularity that appears with decreasing temperature in the bias-voltage dependence of the ionized acceptor concentration. The capacitance and photocapacitance characteristics for a structure with a silicon electrode doped with In and B are calculated. © *2001 MAIK "Nauka/Interperiodica".*

1. INTRODUCTION

The photocapacitance effect in a unipolar metal–insulator–semiconductor (MIS) capacitor with a semiconductor electrode doped with deep-level acceptor and shallow-level donor impurities (MISd capacitor) was considered previously [1].

In this paper, we examine the capacitance and photocapacitance characteristics for a capacitor with a semiconductor electrode doped with two types of acceptor impurities characterized by different ionization energies (a MISa capacitor). The calculations are carried out for the case of a silicon electrode doped with In and B.

2. CAPACITANCE AND PHOTOCAPACITANCE RESPONSE OF A MIS STRUCTURE

2.1. Capacitance of a MIS Structure

Let us consider a plane capacitor with one of the electrodes made of an extrinsic semiconductor with unipolar conduction. When the voltage V is applied to the capacitor, the space charge is induced in the semiconductor; we denote the charge per unit area by $Q(\varphi_0)$. The semiconductor surface acquires a potential φ_0, which represents the height of the barrier induced in the semiconductor.

The differential electrochemical (thermodynamic) capacitance of the induced barrier is given by

$$C_b = \frac{\varepsilon\rho(\varphi_0)}{4\pi Q(\varphi_0)}, \quad (1)$$

where $\rho(\varphi_0)$ is the space-charge density in the semiconductor near the interface with the insulator [1]. It is assumed here that there is no charge trapped at the semiconductor–insulator interface.

The capacitance C_c of the MIS structure is combined from the barrier capacitance C_b and the insulator layer capacitance C_d connected in series:

$$C_c = \frac{C_b C_d}{C_b + C_d}. \quad (2)$$

The voltage V applied to the capacitor is equal to

$$V = U_d + \varphi_0, \quad (3)$$

where U_d is the voltage across the insulator layer.

Since the absolute values of the charges at the electrodes are equal to each other, we have

$$U_d = \frac{Q(\varphi_0)}{C_d}.$$

It is assumed here that C_d is independent of the voltage U_d and the incident radiation intensity I.

2.2. Photocapacitance Effect

The radiation incident on the MIS structure induces ionization of the neutral impurity atoms in the semiconductor electrode. The photocapacitance response S_c is defined as the ratio of the capacitance increment dC_c to the radiation intensity increment dI:

$$S_c = \frac{dC_c}{dI} = \frac{1}{h\nu}\frac{C_d^2}{(C_d + C_b)^2}S_b, \quad (4)$$

1063-7826/01/3510-1155$21.00

where

$$S_b = \frac{dC_b}{d\phi} = \frac{\varepsilon}{4\pi}\frac{\rho}{Q}\left(\frac{1}{\rho}\frac{d\rho}{d\phi} - \frac{1}{Q}\frac{dQ}{d\phi}\right) \quad (5)$$

is the barrier photocapacitance response, $I = h\nu\phi$ is the radiation intensity, ϕ is the photon flux density, and $h\nu$ is the photon energy.

The more detailed formulas, which facilitate the calculation of C_b, C_c, S_b, and S_c, are given in the appendix.

3. CAPACITANCE AND PHOTOCAPACITANCE CHARACTERISTICS OF A MISa STRUCTURE

Let us consider a one-dimensional model of the MISa capacitor with a semiconductor electrode doped with two types of acceptor impurities characterized by ionization energies E_{ia} and E_{ib}. Let the corresponding impurity densities be N_a and N_b. It is assumed that the average distribution of impurities is uniform.

In the absence of an electric field, the hole density p under excitation by radiation with intensity I can be calculated from the equation

$$p^3 + (p_1^* + p_2^*)p^2 + (p_1^* p_2^* - N_a p_1^* - N_b p_2^*)p - (N_a + N_b)p_1^* p_2^* = 0, \quad (6)$$

where

$$p_1^* = p_1 + \frac{q_1}{c_1}\phi, \quad p_2^* = p_2 + \frac{q_2}{c_2}\phi,$$

$$p_1 = (N_v/g_1)\exp(E_{ia}/kT),$$

$$p_2 = (N_v/g_2)\exp(E_{ib}/kT);$$

T is the temperature, q_1 and q_2 are the cross sections of the photoionization of impurity atoms by radiation with the photon energy $h\nu$, and c_1 and c_2 are the coefficients of the nonequilibrium hole capture by ionized impurity atoms; it is assumed that c_1 and c_2 are independent of temperature.

Under the applied electric field, the space charge appears in the semiconductor, and the charge density at a point with the potential φ is given by

$$\rho(\varphi) = e[p(\varphi) - N_a^-(\varphi) - N_b^-(\varphi)]. \quad (7)$$

For the case of Boltzmann distribution, $p(\varphi) = p_0\exp(-\alpha\varphi)$, where $\alpha = e/kT$ and p_0 is the equilibrium hole density at $\varphi = 0$. Then,

$$\rho(\varphi) = e\left[p_0\exp(-\alpha\varphi) - \frac{N_a p_1^*}{p_1^* + p_0\exp(-\alpha\varphi)} - \frac{N_b p_2^*}{p_2^* + p_0\exp(-\alpha\varphi)}\right]. \quad (8)$$

The space-charge density $\rho(\varphi_0)$ in the semiconductor near the interface with the insulator is related to the charge $Q(\varphi_0)$ induced in the semiconductor by the expression

$$Q^2(\varphi_0) = \frac{\varepsilon}{2\pi}\int_{\varphi_0}^{0}\rho(\varphi)d\varphi, \quad (9)$$

where φ_0 is the potential at the semiconductor surface [1, 2]. Substituting $\rho(\varphi)$ into (9) and performing the integration, we obtain

$$Q^2(\varphi_0) = \frac{\varepsilon kT}{2\pi}\left[N_a\ln\frac{p_1^* + p_0\exp(-\alpha\varphi_0)}{p_1^* + p_0} + N_b\ln\frac{p_2^* + p_0\exp(-\alpha\varphi_0)}{p_2^* + p_0} + (N_a + N_b)\alpha\varphi_0 + p_0\exp(-\alpha\varphi_0) - p_0\right]. \quad (10)$$

Below, the C_c–V and S_c–V characteristics will be calculated for the capacitor with a silicon electrode doped with In and B. The following parameters are assumed: the insulator layer capacitance $C_d = 100$ nF/cm^2, which corresponds to a SiO_2 layer thickness of ~ 35 nm; In concentration $N_a = 1 \times 10^{16}$ cm^{-3}; acceptor atom ionization energy in Si $E_{ia} = 160$ meV and $E_{ib} = 45$ meV for In and B, respectively; and the coefficients of the hole capture by In and B atoms $c_1 = c_2 = c = 5 \times 10^{-6}$ cm^3/s. The cross section for the photoionization of an In atom in Si by radiation with wavelength $\lambda = 4$ μm is $q_1 = 2.5 \times 10^{-16}$ cm^2. Due to the large difference between the radiation photon energy ($h\nu = 0.31$ eV) and the B atom ionization energy (0.045 eV), the photoionization of the B atoms was neglected ($q_2 = 0$). Thus, in all formulas, $p_2^* = p_2$.

Next, the capacitance and photocapacitance characteristics will be analyzed for different B concentrations N_b, temperatures T, and radiation intensities I.

4. DISCUSSION

4.1. Dark C–V Characteristics

A set of C–V characteristics calculated for $T = 70$ K and various B concentrations is shown in Fig. 1. Several features should be noted. Without doping with B, a minimum in the C–V characteristic (curve *a*) appears at $V = \varphi_0 = 0$. In this case, the barrier capacitance $C_b = \varepsilon/4\pi L_{db}$, where L_{db} is the Debye screening length. In the extrinsic unipolar semiconductor doped with a single type of impurity [3]

$$L_{db}^2 = \frac{\varepsilon kT}{4\pi e^2 p_0}\left[1 + \frac{N_a p_1}{(p_1 + p_0)^2}\right]^{-1}. \quad (11)$$

With an increase in the bias voltage, the screening length begins to depart from the Debye length and, for an arbitrary φ, is given by the following expression [2]:

$$L_{sc}(\varphi) + Q(\varphi)/\rho(\varphi). \quad (12)$$

Under increasing negative bias, L_{sc} is reduced due to an increase in the hole density p. Under increasing positive bias, L_{sc} is reduced due to an increase in the concentration of N_a^- ions. This leads to an increase in the capacitance as the absolute value of the bias increases. Since the bias dependences of p and N_a^- are different, asymmetry between the positive and negative portions of the C–V characteristic occurs. Under increasing positive bias, the capacitance increases and reaches its maximum in the vicinity of the voltage corresponding to $N_a^- \approx 0.7N_a$. With a further voltage increase, the C–V characteristic assumes the shape typical of the Schottky barrier under reverse bias.

Under increasing negative bias, the hole density increases exponentially and the barrier capacitance rises sharply, so that insulator layer capacitance begins to limit the total structure capacitance.

With an increase in the B concentration, the minimum and the maximum of the capacitance that originate from an In impurity shift to higher positive bias voltages (see curves *b*–*f*). At low B concentrations, a single maximum exists in the C–V curve; at higher B concentrations, a second maximum, related to the B impurity, appears.

4.2. C–V Characteristics in the Presence of Radiation

Under positive bias, the radiation ionizing neutral In atoms causes a shift of the capacitance maximum to lower voltages (see Fig. 2, curves *a*–*c*). This is related to the fact that the radiation increases ionized In atom concentration and, thus, reduces the barrier width, which leads to an increase in the structure capacitance. As a result, the C–V curve under illumination crosses the dark C–V curve at a certain voltage V_{cr}. Thus, radiation of a given intensity causes an increase in the capacitance at $V < V_{cr}$ and a decrease (negative photocapacitance effect), at $V > V_{cr}$. On the other hand, under negative bias, there is no photocapacitance effect; this is related to an increase in the hole density, which leads to a decrease in the nonequilibrium hole lifetime. For $\varphi_0 < 0$ and $|\alpha\varphi_0| \gg 1$, the nonequilibrium hole lifetime $\tau \approx 1/cp_0\exp(-\alpha\varphi_0)$; thus, e.g., for $\varphi_0 = -100$ mV, $T =$ 70 K, and $N_a = 1 \times 10^{16}$ cm^{-3}, we have $\tau < 1 \times 10^{-10}$ s.

4.3. Temperature Dependence of the C–V Characteristics

In Figs. 3 and 4, we plot the two sets of dark C–V characteristics calculated for the B concentrations $N_b = 0$ and 1×10^{14} cm^{-3}. First, let us consider the case of zero

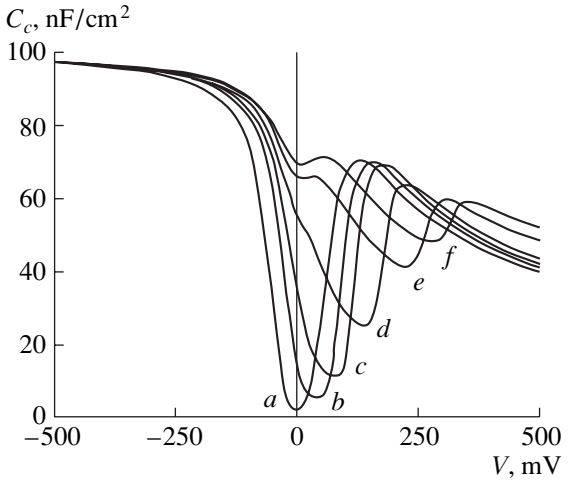

Fig. 1. C–V characteristics for N_b = (*a*) 0, (*b*) 1×10^{13}, (*c*) 1×10^{14}, (*d*) 1×10^{15}, (*e*) 5×10^{15}, and (*f*) 9×10^{15} cm^{-3}; $N_a = 1 \times 10^{16}$ cm^{-3}, $T = 70$ K, and $I = 0$.

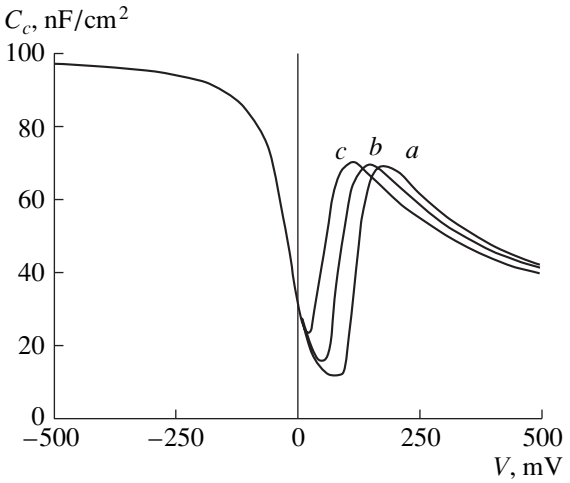

Fig. 2. C–V characteristics for I = (*a*) 0, (*b*) 0.1, and (*c*) 10.0 W/cm^2; $N_a = 1 \times 10^{16}$ cm^{-3}, $N_b = 1 \times 10^{14}$ cm^{-3}, and $T = 70$ K.

B-impurity concentration (Fig. 3). At high temperatures, the C–V characteristic is monotonic (curve *g*). With decreasing temperature, a minimum occurs in the C–V characteristic at $V = \varphi_0 = 0$. This decrease in the capacitance is related to an increase in the Debye screening length. In the extrinsic semiconductor with no compensating or anticompensating doping and at sufficiently low temperatures (such that $p_1 \ll N_a$), the hole density $p = \sqrt{N_a p_1}$. Substituting this into (11), we obtain for the Debye screening length

$$L_{db}^2 = \frac{\varepsilon kT}{8\pi e^2}\frac{1}{\sqrt{N_a p_1}}. \quad (13)$$

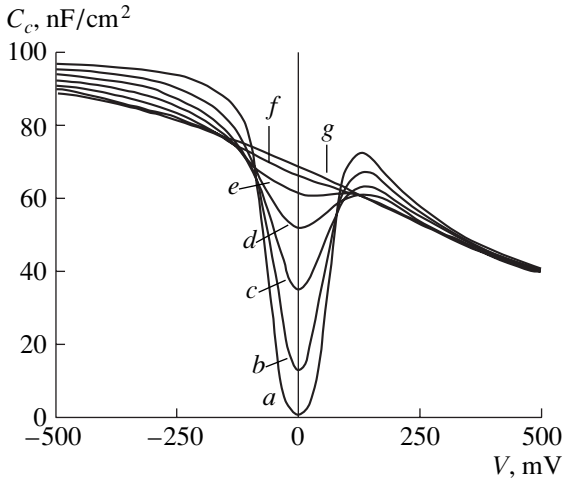

Fig. 3. *C–V* characteristics at T = (*a*) 60, (*b*) 100, (*c*) 140, (*d*) 180, (*e*) 220, (*f*) 260, and (*g*) 300 K; $N_a = 1 \times 10^{16}$ cm^{-3}, $N_b = 0$, and $I = 0$.

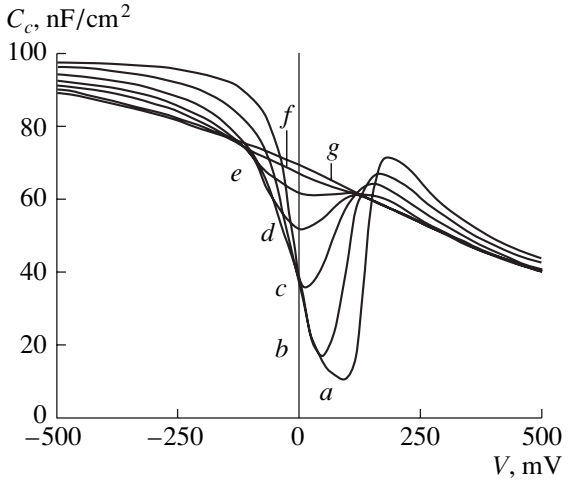

Fig. 4. *C–V* characteristics at T = (*a*) 60, (*b*) 100, (*c*) 140, (*d*) 180, (*e*) 220, (*f*) 260, and (*g*) 300 K; $N_a = 1 \times 10^{16}$ cm^{-3}, $N_b = 1 \times 10^{14}$ cm^{-3}, and $I = 0$.

Consequently, at $T \longrightarrow 0$, we have $L_{db} \longrightarrow \infty$ and, thus, $C_c \longrightarrow C_d \longrightarrow 0$. With an increase in either the positive or negative bias voltage, the *C–V* characteristic corresponding to the lower temperature crosses the *C–V* characteristic corresponding to a higher temperature. At voltages exceeding the crossing voltage, lowering the temperature leads to an increase in the capacitance (rather than to a decrease). At negative bias, such that $p(\varphi_0) \gg N_a^-(\varphi_0)$, the screening is effected mostly by holes. In this case, the screening length

$$L_{sc}^2(\varphi_0) = \frac{\varepsilon kT}{2\pi e^2 p_0 \exp(-\alpha\varphi_0)}.$$

Thus, at a constant negative φ_0, lowering the temperature causes a decrease in L_{sc} and, consequently, an increase in the barrier capacitance. Under positive bias, when $p(\varphi_0) \ll N_a^-(\varphi_0)$, the screening is effected mainly by N_a^- ions. However, in the vicinity of the capacitance maximum, $N_a^- \approx N_a$ and depends only slightly on the temperature. Thus, in this voltage range, $L_{sc}^2 \propto T$, which leads to an increase in the barrier capacitance with decreasing temperature.

With an increase in the B concentration, the maximum and the minimum of the capacitance shift to higher positive bias voltages (Fig. 4), which is related to an increase in the hole density and a decrease in the In ion concentration. In this case, lowering the temperature also causes a decrease in the capacitance minimum and an increase in its maximum. Apart from the crossing of the *C–V* characteristics, a decrease in the temperature also leads to an increase in the slope of the characteristics dC_c/dV (see, e.g., curves *e–a* in Fig. 4 in the positive-bias region). An increase in the derivative of the *C–V* curves at positive bias results from the singularity in the bias voltage dependence of $dN_a^-/d\varphi_0$ at $T \longrightarrow 0$. The dependence of N_a^- on φ_0 is given by $N_a^- = N_a p_1/[p_1 + p_0 \exp(-\alpha\varphi_0)]$. The maximum of the derivative $dN_a^-/d\varphi$ appears at $\varphi_s = (kT/e)\log(p_0/p_1)$, where φ_s is the barrier voltage at which the Fermi level near the semiconductor–insulator interface coincides with the impurity level E_a. The derivative maximum equals

$$\frac{dN_a^-}{d\varphi_0} = \frac{e}{kT}\frac{N_a}{4}; \qquad (14)$$

thus, it increases infinitely at $T \longrightarrow 0$.

4.4. Photocapacitance Effect

The bias-voltage dependences of the photocapacitance response S_c at T = 70 K calculated for various B concentrations are shown in Fig. 5. For all N_b, the photocapacitance response is peaked in a relatively narrow range of bias voltages (bias-voltage selectivity). For a given N_a, the maximum value of S_c and the position of the maximum at the voltage axis depend on the B concentration. The largest value of S_c is attained for the B concentration $N_b \approx 1 \times 10^{14}$ cm^{-3}. Under an increasing positive bias, S_c increases and attains its maximum (e.g., in curve *c* the maximum appears at $V \approx 120$ meV). With a further increase in the voltage, S_c decreases, passes through the zero level, and changes its sign (negative photocapacitance effect). The change in the sign of S_c takes place at the bias voltage corresponding to the maximum capacitance in the absence of the constant

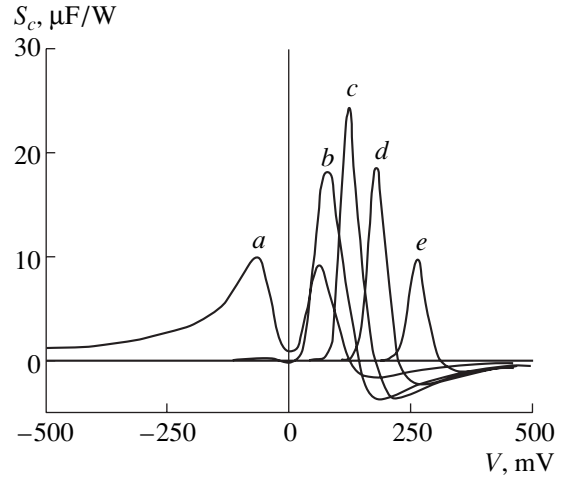

Fig. 5. S_c–V characteristics of the MISa capacitor for N_b = (*a*) 0, (*b*) 1×10^{12}, (*c*) 1×10^{14}, (*d*) 1×10^{15}, and (*e*) 5×10^{15} cm^{-3}; $N_a = 1 \times 10^{16}$ cm^{-3}, T = 70 K, and I = 0.

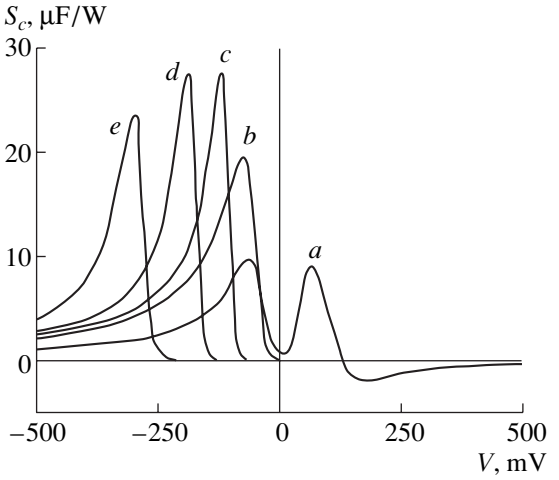

Fig. 6. S_c–V characteristics of the MISd capacitor for the donor concentration N_d = (*a*) 0, (*b*) 1×10^{12}, (*c*) 1×10^{14}, (*d*) 1×10^{15}, and (*e*) 5×10^{15} cm^{-3}; $N_a = 1 \times 10^{16}$ cm^{-3}, T = 70 K, and I = 0.

irradiation, while the maximum in S_c appears at the voltage corresponding to the highest rate of the capacitance variation. The maximum rate occurs at the bias voltage φ_s corresponding to the condition $p_1 = p_0 \exp(-\alpha\varphi_s)$. This means that the maximum capacitance variation takes place when the impurity level crosses the Fermi level as the bias voltage is changed. At this bias, the barrier photocapacitance response is equal to

$$S_b \approx \frac{q}{cp_1} = \frac{q}{cN_v}\exp\left(\frac{E_{ia}}{kT}\right). \quad (15)$$

Thus, an infinite increase in S_b and, consequently, in S_c, with decreasing temperature is related to the singularity in the bias-voltage dependence of the concentration N_a^- with decreasing temperature [see (14)].

4.5. Influence of the Constant Irradiation on the Photocapacitance Response

With an increase in the constant component of the radiation intensity, the slope of the C–V curve decreases (see Fig. 2) and, consequently, S_c is reduced. For example, for the B concentration 1×10^{14} cm^{-3} and the temperature T = 70 K, S_c drops by a factor of 2 when the radiation intensity equals $\sim 5 \times 10^{-2}$ W/cm^2.

4.6. Comparison of the Photocapacitance Characteristics of MISd and MISa Structures

In Fig.6, the S_c–V characteristics (at T = 70 K) of the MISd capacitor with the electrode doped with In and with a shallow-level donor impurity are shown. By comparing Figs. 5 and 6, one can see that introduction of a shallow acceptor impurity, instead of a donor one, radically changes the bias-voltage dependence of S_c. For a MISd capacitor, the maximum of S_c appears at negative bias voltages, in contrast to the MISa capacitor, where the maximum appears at positive voltages. In a MISa capacitor, the sign reversal of the photocapacitance response occurs for any concentration of B atoms. In a MISd capacitor, S_c changes its sign only at a low concentration (or in the absence) of the donor impurity. Note that Fig. 6 in [1] represents the absolute value of S_c, so the sign reversal is not reflected there.

Another significant difference between the two types of the structures is that in the MISa capacitor, the hole density in the neutral region of the semiconductor is significantly higher than that in the MISd capacitor. This diminishes the effect of the series resistance of the neutral region on the frequency characteristics of a MISa capacitor. For example, for $N_b = 1 \times 10^{14}$ cm^{-3} the equilibrium hole density at T = 70 K is $\sim 1 \times 10^{14}$ cm^{-3}, which corresponds to the dielectric relaxation time $\tau_m \approx 1 \times 10^{-9}$ s.

5. CONCLUSION

Thus, we analyzed the capacitance and photocapacitance characteristics of the unipolar MISa structure with one electrode composed of a semiconductor doped with two types of acceptor impurity characterized by different ionization energies. It is shown that the photocapacitance response of such a structure arises in a narrow range of positive (depleting) bias voltages (voltage selectivity). At a given concentration of the deep-level acceptor impurity, the maximum value of the photocapacitance response and the position of the maximum on the bias-voltage axis depend on the shallow-level

acceptor impurity concentration. With increasing positive bias, the sign of the photocapacitance response changes and a smaller negative maximum appears.

With decreasing temperature, the maximum value of the photocapacitance response increases as $\exp(E_{ia}/kT)$. An infinite increase of the photocapacitance response is related to the singularity in the bias-voltage dependence of the concentration of ionized atoms of the major acceptor impurity that appears at low temperatures. In other words, this is related to the appearance of the singularity in the bias-voltage dependence of the screening length in the extrinsic semiconductor at low temperatures.

The capacitance and photocapacitance characteristics were calculated for the structure with a silicon electrode doped with In and B. A unipolar MIS capacitor with an electrode doped with In and B, or by other similar impurities, can be used as a photoparametric detector of modulated infrared radiation sensitive in a narrow range of bias voltages (voltage selectivity).

APPENDIX

Calculation of C_b and S_b

To simplify the calculation of C_b and S_b, we rearrange formulas (1) and (5). For this purpose, we introduce

$$F_1 = p_0\exp(-\alpha\varphi) - \frac{N_a p_1^*}{p_1^* + p_0\exp(-\alpha\varphi)} - \frac{N_b p_2}{p_2 + p_0\exp(-\alpha\varphi)}$$

and

$$F_2 = N_a\ln\frac{p_1^* + p_0\exp(-\alpha\varphi)}{p_1^* + p_0} + N_b\ln\frac{p_2 + p_0\exp(-\alpha\varphi)}{p_2 + p_0} + (N_a + N_b) + p_0\exp(-\alpha\varphi) - p_0.$$

In this notation,

$$\rho = eF_1 \quad \text{and} \quad Q^2 = \frac{\varepsilon kT}{2\pi}F_2;$$

$$C_b = e\sqrt{\frac{\varepsilon}{8\pi kT}}\frac{F_1}{\sqrt{F_2}};$$

and

$$S_b = \frac{C_b}{2}\left(2\frac{1}{F_1}\frac{dF_1}{d\phi} - \frac{1}{F_2}\frac{dF_2}{d\phi}\right),$$

where

$$\frac{dF_1}{d\phi} = \frac{q}{c}\exp(-\alpha\varphi)\left\{N_a\frac{Sp_1^* - p_0}{p_1^* + p_0\exp(-\alpha\varphi)^2} + S\left[1 + \frac{N_b p_2}{p_2 + p_0\exp(-\alpha\varphi)}\right]\right\},$$

$$\frac{dF_2}{d\phi} = \frac{q}{c}\left\{N_a\frac{Sp_1^* - p_0}{[p_1^* + p_0\exp(-\alpha\varphi)](p_1^* + p_0)} + S\left[1 + \frac{N_b p_2}{[p_2 + p_0\exp(-\alpha\varphi)](p_2 + p_0)}\right]\right\},$$

and

$$S = \frac{(N_a - p_0)(p_2 + p_0) + N_b p_2}{3p^2 + 2(p_1^* + p_2)p_0 + p_1^* p_2 - N_a p_1^* - N_b p_2}.$$

ACKNOWLEDGMENTS

This study was supported by the Russian Foundation for Basic Research (project no. 00-02-17542) and the Ministry of Industry, Science and Technology of Russia under the Programs “Physics of the Solid-State Nanostructures” (project nos. 97-1050 and 2000-2F) and “Promising Technologies and Devices of Microelectronics and Nanoelectronics” (project no. 02.04.1.1.16.E.1).

REFERENCES

1. N. A. Penin, Fiz. Tekh. Poluprovodn. (St. Petersburg) **34**, 562 (2000) [Semiconductors **34**, 545 (2000)].
2. N. A. Penin, Fiz. Tekh. Poluprovodn. (Leningrad) **17**, 431 (1983) [Sov. Phys. Semicond. **17**, 266 (1983)].
3. S. M. Ryvkin, *Photoelectric Effects in Semiconductors* (Fizmatgiz, Leningrad, 1963; Consultants Bureau, New York, 1964).

Translated by M. Skorikov

Semiconductors, Vol. 35, No. 10, 2001, pp. 1161–1165. Translated from Fizika i Tekhnika Poluprovodnikov, Vol. 35, No. 10, 2001, pp. 1214–1218.

SEMICONDUCTOR STRUCTURES, INTERFACES, AND SURFACES

Thermoelectric Figure of Merit of a *p–n* Junction

Yu. I. Ravich and D. A. Pshenaĭ-Severin

St. Petersburg State Technical University, Politekhnicheskaya ul. 29, St. Petersburg, 195251 Russia

Submitted January 17, 2001; accepted for publication February 15, 2001

Abstract—The thermoelectric figure of merit of a semiconductor *p–n* junction is calculated in terms of the diode theory taking account of the bipolar thermal conductivity. The thermoelectric figure of merit of a Bi_2Te_3 diode is estimated and it is shown that the Ioffe criterion may be at the same level as the best modern thermoelectric materials but cannot exceed unity. © *2001 MAIK "Nauka/Interperiodica".*

INTRODUCTION

Thermoelectric effects with nonequilibrium carriers in the presence of potential barriers were first considered by Tauc and Trousil and described in a book by Tauc [1]. They observed an anomalous temperature dependence of the thermoelectric power at a point contact of a semiconductor and a metal, attributed to the effect of the barrier thermoelectric power, exceeding that in the bulk by severalfold. Thermoelectric cooling in semiconductor diodes with narrow and wide *p–n* junctions has been considered by Stafeev [2]. The thermoelectric power corresponding to the maximum temperature drop in heat transfer by nonequilibrium carriers appeared to be almost the same as that in the case of equilibrium carriers ($\alpha \approx 172$ μV/K for Ge at room temperature). Balmush *et al.* calculated the thermoelectric power of a *p–n* junction, a semiconductor transistor structure [3], and a semiconductor heterojunction [4, 5]. In [3, 6], experimental data were reported, confirming the authors' conclusions concerning the possibility of obtaining large minority-carrier thermoelectric power in barrier structures.

The thermoelectric power of a set of in-series connected *p–n* and *n–p* junctions is the sum of the components. This factor can be used in order to account for the gigantic thermoelectric power in 3D superlattices in opals [7, 8]. The authors of [7, 8] attributed the thermoelectric power observed to thermionic emission between clusters constituting the superlattice. The calculation of the thermoelectric power in *p–n* junctions suggests an alternative explanation of the high thermoelectric power in opals attributed to the presence of a *p–n–p* structure in links between the *p*-type clusters.

Thus, the use of structures with *p–n* junctions is promising as regards the possibility of obtaining high levels of thermoelectric power. Therefore, it is of interest to study not only the thermoelectric power itself but also the figure of merit of a structure with a *p–n* junction.

1. THERMOELECTRIC POWER OF A *p–n* JUNCTION

The technique used to calculate the thermoelectric power of a *p–n* junction is similar to that commonly employed to calculate the barrier photo emf. A time-independent spatial distribution of nonequilibrium minority carriers is to be found by solving the diffusion equation for quasi-neutral regions near the *p–n* junction. On calculating the electron and hole current densities, the thermoelectric power is determined from the condition that the total current through the diode should be zero. Henceforth, calculations are performed for the case of a thin junction, i.e., in terms of the diode theory. In addition, it is assumed that nondegenerate carrier statistics is applicable.

Let us write the diffusion equation in the presence of a temperature gradient in the *n* region to the right of the *p–n* junction ($x > 0$, see Fig. 1a). Then a nonequilibrium distribution of minority *p* carriers appears in the semiconductor, owing to both the potential difference across the *p–n* junction and the presence of a temperature gradient. In an extrinsic *n*-type semiconductor, at a small concentration of holes, the equation for the minority carrier current can be regarded as an approximation including only the diffusion part:

$$j_p = -eD_p\frac{dp}{dx}, \tag{1}$$

where D_p is the hole diffusion coefficient. It is convenient to introduce instead of p the quantity Δp differing from p by the constant $p_n(T_0)$:

$$\Delta p = p - p_n(T_0), \tag{2}$$

where T_0 is the junction temperature and $p_n(T_0)$ is the equilibrium hole concentration at this temperature. Then p can by replaced by Δp in (1).

The continuity equation can be written in the form

$$\frac{1}{e}\frac{dj_p}{dx} = g_{\text{th}} - r, \tag{3}$$

1063-7826/01/3510-1161$21.00

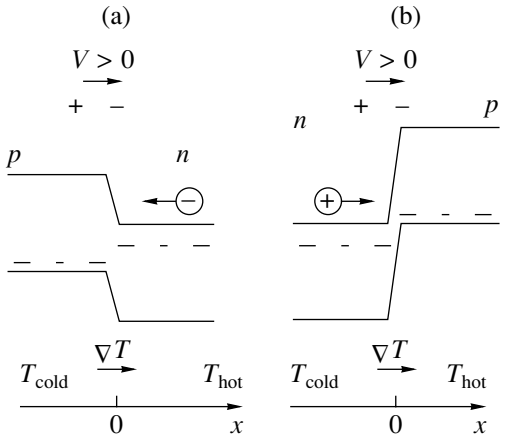

Fig. 1. Thermoelectric power and minority carrier flows in a temperature gradient for junctions: (a) *p–n* and (b) *n–p*.

where g_{th} and r are, respectively, the rates of thermal generation and recombination. At a small hole density, the recombination is linear:

$$t = \frac{p}{\tau_p}, \tag{4}$$

where τ_p is the hole lifetime. In equilibrium at T, $g_{th} = r$ and, therefore,

$$g_{th} = \frac{p_n(T)}{\tau_p}, \tag{5}$$

and this quantity is independent of the nonequilibrium hole concentration.

The difference in (3) can be represented as

$$\begin{aligned} g_{th} - r &= \frac{p_n(T)}{\tau_p} - \frac{p}{\tau_p} \\ &= -\frac{p - p_n(T_0)}{\tau_p} + \frac{p_n(T) - p_n(T_0)}{\tau_p}. \end{aligned} \tag{6}$$

Then the continuity equation reads

$$\frac{1}{e}\frac{dj_p}{dx} = -\frac{\Delta p}{\tau_p} + g(x), \tag{7}$$

where

$$g(x) = \frac{1}{\tau_p}\left(\frac{dp_n(T)}{dT}\right)\bigg|_{T = T_0}\frac{dT}{dx}x. \tag{8}$$

At a small temperature difference, compared with the mean temperature T_0, across the diode we disregard the temperature dependence of the lifetime, giving a contribution of higher order of smallness. Then, substituting (1) and (2) into (7), we obtain a diffusion equation for holes in the form

$$\frac{d^2\Delta p}{dx^2} - \frac{\Delta p}{L_p} = -\frac{g(x)}{D_p}, \tag{9}$$

where $L_p = (\tau_p D_p)^{1/2}$ is the diffusion length. It is noteworthy that Eq. (9) is similar to the corresponding equation for the photovoltage of a *p–n* junction, but with different meaning for the generation function $g(x)$ and the quantity $\Delta p(x)$.

The boundary conditions read

$$\Delta p(0) = p_n(T_0)(e^{eU/k_0T} - 1), \tag{10}$$

$$\Delta p(w) = p_n(T|_{x = w}) - p_n(T_0) = \left(\frac{\partial p_n}{\partial T}\right)_{T = T_0}\frac{dT}{dx}w, \tag{11}$$

where U is the voltage across the *p–n* junction and w is the thickness of the quasi-neutral *n* region. The first condition is well known, while the second assumes an equilibrium at the boundary of the *n* region. At $w \gg L_p$, the condition at the boundary $x = w$ has no effect on the current through the *p–n* junction. Otherwise, the condition (11) corresponds to an ohmic contact.

Solving Eq. (9) with the boundary conditions (10) and (11) yields the hole density distribution in the *n* region:

$$\begin{aligned} \Delta p = p_n(T_0)&\frac{\sinh[(w - x)/L_p]}{\sinh(w/L_p)} \\ &+ \left(\frac{\partial p_n}{\partial T}\right)_{T = T_0}\frac{dT}{dx}x. \end{aligned} \tag{12}$$

Substituting (12) into (1) with account of (2), we obtain the hole current in the junction cross section:

$$\begin{aligned} j_p(0) = &\frac{eD_p p_n(T_0)}{L_p}(e^{eU/k_0T} - 1)\tanh^{-1}\left(\frac{w}{L_p}\right) \\ &- eD_p\left(\frac{\partial p_n}{\partial T}\right)_{T = T_0}\frac{dT}{dx}. \end{aligned} \tag{13}$$

By analogy with the barrier photo emf, the first term in (13) corresponds to the hole component of the ordinary dark current of the photocell and the second term replaces the photocurrent and is called, by analogy, the thermocurrent. Since the *p–n* junction is narrow, the recombination within the junction is negligible and the hole current component in the *p* region is also equal to (13). The electronic current component through the junction is sought similarly by solving the diffusion equation for electrons in the quasi-neutral *p* region. Let us consider for simplicity the case of a wide quasi-neutral region $w \gg L$. Then, taking into account the electronic current in the *p* region, we obtain the total current through the diode:

$$j = j_p(0) + j_n(0) = J_S(e^{eU/k_0T} - 1) - j_{th}, \tag{14}$$

where J_S is the saturation current,

$$J_S = \frac{eD_p p_n(T_0)}{L_p} + \frac{eD_n n_p(T_0)}{L_n}, \tag{15}$$

and $j_{th} = j_{th}^{(p)} + j_{th}^{(n)}$ is the total thermocurrent trough the junction, due to the electronic and hole thermocurrents.

Let us write an explicit expression for the thermocurrent. We can simplify the derivative in the hole current component, using the relation $p_n n_n = n_i^2$, where n_i is the intrinsic density and n_n is the density of majority carriers in the n region, which is assumed to be equal to the impurity concentration and independent of T in the impurity depletion region:

$$\frac{\partial n_p}{\partial T} = \frac{1}{n_n}\frac{dn_i^2}{dT} = \frac{n_i^2}{n_n}\frac{d}{dT}\ln(n_i^2) = p_n\frac{d}{dT}\ln(n_i^2). \quad (16)$$

The intrinsic density is proportional to the known function of temperature

$$n_i \sim T^{3/2}\exp\left(-\frac{\varepsilon_g}{2k_0T}\right), \quad (17)$$

which yields

$$\frac{\partial p_n}{\partial T} = \frac{p_n}{T}\left(3 + \frac{\varepsilon_g}{k_0T}\right), \quad (18)$$

$$j_{th}^{(p)} = \frac{eD_p p_n}{T}\left(3 + \frac{\varepsilon_g}{k_0T}\right)\frac{dT}{dx}. \quad (19)$$

The second component of the thermocurrent j_{th}, coming from the p region, has the opposite sign:

$$j_{th}^{(n)} = -\frac{eD_n n_p}{T}\left(3 + \frac{\varepsilon_g}{k_0T}\right)\frac{dT}{dx}. \quad (20)$$

The total thermocurrent equals

$$j_{th} = e(D_p p_n - D_n n_p)\left(3 + \frac{\varepsilon_g}{k_0T}\right)\frac{1}{T}\frac{dT}{dx}. \quad (21)$$

If the overall current through the p–n junction is zero ($j = 0$), and the potential difference U is small ($U \ll k_0T/e$), then it follows from (21) that

$$U = \frac{k_0T}{eJ_S}j_{th}. \quad (22)$$

Substituting (21) and (15) into (22), we obtain

$$U = \frac{k_0}{e}\frac{D_p p_n - D_n n_p}{D_p p_n/L_p + D_n n_p/L_n}\left(3 + \frac{\varepsilon_g}{k_0T}\right)\frac{dT}{dx}. \quad (23)$$

As can be seen from (23), there is no thermoelectric power in the completely symmetric p–n junction. The sign of the voltage is determined both by the type of junction asymmetry and by the sign of the temperature gradient. The occurrence of essentially asymmetric junctions is frequent and is of interest for obtaining a large thermoelectric power. Let us consider a diode with a more heavily doped p region, i.e., with $p_p \gg n_n$ and, therefore, $p_n \gg n_p$. The main contribution to the thermocurrent comes in this case from the hole current, and the voltage across the junction is positive at $dT/dx > 0$:

$$U = \frac{k_0}{e}\left(3 + \frac{\varepsilon_g}{k_0T}\right)L_p\frac{dT}{dx} > 0. \quad (24)$$

If the temperature T changes mainly within a region of size l_{ef} near the p–n junction, then

$$\frac{dT}{dx} = \frac{\Delta T}{l_{ef}}. \quad (25)$$

The thermoelectric power $\alpha = V/\Delta T$ then equals

$$\alpha = \frac{k_0}{e}(3 + \varepsilon_g^*)a, \quad (26)$$

where $\varepsilon_g^* = \varepsilon_g/k_0T$, and $a = L_p/l_{ef}$ is the geometric factor.

In order to obtain large α values, it is necessary to fabricate a p–n junction with the largest a possible; i.e., the temperature drop must take place mainly in a region of size of about L_p near the junction. This means that the p region must be thin or have high thermal conductivity. The use of heterojunctions could be helpful in constructing asymmetric systems. For instance, if a material with large thermal conductivity in the p region can be chosen in the case when the p region is more heavily doped, this reduces the temperature drop ∇T across the n region, making the thermoelectric power higher.

If we consider a system comprising an array of in-series connected p–n and n–p junctions, then the total thermoelectric power is a sum of the ones for all the junctions. The reason is that if we transpose the p and n regions (see Fig. 1b), the lightly doped n region will be on the left, where the temperature is lower and, therefore, the thermocurrent signs are reversed ($j_{th}^{(p)} < 0$). On the other hand, the sign at U should be reversed, since the n region is positive. Therefore, the sign and magnitude of the thermoelectric power remain the same in the cases shown in Figs. 1a and 1b, and the thermoelectric powers of junctions in the p–n–p–n structure add up.

The high thermoelectric power in p–n–p–n structures account for the anomalously high thermoelectric power observed in opals with introduced GaAs clusters [7, 8]. If the clusters constituting a 3D superlattice are p-type and n-type regions are formed in the links, then a p–n–p structure is formed in the links. The summation of thermoelectric powers of a large number of in-series connected junctions can account for the high measured thermoelectric power. Assuming that the links have a lower carrier (electron) density than the clusters, we obtain a positive sign of the thermoelectric power for all the p–n junctions. This conclusion is in agreement with the experimental data, whereas the thermionic emission through the vacuum gap between clusters leads to a negative thermoelectric power.

2. THERMOELECTRIC FIGURE OF MERIT OF A *p–n* JUNCTION

Let us now find the dimensionless thermoelectric efficiency ZT (Ioffe criterion) of a sample with a *p–n* junction. It is expressed in terms of the thermoelectric power α, resistance R, and thermal conductance K of the diode:

$$ZT = \frac{\alpha^2 T}{KR}. \quad (27)$$

In order to find R, we note that the main part of the resistance R falls in the depleted region. Linearizing the current density (14) we obtain, taking into account that the *p* region is doped much more heavily:

$$j = \frac{e\mu_p p_n}{L_p} U. \quad (28)$$

Here, the Einstein relation between the mobility and the diffusion coefficient, $D = \mu(k_0 T/e)$, was used. As a result we obtain the resistance per unit sample cross-section area:

$$R = \frac{L_p}{e\mu_p p_n} = \frac{L_p}{\sigma_p}, \quad (29)$$

where σ_p is the conductivity by minority carriers in the *n* region.

In calculating the thermal conductivity, account should be taken of the fact that the barrier region does not impede heat transfer, in contrast to the case of the electrical resistance, since the total thermal conductivity includes the phonon component κ_{ph}. That is why the main temperature drop occurs across rather wide neutral regions. Both electrons and holes are to be taken into account, since the minority carrier current cannot be neglected in this case. Therefore, the bipolar thermal conductivity is an important component of the total thermal conductivity. The kinetic theory of heat transport gives the following expression for the thermal conductivity:

$$\kappa_e = \kappa_n + \kappa_p + \frac{\sigma_n \sigma_p}{\sigma_n + \sigma_p} T\left(\frac{k_0}{T}\right)^2 (5 + r_n + r_p + \varepsilon_g^*)^2, \quad (30)$$

where r_n and r_p are the scattering parameters equal to $-1/2$ for scattering on phonons. The partial thermal conductivities can be related to the electrical conductivities by means of the Lorentz number. As a result, we obtain

$$\kappa_e = T\left(\frac{k_0}{T}\right)^2 \left[2(\sigma_n + \sigma_p) + \frac{\sigma_n \sigma_p}{\sigma_n + \sigma_p}(4 + \varepsilon_g^*)^2\right]. \quad (31)$$

The total thermal conductance $K = (\kappa_{ph} + \kappa_e)/l_{ef}$, where l_{ef} is, as before, the size of the region near the junction in which the main temperature drop takes place. Substituting (29) and (31) into (27), we obtain

$$ZT = \frac{(3 + \varepsilon_g^*)^2 a}{\dfrac{(4 + \varepsilon_g^*)^2}{1 + \sigma_p/\sigma_n} + 2\left(1 + \dfrac{\sigma_n}{\sigma_p}\right) + \dfrac{\kappa_{ph}}{(k_0/e)^2 T \sigma_p}}. \quad (32)$$

It follows from the inequality $p_n \ll n_n$ that, if the electron and hole mobilities are of the same order of magnitude, then $\sigma_p \ll \sigma_n$ and

$$ZT = \frac{(3 + \varepsilon_g^*)^2 a}{(4 + \varepsilon_g^*)^2 + 2\dfrac{\sigma_n}{\sigma_p} + \dfrac{\kappa_{ph}}{(k_0/e)^2 T \sigma_p}}. \quad (33)$$

If the bipolar thermal conductivity gives the main contribution, the first term in the denominator of (33) is dominant and $ZT \approx 1$ since $\varepsilon_g^* \gg 1$. Therefore, the thermoelectric figure of merit of the system with *p–n* junctions may compare well with that in the best modern thermoelectric materials. Although, as seen from (33), ZT cannot exceed unity, the statement that the thermoelectric figure of merit of thermoelectric devices operating on minority carriers is always significantly less than that in the case of majority carriers [9] is too pessimistic.

Let us numerically estimate the Ioffe criterion for a Bi_2Te_3 *p–n* junction. The energy gap of this material $\varepsilon_g = 0.13$ eV, the lattice thermal conductivity $\kappa_{ph} \approx 1.45$ W/(m K) [10]. Using the available data on the temperature dependence of the effective mass, we obtain $n_i = 0.9 \times 10^{18}$ cm^{-3} at room temperature. The electron mobility is higher than that of holes: $\mu_n = 1200$ cm^2/(V s), $\mu_p = 510$ cm^2/(V s); therefore, to obtain large Z, it is desirable to have a more weakly doped *p* region, in which the minority carriers are electrons. Let $p_p = 3n_i$, $n_p = 0.3n_i$; then calculation by means of formula (33) with transposed *p* and *n* indices gives $ZT \approx 0.33$.

CONCLUSION

Thus, the calculation shows that the Ioffe criterion for a structure with a *p–n* junction may be about the same as that in the best modern thermoelectric materials. It follows from the derived formulas that, to achieve high thermoelectric figures of merit, the junction should be essentially asymmetric and be fabricated in such a way that the main temperature drop takes place in the region of size approximately equal to the minority carrier diffusion length near the interface in the more weakly doped region.

REFERENCES

1. J. Tauc, *Photo- and Thermoelectric Effects in Semiconductors* (Pergamon, Oxford, 1962; Inostrannaya Literatura, Moscow, 1962).
2. V. I. Stafeev, Fiz. Tverd. Tela (Leningrad) **2**, 438 (1960) [Sov. Phys. Solid State **2**, 406 (1960)].
3. I. I. Balmush, Z. I. Dashevskiĭ, and A. I. Kasiyan, *Thermoelectric Effects in Multilayered Semiconductor Structures* (Shtiintsa, Kishinev, 1992).
4. I. I. Balmush, Z. M. Dashevskiĭ, A. I. Kasiyan, and N. V. Kolomoets, Dokl. Akad. Nauk SSSR **272**, 855 (1983) [Sov. Phys. Dokl. **28**, 888 (1983)].
5. N. S. Lidorenko, I. I. Balmush, Z. M. Dashevskiĭ, *et al.*, Dokl. Akad. Nauk SSSR **299**, 355 (1988) [Sov. Phys. Dokl. **33**, 217 (1988)].
6. I. I. Balmush, Z. M. Dashevskiĭ, and A. I. Kasiyan, Fiz. Tekh. Poluprovodn. (St. Petersburg) **29**, 1796 (1995) [Semiconductors **29**, 937 (1995)].
7. V. N. Bogomolov, D. A. Kurdyukov, A. V. Prokofiev, *et al.*, in *Proceedings of the International Conference on Thermoelectrics, St. Petersburg, 1995*, p. 280.
8. V. N. Bogomolov, D. A. Kurdyukov, A. V. Prokofiev, *et al.*, Phys. Low-Dimens. Struct. **11/12**, 63 (1994).
9. W. M. Bullis, J. Appl. Phys. **34**, 1648 (1962).
10. B. M. Gol'tsman, V. A. Kudinov, and I. A. Smirnov, *Semiconducting Thermoelectric Materials Based on* Bi_2Te_3 (Nauka, Moscow, 1972).

Translated by S. Ktitorov

Semiconductors, Vol. 35, No. 10, 2001, pp. 1166–1170. Translated from Fizika i Tekhnika Poluprovodnikov, Vol. 35, No. 10, 2001, pp. 1219–1223.

SEMICONDUCTOR STRUCTURES, INTERFACES, AND SURFACES

The Influence of the Illumination Direction on the Field Distribution in High-Resistivity Metal–Semiconductor Structures

B. I. Reznikov

Ioffe Physicotechnical Institute, Russian Academy of Sciences, Politekhnicheskaya ul. 26, St. Petersburg, 194021 Russia

Submitted January 18, 2001; accepted for publication March 12, 2001

Abstract—The dependence of the field distribution on the illumination intensity in a heavily biased high-resistivity metal–semiconductor structure exposed to intrinsic-absorption monochromatic light was investigated. The distinctions in the field distribution under illumination from the anode and cathode sides are revealed. In the bulk, these distinctions are caused by a difference in the photocarrier mobility, whereas near the surface they are caused by the different directions of diffusion and drift flows for more mobile electrons. It is demonstrated that if the cathode is illuminated, the field distribution is nonuniform. In this case, the field decreases in a thin layer with a distance from the illuminated cathode, passes through a minimum, and increases toward the anode. With increasing illumination intensity, the quasi-neutral region in the vicinity of the field minimum expands toward the anode and the lowest field decreases. On the other hand, near the illuminated cathode, the field increases for low intensities and decreases for high intensities. For sufficiently high illumination intensities, the field dependence on the coordinate in the bulk of pure crystals as a function of the distance from the illuminated electrode is independent of the illumination direction. © *2001 MAIK "Nauka/Interperiodica".*

1. INTRODUCTION

Spatial transformation of the electric field under illumination is a fundamental physical effect used in modern optoelectronic devices. These include radiation detectors and light-controlled optoelectronic devices used in information processing and recording the signals of optical images [1]. These devices are based on the metal–semiconductor–metal (MSM) structures with a tunneling thin insulator at the interface. In these structures, wide-gap high-resistivity compensated crystals, for example, CdTe, are used. The device operation relies on the dependence of the properties of the optical medium on the electric field, which varies in the crystal bulk due to the accumulation and redistribution of the photoinduced bulk charge of free carriers.

The theoretical investigation of the field distribution in high-resistivity MSM structures exposed to intrinsic-absorption light revealed the dependences of field distributions on the intensity I_i of the radiation entering the semiconductor $E(x, I_i)$ [2–5]. With increasing illumination intensity, the field decreases near the illuminated electrode and increases near the dark electrode. The characteristic scale of intensity

$$I_* = \frac{8}{9}\frac{j_*}{e} = \frac{\varepsilon}{4\pi}\frac{\mu V^2}{ed^3}$$

separates the regions of high and low intensities, and corresponds to the screening of approximately one-half of the field applied. Here, μ is the majority carrier mobility, j_* is the current limited by a bulk charge, and ε is the dielectric constant. In the region of small intensities $I_i < I_*$, the field distribution $E(x)$ is linear. Deviations of boundary values of the field $E_{0,d}$ from the effective field $E_e = V/d$ are small: $|E_{0,d} - E_e|/E_e \ll 1$. These deviations depend linearly on the intensity [2].

For high illumination intensities, which noticeably exceed the upper limit of the linear mode $I_i \gtrsim I_*$, the field distribution substantially depends on the ratio between the emission rate $V_{n,p}$ and the drift rate $v^{\mathrm{dr}}_{n,p}$, especially close to the electrodes [3, 5]. For high emission rates exceeding the drift rates $V_{n,p} \gtrsim v^{\mathrm{dr}}_{n,p}$, and illumination intensities exceeding a certain characteristic value I_{inv}, the region of the negative (inverse) field of several absorption lengths thick is formed in the vicinity of the anode illuminated [3]. Otherwise, for low emission rates $V_{n,p} \lesssim v^{\mathrm{dr}}_{n,p}$, carriers accumulate close to the electrodes of the opposite sign, and the field in the layer several $l_E = kT/eE_e$ thick adjacent to the electrodes is of the same sign and rises [5]. Thus, for luminous fluxes large enough, the region of high electric fields is formed in thin boundary layers adjacent to electrodes, whereas the total screening of the external electric field and the band straightening for MSM structures at the illuminated surface itself are nonexistent [6].

All trends related to the dependence of the field distribution in MSM structures on the illumination intensity were obtained for the exposure of the structure from the anode side [2–5]. They agreed qualitatively

with the experimental data on the field distribution in the bulk of a heavily biased ($d \approx 0.3$ cm, $V = 100$–500 V) high-resistivity p-type semi-insulating structure ($N_a \approx 10^8$–10^9 cm^{-3}) with a moderate concentration of deep-level impurities ($N_t \approx 10^{13}$ cm^{-3}) [7]. The data on the field distribution for the cathode illuminated were reported [7]. However, these data corresponded to the limited range of incident radiation intensities, and no comprehensive comparison of the field distribution dependence on the illumination direction was carried out. The authors of [7] restricted themselves to the remark that the measured field distributions were fairly symmetric.

The purpose of this study, which continues and supplements previous studies [2, 3], is to investigate in detail the field dependence in a pure high-resistivity structure on the illumination intensity for illumination from the cathode side. The distinctions in the field distribution depending on the illumination direction are to be revealed.

2. RESULTS AND DISCUSSION

2.1. The mathematical formulation of the problem coincides with that considered previously [2–5]. The symmetric MSM structure $0 < x < d$ is considered, which is based on a p-type high-resistivity semiconductor in which the effective concentration of compensated completely ionized acceptors is N_a. The energy band diagram of the structure is given in Fig. 1 of publication [2]. The voltage V sufficiently exceeding the semiconductor–metal contact potential difference is applied to the structure. The point $x = 0$ is located at the anode, so that the external field applied $E_e = V/d > 0$. The monochromatic luminous flux is incident on the semitransparent surface of the structure. The generation rate of the pairs by the external radiation $g(x) = \alpha I_i \exp(-\alpha\xi)$. If the cathode is illuminated, then $\xi = d - x$; if the anode is illuminated, $\xi = x$. Here, α is the optical absorption coefficient, and I_i is the density of the photon flux entering the semiconductor. The initial set of continuity equations to a diffusion–drift approximation and a Poisson equation, which describe the carrier transport and a field variation on illumination of a pure high-resistivity structure, are given elsewhere [2].

At the metal–semiconductor interfaces $x = 0$ and $x = d$, allowance is made for the electron and hole exchange by the thermionic emission with the rates V_n and V_p, and a surface recombination. If there is neither illumination nor surface recombination, then these boundary conditions lead to the known expression for the current density across the metal–semiconductor reverse-biased contact [2, 8].

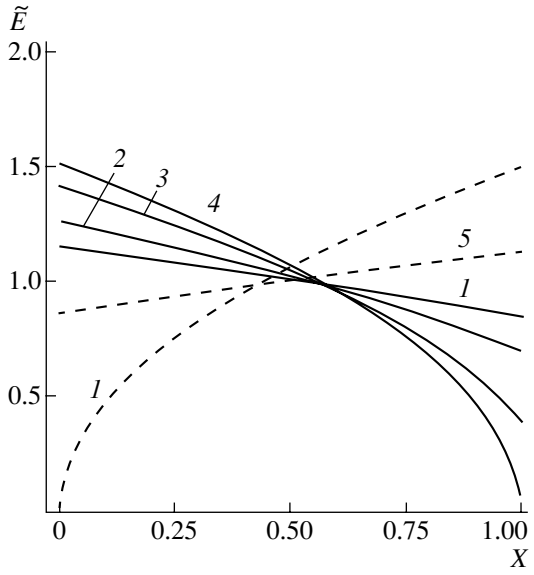

Fig. 1. Electric field distribution in the semiconductor bulk $\tilde{E} = E/E_e$ for moderate illumination intensities, $I_i = (1)\ 1 \times 10^{16}$, $(2)\ 2 \times 10^{16}$, $(3)\ 4 \times 10^{16}$, and $(4)\ 1 \times 10^{17}$, and $(5)\ 1 \times 10^{15}$ cm^{-2} s^{-1}. Solid and dashed lines correspond to the illumination from the cathode and anode sides respectively.

Numerical values for most of the parameters coincide with those used previously [2]:

$$d = 0.25 \text{ cm}, \quad V = 400 \text{ V}, \quad T = 300 \text{ K},$$

$$N_a = 10^8 \text{ cm}^{-3},$$

$$\alpha = 10^4 \text{ cm}^{-1}, \quad \mu_n = 500 \text{ cm}^2/(\text{V s}),$$

$$\mu_p = 50 \text{ cm}^2/(\text{V s}),$$

$$V_n = 8.5 \times 10^6 \text{ cm/s}, \quad V_p = 6 \times 10^6 \text{ cm/s}.$$

2.2. The results of calculations of the field distribution $\tilde{E}(X) = E/E_e$ ($X = x/d$, $E_e = V/d$) for moderate intensities $I_i \approx I_* \approx 3.1 \times 10^{16}$ cm^{-2} s^{-1} are shown in Fig. 1. The values of the parameters used correspond to the almost uniform distribution of the field without illumination ($|\tilde{E}_{0,d} - 1| \approx 10^{-3}$). With increasing intensity, the distribution becomes more and more nonuniform. The field decreases near the cathode illuminated and rises near the unilluminated anode, which qualitatively coincides with the case of the illuminated anode [2]. For low intensities $I_i \lesssim I_*$, if the photoinduced charge density is relatively low, the field is the linear function of the coordinate and no specific features are observed in the distribution. For intensities $I_i \gtrsim I_*$, a thin positively charged layer adjacent to the cathode exists (curves *4*, *3*).

The coordinate dependences of the field $E_a(x)$ and $E_c(d - x)$ for identical intensities (curves *1*) as functions

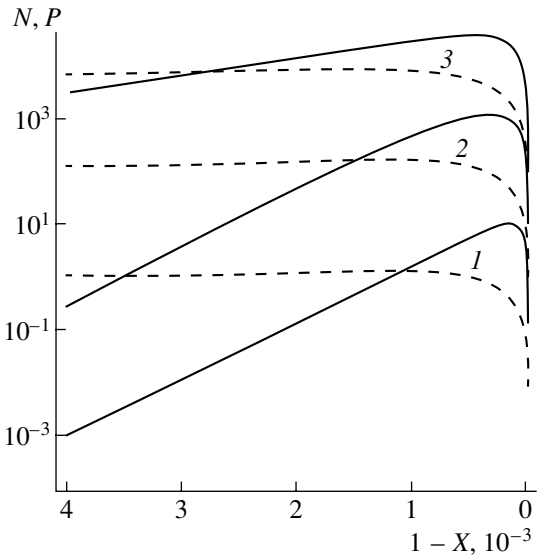

Fig. 2. Distribution of electron concentrations $N = n/N_a$ (dashed lines) and holes $P = p/N_a$ (solid lines) near the cathode illuminated for illumination intensities I_i = (*1*) 1×10^{15}, (*2*) 5×10^{16}, and (*3*) 1×10^{17} cm^{-2} s^{-1}.

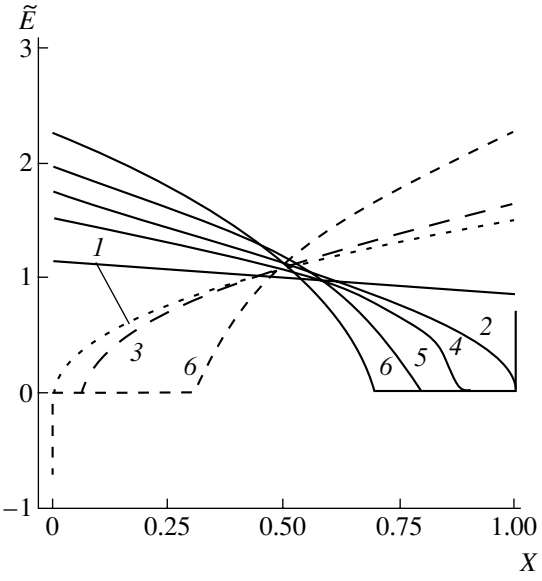

Fig. 3. Electric field distribution $\tilde{E} = E/E_e$ in the semiconductor bulk for high illumination intensities I_i = (*1*) 1×10^{16}, (*2*) 1×10^{17}, (*3*) 1×10^{18}, (*4*) 2×10^{18}, (*5*) 5×10^{18}, and (*6*) 1×10^{19} cm^{-2} s^{-1}. The illumination from the cathode and anode sides is shown by solid and dashed lines, respectively.

of the distance from the illuminated electrode are different ($E_{a,\,c}$ are the field distributions for the anode and cathode illuminated). This is related to a difference in mobilities $\mu_{p,\,n}$ of carriers, which transport the charge in the semiconductor bulk. This determines various characteristic scales $I_*^{p,\,n} \propto \mu_{p,\,n}$, which correspond to noticeable screening of the field applied in the vicinity of the illuminated surface. For this reason, for various directions of the illumination and identical intensities, the field distributions as a function of a distance from the illuminated electrode are different. The distributions $E_a(x) = E_c(d - x)$ in the bulk coincide only if the ratio I_i/I_* for low intensities $I_i/I_* \ll 1$ is the same in both cases. This theoretical result is supported by the numerical calculation (see the comparison of solid curve *1* with dashed curve *5* in Fig. 1).

A decrease in the field near the illuminated cathode with increasing illumination intensity and an increase near the unilluminated anode (Fig. 1) is due to the separation of photogenerated carriers by the external field, with the potential difference across the structure remaining constant. Due to a drift in the field, electrons form a negative spatial charge density in the bulk, where the inequality $n \gg p$ is satisfied. In contrast, holes are kept close to the cathode by the field and occupy a layer several generation lengths thick ($\sim\alpha^{-1}$), until the field of this region is weakly screened. Here, $p \gg n$ for intensities generating the photocarriers with concentrations exceeding the dark ones, and the space charge density is positive (Fig. 2), since the electrons leave the generation region due to diffusion and drift. In this region, the field increases toward the cathode. The hole concentration decreases with distance from the cathode and becomes equal to the electron concentration at the point $x = x_{qn}$, whereas the field attains the minimum $E(x_{qn}) = E_{\min}$. For $x < x_{qn}$, the charge density $\rho = e(p - n) < 0$, and decreases rapidly with distance from the generation region (Fig. 2), whereas the field increases toward the anode.

For low illumination intensities $I_i \lesssim I_*$, the positive charge $e(p - n)$ near the illuminated cathode is insufficient for a noticeable field variation in the near-electrode layer, whereas the quasi-neutral region is rather narrow (Fig. 2). The field E_d is equal to $E_{\min}$ to a high accuracy and decreases with increasing illumination intensity (Fig. 1, curves *1–3*). The law of variation of the near-electrode field $\tilde{E}_d$ with increasing intensity is given by formula (37) from publication [2] (with the substitution of d for 0).

For $I_i \gtrsim I_*$, the difference in concentrations $|p - n|$ near the illuminated surface and in the bulk increases with increasing illumination intensity. In the vicinity of the illuminated cathode, as the field in the generation region decreases, the region occupied by holes $x_{qn} < x < d$ expands into the semiconductor bulk from the cathode due to diffusion (Fig. 2). In this intensity range, the field distribution displays a series of specific features (Fig. 3). These include a decrease in the field from the anode in the region $0 \le x \le x_{qn}$, a wide quasi-neutral region expanding toward the anode with increasing

intensity, and a noticeable increase in the field in the near-electrode layer adjacent to the illuminated cathode (Fig. 4). The coordinate dependence of the field $E(d-x)$ in the region adjacent to the unilluminated electrode $x < x_{qn}$ is similar to the dependence of the field distribution on the anode illumination intensity investigated previously [3]. The fundamental distinction is in the field behavior in the vicinity of the illuminated cathode. The field inversion (sign change) for the illuminated anode was investigated previously [3, 4] (Fig. 3, dashed curves *3*, *6*). In contrast with this case, the field E_d passes through the minimum with increasing intensity and then increases (Figs. 4, 5). This behavior of the field is the consequence of several factors, namely, the conservation of the potential difference across the structure, a high density of the positive space charge close to the cathode, and a sign-variable distribution of the space charge density. For a low intensity, the positive space charge in the vicinity of the cathode is small and the first factor prevails. Due to an increasing field in the unilluminated region, the field decreases near the cathode. For a higher intensity, conversely, the effect of the second local factor is dominant. The first two factors are also present if the anode is illuminated. However, in this case, the combination of diffusion and drift electron fluxes to the illuminated electrode gives rise to a higher hole concentration near the anode and to a positive space charge density in the semiconductor bulk and near the illuminated electrode. In this case, the field minimum is attained near the anode and the field in the vicinity of the anode becomes negative with an unlimited increase in the space charge as the illumination intensity increases.

If the cathode is illuminated, the field counteracts the electron diffusion toward the cathode and forces out the electrons into the sample bulk. The charge density is positive near the illuminated electrode of the opposite sign and negative in the bulk. This factor gives rise to the field minimum in the bulk and to the field increase in the vicinity of the cathode due to the local factor of high density of the positive space charge. Similar behavior of the field was noted previously [9]. In this study, the space charge density near the illuminated anode was negative due to the electron trapping by deep impurity levels.

Figure 3 demonstrates that the dependences $E_c(d-x)$ and $E_a(x)$ for high illumination intensities $I_i \gg I_*$ nearly coincide in the bulk. They may be made coincident by rotating the $E_c(x)$ curve around the axis $X = 0.5$. The distinction is in the vicinity of illuminated electrodes only, where $E_c(d-x) \approx |E_a(x)|$.

The field distributions in the near-electrode layer adjacent to the cathode (Fig. 4) demonstrate a decrease in the lowest field $\tilde{E}_{\min}$ with increasing illumination. In this case, the field remains positive. In the layer $\sim 5\alpha^{-1}$ thick immediately adjacent to the cathode, the field $\tilde{E}_d$ increases. This behavior of the field is the consequence

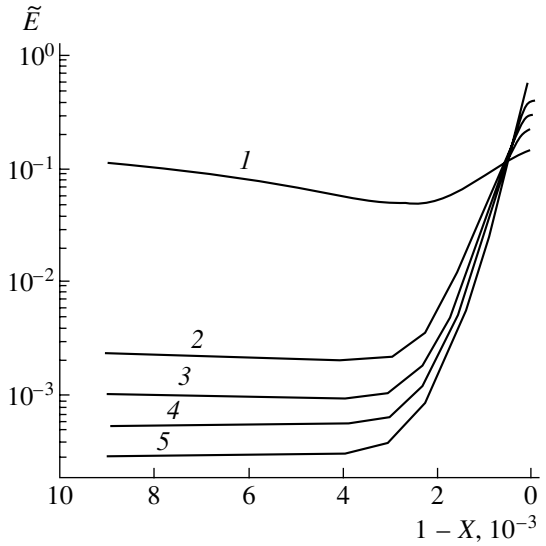

Fig. 4. Distribution of electric field $\tilde{E} = E/E_e$ at high illumination intensities I_i near the illuminated cathode. I_i = (*1*) 1×10^{17}, (*2*) 2×10^{17}, (*3*) 1×10^{18}, (*4*) 2×10^{18}, and (*5*) 5×10^{18} cm^{-2} s^{-1}.

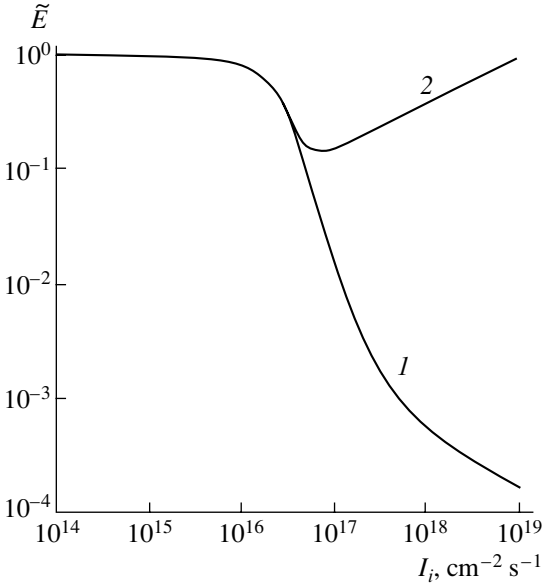

Fig. 5. Dependences of (*1*) minimal electric field $\tilde{E}_{\min}$ and (*2*) the field near the illuminated cathode E_d on the illumination intensity.

of an increase in the negative space charge in the bulk and in the positive space charge near the cathode with increasing illumination intensity. It can be seen from Fig. 5 that the distinctions between the fields $\tilde{E}_{\min}$ and $\tilde{E}_d$ start to manifest themselves at $I_i \gtrsim I_*$. In this intensity range, the field minimum decreases nearly according to the power law ($E_{\min} \propto I_i^{-\beta(I_i)}$, $\beta \approx 1$). In contrast, the field near the electrode E_d increases, and for inten-

sities significantly exceeding the value I_*, at which the field E_d attained the minimum, its value becomes equal to the external field.

Note that the considerable width of the quasi-neutral region (Fig. 3) is related to a low-rate bulk recombination. As it was demonstrated previously [4], the allowance made for the bulk recombination at deep impurity levels leads to a noticeable narrowing of the width of the quasi-neutral region.

2.3. The specific features of the field distribution obtained for an intense illumination of pure crystals are also retained for the structures containing deep impurity levels. The reason is that the charge of the levels is restricted by the quantity $|eN_t|$. This charge becomes less than the charge of free electrons and holes for sufficiently high intensities. The details of the field distribution both in the semiconductor bulk and in the vicinity of the illuminated electrode depend on the concentration and parameters of the impurity level. These include the level energy and capture cross sections for electrons (σ_n) and holes (σ_p) [10]. Numerical calculations for the case of the illuminated cathode were carried out. They demonstrated that the field sign for a quasi-neutral region, the width of this region, and the field magnitude near the unilluminated electrode strongly depend on the ratio of cross sections for capture by an impurity. Specifically, for $\sigma_n \ll \sigma_p$, the field in the bulk depends on the illumination intensity rather weakly. In the quasi-neutral region, the field is negative.

3. CONCLUSION

The results of calculations make it possible to draw the following conclusions.

(1) For high illumination intensities, no band straightening in the vicinity of the electrode illuminated is observed irrespective of the illumination direction.

(2) Nonmonotonic field dependence in the semiconductor bulk always appears if the sign of the space charge adjacent to the illuminated electrode is opposite to the sign of this electrode.

(3) Various directions of the diffusion and drift fluxes under illumination from the anode and cathode sides should give rise to the dependence of the current–intensity characteristic on the illumination direction.

REFERENCES

1. P. G. Kasherininov, A. V. Kichaev, Yu. N. Perepelitsin, *et al.*, Elektrosvyaz', No. 10, 37 (1990).
2. P. G. Kasherininov, B. I. Reznikov, and G. V. Tsarenkov, Fiz. Tekh. Poluprovodn. (St. Petersburg) **26** (8), 1480 (1992) [Sov. Phys. Semicond. **26**, 832 (1992)].
3. B. I. Reznikov and G. V. Tsarenkov, Fiz. Tekh. Poluprovodn. (St. Petersburg) **27** (8), 1262 (1993) [Semiconductors **27**, 699 (1993)].
4. B. I. Reznikov and G. V. Tsarenkov, Fiz. Tekh. Poluprovodn. (St. Petersburg) **28** (5), 867 (1994) [Semiconductors **28**, 506 (1994)].
5. B. I. Reznikov and G. V. Tsarenkov, Fiz. Tekh. Poluprovodn. (St. Petersburg) **31** (1), 23 (1997) [Semiconductors **31**, 19 (1997)].
6. V. A. Zuev and V. G. Popov, *Photoelectric MIS Devices* (Radio i Svyaz', Moscow, 1983).
7. P. G. Kasherininov, A. V. Kichaev, and A. A. Tomasov, Fiz. Tekh. Poluprovodn. (St. Petersburg) **29** (11), 2092 (1995) [Semiconductors **29**, 1092 (1995)].
8. S. Sze, *Physics of Semiconductor Devices* (Wiley, New York, 1981; Mir, Moscow, 1984), Vol. 1.
9. B. I. Reznikov and G. V. Tsarenkov, Fiz. Tekh. Poluprovodn. (St. Petersburg) **29** (8), 1430 (1995) [Semiconductors **29**, 743 (1995)].
10. B. I. Reznikov and G. V. Tsarenkov, Fiz. Tekh. Poluprovodn. (St. Petersburg) **28** (5), 1788 (1994) [Semiconductors **28**, 991 (1994)].

Translated by N. Korovin

Semiconductors, Vol. 35, No. 10, 2001, pp. 1171–1174. Translated from Fizika i Tekhnika Poluprovodnikov, Vol. 35, No. 10, 2001, pp. 1224–1227.

SEMICONDUCTOR STRUCTURES, INTERFACES, AND SURFACES

Effect of the Annealing Temperature on Erbium Ion Electroluminescence in Si:(Er,O) Diodes with (111) Substrate Orientation

N. A. Sobolev, A. M. Emel'yanov, and Yu. A. Nikolaev

Ioffe Physicotechnical Institute, Russian Academy of Sciences, Politekhnicheskaya ul. 26, St. Petersburg, 194021 Russia

Submitted March 30, 2001; accepted for publication April 3, 2001

Abstract—The influence of the temperature of secondary annealing, stimulating the formation of optically and electrically active centers, on the erbium ion electroluminescence (EL) at $\lambda \approx 1.54$ μm in (111) Si:(Er,O) diodes has been studied. The diodes were fabricated by the implantation of 2.0 and 1.6 MeV erbium ions at doses of 3×10^{14} cm^{-2} and oxygen ions (0.28 and 0.22 MeV, 3×10^{15} cm^{-2}). At room temperature, the EL intensity in the breakdown mode grows with the annealing temperature increasing from 700 to 950°C. At annealing temperatures of 975–1100°C, no erbium EL is observed in the breakdown mode owing to the formation of microplasmas. The intensity of the injection EL at 80 K decreases with the annealing temperature increasing from 700 to 1100°C. © *2001 MAIK "Nauka/Interperiodica".*

1. INTRODUCTION

Semiconductor structures doped with rare-earths attract considerable interest owing to their possible applications in optoelectronics. Emission from trivalent erbium (peaked at $\lambda \approx 1.54$ μm [1–7]) and holmium ions (at $\lambda \approx 1.96$ μm [8, 9]) has been observed in diodes fabricated from single-crystal silicon. Generally, the maximum intensity of emission from rare-earth ions at room temperature is observed in reverse-biased diodes in the tunneling or avalanche breakdown mode. The intensity of the injection luminescence is substantially lower. This is commonly attributed to differences between the EL excitation/deexcitation mechanisms in the forward-bias and breakdown modes [1]. Calculations show, however, that in the breakdown mode also, the concentration of emitting rare-earth ions is usually several orders of magnitude lower than that of rare-earth ions introduced by implantation. As a result, the intensity of the presently developed Si:(Er,O) and Si:(Ho,O) light-emitting diodes (LEDs) is insufficient for their wide application even in the case of a virtually uniform distribution of current density over the *p–n* junction area [3, 5]. The majority of implanted rare-earth ions are optically inactive. Furthermore, ion implantation at high doses ($D \gtrsim 10^{14}$ cm^{-2}) causes the amorphization of silicon. The thus-amorphized layer is commonly subjected to solid-phase recrystallization by means of a postimplantation annealing at $T_1 = 620$°C, with the introduced impurities optically activated by annealing at a higher temperature, T_2. In virtually all of the previous studies of Si:(Er,O) diodes, T_2 was 900°C. This temperature was chosen on extending to the LED fabrication technology the results obtained in studying the dependence of the photoluminescence on the annealing temperature [10–12].

The goal of this study was to investigate the effect of the annealing temperature T_2 on the intensity of EL from Si:(Er,O) LEDs fabricated on (111) Si at Er implantation doses $D = 3 \times 10^{14}$ cm^{-2}.

2. EXPERIMENTAL PROCEDURE

Erbium ions with energies $E = 2.0$ and 1.6 MeV and oxygen ions with $E = 0.28$ and 0.22 MeV were implanted at doses $D = 3 \times 10^{14}$ and 3×10^{15} cm^{-2}, respectively, into polished *n*-type Czochralski grown (111) Si wafers with a resistivity of 5 Ω cm. The dose of Er implantation was chosen to be 3×10^{14} cm^{-2} since the maximum intensity of the erbium ion–related EL was achieved with the fabrication technology employed at $T_2 = 900$°C in our previous study [6]. Boron ($E = 40$ keV, $D = 5 \times 10^{15}$ cm^{-2}) and phosphorus ions ($E = 80$ keV, $D = 1 \times 10^{15}$ cm^{-2}) were implanted into the front and back sides of the wafers, respectively, to produce heavily doped p^+ and n^+ layers. Annealing at $T_1 = 620$°C (1 h) led to the recrystallization of the amorphized Si:(Er,O) layer. A second isochronous (0.5 h) annealing at $T_2 = 700$–1100°C was used to form optically and electrically active erbium-related centers. Mesa diodes with working area $S = 4.0$–4.5 mm^2 were fabricated by conventional technology [2–7]. More than half of the working area of p^+ layers was free of metallization. In this part of the structure, EL could be observed in the visible spectral range. For this purpose, the diodes were placed in the dark in the viewing field of an MBS-9 microscope. Current–voltage (*I–V*) characteristics were recorded at a frequency of 32 Hz, with

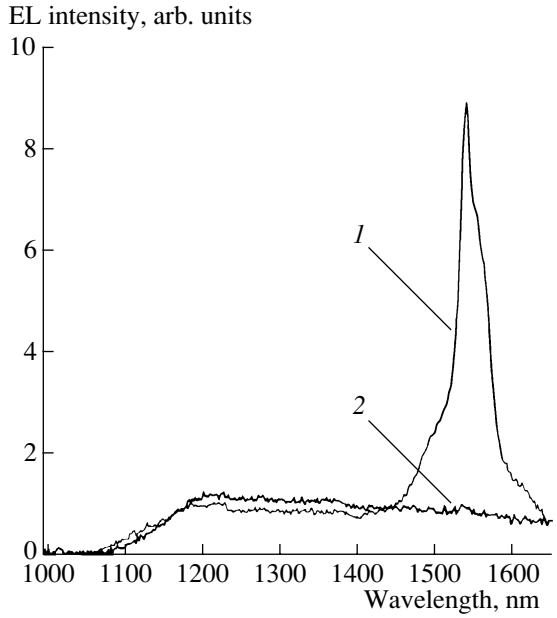

Fig. 1. EL spectra in the breakdown mode for *p–n* structures annealed at T_2: (*1*) 950 and (*2*) 1000°C.

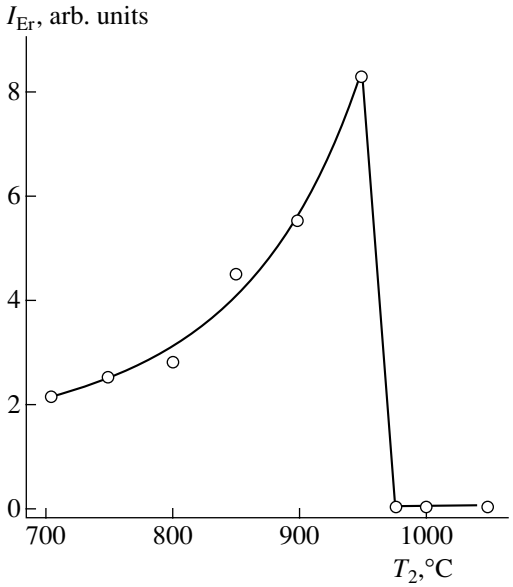

Fig. 2. Maximum intensity of the Er^{3+}-related EL vs. the second annealing temperature T_2. λ = 1.538 μm, breakdown mode.

0.5-ms pulse duration. The EL was excited by 2- or 5-ms square pulses with a repetition frequency of 32 Hz. A system of lenses focused the light emitted by a diode structure onto the entrance slit of an MDR-23 monochromator, with the EL spectrum detected at the output with an uncooled InGaAs diode (7-nm resolution in the range λ = 1.0–1.65 μm). Pulsed voltage in the form of a half-wave-rectified 50 Hz sine was used for the EL studies in the visible range.

3. EXPERIMENTAL RESULTS AND DISCUSSION

Figure 1 presents the EL spectra of reverse-biased diodes at T = 300 K. The dependences of type *1* in Fig. 1 were observed in diodes annealed at T_2 = 700–950°C, and those of type *2*, in diodes annealed at T_2 = 975–1100°C. In the first kind of spectra, peaks at λ = 1.538 μm, associated with radiative electron transitions between the crystal-field-split $^4I_{13/2}$ and $^4I_{15/2}$ levels of Er^{3+} ions, are observed along with the relatively weak and nearly λ-independent emission due to transitions of "hot" electrons within the conduction band of silicon (the so-called "hot" EL [2]). The second kind of spectra is characterized by the presence of virtually only the hot EL. The peak intensity of the EL from Er^{3+} ions grows with increasing reverse current, tending to a constant value I_{Er}. Figure 2 shows I_{Er} as a function of temperature T_2. The intensity I_{Er} grows with increasing temperature in the range 700°C ≤ T_2 ≤ 950°C. At higher temperatures (975°C ≤ T_2 ≤ 1100°C), the erbium-related EL is practically zero.

Figure 3 presents reverse *I–V* curves for several diodes at 300K. The breakdown voltage of a *p–n* junction, V_{th}, was determined by extrapolating the quasi-linear portion of the *I–V* curve at high currents to zero current. The V_{th} varies with T_2 nonmonotonically: it decreases substantially with the annealing temperature increasing from 700 to 900°C, and rises sharply at T_2 ≥ 975°C. The increase in V_{th} is accompanied by a significant decrease in the slope of the reverse *I–V* curve; i.e., the differential resistance of a reverse-biased *p–n* junction increases. It is noteworthy that the forward *I–V* curves show no such increase in the differential resistance on raising the annealing temperature to above 950°C. In the diodes annealed at T_2 ≤ 950°C, the breakdown voltage does not exceed 5 V, which is typical of the tunneling breakdown mechanism. At T_2 ≥ 975°C, the breakdown voltage is no less than 7 V, which corresponds to the voltage range typical of the avalanche breakdown. No emission could be observed visually in the breakdown mode and at current densities of up to 10 A/cm^2 from structures annealed at T_2 ≤ 950°C and placed in the dark in the viewing field of a microscope. At annealing temperature T_2 ≥ 975°C, the glow of separate microplasmas was observed in the breakdown from that part of the *p–n* junction working area which was free of metal coating. Therefore, the virtual absence of an erbium-related EL signal from diodes annealed at T_2 ≥ 975°C can presumably be attributed to the appearance of a significant nonuniformity of the reverse current distribution over the *p–n* junction area and the resulting substantial reduction in the number of

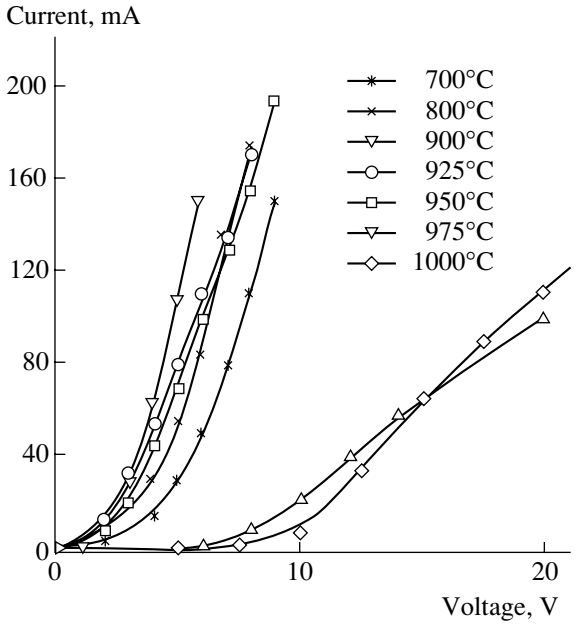

Fig. 3. Reverse *I–V* characteristics of diodes subjected to a second annealing at different temperatures T_2.

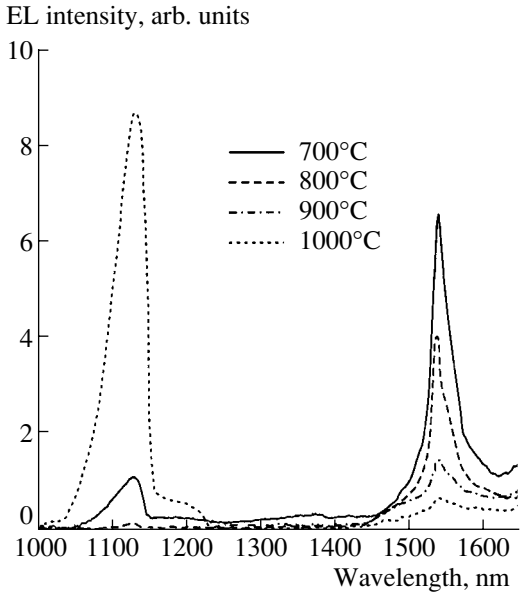

Fig. 4. EL spectra of diodes subjected to a second annealing at different temperatures T_2. Forward current density ~10 A/cm^2, T = 80 K.

optically active ions excited within the space-charge region of the *p–n* junction.

No room-temperature EL from erbium ions could be observed in any of the structures studied under forward-bias, at least at current densities of up to ~10 A/cm^2. Figure 4 presents EL spectra for several samples annealed at different T_2, recorded at a forward current density of ~10 A/cm^2, at T = 80 K. Along with the erbium-related EL peak at $\lambda \approx 1.54$ μm, an exciton emission peak at $\lambda \approx 1.13$ μm and a defect emission band are observed. The spectra in Fig. 4 were recorded at currents corresponding to the maximum intensity of the $\lambda \approx 1.54$ μm EL. With increasing annealing temperature T_2, the intensity of the EL from erbium ions decreases (see Fig. 4 and curve *1* in Fig. 5), and at T_2 = 1100°C the emission at $\lambda \approx 1.54$ μm is mainly due to EL from defects. The dependence *1* in Fig. 5 differs fundamentally from previously reported curves of this kind [10–12]. This difference is due to the use in the present study of higher erbium and oxygen implantation doses (leading to silicon amorphization) and silicon wafers of another orientation, which leads to another spectrum of the forming structural defects and, presumably, of the electrically and optically active centers. The intensity of the excitonic line at a fixed current density of 10 A/cm^2 varies nonmonotonically with T_2 (see curve *2* in Fig. 5): it decreases in the temperature range from 700 to 950°C and increases sharply at T_2 > 950°C. As stated above, microplasmas were observed in the breakdown mode at T_2 > 950°C.

According to modern concepts, the excitation of forward EL and photoluminescence from erbium ions requires that optically and electrically active centers should be formed in silicon. These centers contain trivalent Er^{3+} ions and give rise to levels in the energy gap of silicon, favoring energy transfer from free carriers to rare-earth ions. In the *p–n* junction breakdown mode, hot carriers appear in the erbium-doped space-charge region, capable of exciting erbium ions via the

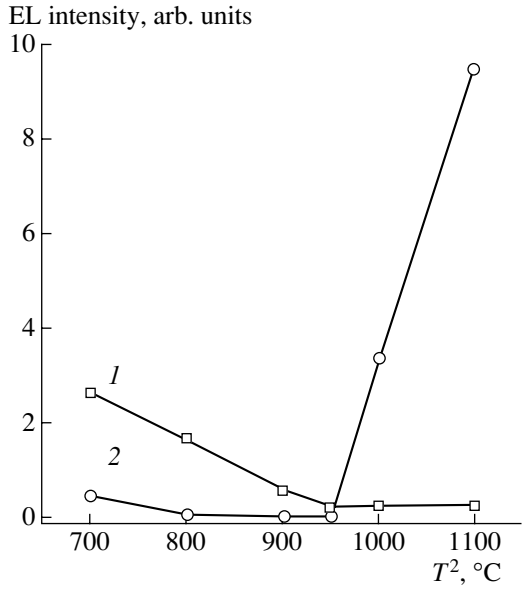

Fig. 5. EL intensity vs. the second annealing temperature T_2. Forward current density ~10 A/cm^2, T = 80 K. (*1*) $\lambda \approx$ 1.54 μm and (*2*) $\lambda \approx$ 1.13 μm.

impact mechanism. In this case, an excitation of the electronic subsystem of the crystal is transferred to an Er^{3+} ion directly in a collision of a hot carrier with a rare-earth ion. Correspondingly, the mechanisms of de-excitation of Er^{3+} ions are also different for the forward and reverse current modes. It is the difference in the excitation and de-excitation mechanisms of Er^{3+} ions that can account for the different dependences of the intensity of erbium ion–related EL on T_2 under forward bias at T = 80 K and in the breakdown mode at T = 300 K.

4. CONCLUSION

The intensity of EL from erbium ions at 300 K in the *p–n* junction breakdown mode grows steadily with the second annealing temperature T_2 increasing from 700 to 950°C for the implantation modes of erbium, oxygen, phosphorus, and boron, employed in the present study. At higher T_2 (975–1100°C), no EL from erbium ions is observed in the breakdown mode owing to the appearance of microplasmas causing a substantial nonuniformity of the reverse current distribution over the diode area. Under forward bias, the intensity of erbium-related EL at 80 K decreases with increasing annealing temperature T_2. The results obtained indicate that the intensity of room temperature EL from erbium ions EL in (111) Si:(Er,O) diodes can be raised further by elevating the annealing temperature to $T_2 \geq 975$°C if it is possible to prevent the formation of microplasmas.

ACKNOWLEDGMENTS

We are grateful to E.O. Parshin and R.V. Tarakanova for their assistance in sample preparation.

This study was supported in part by the Russian Foundation for Basic Research (project no. 99-02-17750), INTAS (grant no. 99-01872), and the Russian Foundation for Basic Research–Office for Scientific and Technical Cooperation, Austria (grant no. 01-02-02000 OSTC).

REFERENCES

1. G. Franzo, S. Coffa, F. Priolo, and C. Spinella, J. Appl. Phys. **81**, 2784 (1997).
2. N. A. Sobolev, A. M. Emel'yanov, and K. F. Shtel'makh, Appl. Phys. Lett. **71**, 1930 (1997).
3. N. A. Sobolev, A. M. Emel'yanov, S. V. Gastev, *et al.*, Mater. Res. Soc. Symp. Proc. **486**, 139 (1998).
4. A. M. Emel'yanov, N. A. Sobolev, and A. N. Yakimenko, Appl. Phys. Lett. **72**, 1223 (1998).
5. N. A. Sobolev, Yu. A. Nikolaev, A. M. Emel'yanov, *et al.*, Izv. Akad. Nauk, Ser. Fiz. **63**, 388 (1999).
6. N. A. Sobolev, A. M. Emel'yanov, and Yu. A. Nikolaev, Fiz. Tekh. Poluprovodn. (St. Petersburg) **34**, 1069 (2000) [Semiconductors **34**, 1027 (2000)].
7. A. M. Emel'yanov, N. A. Sobolev, M. A. Trishenkov, and P. E. Khakuashev, Fiz. Tekh. Poluprovodn. (St. Petersburg) **34**, 965 (2000) [Semiconductors **34**, 927 (2000)].
8. N. A. Sobolev, A. M. Emel'yanov, and Yu. A. Nikolaev, Fiz. Tekh. Poluprovodn. (St. Petersburg) **33**, 931 (1999) [Semiconductors **33**, 850 (1999)].
9. N. A. Sobolev, A. M. Emel'yanov, R. N. Kyutt, and Yu. A. Nikolaev, Solid State Phenom. **67–70**, 371 (1999).
10. J. Michel, J. I. Benton, R. F. Ferrante, *et al.*, J. Appl. Phys. **70**, 2672 (1991).
11. N. A. Sobolev, M. S. Bresler, O. B. Gusev, *et al.*, Fiz. Tekh. Poluprovodn. (St. Petersburg) **28**, 1995 (1994) [Semiconductors **28**, 1100 (1994)].
12. N. A. Sobolev, O. V. Alexandrov, M. S. Bresler, *et al.*, Mater. Sci. Forum **196–201**, 597 (1995).

Translated by D. Mashovets

Semiconductors, Vol. 35, No. 10, 2001, pp. 1175–1181. Translated from Fizika i Tekhnika Poluprovodnikov, Vol. 35, No. 10, 2001, pp. 1228–1234.

LOW-DIMENSIONAL SYSTEMS

Study of Electron Capture by Quantum Dots Using Deep-Level Transient Spectroscopy

M. M. Sobolev, I. V. Kochnev†, V. M. Lantratov, and N. N. Ledentsov

Ioffe Physicotechnical Institute, Russian Academy of Sciences, Politekhnicheskaya ul. 26, St. Petersburg, 194021 Russia

Submitted January 23, 2001; accepted for publication January 24, 2001

Abstract—The electron emission from and capture by quantum dots in InGaAs/GaAs *p–n* heterostructures were studied using deep-level transient spectroscopy in relation to the conditions of isochronous annealing with a switched-on or -off bias voltage ($U_{ra} < 0$ or $U_{ra} = 0$). The results indicate that, as a result of annealing with $U_{ra} < 0$, a dipole that consists of charge carriers localized in the quantum dots and the ionized lattice defects is formed. The electrostatic potential of this dipole reduces the barrier for the electron emission from and capture by a quantum dot. If the annealing is performed at $U_{ra} = 0$, no dipole is formed and the band offset is controlled by the conditions of heteroboundary formation during the structure growth. The dependence of the barrier height on the filling-pulse duration was also observed; this dependence is related to the manifestation of the Coulomb blockade for the electron capture by the ground and excited states of a quantum dot. The structures with quantum dots studied were grown by gaseous-phase epitaxy from metal-organic compounds using self-organization effects. © *2001 MAIK "Nauka/Interperiodica".*

1. INTRODUCTION

Quantum dots (QDs) obtained as a result of the self-organized growth of heteroepitaxial strained layers are finding more and more applications as lasers [1]. However, it is not often that the characteristics of the lasers with QDs can be improved appreciably; this may be caused, in particular, by the presence of a potential barrier to the charge-carrier capture by QDs. This barrier can also profoundly affect the operation of the one-electron transistors and memory elements [2, 3]. The possibility of a potential barrier existing at the InAs/GaAs interface, which restricts the charge-carrier capture by QDs, has been considered previously [4, 5] when calculating the voltage distribution around a pyramidal InAs QD. Studies of the QD-containing InAs/GaAs layers using a scanning transmission electron microscope [6] showed that the boundary between a QD and the GaAs matrix is not abrupt and that there is a confining $In_xGa_{1-x}As$ layer, in which the potential changes slightly. Recently [6], deep-level transient spectroscopy (DLTS) has been used to determine the cross sections of thermal charge-carrier capture and the activation energies for capture by self-organized InGaAs/GaAs QDs. It has been shown that the charge carriers have to overcome a potential barrier before being captured by a QD; it is argued [7] that this barrier is caused by a built-in voltage of the self-organized system, which gives rise to a peak at the InAs–GaAs interface in the plane of the carrier-confining potential along the growth direction. Previously [8–13], DLTS has been used to detect Coulomb interaction between the charge carriers localized in QDs and the ionized lattice defects located in the immediate vicinity of a QD. These defects appear in the course of the In(GaAs) QD formation and the GaAs epilayer growth. It has been shown that an electrostatic dipole is formed as a result; the built-in potential of this dipole affects the height of the potential barrier to the charge-carrier emission from a QD. The features of the dipole formation depended on the conditions of the isochronous thermal treatment with reverse-bias voltage either being applied or not and on exposure to white light. Thermal treatment induced changes in the positions of the DLTS peaks related to the emission of charge carriers from the states of the QDs. It seems of interest to use DLTS to study the barrier height in relation to the conditions of isochronous heat treatments.

In this paper, we report the results of DLTS studies of the electron emission from and capture by the states of InGaAs/GaAs QDs in relation to the conditions of isochronous heat treatments with and without reverse-bias voltage being applied ($U_{ra} < 0$ or $U_{ra} = 0$). We studied the effect of the built-in electrostatic potential of a dipole on the height of the barrier to the capture of electrons by a QD in relation to the conditions of isochronous heat treatment; this dipole is formed by the charge carriers localized in a QD and the ionized lattice defects. We assessed the effect of the Coulomb blockade on the electron capture by the ground and excited states. The structures we studied were grown by gas-

† Deceased.

1063-7826/01/3510-1175$21.00 © 2001 MAIK "Nauka/Interperiodica"

eous-phase epitaxy from metal–organic compounds (GPE-MOC); the self-organization effects were used.

2. EXPERIMENTAL

The InGaAs/GaAs heterostructure under investigation was obtained by MOC-GPE using a horizontal low-pressure (76 Torr) reactor. Trimethylgallium, trimethylaluminum, ethyldimethylindium, and arsine were used as sources of the main components and Cp_2Mg was used for the *p*-type doping of GaAs. The temperature of structure growth was 480°C. An undoped GaAs layer ($n = 3 \times 10^{15}$ cm^{-3}) 0.5 μm thick was grown on the n^+-GaAs substrate. Thereafter, an InGaAs layer was deposited with interruption subsequent to the growth of a layer of InGaAs QDs. A thin GaAs layer 50 Å thick was then deposited on QDs with a subsequent increase in the temperature to 600°C and heat treatment *in situ* for 10 min. Later, an *n*-GaAs layer ($n = 3 \times 10^{15}$ cm^{-3}) 0.5 μm thick was deposited at a temperature of 480°C. In order to form a *p–n* junction, we coated the *n*-GaAs layer with a 0.1-μm-thick layer of doped p^+-GaAs at the same temperature. The *in situ* heat treatment of the InGaAs layer in the InGaAs/GaAs heterostructures is conducive (as was first reported in our previous publications [12–14]) to producing dislocation-free QDs; in addition, this heat treatment results in the disappearance of the *EL*2 and *EL*3 defects related to dislocation formation and reduces the concentrations of other point defects that act as nonradiative-recombination centers by more than an order of magnitude. The deep-level traps in the heterostructures were studied by DLTS using a DL4600 BIO-RAD spectrometer, which operated in the mode of two-window integration. Capacitance was measured with a Boonton-72B bridge, which operated at a frequency of 1 MHz. The sensitivity of the experimental setup was equal to $\Delta C/C_0 \approx 10^{-4}$. Preliminarily, nonrectifying contacts were thermally deposited onto the n^+-GaAs substrate and the p^+-GaAs layer. Prior to each DLTS measurement, the sample was annealed isochronously for 1 min at a fixed temperature; during annealing, either a reverse-bias voltage ($U_{ra} < 0$) was applied to the sample or the voltage was not applied ($U_{ra} = 0$). Prior to annealing, the sample was heated to 450 K, kept at this temperature for 1 min without any voltage applied to the sample ($U_{ra} = 0$) if the annealing was to be performed at $U_{ra} < 0$, and then cooled to the annealing temperature. If the annealing was to be performed at $U_{ra} = 0$, the sample was preliminarily kept at 450 K with the reverse bias applied ($U_{ra} < 0$). The annealing temperatures were varied in the range of 80–450 K. After all the above heat treatments, the sample was cooled to $T = 80$ K at either $U_{ra} < 0$ or $U_{ra} = 0$, and we then performed the DLTS measurements in the dark (unless otherwise specified) or under exposure to white light. In order to determine the carrier concentration profile in the heterostructure, we measured the capacitance–voltage (*C–V*) characteristics. The results of these measurements (and also the results of studying the photoluminescent and structural properties for this structure), which made it possible to determine the region of the spatial localization of QDs and the conditions of their observation in the DLTS spectra, have been reported previously [12, 13] and, therefore, are not presented in this paper. The thermal-activation energies E_a and the cross sections of electron capture σ_n by the traps were determined using the rate window in the conventional DLTS measurements, unless otherwise stated.

Parameters of deep levels of defects and the states of quantum dots and of a quantum well

Designations of levels	Energy E_a, meV	Capture cross section σ_n, cm^2	Identification of levels
*ED*1	122	2.3×10^{-15}	
*ED*1#	156	1.8×10^{-13}	
*ED*2	347	4.5×10^{-16}	
*ED*2#	369	7.2×10^{-16}	
*ED*3	667	7.4×10^{-14}	*E*4 [15]

3. RESULTS

In. Fig. 1, we show the DLTS spectra measured in the dark under different conditions of preliminary isochronous heat treatment ($U_{ra} = 0$ or $U_{ra} < 0$) (curves *1*, *2*). We observed three clearly discernible peaks in all the measured spectra. The parameters of the levels corresponding to the DLTS peaks are listed in the table. The peak *ED*3, for which the thermal-activation energy is $E_a = 667$ meV and the electron-capture cross section is $\sigma_n = 7.4 \times 10^{-14}$ cm^2, has almost the same parameters (as has been shown previously [12, 13]) as those of the defect *E*4 [15]. This defect is formed in GaAs under irradiation, is related to a cluster composed of arsenic vacancies V_{As} and an antisite defect As_{Ga}, and resides in the immediate vicinity of a QD. The peaks *ED*2 and *ED*2#, as has been established recently [12, 13], are related to the ground state of a QD. As for the DLTS peaks *ED*1 and *ED*2#, they can be related either to the excited state of a QD or to a state of the quantum well in the wetting layer. Positions of the DLTS peaks *ED*1 (*ED*1#) and *ED*2 (*ED*2#) depend on the conditions of the preliminary annealing. If the samples were annealed under the conditions of $U_{ra} < 0$, the thermal-activation energy and the cross sections of electron capture by the levels related to the peaks *ED*1 and *ED*2 were equal to $E_a = 122$ meV and $\sigma_n = 2.3 \times 10^{-15}$ cm^2 (*ED*1) and $E_a = 347$ meV and $\sigma_n = 4.5 \times 10^{-16}$ cm^2 (*ED*2). An annealing with $U_{ra} = 0$ resulted in the DLTS peaks shifting to higher temperatures. These new positions of the DLTS peaks corresponded to the levels designated as *ED*1# and *ED*2#; for these levels, we

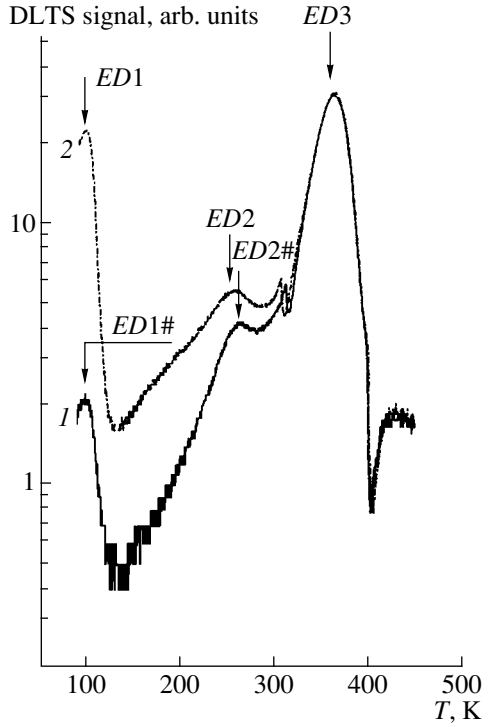

Fig. 1. The DLTS spectra of a *p–n* InGaAs/GaAs heterostructure with quantum dots; the spectra were measured using a reverse-bias pulse of $U_r = 0.5$ V and the filling-pulse amplitude of $U_p = 0$ following isochronous heat treatment at $T_a = 450$ K. Cooling after heat treatment was performed under the conditions of (*1*) $U_{ra} = 0$ and (*2*) $U_{ra} < 0$. All the spectra were obtained using the emission-rate window of 200 s^{-1} and the filling-pulse duration of 25 μs.

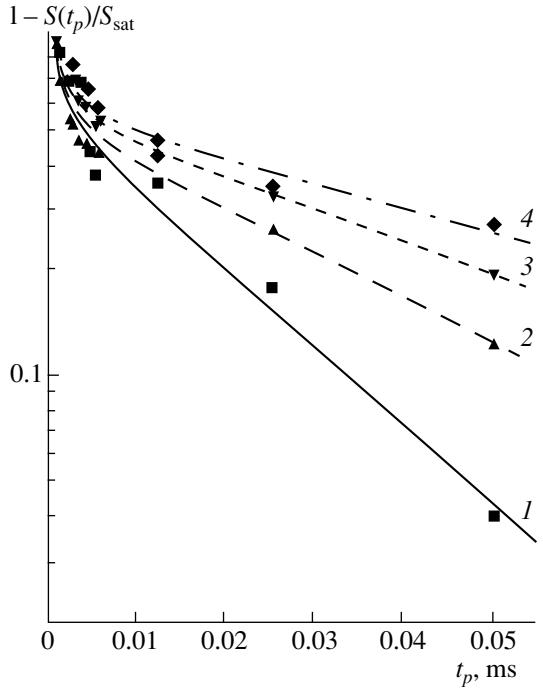

Fig. 2. The amplitude of the normalized DLTS signal as a function of the filling-pulse duration at temperatures of (*1*) 252.7, (*2*) 241.6, (*3*) 238.7, and (*4*) 222.7 K after isochronous heat treatment under the conditions of $U_{ra} = 0$.

obtained $E_a = 156$ meV and $\sigma_n = 1.8 \times 10^{-13}$ cm^2 (*ED*1#) and $E_a = 369$ meV and $\sigma_n = 7.2 \times 10^{-16}$ cm^2 (*ED*2#). If the DLTS spectra were measured with different rate windows, we observed variations in the amplitudes of the *ED*1 (*ED*1#) and *ED*2 (*ED*2#) peaks in addition to the shifts of the temperatures corresponding to their positions. As it has been shown previously [7, 16], these variations in the amplitudes of the DLTS peaks occur if the carrier-capture cross section depends heavily on temperature; furthermore, they are related to the occupancy of the traps. Special methods of DLTS measurement and signal processing have been suggested [7, 16]; these methods make it possible to determine the parameters of thermal capture by a trap (the thermal cross section of capture σ and its activation energy E_σ calculated from the capture cross section) and are also applicable to highly nonexponential processes of relaxation. In order to determine σ, we measured the dependence of the height of DLTS peaks on the filling-pulse width t_p. In these circumstances, the capture kinetics is described by the relation [7, 16]

$$S(t_p) = S_{sat}[1 - \exp(-c_n t_p)], \quad (1)$$

where $S(t_p)$ is the height of the DLTS peak; S_{sat} is the DLTS-peak height when the traps are completely filled with charge carriers; and c_n is the capture rate related to the thermal-capture cross section σ, thermal velocity ν_{th}, and the free-carrier concentration n by the expression $c_n = \sigma\nu_{th}n$. We assumed that n is approximately equal to the dopant concentration. The curves $(1 - S(t_p)/S_{sat})$ vs. t_p, derived from the heights of DLTS peaks *ED*2 and *ED*2#, which were measured under different conditions of preliminary heat treatment ($U_{ra} = 0$ and $U_{ra} < 0$), are shown in Figs. 2 and 3, respectively. Experimental curves feature two exponential portions; one of them has a steep incline (in the range of $t_p = 1$–5 μs), whereas the other has a gentler slope (in the range of 5–100 μs). The temperature dependences of the capture cross section σ were determined by varying the rate windows. The temperature ranges, within which the capture cross sections were determined, were equal to 224.7–256.3 K and 229.5–260.5 K for the levels *ED*2 and *ED*2#, respectively. Assuming that, within narrow temperature ranges corresponding to the determination of the capture cross section σ, the quantities n and S_{sat} are temperature-independent and the thermal velocity ν_{th} depends on temperature as $T^{1/2}$, we obtain the following expression for the temperature dependence of the thermal-capture cross section:

$$\sigma = \sigma_\infty \exp(-E_\sigma/k_B T). \quad (2)$$

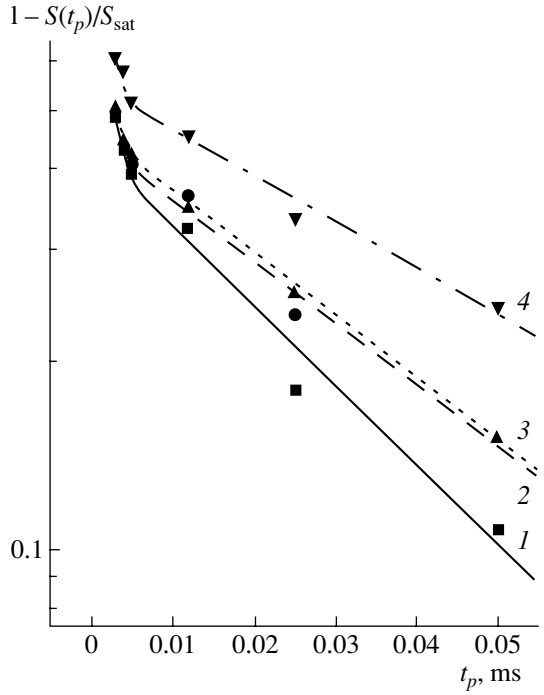

Fig. 3. The amplitude of the normalized DLTS signal as a function of the filling-pulse duration at temperatures of (*1*) 256.6, (*2*) 245.7, (*3*) 242.0, and (*4*) 227.0 K after isochronous heat treatment under the conditions of $U_{ra} < 0$.

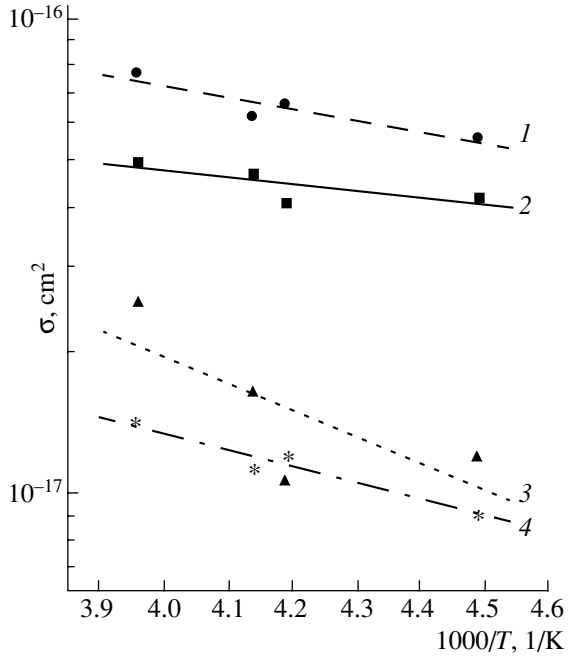

Fig. 4. Temperature dependence of a cross section for electron capture by a quantum dot after isochronous heat treatment at (*1, 3*) $U_{ra} = 0$ and (*2, 4*) $U_{ra} < 0$. Curves *1* and *2* correspond to the filling-pulse widths of t_p = 1–5 μs, and curves *3* and *4* are for $t_p > 5$ μs.

Here, σ_∞ is the cross section of carrier capture by the trap at a very high temperature, and k_B is the Boltzmann constant. We used the Arrhenius plots (Fig. 4) to determine the cross section σ_∞ and the barrier height for electron capture E_σ. For the steep portion measured after a preliminary isochronous annealing with $U_{ra} < 0$, we obtained $E_{\sigma f} = 27$ meV and $\sigma_{\infty f} = 1.7 \times 10^{-16}$ cm^2; for the gently sloping portion, we have $E_{\sigma 1} = 77$ meV and $\sigma_{\infty f} = 4.4 \times 10^{-16}$ cm^2. After a preliminary heat treatment with $U_{ra} = 0$, we obtained $E^*_{\sigma f} = 48$ meV and $\sigma_{\infty f} = 6.7 \times 10^{-16}$ cm^2 for the steep portion (the fast component) and $E^*_{\sigma 1} = 104$ meV and $\sigma_{\infty 1} = 2.5 \times 10^{-15}$ cm^2 for the gently sloping portion (the slow component). It is noteworthy that the accuracy of determining σ_∞ (Fig. 4) is low due to the narrow temperature range within which variations in the DLTS-peak heights are determined. This special feature related to the accuracy of determination of σ_∞ has been noted previously [7, 16]. For the peaks *ED*1 and *ED*1#, the range of temperature variation was even more narrow and the spread in the values of σ_∞ for different rate windows was appreciable, which precluded the determination of the corresponding thermal-capture parameters. However, we still managed to find that experimental plots of $(1 - S(t_p)/S_{sat})$ vs. t_p are indicative of the presence of only one exponential portion (in the range of t_p = 1–5 μs); for $t_p > 5$ μs, leveling-off was observed.

4. DISCUSSION

The observed variations in the peak *ED*2 in the DLTS spectra (Fig. 1) as a result of isochronous heat treatment are caused (as has been discovered recently [12, 13]) by an electrostatic dipole that exhibits Coulomb interaction and is formed from electrons localized in a QD and ionized deep donor levels of defects. After heat treatment at a temperature of 450 K and subsequent cooling to 80 K at $U_{ra} < 0$, the deep donor levels and the states of the QDs remain ionized. As a result of a filling pulse applied to the structure at low temperatures in the course of DLTS measurements, electrons are captured by the states of QDs. At the same time, the deep donor levels of defects in the self-trapping configuration [17] remain ionized because the electron energy is insufficient at a low temperature to overcome the potential configuration barrier and to trap the electron at this level. A dipole is formed from the closely spaced charged deep-level donor defects and electrons localized at the QD; the electric field of the dipole is oriented along the same direction as the *p–n*-junction field. The thermal-activation energy for electron emission from the quantum state decreases as a result of the field

effect. After a heat treatment at a temperature of 450 K with subsequent cooling at $U_{ra} = 0$, free electrons in the conduction band possess sufficient energy to overcome the barrier and to be captured by deep-level donor traps. However, this energy may be insufficient for the electron emission from the trap. As a result, the donor traps become partially occupied and neutral, the electrostatic dipole field decreases, and, correspondingly, the thermal-activation energy for electron emission from the state of the QD increases. A shift of the *ED*2# peak to higher temperatures is observed in the DLTS spectra (Fig. 1). Similar changes after isochronous heat treatment with subsequent cooling at $U_{ra} < 0$ or $U_{ra} = 0$ are also observed for the DLTS peaks *ED*1 and *ED*1# (Fig. 1). In order to draw certain interesting inferences from our experimental results, we perform the simplest arithmetical calculations. The difference between the energies of thermal electron emission determined for two conditions of the heat treatment ($U_{ra} = 0$ and $U_{ra} < 0$) is equal to $\Delta E_a = ED2\# - ED2 = 369 - 347$ meV = 22 meV. The differences between the electron thermal-capture energies determined for the heat treatments with $U_{ra} = 0$ and $U_{ra} < 0$ are equal to $\Delta E_{\sigma f} = E^*_{\sigma f} - E_{\sigma f} = 48 - 27$ meV = 21 meV for the fast process and to $\Delta E_{\sigma 1} = E^*_{\sigma 1} - E_{\sigma 1} = 104 - 77$ meV = 27 meV for the slow process. It can be seen that the change in the heat-treatment conditions from $U_{ra} < 0$ to $U_{ra} = 0$ results both in an increase in the thermal-emission energy and in heightening of the barrier for the thermal electron capture by a QD; these changes in the energy and the barrier height are almost the same in magnitude (21–27 meV) irrespective of the filling-pulse duration. At the same time, the differences between the barrier heights for the fast- and slow-capture processes for the heat treatments with $U_{ra} < 0$ and $U_{ra} = 0$ are also close to each other and are equal to $\Delta E_{\sigma 1f} = E_{\sigma 1} - E_{\sigma f} = 56$ meV and $\Delta E^*_{\sigma 1f} = E^*_{\sigma 1} - E^*_{\sigma f} = 61$ meV. These results indicate that the same mechanism is responsible for the observed decrease in the energy of electron capture by QDs for both the fast and slow processes when the heat-treatment conditions are changed from $U_{ra} = 0$ to $U_{ra} < 0$. This mechanism is related to the formation of an electrostatic dipole composed of QD electrons and charged defects. This dipole is formed as a result of heat treatment at $U_{ra} < 0$; the built-in electrostatic potential of the dipole reduces the band offset at the interface and lowers the barrier to the electron emission from and capture by a QD. If $U_{ra} = 0$ in the course of heat treatment, no dipole emerges and the band-offset magnitude is controlled by the conditions of forming the heterointerface during the structure growth. However, the formation of the dipole in the case of heat treatment with $U_{ra} < 0$ does not lead to a complete disappearance of the barrier to electron capture; the barrier height for the filling-pulse widths $t_p < 5$ μs remains equal to $E_{\sigma f} = 27$ meV. In this situation, the presence of the barrier to electron capture may be related either to the fact that the built-in field of the electrostatic dipole is insufficient to completely smooth out the barrier to the capture or to a manifestation of the Coulomb blockade [18, 19] for the capture of the second electron by the QD ground state. For the filling-pulse widths of $t_p < 1$ μs, the QD ground state has apparently time to capture only a single electron. It is conceivable that the capture of the second electron by the QD ground *s* state may become probable if t_p increases from 1 to 5 μs. In order to overcome the Coulomb blockade formed by the first electron in the QD ground *s* state [18, 19], the second electron should possess additional energy. The energy of the Coulomb charge (E_c) necessary for the accommodation of an additional electron with charge q in an InGaAs QD, which is embedded in GaAs and is disk-shaped with a diameter d, can be estimated as $q^2/2C$, where $C = 4\varepsilon\varepsilon_0 d$ is the inherent capacitance of a QD. For the structure we studied, the typical lateral QD size measured using the transmission electron microscopy was equal to $d \approx 13$ nm. The Coulomb charge energy estimated using the above expression was found to be equal to $E_c \approx 27$ meV and, thus, is consistent with the experimentally measured value of $E_{\sigma f} = 27$ meV. For the filling-pulse widths of $t_p > 5$ μs, we found that the capture-barrier height increased approximately twofold irrespective of the conditions of isochronous heat treatment, which may be related to the capture of the third electron by the *p* state of a QD. The third electron must have an energy equal to $2E_c \approx 54$ eV in order to overcome the Coulomb blockade induced by two electrons. It is notable that, in the DLTS spectra studied, we did not observe either an appreciable temperature shift of the DLTS peaks *ED*2 and *ED*2# or a change in their shape with variations in t_p, which would have been induced by the effect of the Coulomb charge. The absence of these changes may be related to the considerable spread of the QD sizes in the structure under consideration. The measured spectral width of the photoluminescence peak was almost twofold larger than the width accounted for by the effect of the Coulomb charge energy and was equal to about 100 meV [12, 13]. In addition, in the DLTS measurements, the signals from the QDs and defects became intermixed, which resulted in the QD DLTS spectrum leveling off. However, the effect of the Coulomb blockade in the DLTS spectra for the *ED*2 and *ED*2# peaks manifested itself in special features in the dependences of the heights of these peaks on the filling-pulse duration [$S(t_p)$] (Figs. 2, 3). For $t_p \le 1.2$ μs, the DLTS signal was controlled (as was mentioned above) by the emission of the first electron from the QD ground state and, for $t_p = 1.2$ μs, was equal to 160 fF for the *ED*2 peak. For $t_p > 1.2$ μs, two electrons were involved in the process of capture by the QD ground state. For $t_p = 5.0$ μs, the peak

was higher by a factor of 2 and became equal to 320 fF. As t_p increased further for $t_p > 5$ μs, three electrons were already involved in the capture process. The dependence $S(t_p)$ leveled off for $t_p > 50.0$ μs. In this situation, the peak *ED*2 was as high as 510 fF, which was about three times higher than for $t_p = 1.2$ μs.

We now discuss the results that concern the DLTS peaks *ED*1 and *ED*1#. The behavior of these peaks in relation to the conditions of isochronous heat treatment was similar to that observed for the DLTS peaks *ED*2 and *ED*2# (Fig. 1). Thus, there is reason to believe that the peaks *ED*1 (*ED*1#) and *ED*2 (*ED*2#) have almost the same origin; therefore, we may relate the specificities in the behavior of the DLTS peaks *ED*1 and *ED*1# to the formation of an electrostatic dipole at the InGaAs/GaAs heterointerface. However, in contrast to the *ED*2 (*ED*2#) peaks, the curves $(1 - S(t_p)/S_{sat} = f(t_p)$ for the peaks *ED*1 and *ED*1# include only a single exponential portion; the latter corresponds to the range of the filling-pulse widths of $t_p = 1$–5 μs. Furthermore, we found that the thermal-activation energy for electron emission from the states *ED*1 and *ED*1# is lower than the corresponding energy for the states *ED*2 and *ED*2# (see table). These results indicate that the peaks *ED*1 and *ED*1# cannot be related to the excited states of a QD; rather, these peaks are formed as a result of electron emission from the quantum well of the wetting layer.

Thus, we detected the effect of Coulomb interaction between electrons localized in QDs and ionized deep-level defects; this effect gives rise to a bistable electric dipole, the built-in potential of which affects the height of the potential barrier for the electron emission from and capture by a QD, and, in our opinion, is not only of pure scientific interest but also of practical importance. Recently, the feasibility of using heterostructures with QDs to develop high-density memory elements has been actively discussed. It has been suggested to implement such an element using a field-effect transistor with an optical gate [3]. Our studies show that the complexes composed of point defects and QDs may serve as the memory elements; in this case, a point defect (rather than a two-dimensional electron gas) may be used as a trap for erasing the data. The use of such systems as the media for the reversible recording of optical and electrical data may be conducive to the development of memory elements with high spatial resolution (10^{10}–10^{11} bit/cm^2).

5. CONCLUSION

We performed detailed DLTS studies of the electron emission from and capture by the states of quantum dots; we also studied the effect of electrostatic interaction between the charge carriers localized in the quantum dots and the ionized lattice defects on the above emission and capture processes in InGaAs/GaAs semiconductor heterostructures. The structures with quantum dots studied were grown by gaseous-phase epitaxy from metal–organic compounds using self-organization effects. The DLTS studies showed that charge carriers had to overcome a potential barrier, the height of which depends on the conditions of isochronous heat treatment with applied ($U_{ra} < 0$) or switched off ($U_{ra} = 0$) bias voltage and also on the filling-pulse duration. During heat treatment at $U_{ra} < 0$, a dipole is formed; the built-in electrostatic potential of this dipole reduces the band offset at the heterointerface and lowers the barrier for the electron emission from and capture by a quantum dot. During heat treatment under the conditions of $U_{ra} = 0$, the dipole is not formed. The band-offset magnitude is now controlled by the conditions of forming the heteroboundary during the structure growth and varies from 48 to 105 meV depending on the filling-pulse duration t_p. As a result of heat treatment with $U_{ra} < 0$, the barrier to the electron capture does not disappear completely. The height of this barrier remains equal to $E_{\sigma f} = 27$ meV for the filling-pulse widths of $t_p < 5$ μs and is related to the manifestation of the Coulomb blockade for capturing the second electron by the ground state of a quantum dot. For the filling-pulse widths of $t_p > 5$ μs, the barrier height increases by ~56 meV, which is related to the manifestation of the Coulomb blockade for the capture of electrons by the excited state of the quantum dot.

ACKNOWLEDGMENTS

This study was supported by the Scientific Program "The Physics of Solid-State Nanostructures" (project no. 99-1115), the Russian Foundation for Basic Research (project no. 00-02-16848), and the SNSF (Switzerland) (project no. 7SUPJ 062392).

REFERENCES

1. D. Bimberg, M. Grundmann, and N. N. Ledentsov, in *Quantum Dot Heterostructures* (Wiley, Chichester, 1998), p. 328.
2. M. Koltonyuk, D. Berman, N. B. Zhitenev, *et al.*, Appl. Phys. Lett. **74**, 555 (1999).
3. G. Yusa and H. Sakali, Appl. Phys. Lett. **70**, 345 (1997).
4. M. Grundmann, N. N. Ledentsov, O. Stier, *et al.*, Appl. Phys. Lett. **68**, 979 (1996).
5. M. A. Cusak, P. R. Briddon, and M. Jaros, Phys. Rev. B **54**, 3284 (1997).
6. P. D. Siverns, S. Malik, G. McPherson, *et al.*, Phys. Rev. B **58**, R10127 (1998).
7. H. L. Wang, F. H. Yang, S. L. Feng, *et al.*, Phys. Rev. B **61**, 5530 (2000).
8. M. M. Sobolev, F. R. Kovsh, V. M. Ustinov, *et al.*, Fiz. Tekh. Poluprovodn. (St. Petersburg) **31**, 1249 (1997) [Semiconductors **31**, 1074 (1997)].

9. M. M. Sobolev, A. R. Kovsh, V. M. Ustinov, *et al.*, in *Proceedings of the 19th International Conference on Defects in Semiconductors, Aveiro, Portugal, 1997*; Mater. Sci. Forum **258–263**, 1619 (1997).
10. M. M. Sobolev, F. R. Kovsh, V. M. Ustinov, *et al.*, Fiz. Tekh. Poluprovodn. (St. Petersburg) **33**, 184 (1999) [Semiconductors **33**, 157 (1999)].
11. M. M. Sobolev, A. R. Kovsh, V. M. Ustinov, *et al.*, J. Electron. Mater. **28** (5), 491 (1999).
12. M. M. Sobolev, I. V. Kochnev, V. M. Lantratov, *et al.*, Physica B (Amsterdam) **273–274**, 959 (1999).
13. M. M. Sobolev, I. V. Kochnev, V. M. Lantratov, *et al.*, Fiz. Tekh. Poluprovodn. (St. Petersburg) **34**, 200 (2000) [Semiconductors **34**, 195 (2000)].
14. N. N. Ledentsov, M. V. Maximov, D. Bimberg, *et al.*, Semicond. Sci. Technol. **15**, 604 (2000).
15. D. Pons, P. M. Monney, and J. C. Bourgoin, J. Appl. Phys. **51**, 2038 (1980).
16. J. H. Zhao, T. E. Schlesinger, and A. G. Milnes, J. Appl. Phys. **62**, 2865 (1987).
17. Y. Toyozawa, Physica B (Amsterdam) **116**, 7 (1983).
18. H. Drexler, D. Leonard, W. Hansen, *et al.*, Phys. Rev. Lett. **73**, 2252 (1994).
19. W.-H. Chang, T. M. Hsu, N. T. Yeh, and J.-I. Chyi, Phys. Rev. B **62**, 13040 (2000).

Translated by A. Spitsyn

Semiconductors, Vol. 35, No. 10, 2001, pp. 1182–1186. Translated from Fizika i Tekhnika Poluprovodnikov, Vol. 35, No. 10, 2001, pp. 1235–1239.

LOW-DIMENSIONAL SYSTEMS

The Role of Nitrogen in the Formation of Luminescent Silicon Nanoprecipitates during Heat Treatment of SiO_2 Layers Implanted with Si^+ ions

G. A. Kachurin*, S. G. Yanovskaya*, K. S. Zhuravlev*, and M.-O. Ruault**

** Institute of Semiconductor Physics, Siberian Division, Russian Academy of Sciences, pr. Akademika Lavrent'eva 13, Novosibirsk, 630090 Russia*

*** CSNSM-CNRS/IN2P3, 91405 Orsay, France*

Submitted February 6, 2001; accepted for publication March 15, 2001

Abstract—Twenty-five kiloelectronvolt Si^+ ions with doses of $(1–4) \times 10^{16}$ cm^{-2} and 13-keV N^+ ions with doses of $(0.2–2) \times 10^{16}$ cm^{-2} were implanted into SiO_2 layers, which were then annealed at 900–1100°C to form luminescent silicon nanoprecipitates. The effect of nitrogen on this process was deduced from the behavior of the photoluminescence spectra. It was found, for a certain ratio between the concentrations of implanted silicon and nitrogen, that the photoluminescence intensity increases significantly, and its peak shifts to shorter wavelengths. It is concluded that the number of precipitation nuclei increases owing to the interaction of nitrogen with excess silicon. Eventually, this results in an increase in the number of nanocrystals and in a decrease in their average sizes. In spite of introducing additional precipitation nuclei, the minimal concentrations of excess Si on the order of 10^{21} cm^{-3} and heat treatments at temperatures higher than 1000°C were still required for the formation of nanocrystals. © *2001 MAIK "Nauka/Interperiodica".*

1. INTRODUCTION

The persistent decrease in the device sizes in microelectronics and the discovery of intense visible luminescence of quantum-confinement Si crystals have stimulated interest in the formation mechanisms and properties of silicon nanocrystals. The implantation of Si ions into SiO_2 with subsequent high-temperature annealing is one of the most promising methods for obtaining Si nanocrystals [1–3]. These are formed as a result of the decomposition of a supersaturated solid solution of Si in SiO_2; it is notable that the required sizes and properties of the crystallites are attained in fairly narrow ranges of supersaturation (~10 at. %) and annealing temperatures (900°C < T_a < 1200°C). The latter circumstance restricts the feasibility of controlling the properties of nanocrystals by varying the synthesis conditions. At the same time, methods for modifying the properties of silicon nanostructures are absolutely necessary; a search for these methods is being carried out along diverse avenues. The potentialities of an additional introduction of impurities [4–9], pulsed annealing [3, 10], annealing under pressure [11], and radiation treatment have been and are being investigated.

The introduction of elements capable of affecting the decomposition kinetics into supersaturated solid solutions is one method for controlling the properties of synthesized nanostructures. For example, it is well known that precipitation is aided significantly if additional nuclei are introduced. It has been noted previously that the decomposition of a supersaturated solid solution of Si in SiO_2 is significantly affected by the presence of nitrogen [14–19]. In particular, nitrogen was found to be conducive to forming the centers of photoluminescence (PL) in the wavelength range of λ = 300–600 nm [14–17]. By contrast, it has been also argued [14, 15, 18, 19] that nitrogen moderates the segregation of excess Si from SiO_2 and the growth of silicon precipitates. We note that Si nanocrystals with a characteristic intense PL in the wavelength region of $\lambda \gtrsim 700$ nm have not been obtained in any of the previous studies [14–19]. Thus, the issue concerning the effect of nitrogen on the formation of light-emitting Si nanocrystals remains in fact unresolved. The objective of this study was to gain insight into this effect.

2. EXPERIMENTAL

The 75-nm-thick SiO_2 layers were formed on the Si substrates using thermal oxidation. The 25-keV Si^+ ions were implanted into the layers with three doses: low (1×10^{16} cm^{-2}), medium (2×10^{16} cm^{-2}), and high (4×10^{16} cm^{-2}). This dose range was chosen because it is within this range that the concentrations of implanted Si are optimal for the formation of Si nanocrystals. The 13-keV N^+ ions were then implanted into the same layer. According to computations based on the TRIM-95 program, the projected ranges of N^+ and Si^+ ions are the same in the case under consideration and are equal to

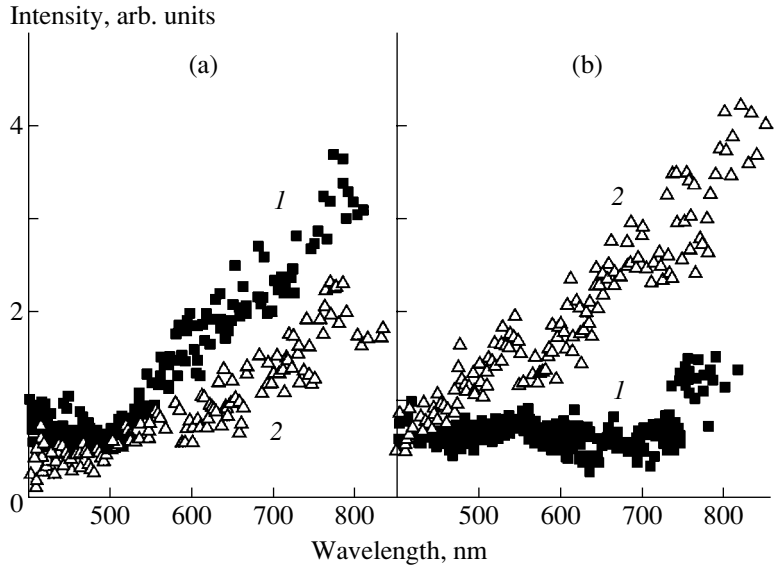

Fig. 1. Photoluminescence spectra of SiO_2 layers implanted with Si^+ and N^+ ions and then annealed at T_a = 900°C. The doses of N^+ ions were equal to (a) 2×10^{15} and (b) 2×10^{16} cm^{-2}; the doses of Si^+ ions were (*1*) 2×10^{16} and (*2*) 4×10^{16} cm^{-2}.

~35 nm. For each Si^+ dose, three doses of N^+ ions were also used: 2×10^{15}, 6×10^{15}, and 2×10^{16} cm^{-2}. The implanted samples were annealed in a nitrogen atmosphere for 30 min at temperatures of T_a = 900, 1000, and 1100°C. The PL of implanted and annealed samples was studied at a temperature of T = 20°C under pulsed excitation, with (pulse duration being $\tau \approx 7$ ns) laser radiation with λ = 337 nm. The layers implanted only with 25-keV Si^+ ions at doses of $(3–5) \times 10^{16}$ cm^{-2} were used as reference samples. The PL spectra were normalized taking into account the spectrometer sensitivity; the scales on the vertical axes in the figures give an insight into the changes of emission intensities at different annealing stages.

3. RESULTS

The initial annealing for 30 min at 900°C of all the samples studied was found to be insufficient for obtaining the intense PL band characteristic of Si nanocrystals. For the sample implanted with a low dose of Si^+ ions, the PL signal amplitude was comparable to the noise. In Fig. 1, we show the PL spectra observed for the samples implanted with medium and high doses of Si^+. Low-intensity PL was observed in the entire visible region of the spectrum, without any pronounced peaks. An additional implantation of N^+ ions affects the PL in two ways. In the samples with a high concentration of implanted Si, an increase in the nitrogen concentration leads to intensification of PL, predominantly in the long-wavelength region. If the samples were implanted with a medium dose of Si^+ ions, an increase in the nitrogen concentration reduced the PL intensity, again mostly in the long-wavelength region of the spectrum. In the wavelength region in the vicinity of λ = 550 nm, evidence of the emergence of a new broad emission band can be detected.

In the samples subjected to postimplantation annealing for 30 min at 1000°C, the introduction of nitrogen at first intensified the PL as compared to the samples implanted with Si^+ ions alone (Fig. 2). Intensification was mostly observed for the wavelengths $\lambda >$ 700 nm; this spectral region is characteristic of emission from Si nanocrystals. However, the increase in the dose of nitrogen ions from 2×10^{15} to 2×10^{16} cm^{-2} quenched this emission and led to the formation of a broad low-intensity band with the peak located between λ = 650 and 700 nm. It is also noteworthy that annealing at T_a = 1000°C was still found to be insufficient for complete activation of the long-wavelength PL related to emission from Si nanocrystals. This can be seen from a comparison with the spectrum of the reference sample (without nitrogen implantation) annealed at a higher temperature (1100°C) (Fig. 2). For this sample, the intensity of the band peaked at about λ = 800 nm and related to the Si nanocrystals is close to the largest value attained for the reference samples.

Figure 3 illustrates the results of annealing the samples at T_a = 1100°C. As was mentioned above, the annealing led to a significant enhancement of the PL with the emergence of a high-intensity long-wavelength band, which was indicative of the large-scale formation of Si nanocrystals. We at once note two features. First, the optimal dose of Si^+ ions does fall within the selected dose range and is approximately equal to 2×10^{16} cm^{-2}. Second, as the Si^+ dose decreases, the PL

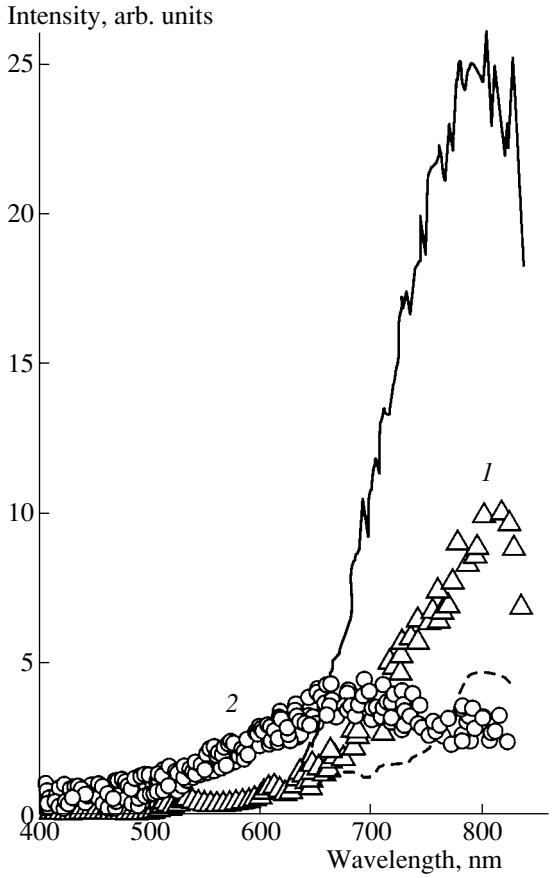

Fig. 2. Photoluminescence spectra of SiO_2 layers implanted with Si^+ and N_+ ions and then annealed at T_a = 1000°C. The dose of Si^+ ions was 4×10^{16} cm^{-2}; the doses of N_+ ions were (*1*) 2×10^{15} and (*2*) 2×10^{16} cm^{-2}. The lines represent the photoluminescence spectra of the reference samples (implanted only with Si^+ ions) after heat treatment at T_a = 1000°C (dashed line) and 1100°C (solid line).

peak shifts to shorter wavelengths, which indicates that the average size of Si nanocrystals decreases. As for the effect of nitrogen, its presence in the layers that had a large excess of Si and were implanted with 5×10^{15} cm^{-2} of N^+ led to a higher intensity of PL compared to that in the reference samples (Fig. 3a). However, a further increase in nitrogen concentration results in a rapid decrease in the intensity of the long-wavelength band in the samples implanted with a medium dose of Si^+ ions; for the samples implanted with a low dose of Si^+ ions, this band was completely quenched (Figs. 3b, 3c). It is only when the dose of Si^+ ions was high that the PL intensity was invariably higher than in the reference samples, although this intensity decreased as the dose of N^+ ions increased. We note that a decrease in the PL intensity was accompanied with a shift of its peak to shorter wavelengths (from ~760 to ~720 nm, see Figs. 3a–3c).

4. DISCUSSION

The above data on the effect of nitrogen on the formation of PL centers in SiO_2 supersaturated with silicon can be interpreted in the following way. In all situations, nitrogen is conducive to an increase in the number of precipitates with an accompanying inevitable decrease in their average sizes. If the degree of supersaturation with silicon was high, the precipitate sizes remained sufficiently large for the formation of Si nanocrystals during annealing at T_a = 1100°C, notwithstanding the fact that the number of precipitates increased. As a result, the PL related to Si nanocrystals is intensified (Fig. 3). Preliminary experiments with measuring the PL decay time showed that this time is approximately the same in reference samples and in the samples implanted with N^+ ions and is as long as hundreds of microseconds. This may serve as an argument in support of the assumption that an increase in the PL intensity is caused by an increase in the number of Si nanocrystals rather than by an increase in the radiative-recombination rate (for example, due to doping). If the amount of excess Si is small, an increase in the number of the precipitation nuclei (caused by the introduction of N) results in a decrease in the average sizes of precipitates to the level at which the silicon crystal lattice becomes unstable. According to Veprek *et al.* [20], the smallest sizes of the stable Si crystallites are in the range of 2–3 nm. In such situation, even the high-temperature heat treatments do not result in the emergence of Si nanocrystals; correspondingly, the long-wavelength PL band becomes quenched. The fact that, as the nitrogen concentration increases, the PL peak shifts to shorter wavelengths can be considered as evidence of a decrease in the average sizes of Si nanocrystals.

The results of PL studies after heat treatment at T_a = 900 and 1000°C are also consistent with the suggested interpretation of the role of nitrogen. An increase in the nitrogen concentration leads (after postimplantation annealing at T_a = 900°C) to a decrease in the intensity of long-wavelength PL and to the emergence of a band peaked in the vicinity of 550 nm (Fig. 1). A similar effect is also observed after heat treatment at T_a = 1000°C; however, the PL band stimulated by the nitrogen implantation becomes more intense and its peak shifts to λ = 650–700 nm (Fig. 2). A yellow-orange emission with relatively low intensity has been previously observed by many researchers in insufficiently annealed samples and has been typically attributed to the PL of noncrystalline silicon precipitates. The quenching of the PL band peaked at $\lambda \approx 800$ nm and the emergence of the yellow-orange emission as the N^+ dose increases (Fig. 2) can be explained by the fact that the nitrogen-stimulated increase in the number of precipitation nuclei results ultimately in the growth of the predominantly noncrystalline Si precipitates owing to a decrease in their sizes. Obviously, as the annealing temperature is increased from 900 to 1000°C, the sizes and the number of light-emitting precipitates increase,

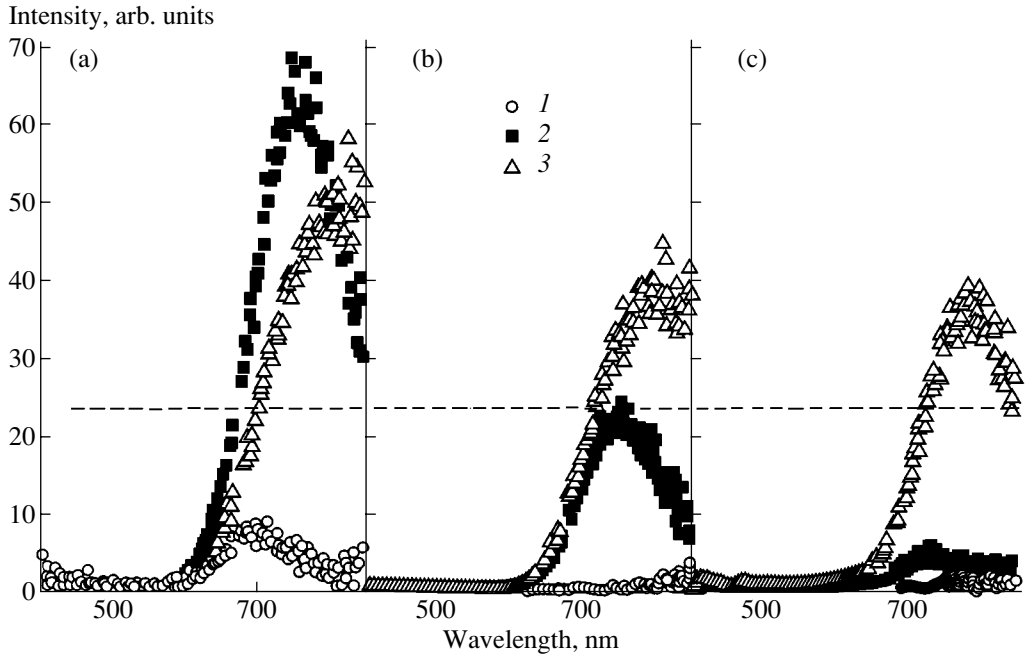

Fig. 3. Photoluminescence spectra of SiO_2 layers implanted with Si^+ and N_+ ions and then annealed at T_a = 1100°C. The doses of N_+ ions were (a) 2×10^{15}, (b) 6×10^{15}, and (c) 2×10^{16} cm^{-2}. The doses of Si^+ ions were (*1*) 1×10^{16}, (*2*) 2×10^{16}, and (*3*) 4×10^{16} cm^{-2}. The dashed line corresponds to the photoluminescence-intensity level of the reference sample (implanted only with Si^+ ions).

which accounts for the distinctions between the spectra in Figs. 1 and 2.

It is also necessary to discuss the mechanism of the effect of nitrogen on the decomposition of a Si–SiO_2 solid solution. According to Ehara and Machida [18], the Si–N bonds are fairly strong; i.e., they can serve as the initiation centers for silicon nuclei at elevated temperatures. In our experiments, the nitrogen concentration was ~10^{21} cm^{-3}, which is much higher than the typically observed concentrations of ~10^{18} cm^{-3} for Si nanocrystals. At a temperature of 1100°C, the diffusion length of Si atoms in SiO_2 is as large as ~4 nm [21]. If the formation of Si nanocrystals proceeds according to the mechanism of diffusion-controlled growth, we can hardly expect the observed abrupt decrease in the PL intensity when the dose of Si^+ ions decreases merely by a factor of 2 (from medium dose to low dose, see Fig. 3). Nevertheless, both with and without N^+ implantation, the Si concentration on the order of ~10^{21} cm^{-3} is found to be the lowest for which the formation of crystalline precipitates is still possible. Apparently, a critical factor for the formation of Si nanocrystals remains the possibility of direct interaction between the nearest-neighbor Si atoms in the situation when the average distance between Si atoms is reduced to ~1 nm [22], which is the case for the concentrations of excess Si on the order of ~10^{21} cm^{-3}. Owing to the Si–N interaction, the role of nitrogen amounts to the formation of increased concentration of competing stable precipitation centers. If the degree of supersaturation with silicon is high, the above effect increases the number of Si nanocrystals, prevents them from coalescing, and results in an increase in the PL intensity. However, if the degree of supersaturation is lowered, a nitrogen-stimulated increase in the PL intensity gives way to a decrease in intensity caused by the fact that the Si concentration is insufficient for the precipitates to attain the critical sizes for their crystallization.

We note in conclusion that, after the introduction of N, there is evidence of heterogeneous decomposition of a Si solid solution in SiO_2. In addition, the highest content of nitrogen in SiO_2 was about 10 at. % in our experiments. Nevertheless, even under these conditions, the Si^+ dose range for the formation of Si nanoprecipitates, the characteristic temperature of their crystallization ($\gtrsim$1000°C), and the typical spectral range of emission from the Si nanocrystals remained unchanged. The long lifetime of excited charge carriers was also preserved. The importance of the quality of the Si–SiO_2 interface for PL observation has been emphasized in many publications. If we take into account that even a single dangling bond in a nanocrystal composed of 10^3–10^4 atoms is sufficient for quenching the PL [12, 23], then we may conclude that interfaces between Si nanocrystals and SiO_2 remained of quite a high quality.

5. CONCLUSION

During the decomposition of a supersaturated solid solution of Si in SiO_2, nitrogen atoms appreciably affect the formation of luminescent nanoprecipitates. Variations in the intensity of PL bands observed after heat treatments are indicative of changes in the number of emitting centers, whereas the shifts of PL peaks to shorter wavelengths indicate that the sizes of these centers decrease. An increase in the number of nanoprecipitates and a decrease in their average sizes as a result of the introduction of N is probably related to an increase in the number of precipitation nuclei due to the interaction of N with excess Si. In spite of the introduction of additional precipitation centers, the Si concentrations higher than 10^{21} cm^{-3} and the annealing temperatures higher than 1000°C were still found to be necessary for the formation of Si nanocrystals. The degree of supersaturation with silicon necessary for the precipitates to attain the sizes for which the crystal lattice is still stable is a prerequisite to the formation of Si nanocrystals during heat treatment of the layers with implanted nitrogen.

ACKNOWLEDGMENTS

We are grateful to N.Kh. Talipov and A.M. Gilinskiĭ for their help in carrying out this study.

This study was supported by the Russian Foundation for Basic Research (project no. 00-02-17963) and the Interdisciplinary Scientific and Technological Program "Physics of Solid-State Nanostructures."

REFERENCES

1. T. Shimizu-Iwayama, S. Nakao, and K. Saitoh, Appl. Phys. Lett. **65**, 1814 (1994).
2. P. Mutti, G. Gkislotti, S. Bertori, *et al.*, Appl. Phys. Lett. **66**, 851 (1995).
3. G. A. Kachurin, I. E. Tyschenko, K. S. Zhuravlev, *et al.*, Fiz. Tekh. Poluprovodn. (St. Petersburg) **31**, 730 (1997) [Semiconductors **31**, 626 (1997)].
4. M. Fujii, A. Mimura, S. Hayashi, *et al.*, J. Appl. Phys. **87**, 1855 (2000).
5. D. I. Tetel'baum, I. A. Karpovich, M. V. Stepikhova, *et al.*, Poverkhnost, No. 5, 31 (1998).
6. S. P. Withrow, C. W. White, A. Meldrum, *et al.*, J. Appl. Phys. **86**, 396 (1999).
7. L. Patrone, D. Nelson, V. Safarov, *et al.*, J. Appl. Phys. **87**, 3829 (2000).
8. M. Fujii, S. Hayashi, and K. Yamamoto, J. Appl. Phys. **83**, 7953 (1998).
9. J. Zhao, D. S. Mao, Z. X. Lin, *et al.*, Appl. Phys. Lett. **73**, 1838 (1998).
10. J.-H. Tsai, A.-T. Yu, and B. C. Shen, Jpn. J. Appl. Phys. **39**, L107 (2000).
11. I. E. Tyschenko, L. Rebohle, R. A. Yankov, *et al.*, J. Lumin. **80**, 229 (1999).
12. G. A. Kachurin, M.-O. Ruault, A. K. Gutakovskiĭ, *et al.*, Nucl. Instrum. Methods Phys. Res. B **147**, 356 (1999).
13. G. A. Kachurin, S. G. Yanovskaya, M.-O. Ruault, *et al.*, Fiz. Tekh. Poluprovodn. (St. Petersburg) **34**, 1004 (2000) [Semiconductors **34**, 965 (2000)].
14. B. H. Augustine, E. A. Irene, Y. J. He, *et al.*, J. Appl. Phys. **78**, 4020 (1995).
15. Q. Zhang, S. C. Bayliss, and D. A. Hutt, Appl. Phys. Lett. **66**, 1977 (1995).
16. Q. Zhang, S. C. Bayliss, A. Al-Aljili, *et al.*, Nucl. Instrum. Methods Phys. Res. B **97**, 329 (1995).
17. J. Zhao, D. S. Mao, Z. X. Lin, *et al.*, Appl. Phys. Lett. **74**, 1403 (1999).
18. T. Ehara and S. Machida, Thin Solid Films **346**, 275 (1999).
19. K. Oyoshi, T. Tagami, and S. Tanaka, J. Appl. Phys. **68**, 3653 (1990).
20. S. Veprek, Z. Iqbal, and F.-A. Sarrot, Philos. Mag. B **45**, 137 (1982).
21. L. A. Nesbit, Appl. Phys. **46**, 38 (1985).
22. G. A. Kachurin, A. F. Leĭer, K. S. Zhuravlev, *et al.*, Fiz. Tekh. Poluprovodn. (St. Petersburg) **32**, 1371 (1998) [Semiconductors **32**, 1222 (1998)].
23. C. Delerue, G. Allan, and M. Lanno, Phys. Rev. B **48**, 11024 (1993).

Translated by A. Spitsyn

Semiconductors, Vol. 35, No. 10, 2001, pp. 1187–1190. Translated from Fizika i Tekhnika Poluprovodnikov, Vol. 35, No. 10, 2001, pp. 1240–1243.

AMORPHOUS, VITREOUS, AND POROUS SEMICONDUCTORS

Special Features of Photoelectric Properties of Nanostructured Films of Hydrogenated Silicon

O. A. Golikova and M. M. Kazanin

Ioffe Physicotechnical Institute, Russian Academy of Sciences, Politekhnicheskaya ul. 26, St. Petersburg, 194021 Russia

Submitted January 21, 2001; accepted for publication January 24, 2001

Abstract—Nanostructured Si films differing in hydrogen content, in the forms of Si–H bonds, and in certain characteristics of Si inclusions in an amorphous matrix (volume fraction, size, and structure) were studied. The behavior common to all the studied films, i.e., an increase in the defect density and nonmonotonic enhancement of photoconductivity at the "red wing" of the spectral characteristic compared to *a*-Si:H, was assessed. At the same time, there are films with either enhanced or reduced photoconductivity compared to *a*-Si:H. © *2001 MAIK "Nauka/Interperiodica".*

1. INTRODUCTION

Nanostructured hydrogenated silicon containing nanoinclusions of Si in an amorphous matrix of the film (*ns*-Si:H) is attracting considerable attention in connection with the possibility of obtaining the material with photoconductivity (σ_{ph}) much higher than σ_{ph} observed in conventional *a*-Si:H and measured under identical conditions [1, 2]. However, the reasons for this enhancement of σ_{ph} remain unknown, which impedes the control and optimization of the grown-film properties. Therefore, the need for further investigations of *ns*-Si:H is obvious.

The objective of this investigation was to determine the effect of nanoinclusions on the results of studying the *ns*-Si:H films by the constant-photocurrent method (CPM) and by measuring the spectral characteristics of σ_{ph}. To this end, we intentionally selected the films that had different sizes, contents, and structures of nanoinclusions and also had different Si–H bonds and hydrogen contents.

When analyzing the experimental results, we used data obtained previously for certain similar films using optical modulation spectroscopy (OMS) at the University of Leuven (Belgium).

2. EXPERIMENT, RESULTS, AND DISCUSSION

The *ns*-Si:H films were deposited using two methods: radio-frequency plasma-enhanced chemical vapor deposition (rf-PECVD) based on silane (SiH_4) decomposition [1] and dc magnetron-assisted SiH_4 decomposition (dc-MASD) [3]. In what follows, the corresponding films will be referred to as the PECVD and MASD films, respectively. The deposition temperature was 380°C in both cases, but the films differed significantly in hydrogen content C_H: we had C_H = 4–5 at. % in the MASD films, whereas C_H was larger by approximately a factor of 2 in the PECVD films. In addition, the films also had different types of Si–H bond. The MASD films contained monohydride (SiH) and dihydride (SiH_2) bonds, which formed clusters at the surface of nanoinclusions; the value of the microstructure parameter R varied from 0.65 to 1. The PECVD films included monohydride bonds and, in addition (judging from the presence of the band at 2034 cm^{-1} in the IR spectra), silicon–hydrogen clusters also referred to as plateletlike SiH groups and well known for hydrogen present in crystalline silicon [4].

The bands at 516–517 cm^{-1} characteristic of nanocrystalline Si inclusions were observed in the Raman spectra of the *ns*-Si:H films for which the value of R was close to unity. The size of the nanocrystals was d_R = 4–5 nm, and the volume crystal fraction X_c was no larger than 20%. These bands were not observed in the Raman spectra of all the other films; apparently, the values of d_R and/or X_c were much smaller for these films. However, we should note that the high-intensity LA-phonon bands peaked at 300 cm^{-1} were observed in the Raman spectra of PECVD films. This has been interpreted [5] as an indication of the formation of ordered inclusions in the form of Si nanoclusters. It is possible that such films simultaneously contain nanocrystals and nanoclusters or nanoclusters alone.

We emphasize that the electrical conductivity is effected over the amorphous matrix in all the films, whereas the nanoinclusions play the role of the structure modifier, which ultimately controls the photoelectric properties of the material under consideration.

In Fig. 1, we show the quantity $\sigma_{ph}/\sigma_{ph}^{St}$ as a function of the dark-conductivity activation energy $\Delta E = (\varepsilon_C - \varepsilon_F)_{T=0}$ for a number of films. Here, σ_{ph} and σ_{ph}^{St} are the photoconductivities of *ns*-Si:H and conventional *a*-Si:H, respectively, measured for ΔE = const at T = 300 K

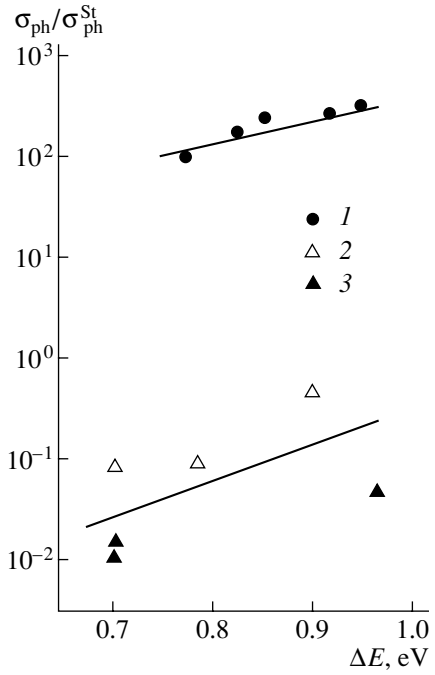

Fig. 1. Dependences of $\sigma_{ph}/\sigma_{ph}^{St}$ on the activation energy for the dark conductivity for (*1*) the PECVD films, (*2*) the MASD films with $R = 0.65$ and 0.75, and (*3*) the MASD films with $R \approx 1$.

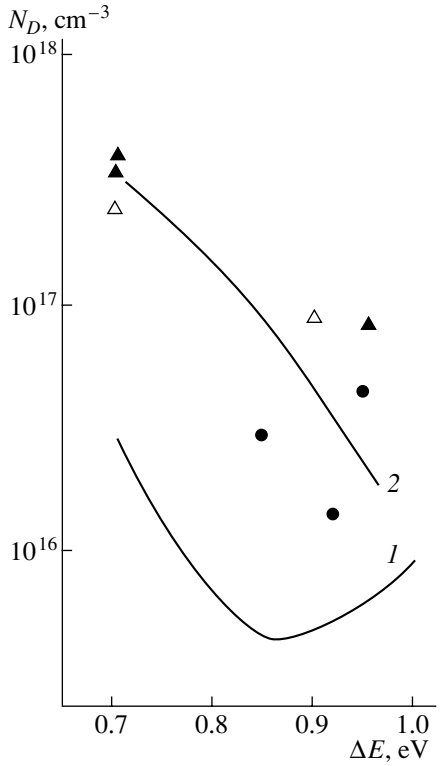

Fig. 2. The defect density N_D as a function of the activation energy for the dark electrical conductivity ΔE for (curve *1*) a conventional *a*-Si:H film and (curve *2*) an *ns*-Si:H film. The symbols used are the same as in Fig. 1.

under identical conditions (with an optical quantum energy of 2 eV and a photocarrier generation rate of 10^{19} cm^{-3} s^{-1}); ε_C is the conduction-band bottom; and ε_F is the Fermi level.

It can be seen from Fig. 1 that the photoconductivity σ_{ph} of PECVED films is much higher than in conventional *a*-Si:H; however, σ_{ph} of the MASD films is smaller than σ_{ph}^{St}, especially for the films with $R \approx 1$. The curves are presented in order to facilitate the consideration of experimental data.

We now direct our attention to the results of determining the defect density N_D using the CPM. It follows from Fig. 2 that, for a constant position of ε_F relative to ε_C, the defect density N_D is higher in the *ns*-Si:H films than in *a*-Si:H; this effect is especially pronounced for the MASD films. Curve *1* represents the universal dependence of N_D on the Fermi level for conventional *a*-Si:H [6]. Curve *2* is of course not universal because, as was mentioned above, the *ns*-Si:H films differ widely from each other in structure and composition. This curve is shown in order to clearly illustrate the trend for an increase in N_D in *ns*-Si:H compared to *a*-Si:H. However, as can be seen from Fig. 1, an increase in the defect density affects the photoconductivity in the PECVD and MASD films in opposite ways.

If we attribute an increase in N_D to additional defects at the surfaces of nanoinclusions and assume that, as a result, the number of recombination centers for photogenerated charge carriers is larger than in *a*-Si:H, the decrease in the photoconductivity of the MASD films becomes understandable.

At the same time, there is a clear contradiction between the behavior of N_D and that of σ_{ph} for the PECVD films. This contradiction motivated us to reconsider the OMS data obtained previously for the same films.

Without going into details, the OMS method consists in the following [7]. Two optical beams are directed onto the film: a probing monochromatic beam and a pump beam. The nonequilibrium charge carriers generated by the pumping (an Ar^+ laser with a power density of 30 mW/cm^2) change the occupancy of localized states, which, in turn, affects the transitions of charge carriers between these states and the band states. The experimentally measured quantity is the ratio $-\Delta T^*/T^*$, where T^* is the transmission (without pumping) of the probing beam generated by an incandescent lamp and passed through a monochromator and $-\Delta T^*$ is a change in the transmission of the probing beam in the presence of pumping. The quantity $-\Delta T^*/T^*$ is proportional to N_D for $E \approx 1$ eV.

In Fig. 3, we show the OMS spectra for three PECVD films; one of them is a film of conventional *a*-Si:H, which features $\Delta E = 0.8$ eV, $N_D = 10^{16}$ cm^{-3} (see Fig. 2), and $\sigma_{ph} = 10^{-6}\ \Omega^{-1}$ cm^{-1}. The other two films are those of *ns*-Si:H with σ_{ph} increased by more than two

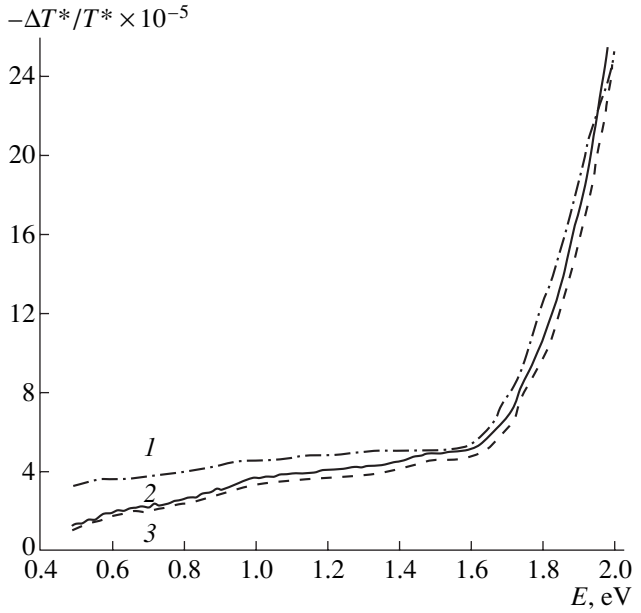

Fig. 3. The transmission spectra obtained using optical modulation spectroscopy for (*1*) conventional *a*-Si:H with $\Delta E = 0.8$ eV and (*2*, *3*) *ns*-Si:H with $\Delta E = 0.95$ and 0.92 eV, respectively.

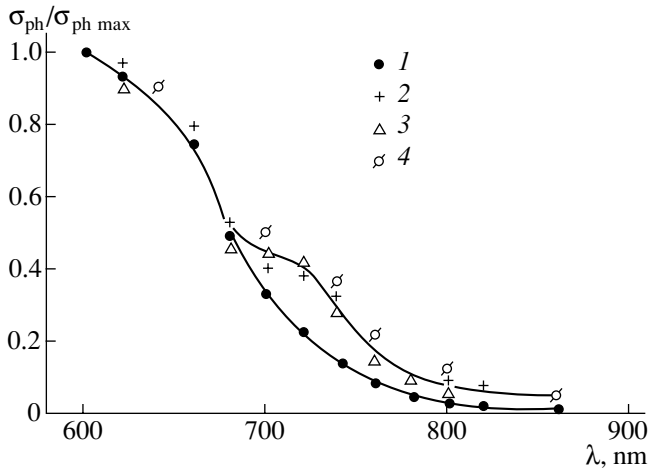

Fig. 4. The red wing in the spectral characteristic of photoconductivity for (*1*) an *a*-Si:H film ($\Delta E = 0.85$ eV), (*2*) a PECVD film ($\Delta E = 0.95$ eV), and (*3*, *4*) the MASD films with $\Delta E = 0.9$ and 0.78 eV, respectively.

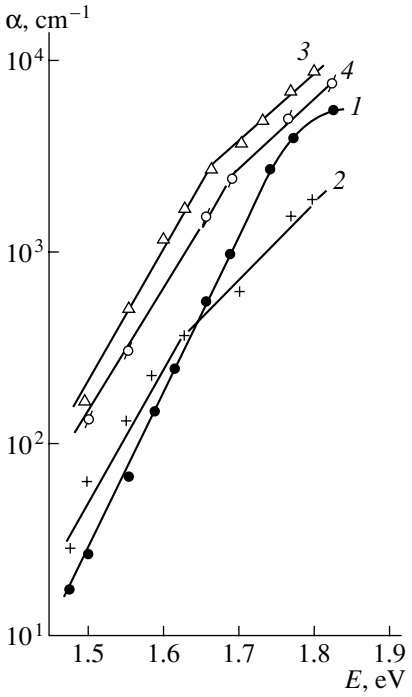

Fig. 5. The absorption coefficient of the films according to the constant-photocurrent method. The numbers at the curves correspond to those in Fig. 4.

orders of magnitude compared to *a*-Si:H (see Fig. 1). If $-\Delta T^*/T^* \sim N_D$, a new contradiction between the values of σ_{ph} and N_D is evident: all three films have almost the same values of N_D according to the OMS data (Fig. 3). However, the relation $-\Delta T^*/T^* \sim N_D$ becomes invalid if an increased recombination rate of the photogenerated charge carriers is characteristic of some of the defects compared to other defects. Therefore, small values of $-\Delta T^*/T^*$ may be observed for this reason rather than due to a low defect density in the films.[1]

On this basis, we may assume that the PECVD films modified by nanoinclusions contain defects of two types, which feature widely different recombination rates due to a sharp distinction between the cross sections for the capture of photogenerated charge carriers.

If the photoconductivity of *ns*-Si:H PECVD films is controlled by recombination at the defects that feature the capture cross section *s* smaller than *s* of defects in *a*-Si:H by orders of magnitude, the increase in σ_{ph} (in spite of an increase in N_D) becomes understandable (Figs. 1, 2).

For the MASD *ns*-Si:H films, the relation between σ_{ph} and N_D, as was emphasized above, is the opposite. The causes of this are still unclear. We may only assume that these causes should be related to distinctions in the film structure, which were mentioned above. However, in all the cases, the results obtained by the CPM (increased values of N_D) may be considered as a verification of the existence of nanoinclusions in the films.

[1] G.J. Adriaenssens (private communication).

We now consider the special features of the "red wing" in the spectral characteristics of photoconductivity ($\lambda \approx 850$–600 nm) obtained under the conditions of a constant luminous flux. In Fig. 4, these characteristics are shown for a number of the PECVD and MASD films.

Starting with $E \approx 1.4$ eV ($\lambda = 860$ nm), the photoconductivity of *ns*-Si:H films increases with increasing

E as a result of electron transitions from the tail of the density of states of the valence band to the conduction band; however, for E larger than about 1.7 eV (λ = 720 nm), this increase in σ_{ph} becomes significantly less steep for all films. For $E > 1.82$ eV ($\lambda < 680$ nm), all the experimental points fall satisfactorily on a common straight line obtained for a film of conventional intrinsic *a*-Si:H ($\Delta E = 0.85$ eV); the latter material has, as is well known, the most ordered structure.

Previously, a less sharp increase in the absorption coefficient for $E > 1.7$ eV in some of the *a*-Si:H films has been observed; this effect has been related to the existence of an additional valence-band tail that was attributed to fluctuations of the top of this band as a result of a certain unordering of the film structure. Obviously, this tail is located at higher energies than the Urbach tail [8, 9]. We may assume that the fluctuations of the valence-band top are more important for *ns*-Si:H, especially if the distribution of nanoinclusions in the films is nonuniform. Therefore, the existence of a slow-increase portion in the spectral characteristics of photoconductivity in the *ns*-Si:H films (Fig. 4) may be attributed to the formation of an additional valence-band tail. In Fig. 4, the common curve was drawn through all the points related to such films.

The data on the absorption coefficient obtained by the CPM for a number of *ns*-Si:H films support the above assumption (Fig. 5).

3. CONCLUSION

Studies of the *ns*-Si:H films by the constant-photocurrent method showed that, for $\varepsilon_C - \varepsilon_F = \text{const}$, the density of defects in this material is higher than in conventional *a*-Si:H. Notwithstanding this fact, the PECVD films feature a much higher photoconductivity, whereas the photoconductivity of MASD films is lower than in *a*-Si:H. This indicates that the nanoinclusions modify the amorphous matrix differently in the PECVD and MASD films.

The results obtained for the PECVD films compel us to assume that the defects with a cross section of electron capture orders of magnitude smaller than in *a*-Si:H are formed in these films, whereas we may not conclude the same for the MASD films.

Undoubtedly, distinctions between photoconductivities in the PECVD and MASD films are caused by differences between the structure of these two types of films, although the available data are insufficient to decide which differences are most important. However, in our opinion, only the resolution of this issue can give insight into the origin of the defects present in the PECVD films and responsible for the enhancement of photoconductivity.

It should be noted that the results obtained by the constant-photocurrent method and by studying the features of the red wing in the spectral characteristic of photoconductivity may be considered as comparatively simple tests for detecting the nanoinclusions both in the PECVD and MASD films.

ACKNOWLEDGMENTS

We thank Professor G.J. Adriaenssens for his persistent interest in this study and his collaboration.

REFERENCES

1. P. Roca i Cabarrocas, S. Hamma, P. Stahel, *et al.*, in *Proceedings of the 14th European Photovoltaic Energy Conference, Barcelona, 1997*, Part 5A, p. 20.
2. O. A. Golikova and M. M. Kazanin, Fiz. Tekh. Poluprovodn. (St. Petersburg) **33**, 110 (1999) [Semiconductors **33**, 97 (1999)].
3. O. A. Golikova, M. M. Kazanin, A. N. Kuznetsov, and E. V. Bagdanova, Fiz. Tekh. Poluprovodn. (St. Petersburg) **34**, 1125 (2000) [Semiconductors **34**, 1085 (2000)].
4. A. von Keudell and J. R. Abelson, J. Appl. Phys. **84**, 489 (1998).
5. O. A. Golikova and M. M. Kazanin, Fiz. Tekh. Poluprovodn. (St. Petersburg) **34**, 762 (2000) [Semiconductors **34**, 737 (2000)].
6. O. A. Golikova, Fiz. Tekh. Poluprovodn. (St. Petersburg) **31**, 281 (1997) [Semiconductors **31**, 228 (1997)].
7. G. J. Adriaenssens, W. Grevendonk, and O. A. Golikova, Fiz. Tekh. Poluprovodn. (St. Petersburg) **32**, 121 (1998) [Semiconductors **32**, 109 (1998)].
8. M. Stutzman, Philos. Mag. B **60**, 531 (1989).
9. V. M. Novikov and A. P. Sokolov, Fiz. Tverd. Tela (Leningrad) **32**, 1515 (1990) [Sov. Phys. Solid State **32**, 884 (1990)].

Translated by A. Spitsyn

Semiconductors, Vol. 35, No. 10, 2001, pp. 1191–1196. Translated from Fizika i Tekhnika Poluprovodnikov, Vol. 35, No. 10, 2001, pp. 1244–1249.

AMORPHOUS, VITREOUS, AND POROUS SEMICONDUCTORS

Numerical Calculation of the Temperature Dependences of Photoconductivity in the *p*-type *a*-Si:H

S. V. Kuznetsov

Moscow State University, Vorob'evy gory, Moscow, 119899 Russia

e-mail: sergkuz@mail.ru

Submitted October 19, 2000; accepted for publication January 25, 2001

Abstract—Temperature dependences of photoconductivity in *p*-type *a*-Si:H were calculated numerically. The calculations were performed in terms of a simple recombination model in which the tunneling recombination of electrons captured by the states in the conduction-band tail and holes trapped at the states of the valence-band tail is accounted for at low temperatures. The results of calculations are consistent with experimental data, according to which the photoconductivity of *p*-type *a*-Si:H depends only slightly on the Fermi level position and on the total concentration of dangling bonds. The computer-assisted numerical simulation suggests that the possible cause of this weak dependence may consist in the differing extent of the valence- and conduction-band tails. It is shown that the statistics of occupancy of the states in the mobility gap in *a*-Si:H under illumination differs vastly from that in the state of equilibrium. © *2001 MAIK "Nauka/Interperiodica".*

1. INTRODUCTION

The study of temperature dependences of photoconductivity in *a*-Si:H gives a deeper insight into recombination processes in this unordered semiconductor. Scientists are unanimous in their opinion that the main recombination channel at high temperatures is free-carrier recombination via the dangling bonds (the *D* centers) [1–3]. However, in spite of a large number of studies concerned with *a*-Si:H properties, the most important recombination channels at medium and low temperatures remain unclear. Basically, the following models of recombination are used in order to interpret the temperature dependence of photoconductivity in the above temperature ranges:

(i) The "band-to-tail" recombination model [4–6] according to which recombination occurs by capturing a nonequilibrium charge carrier from the free band by a state in the tail of the opposite band, which captured a charge carrier of the opposite sign beforehand. The number of tail states acting as recombination centers increases as the spacing between the quasi-Fermi levels increases with decreasing temperature.

(ii) The "tail-to-(dangling bond)" recombination model [7, 8]; here, tunneling of charge carriers captured by the states in the band tails to the dangling-bond states occurs.

(iii) The "tail-to-tail" recombination model; here, we have the tunneling recombination of electrons captured by the states in the tail of the conduction band with holes captured by the states in the tail of the valence band.

Each of these models accounts for certain, but not all, experimental data. For example, temperature dependences of photoconductivity calculated in the terms of the "band-to-tail" model for the Fermi level position in the vicinity of the mobility midgap demonstrate a thermal quenching of photoconductivity, which is consistent with experimental data. However, the calculated slope of the activated portion in the temperature dependence of photoconductivity at low temperatures is smaller than the experimental value by a factor of two. In contrast, the "tail-to-(dangling bond)" model reproduces this slope but does not ensure the manifestation of the thermal quenching of photoconductivity [11]. It is noteworthy that the role of the "tail-to-(dangling bond)" recombination becomes evidently more important as the *D*-center concentration increases. For *a*-Si:H films with a low concentration of defects, the "tail-to-tail" recombination should be taken into account [10, 12]. By analyzing the limited applicability of the above models, we may conclude that it is in fact necessary to take into account all the possible recombination mechanisms and separate from them the most important one, depending on the special features of the spectrum of the density of states within the mobility gap (the type and concentration of defects, and so on) and on the experimental conditions (temperature, illumination intensity, and so on). As a rule, both the experimental studies and numerical calculations are concerned with either undoped *a*-Si:H or *n*-type *a*-Si:H. The photoconductivity of *p*-type *a*-Si:H has been studied to a much lesser extent. Recent experimental data [13] indicate that the photoconductivity of B-doped *a*-Si:H films depends only slightly on the doping level and the *D*-center concentration in the range of moderate temperatures. These data make it possible to suggest a recombination model in *a*-Si:H; this model attributes the origin of distinctions between the recombination processes in *a*-Si:H of the *n*- and *p*-types to the different

1063-7826/01/3510-1191$21.00

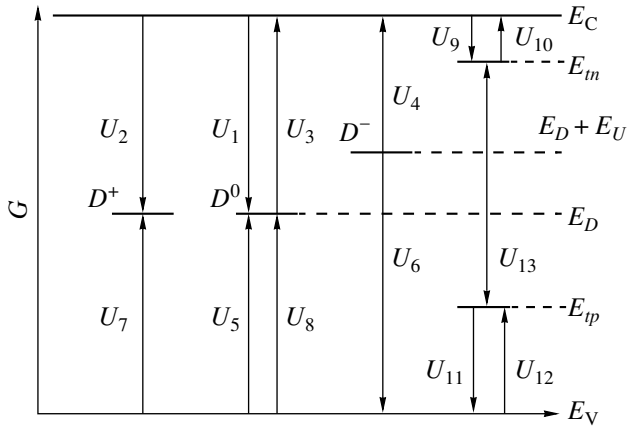

Fig. 1. Schematic representation of electron transitions in the simplified model of the density of states in the mobility gap.

extent of the valence- and conduction-band tails. According to this model, illumination of the *p*-type *a*-Si:H films affects profoundly the occupancy of states in the mobility gap. Furthermore, the D^0-center concentration is equal to the concentration of holes captured by the states in the valence-band tail and is independent of the Fermi level position. It is assumed that the photoconductivity in the activated portion of its temperature dependence in the *p*-type *a*-Si:H films is controlled by the direct capture of holes by the D^0 centers. In order to verify this model of recombination, we performed a numerical calculation for the temperature dependence of photoconductivity in a *p*-type *a*-Si:H film.

2. MODEL

We performed the calculations in terms of a simplified model of the density of states in the mobility gap; four discrete states in the gap were considered (Fig. 1): E_{tp}, E_D, $E_D + E_U$, and E_{tn}. The levels E_{tp} and E_{tn} with the densities of states for N_{tp} and N_{tn} are the effective levels in the valence- and conduction-band tails, respectively. The levels E_D and $E_D + E_U$ are the energy levels of positively correlated states induced by dangling bonds. As a rule, the band-tail states may be considered as shallow-level traps that are in thermodynamic equilibrium with the nearest band. Henceforth, we refer to the levels E_{tp} and E_{tn} as "hole traps" and "electron traps," respectively. Such a simplified representation of the density of states in the mobility gap does not significantly affect the results of calculation as has been shown previously [2]. In addition, the introduction of the simple model for the density of states reduces the number of parameters used in the calculations, which makes it possible to determine the role of each parameter more clearly. Figure 1 illustrates the recombination and emission fluxes taken into consideration in the calculations. Two possible recombination channels were considered in this study: the direct capture of free electrons and holes by the *D* centers (the fluxes U_1, U_2, U_5, and U_6) and the tunneling recombination of electrons captured by the states in the conduction-band tail with the holes captured by the states in the valence-band tail (the flux U_{13}). For a nonequilibrium steady state, the following kinetic equations can be written:

$$\frac{dn}{dt} = G - U_1 - U_2 + U_3 + U_4 - U_9 + U_{10} = 0,$$

$$\frac{dp}{dt} = G - U_5 - U_6 + U_7 + U_8 - U_{11} + U_{12} = 0,$$

$$\frac{dn_t}{dt} = U_9 - U_{10} - U_{13} = 0, \qquad (1)$$

$$\frac{dp_t}{dt} = U_{11} - U_{12} - U_{13} = 0,$$

$$\frac{d[N_D f^+]}{dt} = U_3 + U_5 - U_1 - U_7 = 0.$$

The relations between the fluxes, on the one hand, and the concentrations of charge carriers and recombination centers, on the other hand, are written on the basis of the Shockley–Read formalism [2, 14] as

$$\begin{gathered} U_1 = nN_D f^+ c_n^+, \quad U_5 = N_D f^0 p c_p^0, \\ U_9 = nN_{tn}(1 - f_{tn})c_n, \\ U_2 = nN_D f^0 c_n^0, \quad U_6 = N_D f^- p c_p^-, \\ U_{10} = N_{tn} f_{tn} e_{tn}, \\ U_3 = N_D f^0 e_n^0, \quad U_7 = N_D f^+ e_p^+, \\ U_{11} = pN_{tp} f_{tp} c_p, \\ U_4 = N_D f^- e_n^-, \quad U_8 = N_D f^0 e_p^0, \\ U_{12} = N_{tp}(1 - f_{tp})e_{tp}. \end{gathered} \qquad (2)$$

Henceforth, the following notation is used: f^+, f^0, and f^- are the probabilities of finding the *D* center in the states D^+, D^0, and D^-, respectively; f_0^+, f_0^0, and f_0^- are the corresponding probabilities in the thermal equilibrium; c_n^+ and c_n^0 are the electron-capture coefficients for the D^+ and D^0 states; c_p^0 and c_p^- are the hole-capture coefficients for the D^0 and D^- states; e_n^0 and e_n^- are the coefficients of thermal electron emission from the D^0 and D^- states; e_p^+ and e_p^0 are the coefficients of thermal hole emission from the D^+ and D^0 states; f_{tn} and f_{tp} are the probabilities of the traps being occupied by electrons and holes, respectively; f_{tn}^0 and f_{tp}^0 are the corresponding probabilities in the thermal equilibrium; c_{tn} and c_{tp} are the coefficients of the electron and hole cap-

ture for the relevant traps; e_{tn} and e_{tp} are the coefficients of thermal electron emission from relevant traps; N_D is the D-center concentration; and G is the optical-generation rate. It is convenient to introduce the following additional designations: $n_t = N_{tn} f_{tn}$ and $p_t = N_{tp} f_{tp}$, where n_t and p_t are the concentrations of electrons and holes captured by the relevant traps; also, let n_{t0} and p_{t0} be the corresponding concentrations under the thermal-equilibrium conditions. It is worth noting that "equilibrium" and "equilibrium conditions" refer to the state of *a*-Si:H films in the dark, in which case the occupancies of all the states are governed by the Fermi–Dirac statistics. The statistics of occupancy of the states is nonequilibrium if there is optical generation. In this paper, only the steady-state nonequilibrium occupancies of the states in the bands and the mobility gap are considered.

According to Dunstan [15] and Cleve and Thomas [11], the tunneling-recombination rate U_{13} can be written as

$$U_{13} = n_t p_t T_{np}, \tag{3}$$

where T_{np} stands for the "tail-to-tail" tunneling-recombination coefficient. Using the detailed balancing principle, we can obtain the expressions for the emission coefficients in terms of the capture coefficients and the occupancy probabilities f_0^+, f_0^0, and f_0^- [2]. In turn, f_0^+, f_0^0, and f_0^- are defined by the values of E_F, E_D, and E_U [16, 17]. Since the D centers can be found in three charge states, the following obvious equality can be written:

$$f^+ + f^0 + f^- = 1. \tag{4}$$

The condition for electroneutrality of the *a*-Si:H films in the dark and under illumination can be expressed as [2, 5]

$$\begin{aligned} &n + N_{tn} f_{tn} + N_D f^- - n_0 - N_{tn} f_{tn}^0 - N_D f_0^- \\ &= p + N_{tp} f_{tp} + N_D f^+ - p_0 - N_{tp} f_{tp}^0 - N_D f_0^+. \end{aligned} \tag{5}$$

Thus, we have a system of seven linearly independent equations for seven unknowns: n, p, f_{tn}, f_{tp}, f^+, f^0, and f^-. This system of equations can be solved numerically using a computer.

3. CHOICE OF PARAMETERS

We chose the most widely accepted values of the parameters that appear in the theoretical model under consideration [4, 6, 9]. The value of 10^{21} cm^{-3} was used for the effective density of states in the conduction and valence bands. The mobility gap was assumed to be equal to 1.8 eV; the mobilities of electrons and holes were assumed to be equal to 10 and 1 cm^2 V^{-1} s^{-1}, respectively. The Fermi level position E_F–E_V was varied from 0.4 to 1.6 eV. The photogeneration rate G was assumed to be equal to 10^{19} cm^{-3} s^{-1}. The following values were used for the dangling-bond parameters:

$$E_D = 0.9 \text{ eV}, \quad E_U = 0.3 \text{ eV},$$

$$c_n^0 = c_p^0 = 3 \times 10^{-15} \text{ cm}^{-2},$$

$$c_n^+ = c_p^- = 1.5 \times 10^{-13} \text{ cm}^{-2}.$$

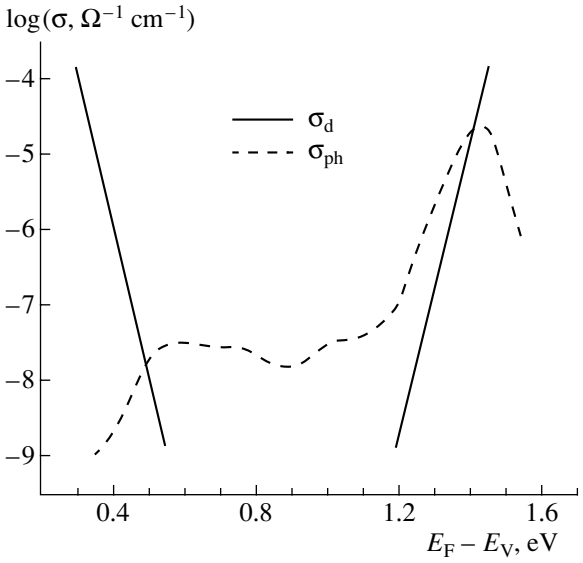

Fig. 2. Dependences of the dark conductivity (σ_d) and photoconductivity (σ_{ph}) on the Fermi level position $E_F - E_V$.

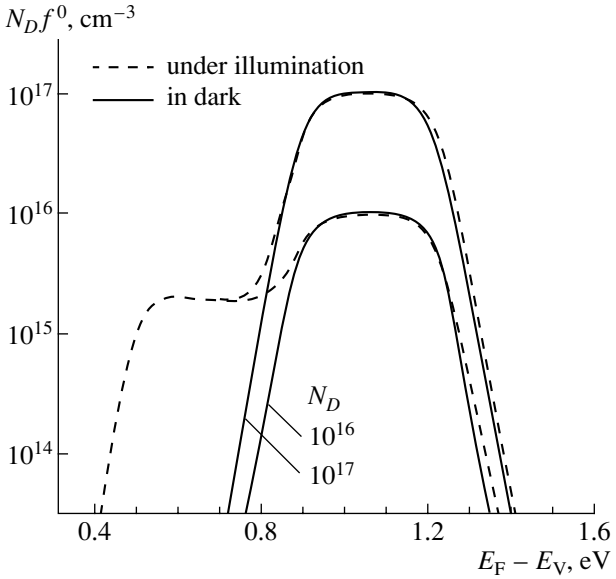

Fig. 3. Dependences of the D^0-center concentration ($N_D f^0$) on $E_F - E_V$ in the dark (the solid lines) and under illumination (the dotted lines). The values of N_D used in the calculations and indicated by the arrows are expressed in cm^{-3}.

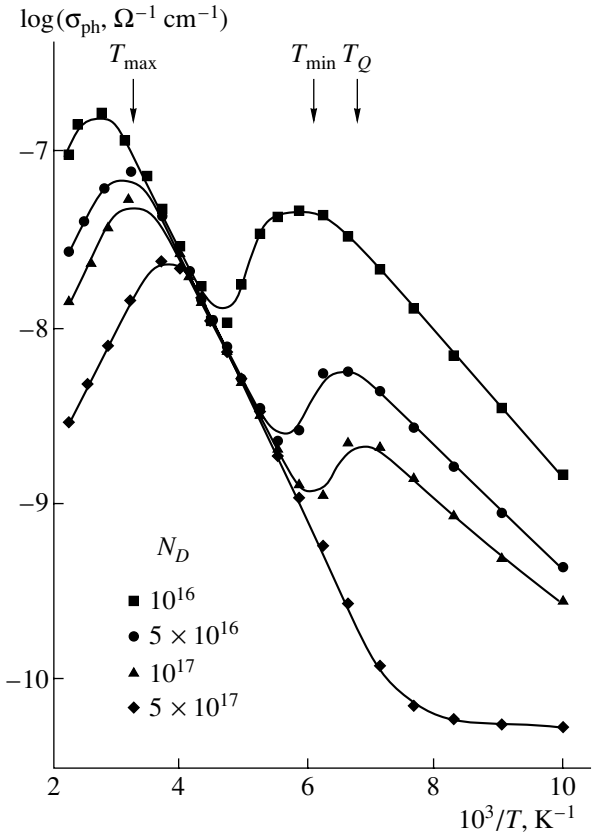

Fig. 4. Temperature dependences of photoconductivity for $E_F - E_V = 0.75$ eV and several values of N_D indicated at the symbols and expressed in cm^{-3}. The arrows indicate the temperatures characteristic of the dependence $\sigma_{ph}(1/T)$ for $N_D = 10^{17}$ cm^{-3}.

The value of N_D was varied from 10^{16} to 5×10^{17} cm^{-3}. The parameters of effective traps were assumed to be equal to

$$E_C - E_{tn} = 0.1 \text{ eV}, \quad E_{tp} - E_V = 0.3 \text{ eV},$$

$$N_{tn} = N_{tp} = 10^{19} \text{ cm}^{-3}, \quad c_{tn} = c_{tp} = 10^{-15} \text{ cm}^{-3}.$$

4. RESULTS OF THE NUMERICAL CALCULATION AND DISCUSSION

We solved numerically the system of equations (1), (4), and (5) and obtained the temperature dependences of n, p, f_{tn}, f_{tp}, f^+, f^0, and f^-. First of all, we consider the dependence of photoconductivity

$$\sigma_{ph} = e\mu_n n + e\mu_p p \qquad (6)$$

on the Fermi level position (see Fig. 2). The dependence of dark conductivity (σ_d) on the Fermi level position is also shown in Fig. 2. The values of σ_{ph} and σ_d were calculated for $T = 250$ K and $N_D = 10^{16}$ cm^{-3}. This temperature, according to experimental data [13], is better suited than $T = 300$ K for studies in the range of so-called "intermediate" (medium) temperatures, within which photoconductivity increases exponentially with temperature [9, 13]. According to Fig. 2, the dependence of σ_{ph} on $E_F - E_V$ is highly asymmetric in contrast to the dependence $\sigma_d(E_F - E_V)$. Notably, σ_{ph} is independent of the Fermi level position in the range of $E_F - E_V = 0.5$–0.75 eV, which corresponds to *p*-type *a*-Si:H with low or medium doping levels. In contrast to *p*-type *a*-Si:H, an increase in the doping level of *n*-type *a*-Si:H induces an increase in σ_{ph} for $E_F - E_V = 1.15$–1.45 eV. However, in both cases, heavy doping leads to a decrease in photoconductivity. It is noteworthy that the calculated dependence of σ_{ph} on $E_F - E_V$ is consistent with experimental data [13, 17, 18].

Since the main recombination states for holes in *p*-type *a*-Si:H are those of the D^0 centers, the dependence of $N_D f^0$ on $E_F - E_V$ is of particular interest. Such dependences calculated for two values of N_D and for $T = 250$ K are shown in Fig. 3. As can be seen, these dependences are pronouncedly asymmetric if the sample is illuminated and demonstrate the following three important special features for the range of $E_F - E_V = 0.5$–0.75 eV:

(i) The nonequilibrium concentration of D^0 centers $N_D f^0$ differs significantly from the equilibrium one.

(ii) $N_D f^0$ is independent of N_D.

(iii) $N_D f^0$ is independent of $E_F - E_V$.

The above special features are valid for the range of moderate ("intermediate") temperatures.

In order to facilitate considering the effects of temperature and N_D on σ_{ph}, the temperature dependences of photoconductivity calculated for $E_F - E_V = 0.75$ eV and several values of N_D are shown in Fig. 4. The temperature demarcation lines between the characteristic temperature conditions for the temperature dependence of photoconductivity for $N_D = 10^{17}$ cm^{-3} are denoted as T_{max}, T_Q, and T_{min}. As can be seen from Fig. 4, all the dependences $\sigma_{ph}(1/T)$ coincide in the region of medium temperatures; in this region, σ_{ph} obeys the Arrhenius equation with the activation energy of $E_{A1} = 0.15$ eV, which is equal to the halved energy position of electron traps, i.e., $0.5(E_{tp} - E_V)$. Furthermore, σ_{ph} is independent of N_D in this temperature region. Contrastingly, the photoconductivity is inversely proportional to N_D at lower and higher temperatures. For $N_D \le 10^{17}$ cm^{-3}, the calculated dependences $\sigma_{ph}(1/T)$ demonstrate the thermal quenching of photoconductivity. The activation energy of σ_{ph} at low temperatures ($T < T_Q$) is equal to $E_{A2} = 0.08$–0.09 eV, which almost coincides with $E_C - E_{tn} = 0.1$ eV. Conventionally, the value of E_{A2} is related to the position of the effective level of the traps for electrons [7, 9]. This convention is based on two assumptions concerning the electronic properties of undoped or acceptor-doped *a*-Si:H at low temperatures *T*. It is

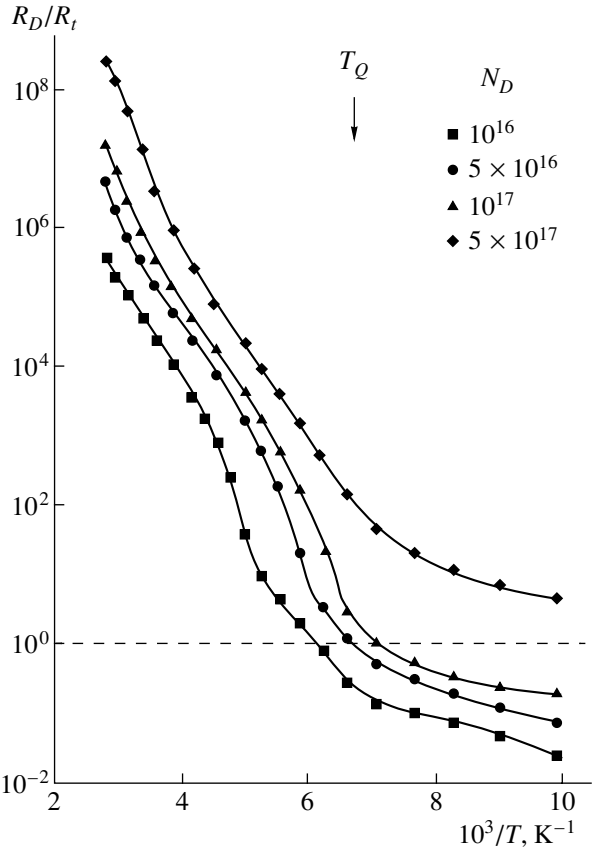

Fig. 5. Temperature dependence of the ratio R_D/R_t for $E_F - E_V = 0.75$ eV and several values of N_D expressed in cm^{-3}.

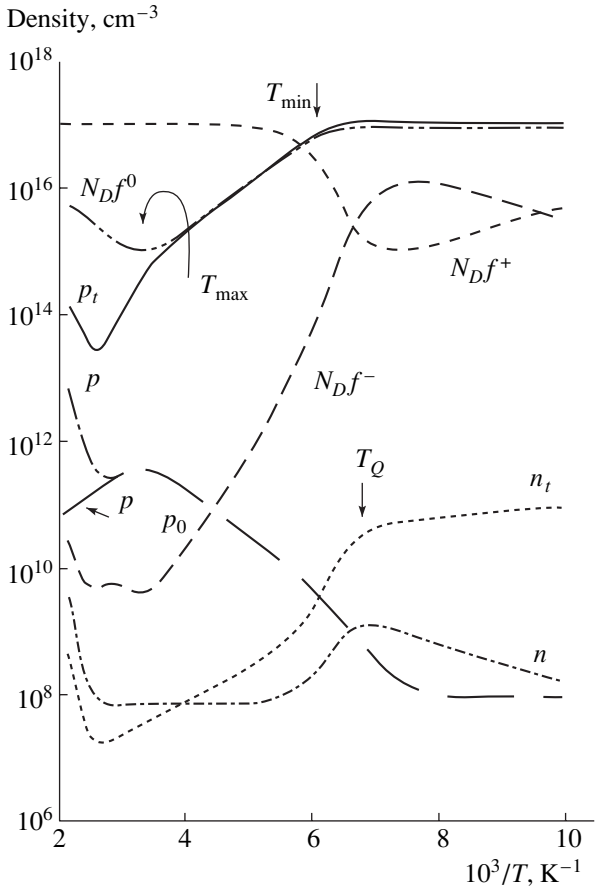

Fig. 6. Temperature dependences of concentrations of the D^+, D^0, and D^- states, and also of concentrations of free charge carriers (n and p) and of the carriers localized at the traps (n_t and p_t) for $N_D = 10^{17}$ cm^{-3}. The characteristic temperatures T_{max}, T_{min}, and T_Q are indicated.

assumed that, first, the conduction band is in thermal equilibrium with electron traps, i.e.,

$$n = n_t(N_C/N_{tn})\exp[(E_{tn} - E_C)/kT],$$

and, second, the tunneling recombination is dominant (i.e., n_t is temperature-independent).

A numerical calculation of the "band-to-(D center)" (R_D) and "tail-to-tail" (R_t) recombination rates verifies the assumption that $R_t > R_D$ at $T < T_Q$ (Fig. 5). As can be seen from Fig. 5, the low-temperature photoconductivity peak (see Fig. 4) corresponds to a change in the recombination type. At medium temperatures, we have $R_D \gg R_t$; consequently, in the p-type a-Si:H, the recombination of free charge carriers at the D centers governs the activation behavior of temperature dependence of photoconductivity.

In order to analyze the temperature dependences of photoconductivity (see Fig. 4) in more detail, we turn our attention to Fig. 6, where the temperature dependences of seven quantities corresponding to calculations for $N_D = 10^{17}$ cm^{-3} are shown. According to Fig. 6, $p_t = N_D f^0$ at medium temperatures. This relation provides a key to understanding the special features of the temperature dependence of photoconductivity in p-type a-Si:H. As has been shown previously [13], the above relation can be derived from the electroneutrality condition for p-type a-Si:H as a consequence of the fact that the valence-band tail is larger than the conduction-band tail. On the one hand, this relation signifies that the nonequilibrium positive charge is localized in the valence-band tail in p-type a-Si:H at medium and low temperatures, whereas the nonequilibrium negative charge is localized at the dangling bonds. On the other hand, it follows from the relation $p_t = N_D f^0$ that $N_D f^0$ is controlled only by the value of p_t, which, in turn, is defined by the parameters E_{tp} and N_{tp} (the same values of p_t and $N_D f^0$ correspond to the same values of E_{tp} and N_{tp}). Assuming that the main recombination channel is represented by transitions from the band to the D center, we arrive at the conclusion that σ_{ph} is independent of both $E_F - E_V$ and N_D, which was observed experimentally [13]. As can be seen from Fig. 6, the high-temperature peak of photoconductivity corresponds to a minimum in $N_D f^0$, whereas a decrease in σ_{ph} at $T > T_{max}$

is related to an increase in $N_D f^0$, as follows from the equilibrium statistics. According to Fig. 4, an increase in N_D results in a lowering of the peaks in the $\sigma_{ph}(1/T)$ curve at $T = T_{max}$ and $T = T_Q$ and in their shift to lower temperatures. However, σ_{ph} is independent of N_D at medium temperatures. This is consistent with experimental data on the effect of preliminary illumination on the temperature dependence of photoconductivity [13].

5. CONCLUSION

Thus, the numerical calculation performed for the temperature dependence of photoconductivity in *p*-type *a*-Si:H showed that (I) photoconductivity is independent of the doping level and the concentration of defects in a wide range of variations in these parameters, (II) the occupancy of the *D* centers differs significantly from that at equilibrium, and (III) the activation behavior of the temperature dependence of photoconductivity at intermediate temperatures is not related to the tunneling recombination.

The results of this study suggest that the independence of photoconductivity in *p*-type *a*-Si:H from the doping level and the concentration of dangling bonds represents an inherent property of this material and is brought about by distinctions in the extents of the band tails and by asymmetry of the D^0 and D^- states in reference to the mobility midgap.

ACKNOWLEDGMENTS

I am grateful to A.G. Kazanskiĭ for his invariably helpful participation in discussions.

REFERENCES

1. M. Hoheisel and W. Fuhs, Philos. Mag. B **57**, 411 (1988).
2. F. Vaillant and D. Jousse, Phys. Rev. B **34**, 4088 (1986).
3. E. Morgado, Philos. Mag. B **63**, 529 (1991).
4. T. J. McMahon and J. P. Xi, Phys. Rev. B **34**, 2475 (1986).
5. E. Morgado, Mater. Res. Soc. Symp. Proc. **336**, 419 (1994).
6. F. Vaillant, D. Jousse, and J.-C. Bruyere, Philos. Mag. B **57**, 649 (1988).
7. A. Vomvas and H. Fritzsche, J. Non-Cryst. Solids **97/98**, 823 (1987).
8. W. Fuhs, J. Non-Cryst. Solids **77/78**, 593 (1985).
9. J.-H. Zhou and S. R. Elliott, Phys. Rev. B **48**, 1505 (1993).
10. R. A. Street, in *Semiconductors and Semimetals* (Academic, Orlando, 1984), Vol. 21, Part B, p. 197.
11. B. Cleve and P. Thomas, Mater. Res. Soc. Symp. Proc. **192**, 317 (1990).
12. R. A. Street, J. C. Knight, and D. K. Biegelsen, Phys. Rev. B **18**, 1880 (1978).
13. S. V. Kuznetsov, Fiz. Tekh. Poluprovodn. (St. Petersburg) **34**, 748 (2000) [Semiconductors **34**, 723 (2000)].
14. W. Shockley and W. T. Read, Phys. Rev. **87**, 835 (1952).
15. D. Dunstan, Philos. Mag. B **46**, 579 (1982).
16. H. Okamoto and Y. Hamakawa, Solid State Commun. **24**, 23 (1977).
17. P. E. Vanier, Sol. Cells **9**, 85 (1983).
18. A. G. Kazanskiĭ, Fiz. Tekh. Poluprovodn. (Leningrad) **24**, 1462 (1990) [Sov. Phys. Semicond. **24**, 915 (1990)].

Translated by A. Spitsyn

Semiconductors, Vol. 35, No. 10, 2001, pp. 1197–1202. Translated from Fizika i Tekhnika Poluprovodnikov, Vol. 35, No. 10, 2001, pp. 1250–1255.

AMORPHOUS, VITREOUS, AND POROUS SEMICONDUCTORS

Effect of Doping with Nitrogen on Electrical Properties and Erbium Electroluminescence of *a*-Si:H(Er) Films

O. I. Kon'kov, E. I. Terukov, and L. S. Granitsyna

Ioffe Physicotechnical Institute, Russian Academy of Sciences, Politeknicheskaya ul. 26, St. Petersburg, 194021 Russia

Submitted February 6, 2001; accepted for publication February 7, 2001

Abstract—The effect of nitrogen doping on the electrical and electroluminescence properties of amorphous hydrogenated silicon films doped with erbium has been studied. The parameters of the material, the characteristics of structures on its base, and the efficiency of Er electroluminescence (λ = 1.54 μm) are determined by the excess of the nitrogen doping level over the background value depending on the Er concentration. It is shown that effectively luminescing structures can be obtained by reducing the background concentration, with nitrogen doping remaining at the level of ~10^{21} cm^{-3}. A possible mechanism is proposed, accounting for this effect in terms of two possible forms of nitrogen incorporation into an Er-doped *a*-Si:H structure: with either an Er–N complex or a $Na_4^+ - Si_3^-$ charged defect pair formed. In this case, the electroluminescence efficiency is determined by the number of these pairs. © *2001 MAIK "Nauka/Interperiodica".*

1. INTRODUCTION

The recent intensive studies of the erbium photo- and electroluminescence in amorphous hydrogenated silicon, *a*-Si:H(Er) have been stimulated by the coincidence of the luminescence wavelength λ = 1.54 μm with the absorption minimum in optical quartz fibers, by the weak thermal quenching of the luminescence, and by the simplicity of erbium introduction by magnetron sputtering [1–5].

An analysis of the current–voltage (*I–V*) characteristics of Al/*a*-Si:H(Er)/*c*-Si electroluminescent structures [6] suggested that the Er electroluminescence efficiency can be improved by optimizing the *D*-center (silicon dangling bonds) concentration and the Fermi level position by *n*-type doping, so that the *D* centers be filled with electrons even in equilibrium conditions.

Doping is known to affect and, to a great extent, determine both the Fermi level position and the dangling bond concentration in *a*-Si:H. Phosphorus is a common dopant, although arsenic, nitrogen, oxygen, etc., are also used (see, e.g., [7]).

We chose nitrogen as a dopant for the following reasons.

(i) Nitrogen, along with oxygen and carbon, belongs to the so-called "uncontrolled" impurities; a certain amount of these impurities is always present in amorphous silicon and affects its optoelectronic properties and device characteristics [8]. Even modern vacuum pumping techniques fail to reduce the nitrogen concentration in an *a*-Si:H film to below 5×10^{15} cm^{-3}, and without taking special measures (e.g., the use of a hot-wall reactor), the nitrogen content in a film may be higher by more than two orders of magnitude [9].

(ii) Similarly to phosphorus, nitrogen behaves as a donor in amorphous silicon, increasing the dark conductivity and reducing its activation energy, although the efficiency of doping with nitrogen is substantially lower than that with phosphorus [10, 11].

In this study, we investigated the effect of nitrogen doping on the electrical properties of Er-doped amorphous hydrogenated silicon and the electroluminescence of structures based on this material.

2. EXPERIMENTAL TECHNIQUE

Amorphous hydrogenated silicon films doped with erbium and nitrogen, *a*-Si:H(Er,N), were produced by magnetron sputtering of erbium metal in a silane-containing atmosphere (magnetron-assisted silane decomposition, MASD) [12]. The technological parameters were as follows: initial gas mixture, 12.5% SiH_4 + 37.5% H_2 + 50% Ar; magnetic field, 80 mT; anode voltage, 600 V; discharge power concentration, 0.2 W/cm^2; and total pressure of the gas mixture, 4×10^{-3} Torr. Erbium metal of 99.99% purity was used for doping in the form of a foil. For nitrogen doping, the initial gas mixture was modified by adding 1% N_2 + 99% Ar mixture from a separate feed line. Films 0.3–0.6 μm thick were deposited onto *n*-type crystalline silicon substrates to fabricate Al/*a*-Si:H(Er)/*c*-Si electroluminescent structures and to study the composition; polished quartz substrates were used for conductivity and absorption coefficient measurements. Aluminum contacts were deposited by thermal evaporation. The conductivity was measured in planar configuration at a fixed voltage of 10 V. The photoconductivity was measured under illumination with a quartz lamp and passed through a system of filters to separate the λ = 630 nm

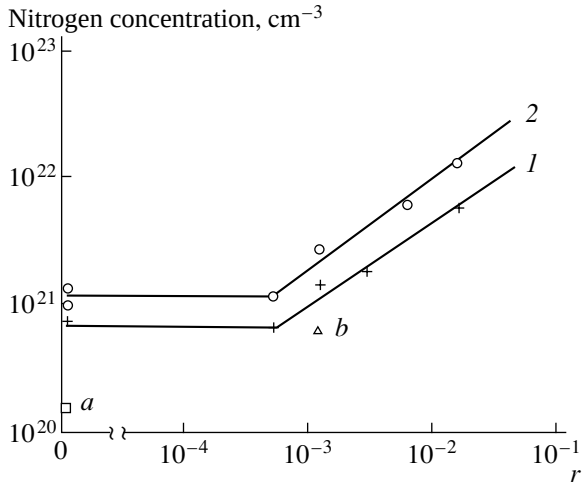

Fig. 1. Nitrogen concentration in *a*-Si:H(Er,N) films vs. the gas phase doping level, *r*, at Er concentrations: (*1*) (2–4) × 10^{20} and (*2*) (6 × 10^{20}–1.3 × 10^{21}) cm^{-3}; the same for Figs. 2 and 3. (*a*) Point for an erbium- and nitrogen-free film and (*b*) that for an erbium-free film.

wavelength, with a photon flux of 10^{15} cm^{-2} s^{-1}. The optical band gap E_g was determined by extrapolating the experimental dependence of the absorption coefficient α on the photon energy $\hbar\omega$ to the abscissa axis, according to the relation $(\alpha\hbar\omega)^{1/2} = B(\hbar\omega - E_g)$. It is necessary to note at once that E_g was about 1.7–1.8 eV and varied only slightly with nitrogen doping in the concentration range studied. The concentrations of erbium, oxygen, and nitrogen in the film were determined by Rutherford backscattering and nuclear reactions with deuterons $^{16}O^{17}O$ and $^{14}N^{15}N$. The erbium content in the films, determined from the Rutherford backscattering spectra, was (2–4) × 10^{20} and 6 × 10^{20}–1.3 × 10^{21} cm^{-3} for the two cases under study. The erbium concentration profile was nearly uniform across the film thickness within the mentioned limits. The oxygen and nitrogen contents were determined from the spectra of nuclear reaction products.

The electroluminescence (EL) was observed in the transmission mode through a crystalline silicon substrate at room temperature. A double-grating spectrometer and cooled germanium photodetector were used to analyze the EL spectra. *I–V* characteristics were recorded in pulse mode at a repetition frequency of 47 Hz. The polarity of the applied voltage, the contact to the amorphous silicon being negative, corresponded to that exciting the erbium EL.

3. EXPERIMENTAL RESULTS

Figure 1 shows the dependences of the nitrogen content in *a*-Si:H(Er,N) films, both with and without Er, on the gas-phase doping level *r*. This parameter was defined as the ratio of molar concentrations of nitrogen and silane in the employed gas mixture, $r = [N_2]/[SiH_4]$. The nitrogen concentrations are shown for a pure erbium-free film nominally undoped with nitrogen (point *a*, 1.3 × 10^{20} cm^{-3}) and an erbium-free *a*-Si:H film doped with nitrogen to $r = 1.3 \times 10^{-3}$ (point *b*, 7 × 10^{20} cm^{-3}). The following specific features can be seen from the figure.

(i) The background nitrogen concentration in the erbium-free film not doped additionally with nitrogen is rather high, ~1.3 × 10^{20} cm^{-3}, in agreement with the value known from the literature for *a*-Si:H obtained without special precautions [9].

(ii) The introduction of Er raises the background nitrogen concentration dramatically, to (7–9) × 10^{20} cm^{-3} for an Er concentration of (2–4) × 10^{20} cm^{-3} and to 9 × 10^{20}–1.4 × 10^{21} cm^{-3} for 6 × 10^{20}–1.3 × 10^{21} cm^{-3} of Er. In this case, no excess nitrogen content over the background value is observed at $r \lesssim 10^{-3}$. The sharp rise in the nitrogen content of an *a*-Si:H film upon the introduction of erbium is accompanied by a substantial increase in the oxygen content, from (1–2) × 10^{21} cm^{-3} in an Er-free film to 6 × 10^{21}–1.2 × 10^{22} cm^{-3} in a film with Er, irrespective of *r*. This behavior of oxygen (and, in our opinion, of nitrogen too) is due to the gettering action of erbium, which binds impurities. The gettering properties of erbium in crystalline and amorphous silicon were discussed in [13, 14]. Apparently, the gettering activity of erbium must be especially pronounced if erbium is deposited under constant in-leakage of air, i.e., the conditions under which our MASD technique for *a*-Si:H film fabrication operates.

(iii) At $r \gtrsim 10^{-3}$, the nitrogen content in a film is proportional to the gas phase doping level. In this case, the gas-phase doping efficiency defined as the ratio of [N]/[Si] in the film to $[N_2]/[SiH_4]$ in the gas, $A = ([N]/[Si])/([N_2]/[SiH_4])$, is ~0.06 under the assumption that the Si content in an *a*-Si:H film is 4 × 10^{22} cm^{-3}. The obtained *A* is in agreement with the value of 0.1, obtained in nitrogen doping of amorphous silicon by rf silane decomposition [10].

Figure 2 shows the dark conductivity σ_d vs. the gas phase doping level *r* for Er concentrations in a film of (2–4) × 10^{20} and 6 × 10^{20}–1.3 × 10^{21} cm^{-3}. At $r \gtrsim 10^{-3}$, the dark conductivity is nearly independent of *r*, being equal to (2–4) × 10^{-6} Ω^{-1} cm^{-1}. At higher *r*, the conductivity falls steeply to about 3 × 10^{-8} Ω^{-1} cm^{-1}.

The temperature dependence of the dark conductivity obeys the activation law for all of the samples studied. The behavior of the activation energy of dark conductivity E_a correlates with that of σ_d, so that E_a is nearly constant (0.48–0.50 eV) and independent of the Er concentration at $r \lesssim 10^{-3}$, increasing to 0.7–0.8 eV at higher *r*. Since E_g is independent of *r*, it is the E_a variation that in all probability determines the behavior of σ_d. At high nitrogen concentrations (over 10^{21} cm^{-3}), σ_d and E_a were observed to behave similarly [10, 11,

15, 16], which can be ascribed to an alternative mechanism by which nitrogen is incorporated in the *a*-Si:H structure at its higher concentrations.

The fact that σ_d and E_a are independent of the gas phase composition at $r \lesssim 10^{-3}$ is quite naturally accounted for by the constant nitrogen concentration in amorphous silicon films produced in this range of gas phase compositions, as can be seen from Fig. 1. For comparison, we measured the dark conductivity σ_d and the activation energy E_a in amorphous silicon films containing no erbium: $\sigma_d = 3 \times 10^{-10}$ Ω^{-1} cm^{-1}, E_a = 0.8 eV in an erbium-free nitrogen-undoped *a*-Si:H film and $\sigma_d = 8 \times 10^{-9}$ Ω^{-1} cm^{-1}, and E_a = 0.68 eV in an erbium-free *a*-Si:H film doped with nitrogen to $r = 1.4 \times 10^{-3}$ (the nitrogen concentration in the film being $\sim 8 \times 10^{20}$ cm^{-3}).

Figure 3 presents the photosensitivity (defined as the photoconductivity to the dark conductivity ratio) vs. *r* for the two Er concentrations studied. The behavior of the photosensitivity is quite similar to that of the dark conductivity; namely, the photosensitivity is practically independent of the gas phase doping level at $r \lesssim 10^{-3}$, and increases at higher *r*. The only remarkable feature is the minimum in the curve at $r = (7–9) \times 10^{-3}$ for the Er concentration of $(2–4) \times 10^{20}$ cm^{-3}. Photosensitivity was reported to behave similarly under *a*-Si:H doping with nitrogen [17].

Figure 4 shows *I–V* curves for several Al/*a*-Si:H(Er)/*c*-Si structures with Er concentration in the amorphous silicon layer of 6×10^{20}–1.3×10^{21} cm^{-3}, and different levels of gas-phase doping with nitrogen, *r*. The measurements were taken at room temperature. An analysis of the curves leads to the following conclusions. At $r \gtrsim 2 \times 10^{-3}$, the *I–V* curves are distinguished by small currents and slope relatively gently over the entire range of voltages under study. At lower *r*, the currents increase. In addition, portions with a steep rise in current *I* with voltage *V* are observed, which can be approximated by power-law dependences of the $I \propto V^n$ type with the exponent *n* exceeding 3. A portion with $n \approx 7$ is observed in the *I–V* curve for a structure with an amorphous silicon layer grown at $r = 1.3 \times 10^{-3}$.

According to [6], a dramatic increase in the slope of the *I–V* curve indicates the occurrence of erbium EL in Al/*a*-Si:H(Er)/*c*-Si structures. Indeed, the structure with $r = 1.3 \times 10^{-3}$, which corresponds to a nitrogen concentration in the film of $\sim 2 \times 10^{21}$ cm^{-3}, is luminescing. Its EL spectrum obtained at a voltage of up to 50 V applied across the structure and a current of ~40 mA is represented by curve *1* in Fig. 5. Both erbium ($\lambda \approx 1.54$ μm) and defect ($\lambda \approx 1.3$ μm) EL bands are observed [1, 12]. For structures with the same Er concentration (6×10^{20}–1.3×10^{21} cm^{-3}), but with other nitrogen concentrations, only a broad defect EL band was observed, without any noticeable Er luminescence. An EL spectrum of a structure with nearly the same nitrogen concentration of 1.4×10^{21} cm^{-3} in the amorphous silicon layer, but with lower Er concentration, $(2–4) \times 10^{20}$ cm^{-3}, is presented in the same figure. The Er EL from this sample is nearly twice as strong, the experimental conditions being the same.

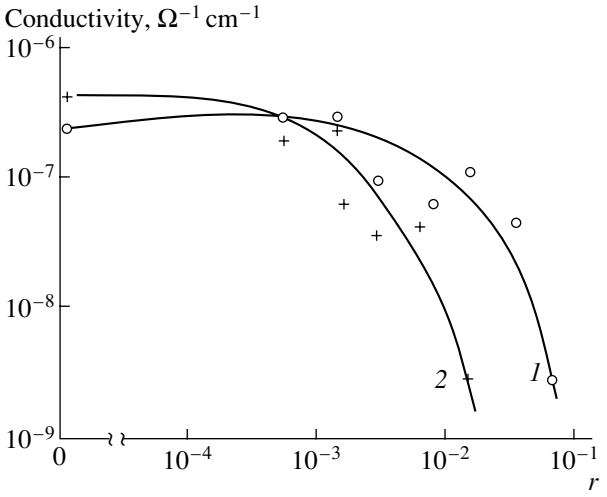

Fig. 2. Dark conductivity of *a*-Si:H(Er,N) films vs. the gas phase doping level *r* for Er concentrations of (*1*) $(2–4) \times 10^{20}$ and (*2*) $(6 \times 10^{20}–1.3 \times 10^{21})$ cm^{-3}.

4. DISCUSSION

It is necessary to note that the nitrogen concentration of $\sim 10^{21}$ cm^{-3} in *a*-Si:H(Er,N) film is a certain singular point. Independently of the method by which this concentration is created (whether it be the background level determined by gas leakage and the gettering properties of Er or that intentionally produced by introducing an additional nitrogen flow into the gas mixture), the mechanism of the incorporation of nitrogen atoms into the amorphous silicon, in all probability, changes above this point; the very structure of *a*-Si:H is transformed and a transition to amorphous silicon nitride *a*-Si:N:H occurs [10, 18, 19]. This transition is followed by a decrease in the dark conductivity, a rise in its activation energy, and a fall of the photoconductivity, which is observed in the present study (see Figs. 1–3) and has been reported elsewhere [10, 11, 15–17]. In this case, the efficiency of erbium EL falls to such an extent that we failed to observe the EL signal in any of the obtained and investigated structures with the nitrogen concentration in the *a*-Si:H(Er,N) layer exceeding 2×10^{21} cm^{-3}.

The results obtained indicate that it is impossible to make the activation energy of the dark conductivity lower than 0.48–0.5 eV, irrespective of the Er concentration. The comparison of Figs. 1 and 2 shows that this is due to the high background concentration of nitrogen in the film, $\sim 10^{21}$ cm^{-3}: the shift of the Fermi level is impossible until the concentration of intentionally

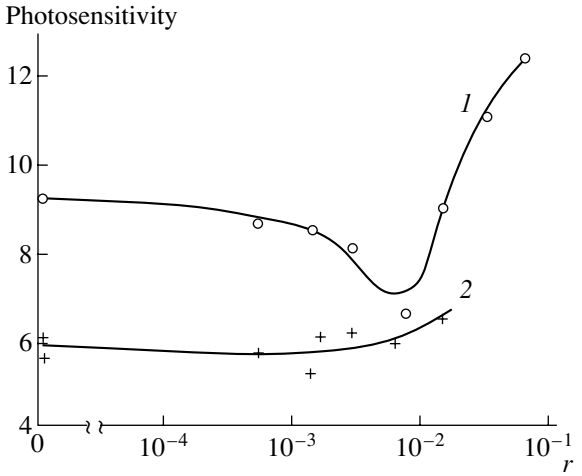

Fig. 3. Photosensitivity of *a*-Si:H(Er,N) films vs. the gas phase doping level *r* for the same Er concentrations as in Fig. 2.

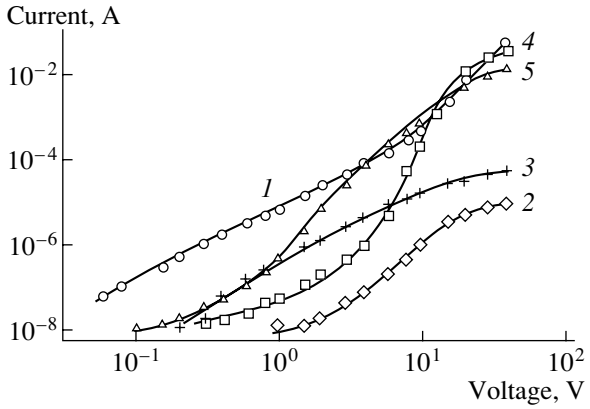

Fig. 4. *I–V* characteristics of Al/*a*-Si:H(Er,N)/*c*-Si structures at different gas phase doping levels *r*: (*1*) 0, (*2*) 5.8×10^{-3}, (*3*) 3.1×10^{-3}, (*4*) 1.3×10^{-3}, and (*5*) 6.6×10^{-4}. Erbium concentration 6×10^{20}–1.3×10^{21} cm^{-3}.

introduced nitrogen exceeds this background value. On the other hand, E_a increases at nitrogen concentrations exceeding ~10^{21} cm^{-3}, in contradiction with our requirement that the activation energy should be reduced to obtain structures with efficient EL. We may conclude that $E_a \approx 0.48$–0.5 eV is the limiting minimum value that can be obtained in doping amorphous silicon with nitrogen in the presence of erbium at nitrogen concentrations of ~10^{21} cm^{-3}. This conclusion is confirmed by published data, according to which the minimum E_a value in nitrogen-doped *a*-Si:H is 0.51 eV [11], 0.5 eV at a nitrogen concentration of ~10^{21} cm^{-3} [10], and 0.65 eV at ~2×10^{21} cm^{-3} [17].

Lowering the nitrogen concentration in the *a*-Si:H film to $\lesssim 10^{21}$ cm^{-3}, with no other impurities present (i.e., without Er in our case), leads to a dependence of the dark conductivity, activation energy, and other parameters characteristic of doping to give *n*-type, similarly to doping with phosphorus but with a lower efficiency [10, 11, 17]. The results obtained in the present study are also in agreement with this assertion. For an Er-free *a*-Si:H film with a nitrogen concentration of ~1.3×10^{20} cm^{-3}, $\sigma_d = 3 \times 10^{-10}$ Ω^{-1} cm^{-1}, $E_a = 0.8$ eV; for an erbium-free *a*-Si:H film doped with nitrogen to ~8×10^{20} cm^{-3}, $\sigma_d = 8 \times 10^{-9}$ Ω^{-1} cm^{-1}, $E_a = 0.68$ eV.

Similar effects are observed on reducing the background nitrogen concentration in erbium-doped amorphous silicon film. A maximum in the σ_d vs. *r* curve (Fig. 2, curve *1*) and a minimum in the dependence of the photosensitivity on *r* (Fig. 3, curve *1*) were observed at a background nitrogen concentration ~10^{21} cm^{-3} in *a*-Si:H films with an erbium concentration of (2–4) × 10^{20} cm^{-3} [10, 11, 15–17]. In addition, several specific features were observed in films with a nitrogen concentration of ~10^{21} cm^{-3}, at $r \approx 10^{-3}$, corresponding to the minimum activation energy $E_a = 0.48$ eV:

(i) A sharp break is observed in the *I–V* curve for a structure grown at $r = 1.3 \times 10^{-3}$ (Fig. 4, curve *4*), corresponding to "complete trap filling" in terms of the space-charge-limited currents and typical of structures exhibiting EL [6].

(ii) An erbium EL signal appears. Figure 5 shows EL spectra of structures in which amorphous silicon was grown with Er concentrations of (2–4) × 10^{20} cm^{-3} (curve *2*) and 6×10^{20}–1.3×10^{21} cm^{-3} (curve *1*) and an overall nitrogen concentration of ~2×10^{21} cm^{-3}, corresponding to excess (over the background level) nitrogen concentrations of 1.6×10^{21} and 1×10^{21} cm^{-3}, respectively. As can be seen in the figure, a higher intensity of the $\lambda = 1.54$ μm erbium EL signal corresponds to a higher excess concentration of nitrogen.

All the above results lead to the conclusion that the efficiency of erbium EL in the structures studied is directly determined by the excess of the nitrogen concentration over its background value. To account for this effect, we propose the following model.

Nitrogen is incorporated into erbium-doped amorphous hydrogenated silicon in two forms.

The first of these is the background nitrogen captured by an atom (or cluster) of erbium during film deposition owing to the gettering effect mentioned above. This nitrogen in a complex with Er creates, similarly to the erbium–oxygen complex (in all probability, Er–O–N complexes are formed), donor states in the forbidden band of amorphous silicon and, simultaneously, dangling bond states, i.e., *D* centers. *D* centers are acceptors and can exist in two charge states, D_0 and D^-. The concentrations of the donor and acceptor states are equal, as suggested in [5] and confirmed by calculations based on the experimental *I–V* characteristics in [6]. Furthermore, as follows from Fig. 1, the Er and background nitrogen concentrations correlate in the

a-Si:H(Er,N) film, being close to each other, which confirms the probability of formation of the Er–N complex.

The energy level of a charged dangling bond D^- lies at (0.9 ± 0.1) eV below the conduction band edge, the effective correlation energy being positive; the level of a neutral dangling bond D^0 lies at (1.0 ± 0.1) eV below the conduction band edge [7]. The mechanism of excitation of the erbium EL in the case of this band structure was discussed in detail in [1, 5].

The second form of nitrogen incorporation into an *a*-Si:H(Er,N) structure is related to the excess nitrogen, whose concentration is defined as the excess over the background value. This nitrogen forms no complexes with erbium, and in our opinion, its behavior is described by the model proposed for erbium-free amorphous silicon [17, 20–22], which is as follows. Nitrogen atoms in the *a*-Si:H matrix exist in the form of N_4^+ (4-coordinated positively charged N_4^+ atoms), form donor states, and contribute to the increase in the dark conductivity, Fermi level shift, etc. At the same time, the electroneutrality condition demands that N_4^+ should produce Si_3^- (a negatively charged 3-coordinated silicon atom). The bound $N_4^+ - Si_3^-$ atoms form a complex named the charged defect pair, or, in terms of [23], a close pair. A remarkable property of this mechanism of nitrogen incorporation is the existence of negatively charged silicon dangling bonds Si_3^-, whose number is strictly determined by the number of nitrogen atoms, and, in our case, by the nitrogen excess over the background level. Presumably, a charged Si_3^- defect can also be involved in the erbium EL via the mechanism proposed in [1, 5].

Our results show that the erbium EL intensity is only determined by the concentration of excess nitrogen, i.e., nitrogen incorporated into the *a*-Si:H structure by the second mechanism proposed in this study and forming no complexes with erbium, and, therefore, by the concentration of silicon dangling bonds Si_3^- in the $N_4^+ - Si_3^-$ charged defect pair configuration. It is not improbable that the excess nitrogen simply stimulates the extent of excitation of erbium atoms, as was assumed in [24].

Our assumption should be verified as follows: all other conditions being the same, lowering the background nitrogen concentration must enhance the erbium EL intensity. Since erbium behaves as a getter of nitrogen and determines its background concentration, lowering the erbium concentration is the only possible way to reduce the nitrogen background concentration with our *a*-Si:H growth facilities.

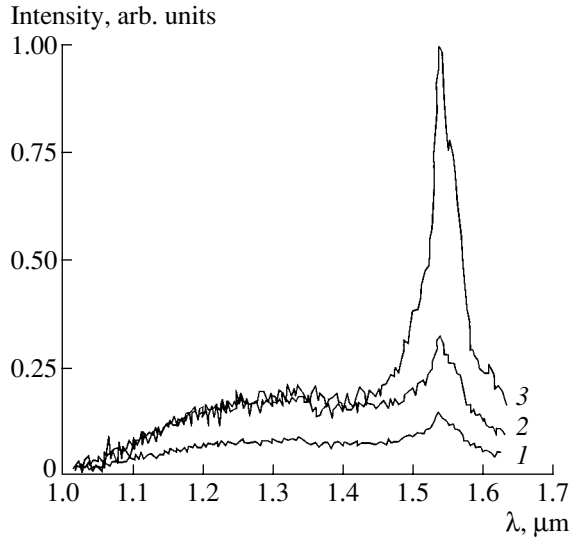

Fig. 5. EL spectra of Al/*a*-Si:H(Er,N)/*c*-Si structures with Er concentration in the amorphous silicon layer: (*1*) $(6 \times 10^{20}$–$1.3 \times 10^{21})$, (*2*) $(2$–$4) \times 10^{20}$, and (*3*) $(5 \times 10^{19}$–$1 \times 10^{20})$ cm^{-3}. Nitrogen concentration $(1$–$2) \times 10^{21}$ cm^{-3}.

Curve *3* in Fig. 5 represents an EL spectrum of an *a*-Si:H(Er,N) structure with the following impurity concentrations: [Er] = 5×10^{19}–1×10^{20} cm^{-3}, which, correspondingly, determines the background nitrogen concentration of $(1$–$6) \times 10^{20}$ cm^{-3}, and the total nitrogen concentration of $(1$–$2) \times 10^{21}$ cm^{-3}, corresponding to the optimal point mentioned above. The figure shows a clearly pronounced signal of erbium EL at λ = 1.54 μm (spectrum *3*), with the intensity exceeding that in the spectra from structures with higher nitrogen background concentrations (curves *1* and *2*). At the same time, according to [14], the erbium EL intensity falls by nearly an order of magnitude with the Er concentration decreasing from 6×10^{20} to 6×10^{19} cm^{-3}, which corresponds to the concentration variation in our experiment.

This experimental result confirms our assumptions concerning the model of nitrogen incorporation into the *a*-Si:H(Er,N) structure and the key role of nitrogen doping for increasing the intensity of erbium EL in amorphous silicon. It is likely that similar effects can be observed in doping *a*-Si:H(Er) with impurities other than nitrogen, e.g., phosphorus.

5. CONCLUSION

The effect of nitrogen doping on the electrical and electroluminescence properties of amorphous hydrogenated silicon films doped with erbium has been studied. At high concentrations of introduced nitrogen, $\gtrsim 10^{21}$ cm^{-3}, the dark conductivity decreases to $\sim 10^{-9}$ Ω^{-1} cm^{-1}, the activation energy increases to 0.7–0.8 eV, and no erbium EL is observed. At low nitrogen concentrations,

$\lesssim 10^{21}$ cm^{-3}, nitrogen behaves as a donor and the characteristics of the material can be modified, with σ_d increasing to $\sim 10^{-6}$ Ω^{-1} cm^{-1} and E_a decreasing to 0.48–0.5 eV. In this case, the parameters of the material, the characteristics of the structures on its base, and the erbium EL efficiency are determined by the excess of the nitrogen doping level over the background value depending on the Er concentration.

It is shown that efficient luminescing structures can be fabricated by lowering the background concentration of nitrogen, with its overall concentration remaining at the level of $\sim 10^{21}$ cm^{-3}. A possible mechanism of nitrogen incorporation into Er-doped *a*-Si:H is proposed, with the formation of either Er–N complexes or $N_4^+ - Si_3^-$ charged defect pairs. The EL efficiency is determined by the number of these pairs.

ACKNOWLEDGMENTS

The authors are grateful to V.M. Lebedev, M.M. Kazanin, and P.E. Pak for performing some measurements.

This study was supported in part by the Russian Foundation for Basic Research (project no. 01-02-17825).

REFERENCES

1. M. S. Bresler, O. B. Gusev, V. Kh. Kudoyarova, *et al.*, Appl. Phys. Lett. **67** (24), 3599 (1995).
2. J. H. Shin, R. Serna, G. N. van den Hoven, *et al.*, Appl. Phys. Lett. **68** (7), 997 (1996).
3. A. R. Zanatta, Z. A. Nunes, and Z. R. Tessler, Appl. Phys. Lett. **70** (4), 511 (1997).
4. M. S. Bresler, O. B. Gusev, P. E. Pak, *et al.*, Fiz. Tekh. Poluprovodn. (St. Petersburg) **33** (6), 671 (1999) [Semiconductors **33**, 622 (1999)].
5. O. B. Gusev, M. S. Bresler, B. P. Zakharchenya, *et al.*, Fiz. Tverd. Tela (St. Petersburg) **41** (2), 210 (1999) [Phys. Solid State **41**, 185 (1999)].
6. P. A. Ivanov, O. I. Kon'kov, and E. I. Terukov, Fiz. Tekh. Poluprovodn. (St. Petersburg) **34** (5), 617 (2000) [Semiconductors **34**, 598 (2000)].
7. A. Madan and M. Shaw, *The Physics and Applications of Amorphous Semiconductors* (Academic, Boston, 1988; Mir, Moscow, 1991).
8. W. Beyer and H. Overhof, in *Semiconductors and Semimetals* (Academic, Orlando, 1984), Vol. 21, Part C.
9. A. Morimoto, M. Matsumoto, M. Kumeda, and T. Shimizu, Jpn. J. Appl. Phys. **29**, L1747 (1990).
10. A. Morimoto, M. Matsumoto, M. Yoshita, *et al.*, Appl. Phys. Lett. **59** (17), 2130 (1991).
11. J.-H. Zhou, K. Yamaguchi, Y. Yamamoto, and T. Shimizu, J. Appl. Phys. **74** (8), 5086 (1993).
12. M. S. Bresler, O. B. Gusev, B. P. Zakharchenya, *et al.*, Fiz. Tverd. Tela (St. Petersburg) **38** (4), 1189 (1996) [Phys. Solid State **38**, 658 (1996)].
13. A. Polman, G. N. van den Hoven, J. S. Custer, *et al.*, J. Appl. Phys. **77** (3), 1256 (1995).
14. V. Kh. Kudoyarova, A. N. Kuznetsov, E. I. Terukov, *et al.*, Fiz. Tekh. Poluprovodn. (St. Petersburg) **32** (11), 1384 (1998) [Semiconductors **32**, 1234 (1998)].
15. T. Noguchi, S. Usui, A. Savada, *et al.*, Jpn. J. Appl. Phys. **21**, L485 (1982).
16. M. Hiramatsu, T. Kamimura, M. Nakajima, and H. Ito, Jpn. J. Appl. Phys. **30**, L7 (1991).
17. A. Matsuda, K. Itoh, K. Matsuda, *et al.*, J. Appl. Phys. **81** (10), 6729 (1997).
18. A. A. Aĭvazov, B. G. Budagyan, and O. N. Stanovov, Fiz. Tekh. Poluprovodn. (Leningrad) **25** (10), 1808 (1991) [Sov. Phys. Semicond. **25**, 1087 (1991)]; A. A. Aĭvazov, B. G. Budagyan, E. L. Prikhod'ko, *et al.*, Fiz. Tekh. Poluprovodn. (Leningrad) **25** (10), 1802 (1991) [Sov. Phys. Semicond. **25**, 1083 (1991)].
19. M. J. Williams, S. S. He, S. M. Cho, and G. Lucovsky, J. Vac. Sci. Technol. A **12** (4), 1072 (1994).
20. M. Kumeda, H. Yokomichi, and T. Shimizu, Jpn. J. Appl. Phys. **23**, L502 (1984).
21. T. Shimizu, H. Kidoh, A. Morimoto, and M. Kumeda, Jpn. J. Appl. Phys. **28**, L586 (1989).
22. M. Kumeda, M. Yoshita, A. Morimoto, and T. Shimizu, Jpn. J. Appl. Phys. **29**, L1578 (1990).
23. J. Kocka, M. Vanecek, and F. Schauer, J. Non-Cryst. Solids **97–98**, 715 (1987).
24. L. N. Tessler and A. C. Iniguez, J. Non-Cryst. Solids **266–269**, 603 (2000).

Translated by D. Mashovets

Semiconductors, Vol. 35, No. 10, 2001, pp. 1203–1207. Translated from Fizika i Tekhnika Poluprovodnikov, Vol. 35, No. 10, 2001, pp. 1256–1260.

PHYSICS OF SEMICONDUCTOR DEVICES

Difference Mode Generation in Injection Lasers

V. Ya. Aleshkin*, A. A. Afonenko, and N. B. Zvonkov*****

** Institute of Microstructure Physics, Russian Academy of Sciences, Nizhni Novgorod, 603600 Russia*

*** Belarussian State University, ul. Leningradskaya 14, Minsk, 220050 Belarus*

**** Nizhni Novgorod Research Physicotechnical Institute, Nizhni Novgorod State University, pr. Gagarina 23/5, Nizhni Novgorod, 603600 Russia*

Submitted January 17, 2001; accepted for publication February 26, 2001

Abstract—The nonlinear generation of a difference mode in an injection laser is considered. A new design based on the InGaP/GaAs/InGaAs heterostructure is suggested in order to generate two laser modes with a wavelength of about 1 μm and a difference mode at a wavelength of about 10 μm. In lasers with a 100-μm-wide waveguide, the power output of the difference mode can be as high as ~10 mW at ~10 W in the short-wavelength modes. *© 2001 MAIK "Nauka/Interperiodica".*

INTRODUCTION

The electric field of an optical wave excited inside an injection laser may be as high as 10^4–10^5 V/cm. Furthermore, in GaAs, the second-order permittivity of the lattice is also comparatively large (170×10^{-10} cm/V [1]). It is thereby evident that, in GaAs-based lasers, additional modes can be generated due to nonlinear effects. Thus, the possibility of second harmonic generation in injection lasers has been discussed for some time [2]. Recently, the second harmonic at a frequency within the visible range was generated in vertical cavity lasers [1, 2]. The possibility of difference mode generation in a laser producing two short-wavelength modes is considered in [3]. Unlike this paper, where we suggest employing the nonlinear properties of GaAs, study [3] is based on the idea of employing the electronic nonlinearity in a quantum well (QW) containing three levels. Under these conditions, however, phase matching may present difficulties and, therefore, effective generation of the difference harmonic is unlikely.

In this paper, we discuss the feasibility of a difference mode generation due to the lattice nonlinearity in QW injection lasers producing two short-wavelength modes in the near infrared (IR) range. A special construction of the dielectric-waveguide injection lasers is suggested permitting, first, the generation of two high-frequency modes and, second, the fulfillment of the phase-matching condition necessary for their effective mixing. We show that, under the phase-matching condition, mixing the two high-frequency modes with λ close to 1 μm and the power of 10 W in each mode yields the difference mode with a wavelength close to 8.66 μm and a power of about 100 mW. The devices similar to that suggested can be used, along with cascade and fountain lasers, as sources of intermediate and far IR radiation.

DIFFERENCE MODE GENERATION IN A DIELECTRIC-WAVEGUIDE LASER

Let us consider the difference mode generation in an injection laser using a laser based on $In_xGa_{1-x}As/GaAs/InGaP$ heterostructure (see, e.g., [4]) as an example. The dielectric waveguide of an injection laser is conventionally three-layered. Made of GaAs, the guiding layer includes one or several $In_xGa_{1-x}As$ QWs and has a higher refractive index than the adjacent confining layers of InGaP. In laser designs of this type, QWs are typically located near the midplane of the GaAs layer. The layer thicknesses are chosen from the condition for minimum loss of the main waveguide mode. The configuration outlined, together with the selection rules for radiative electron transitions (the dipole transitions from the conduction band into the heavy-hole band are allowed for the electric field components lying in the QW plane only), usually results in the excitation of the main *TE* mode. The phase velocity of this mode is close to the phase velocity of light in gallium arsenide (it is slightly higher than the phase velocity in GaAs but is lower than that in InGaP). This design is unsuitable for difference mode generation since phase matching is ruled out by the frequency dispersion of the refractive index in GaAs. In fact, the expression for the effective refractive index of the extraneous current wave with the difference frequency can be written as

$$n = \frac{ck_x}{\omega} = \frac{c(k_{1x} - k_{2x})}{(\omega_1 - \omega_2)} = \frac{n_i(1 - \omega_2 n_2/\omega_1 n_1)}{1 - \omega_2/\omega_1}, \quad (1)$$

1063-7826/01/3510-1203$21.00

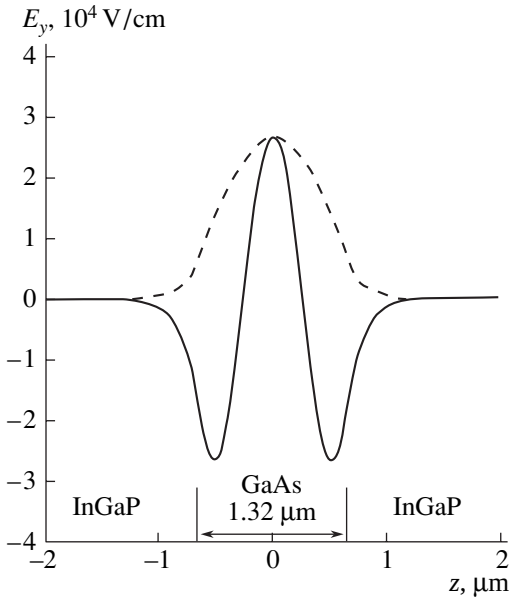

Fig. 1. The electric-field distribution in the two high-frequency modes with (solid curve) $\lambda_1 = 0.95$ μm and (dashed curve) $\lambda_2 = 1.067$ μm. The radiation power in each mode is assumed to be 10 W, the waveguide width is 100 μm.

where ω_j and k_{jx} are the frequency and the x component of the wave vector of the jth high-frequency mode, respectively; the x axis is oriented along the direction of the wave propagation; c is the speed of light; and $n_j = ck_{jx}/\omega_i$ is the effective refractive index for the jth mode. Subscripts 1 and 2 specify the quantities corresponding to the two high-frequency modes, with the higher and lower frequency, respectively. The quantities corresponding to the difference mode will be written without indices. For a rough estimation, the effective refractive index for the main waveguide mode can be assumed equal to the refractive index in GaAs. Since this index increases with frequency in the range $\lambda = 1$–30 μm [5], it follows from (1) that $n > n_1$ and phase matching is impossible. Recall that the phase-matching condition is met if n coincides with the effective refractive index for the waveguide mode with the difference frequency. The conclusion drawn from the rough estimation is entirely confirmed by the corresponding exact calculation. Thus, if we choose the wavelengths $\lambda_1 = 0.95$ μm and $\lambda_2 = 1.067$ μm; assume that the refractive indices of GaAs and InGaP are equal to $n_{\mathrm{GaAs}}(\omega_1) = 3.56$, $n_{\mathrm{GaAs}}(\omega_2) = 3.48$, $n_{\mathrm{InGaP}}(\omega_1) = 3.26$, and $n_{\mathrm{InGaP}}(\omega_2) = 3.18$; and use these parameters in a conventional calculation of the effective refractive indices of a structure containing a GaAs waveguide with thickness $d_{\mathrm{GaAs}} = 1.32$ μm, then we obtain $n_1 = 3.568$, $n_2 = 3.507$, and $n = 3.854$ ($\lambda = 8.66$ μm).

In addition, in a laser of this design, excitation of the mode at frequency ω_1 is hindered because of strong absorption in the QWs generating the mode at frequency ω_2. This difficulty can of course be overcome, for example, by a small increase in the number of QWs generating the mode at the frequency ω_1 in relation to the number of those generating the mode at the frequency ω_2. However, the difference mode generation will still be ineffective because the phase-matching condition is not met. The simulation of lasing in a double-frequency laser based on an asymmetric heterostructure suggests that, when a mode with a shorter wavelength is absorbed in the QWs that produce the mode at a longer wavelength, the lasing conditions are unstable and a self-sustained pulsation of radiation results [6]. However, when choosing the parameters of the barrier layer, which lies between the QWs and ensures their nonuniform excitation, it is possible to make pulses with both frequencies partially overlap in time. If the wavelength separation is not too large or the cavity loss is sufficiently high, then the lasing is continuous [7].

In order to meet the phase-matching condition, we suggest using the main mode of the dielectric waveguide to obtain a wave at the frequency ω_2, while radiation at the frequency ω_1 should coincide with that of a higher mode, for instance, of the second-order mode. Phase velocity of a higher mode is always higher than that of the main mode at the same frequency, and its effective refractive index is correspondingly smaller. Therefore, by using a higher waveguide mode for the wave at the frequency ω_1, one can compensate for the dispersion of the refractive index in GaAs. Moreover, in this case, we would eliminate the considerable absorption of the mode in the QWs producing the light at ω_2 by locating the wells at higher mode nodes. Figure 1 presents distribution of the electric field in the main mode (ω_2, $\lambda_2 = 1.067$ μm) and in the second-order mode (ω_1, $\lambda_1 = 0.95$ μm) in the direction perpendicular to the waveguide layers of the heterostructure (z axis). Here, the GaAs layer thickness $d_{\mathrm{GaAs}} = 1.32$ μm. With the parameters specified, $n = 3.244$.

In order to excite the second-order mode at the frequency ω_1 and the main mode at the frequency ω_2, we suggest the following. The QW generating at ω_1 should be located in the midplane of the GaAs layer, and the QW generating at ω_2, close to the ω_1-mode node (Fig. 1). This arrangement ensures the minimum loss in the second-order mode with frequency ω_1; therefore, it is this mode that will be excited. The main mode and the first-order mode with frequency ω_1 will suffer significant losses due to absorption in the QW generating at frequency ω_2. The main mode is the most favorable for lasing at frequency ω_2 since it has the minimum loss and maximum coefficient of optical confinement. Remember that the coefficient of optical confinement is defined as the power fraction of the wave propagating in a QW. Thus, for the waveguide structure described above, the ratio between coefficients of optical confinement of the main mode and the first-order mode with

the frequency ω_2 is 2.88. The relationship between the coefficients of the optical confinement of the main mode and the second-order mode is similar at 544.

Let us now calculate the power output of the difference mode. We will assume that the laser structure is grown on the (001) plane and that the cavity mirrors are formed by the (110) or $(1\bar{1}0)$ faces. For materials with the zinc blende structure, the nonzero components of the second-order nonlinear-permittivity tensor have three different indices and are equal to each other [8], $\varepsilon^{(2)}_{x'y'z} = \varepsilon^{(2)}$ (in the system of the coordinate with x', y', and z axes along the [100], [010], and [001] crystallographic directions, respectively). All the other components are zero. In this system of axes, the electric-field vectors of the high-frequency modes has nonzero x and y components: $|E_{kx'}| = |E_{jy'}| = E_j/\sqrt{2}$. Consequently, the electric-induction vector associated with the nonlinear interaction of waves is directed along the z axis:

$$D_z^{(2)} = 2\varepsilon^{(2)}(E_{1x} + E_{2x})(E_{1y} + E_{2y}) = \varepsilon^{(2)}(E_1 + E_2)^2. \quad (2)$$

The difference mode should then be *TM*-polarized. On the assumption that

$$E_j(x, z, t) = A_j(z)\{\exp(ik_j x - i\omega_j t) + \exp(-ik_j x + i\omega_j t)\}, \quad (3)$$

the y component of the magnetic field is defined by the following equation (in the coordinate system where the x axis coincides with the direction of the wave propagation):

$$\varepsilon(z, \omega)\nabla\frac{1}{\varepsilon(z, \omega)}\nabla H_y' - \frac{\varepsilon(z, \omega)}{c^2}\frac{\partial^2 H_y'}{\partial^2 t} = -2\varepsilon^{(2)}\frac{k_x\omega}{c} \quad (4)$$
$$\times A_1(z)A_2(z)\{\exp(ik_x x - i\omega t) + \exp(-ik_x x + i\omega t)\},$$

where $\varepsilon(z, \omega)$ stands for permittivity. The solution to Eq. (4) can be evidently presented as a doubled real part of the solution to the equation similar to (4) but with only one exponential term in its right-hand side: $H_y'(x, z, t) = 2\mathrm{Re}[H_y(x, z, t)]$. Assuming that $H_y(x, z, t) = H_y(z)\exp(ik_x x - i\omega t)$, we obtain the following equation for $H_y(z)$:

$$\varepsilon(z, \omega)\frac{d}{dz}\frac{1}{\varepsilon(z, \omega)}\frac{dH_y(z)}{dz} + \left[\frac{\varepsilon(z, \omega)\omega^2}{c^2} - k_x^2\right]H_y(z) = -2\varepsilon^{(2)}\frac{k_x\omega}{c}A_1(z)A_2(z). \quad (5)$$

At the boundaries between the layers with different permittivities, the values $H_y(z)$ and $(1/\varepsilon)(dH_y/dz)$ are continuous. To determine the right-hand side of Eq. (5), the values of A_j should be found from the equation

$$\frac{d^2A_j(z)}{dz^2} + \left[\frac{\varepsilon(z, \omega_j)\omega_j^2}{c^2} - k_{jx}^2\right]A_j(z) = 0. \quad (6)$$

At the boundaries between layers with different refractive indices, the continuous quantities are $A_j(z)$ and the $dA_j(z)/dz$. Boundary conditions for the waveguide modes are represented by the requirements $A_j(z) \longrightarrow 0$ at $z \longrightarrow \pm\infty$. If the z axis originates from the midplane of the GaAs layer, then the solutions to Eq. (6) for the main and the second-order modes can be written as

$$A_j(z) = \begin{cases} B_j\cos(k_{jz}z), & |z| < d_{\mathrm{GaAs}}/2, \\ B_j\cos(k_{jz}d_{\mathrm{GaAs}}/2)\exp\{\mp\chi_j(z \mp d_{\mathrm{GaAs}}/2)\}, & \\ |z| > d_{\mathrm{GaAs}}/2, & \end{cases} \quad (7)$$

where

$$k_{jz} = \sqrt{\frac{\varepsilon(0, \omega_j)\omega_j^2}{c^2} - k_{jx}^2},$$

$$\chi_j = \sqrt{k_{jx}^2 - \frac{\varepsilon(d_{\mathrm{GaAs}}/2 + 0, \omega_j)\omega_j^2}{c^2}}.$$

The values of k_{jz} are defined by the condition that the derivative of $A_j(z)$ is continuous at $z = d_{\mathrm{GaAs}}/2$. The

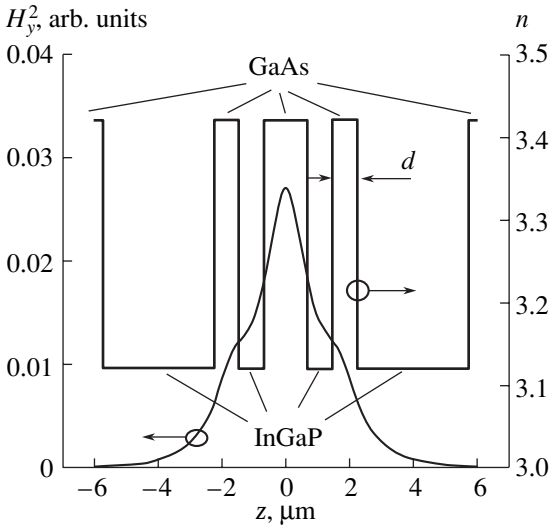

Fig. 2. Schematic representation of the laser structure and z dependence of the real part of the refractive index and the squared magnetic field in the difference mode. The lateral GaAs layers are 0.81 μm thick, which corresponds to the peak of the dashed curve in Fig. 3. The imaginary part of the refractive index $n' = 10^{-3}$.

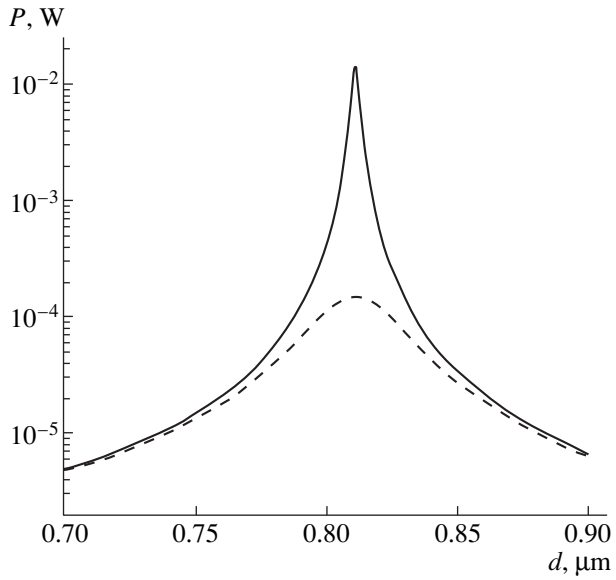

Fig. 3. The difference-mode power output versus the lateral GaAs layers thickness for two values of imaginary part of refractive index: n' = (solid curve) 10^{-4} and (dashed curve) 10^{-3}.

quantities B_j can be expressed in terms of the jth mode power P_j from the equation

$$P_j = \frac{L_y c^2 k_{jx}}{2\pi\omega_j}\int_{-\infty}^{\infty} A_j^2(z)dz, \quad (8)$$

where L_y is the y size of the waveguide.

To satisfy the phase-matching condition, we suggest the design illustrated in Fig. 2. The additional (lateral) GaAs layers are required to better confine the difference mode in space. The layer thickness d can be considered as an adjustable parameter to meet the phase-matching condition. In what follows, we will assume that the two lateral layers of GaAs are equal in thickness.

To estimate the difference-mode power output, it now remains to solve Eq. (5). The refractive index for the difference harmonic in InGaP layers will be assumed to be smaller than that in GaAs by 0.3, as it was for the short-wavelength modes. Upon numerically integrating Eq. (5), we obtain the lasing power of the difference harmonic versus the lateral GaAs layer thicknesses for two concentrations of carriers (Fig. 3). We also used the expression

$$P = -\frac{cL_y}{2\pi}\int_{-\infty}^{\infty} \mathrm{Re}(H_y E_z^*)dz, \quad (9)$$

where the electric field component E_z is to be determined from the expression

$$E_z = -\frac{1}{\varepsilon(z,\omega)}\left[\frac{ck_x}{\omega}H_y(z) + 2\varepsilon^{(2)}A_1(z)A_2(z)\right], \quad (10)$$

which follows from the Maxwell equation containing the magnetic field curl. The lasing power in both short-wavelength modes was assumed to be equal to 10 W, L_y = 100 μm. The solid curve corresponds to the carrier concentration of 10^{17} cm^{-3}; here, the imaginary part of the refractive index at frequency ω is $n' = 10^{-4}$ [5]. The real part of the refractive index for the difference mode was taken to be equal to 3.42 in GaAs [5] and 3.12 in InGaP. The dashed curve is plotted for the carrier concentration of 10^{18} cm^{-3} and the imaginary part of the refractive index of 10^{-3}. It can clearly be seen from Fig. 3 that the dependence of the harmonic power on the lateral layer thickness peaks at d = 0.81 μm. This peak corresponds to the phase-matching condition. With an increase in absorption (the imaginary part of the refractive index), this peak broadens and decreases in height. With the parameters specified as above, the maximum attainable power of the difference mode is as high as ~10 mW for $n' = 10^{-4}$ and ~100 μW for $n' = 10^{-3}$. To ensure a sufficiently high Q factor of the difference mode, the external InGaP layers should be no less than 5 and 3.5 μm thick in the former and the latter case, respectively.

Figure 2 shows z dependences of the H_y^2 and the real part of refractive index for the difference mode. As can be seen, the difference mode being excited is the main one. Note that, if the modes employed for the excitation of the difference mode were the main mode with the frequency ω_2 and the first-order mode with the frequency ω_1, the extraneous current at the difference frequency would be an antisymmetric function of z. In that event, only an odd-order difference mode could be excited.

In conclusion, the design of injection laser suggested allows one to obtain the power output of ~10 mW in the wavelength region of λ = 10 μm. It is interesting to note that the threshold current can be lowered and the efficiency increased by applying a multilayer dielectric coating to the end mirrors to enhance the reflection of the short-wavelength modes.

ACKNOWLEDGMENTS

We are grateful to A.A. Andronov and B.N. Zvonkov for their fruitful participation in discussions and to A. Belyanin and V. Kocharovskiĭ for giving us the opportunity to read paper [3] prior to its publication.

This study was supported in part by the Russian–Belarussian Foundations for Basic Research (project no. 00-02-81022); Interdisciplinary Scientific and

Technological Program “Physics of Solid-State Nanostructures” (project no. 99-1128); State Scientific and Technological Program “Fundamental Spectroscopy” (project no. 8/02.08); the Program for the Russian Federation Leading Schools Support (project no. 00-15-96618); and the Russian–Ukrainian Program “Nanophysics and Nanoelectronics” (project no. 2000-3F).

REFERENCES

1. Y. Kaneko, S. Nakagava, Y. Ichimura, *et al.*, J. Appl. Phys. **87**, 1597 (2000).
2. D. Vakhshoori, R. J. Fischer, N. Hong, *et al.*, Appl. Phys. Lett. **59**, 896 (1991).
3. A. A. Belyanin, F. Capasso, V. V. Kocharovsky, *et al.*, Phys. Rev. A **63**, 53803 (2001).
4. N. B. Zvonkov, S. A. Akhlestina, A. V. Ershov, *et al.*, Kvantovaya Élektron. (Moscow) **26**, 217 (1999).
5. *Handbook of Optical Constants of Solids*, Ed. by E. D. Palik (Academic, Orlando, 1985).
6. A. A. Afonenko, V. K. Kononenko, and I. S. Manak, Pis’ma Zh. Tekh. Fiz. **20** (2), 57 (1994) [Tech. Phys. Lett. **20**, 72 (1994)].
7. S. Ikeda and A. Shimizu, Appl. Phys. Lett. **59**, 504 (1991).
8. *Handbook of Physical Quantities*, Ed. by I. S. Grigoriev and E. Z. Meilikhov (Énergoatomizdat, Moscow, 1991; CRC Press, Boca Raton, 1997).

Translated by A. Sidorova-Biryukova

Semiconductors, Vol. 35, No. 10, 2001, pp. 1208–1212. Translated from Fizika i Tekhnika Poluprovodnikov, Vol. 35, No. 10, 2001, pp. 1261–1265.

PHYSICS OF SEMICONDUCTOR DEVICES

High Power InGaAsSb(Gd)/InAsSbP Double Heterostructure Lasers (λ = 3.3 μm)

M. Aydaraliev, N. V. Zotova, S. A. Karandashev, B. A. Matveev*, M. A. Remennyi, N. M. Stus', and G. N. Talalakin

Ioffe Physicotechnical Institute, Russian Academy of Sciences, Politekhnicheskaya ul. 26, St. Petersburg, 194021 Russia

**e-mail: bmat@iropt3.ioffe.rssi.ru*

Submitted February 28, 2001; accepted for publication March 5, 2001

Abstract—InGaAsSb(Gd)/InAsSbP double heterostructure lasers (λ = 3.3 μm, T = 77 K) yield a multimode power of 1.56 W in pulsed operation (pulse width 30 μs, repetition frequency f = 500 Hz) and 160 mW in the continuous-wave (CW) case. In the single-mode CW operation, the power is 18.7 mW. It is shown that heating of the active region is responsible for sublinear light–current characteristics in "long-cavity" lasers, whereas in "short-cavity" (L = 140–300 μm) lasers the power is mainly limited by internal losses. © *2001 MAIK "Nauka/Interperiodica".*

1. INTRODUCTION

The intensity of absorption bands of formaldehyde (H_2CO), methane (CH_4), and other hydrocarbons in the spectral range λ = 3–4 μm exceeds the intensity of their harmonics in the near-IR range, commonly used to detect gases, by 1–2 orders of magnitude. Therefore, intensive research has been aimed to create high-power diode lasers for the mid-IR range, based both on quantum well (QW) and quantum-cascade structures and on conventional double heterostructures (DHS) (see, e.g., a review of LPE-grown InAsSb/InAsSbP DHS lasers [1]).

Continuous-wave (CW) emission power of up to 215 mW per face has been obtained from InAsSb/InAlAsSb strained-QW lasers (emission wavelength λ = 3.4 μm, operation temperature T = 77 K) [2]. InAs/GaInSb/InAs/AlGaAsSb QW lasers (λ = 3.03 μm, T = 78 K, operation current I = 4 A) yield a CW power of 140 mW, limited by active region heating [3]. Among the quantum-cascade lasers, the shortest wavelength (λ = 3.49 μm, T = 10 K) has been obtained with InGaAs/AlInAs layers [4]. Lasers with a cavity width of 10–14 μm operate in pulse mode (pulse width τ = 50 ns, repetition frequency f = 4.5 kHz) at temperatures of up to 280 K, but the maximum working temperature in the CW mode was 50 K, with emission power no higher than 20 mW (I = 1.7 A). The highest output power and differential quantum efficiency were obtained in [5, 6]. The maximum power of 0.85 W in pulse mode (τ = 4–7 μs, f = 200 Hz) was achieved for a single InAsSbP/InAsSb/InAs DHS laser (λ = 3.2 μm, T = 77 K) [5]. In InAsSb/InAs strained-QW lasers (λ = 3.65 μm, T = 90 K), the output power is 1 W, and the differential quantum efficiency, 70% [6].

The laser structures listed above were grown on (100) substrates. It is known, however, that the growth rate of III–V materials is the lowest for the [111] direction [7]; therefore, high-quality heterojunctions and better morphology of the epilayer surface can be expected for epilayers grown on (111) substrates.

The properties of InGaAsSb/InAsSbP DHS diode lasers on (111)A n-InAs substrates (λ = 3.0–3.6 μm, T = 77 K) were analyzed in our previous studies [8–11]. As shown in [8], either type-I or type-II heterojunctions can be obtained, depending on the composition of the active region and the confining layers. The heterojunction type defines the specific features of radiative recombination, temperature dependences of energy, and the emission polarization. The fact that the band gap and the spin–orbit splitting energy are close in these materials results in the principal mechanism of internal losses being intraband absorption by holes with their transition into the spin–orbit-split band [9], which leads, among other things, to current tuning of the lasing mode to the short-wavelength range [10]. As shown in [11], the optimal doping of the growth solution with Gd, reducing the concentrations of defects and free carriers in the crystallizing solid phase, allows the fabrication of single-mode λ = 3.2–3.3 μm lasers with threshold currents I_{th} < 10 mA. Single-mode lasing was obtained in short-cavity lasers (L < 150 μm) for currents $I \le 6I_{th}$, with a side-mode suppression ratio of up

1063-7826/01/3510-1208$21.00

to ~30 dB, a rate of current tuning of the wave number of 210 cm^{-1}/A, and single-mode tuning range wider than 10 cm^{-1}.

This study is devoted to InGaAsSb(Gd)/InAsSbP DHS high-power lasers. We studied the emission power in wide-contact (w = 200 μm) lasers (multimode operation) and the single-mode emission power in mesa-stripe lasers with the stripe width w = 20 μm.

2. OBJECTS OF STUDY AND EXPERIMENTAL METHODS

LPE-grown DHS consisted of an undoped (111)A n-InAs substrate with electron concentration n = (1–2) × 10^{16} cm^{-3} and three epilayers: (i) a near-substrate wide-gap n-$InAs_{1-x-y}Sb_xP_y$ ($0.05 \le x \le 0.09$, $0.09 \le y \le 0.18$) confinement layer, (ii) a n-$In_{1-v}Ga_vAs_{1-w}Sb_w$ ($v \le 0.07$, $w \le 0.07$) laser active region, and (iii) a p(Zn)-$InAs_{1-x-y}Sb_xP_y$ ($0.05 \le x \le 0.09$, $0.09 \le y \le 0.18$) wide-gap emitter. A gadolinium-containing melt with Gd content X^1_{Cd} = 0.004–0.005 at. % was used to grow the active region. According to [12], this gives the lowest content of residual impurities and defects in the $In_{1-v}Ga_vAs_{1-w}Sb_w$ solid solution and the highest free carrier mobility. The wide-gap layers were 3–5 μm thick, the thickness of the active layer was 1 μm, and the substrate was thinned to 100 μm from the initial 350 μm. "Epi-side-down" stripe lasers with the stripe width w = 200 μm and mesa-stripe lasers with w = 20 μm and cavity length L = 100–700 μm were studied. The structures were cleaved into chips which were soldered onto a copper heat sink with the p-layer facing down.

The electroluminescence and the emission power were measured in CW and pulse (τ = 30 μs, f = 500 Hz) modes at T = 77 K. The power was measured with a Nova Laser Power/Energy Monitor equipped with an Ophir Optronics 2A-SH bolometric sensor, with account taken of the pulse on–off ratio and the fraction of radiation collected by the mirror.

3. EXPERIMENTAL RESULTS AND DISCUSSION

3.1. Threshold Current Density, Differential Quantum Efficiency

The threshold current density and the differential quantum efficiency of stripe lasers with w = 200 μm and mesa-stripe devices with w = 20 μm are virtually the same. This indicates that the behavior of a laser is mainly determined by the bulk of its active region. Figure 1a shows the inverse differential quantum efficiency η_D as a function of the cavity length L. The η_D^{-1} values are 50 and 70% for lasers with cavity lengths of 640 and 140 μm, respectively. An approximation of the dependence presented in Fig. 1a by the function

$$\eta_D^{-1} = \eta_i^{-1}(1 + \alpha_i/L^{-1}\ln R^{-1}),$$

where η_i is the internal quantum efficiency, α_i is the internal loss, $L^{-1}\ln R^{-1}$ is the reflection loss, and R = 0.31, yields an internal quantum efficiency of η_i = 74%, which virtually coincides with the internal quantum efficiency limited by Auger recombination [13]. The internal loss α_i = 5 cm^{-1} is typical of the best lasers operating in this spectral range.

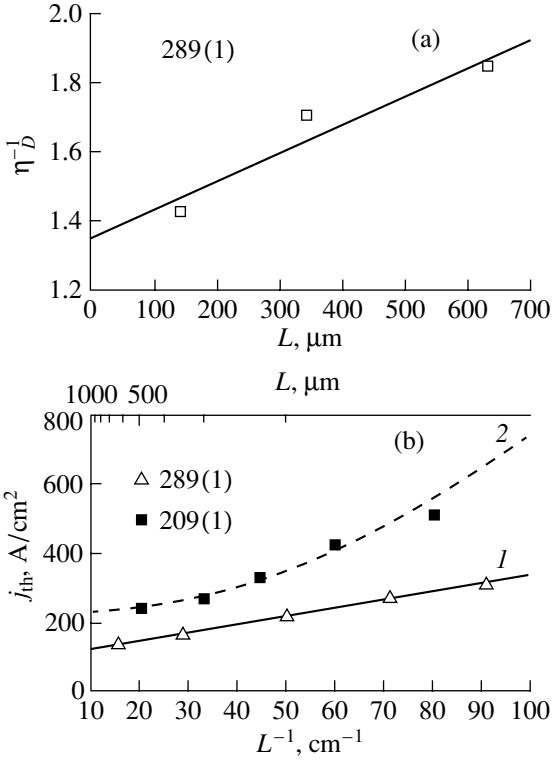

Fig. 1. (a) Inverse efficiency η_D^{-1} vs. cavity length L; (b) threshold current density j_{th} vs. inverse cavity length L^{-1}: (*1*) this study and (*2*) [9]. T = 77K.

Curve *1* in Figure 1b shows the threshold current density as a function of the inverse cavity length; curve *2* represents our previous data [9]. The minimum threshold current density is j_{th} = 130 A/cm^2 (L = 630 μm), which is half the values reported in [9]; we ascribe this circumstance to the optimal doping of the active region with gadolinium. A remarkable feature is that the dependence at high current densities (curve *2*) is superlinear. We believe that this fact reflects the situation when the increase in the threshold concentration is due not only to higher emission losses but also to increased internal losses for intraband absorption. Hence, it follows that the intraband absorption is stron-

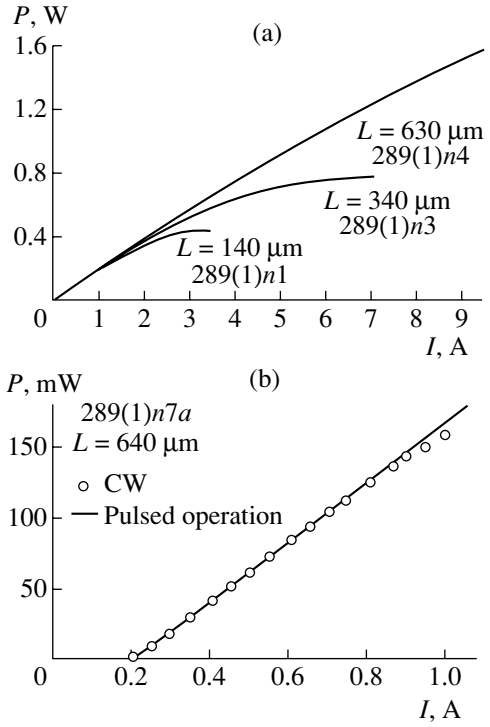

Fig. 2. Light–current characteristics of wide-contact lasers, w = 200 μm in pulsed (τ = 30 μs, f = 500 Hz) (a, b) and CW operation (b). T = 77 K.

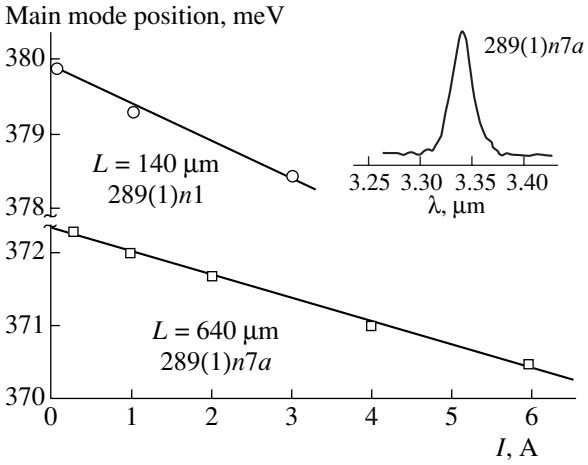

Fig. 3. Spectral peak position for a wide-contact laser with w = 200 μm and cavity lengths L = 140 and 640 μm vs. current I. Insert: emission spectrum at I = 6 A.

ger in lasers with "high" threshold currents (Fig. 1b, curve *2*), compared with "low-threshold" lasers (Fig. 1b, curve *1*).

3.2. Multimode Emission Power

Figure 2a shows the light–current dependences for lasers operating in pulse mode, with the stripe width w = 200 μm and cavity lengths of 140, 340, and 630 μm. The maximum emission power P from two faces is 1.6 W at a current of I = 9.5 A. A CW light–power characteristic of a laser with L = 630 μm is presented in Fig. 2b. The emission power from two faces is 160 mW at I = 1 A. At currents exceeding (4–5)I_{th}, the observed CW characteristic slightly deviates from the "pulse" curve, indicating device heating by dc current. Therefore, this laser was not tested at higher currents.

The emission spectra were of single-mode type near the lasing threshold and of multimode type (with the envelope half-width $\Delta\lambda \approx 0.02$ μm) at currents exceeding the threshold value by 20–50 mA (see the insert of Fig. 3). At T = 77 K, the envelopes of the spectra of lasers with L = 140 and 640 μm shifted to longer wavelengths ($dh\nu/dI$ = 0.5 and 0.3 meV/A) with increasing current, which allowed the estimation of the overheating of the laser active regions to be ΔT = 15 and 30 K for I = 3 and 10 A, respectively (see Fig. 3).

An analysis of the light–current characteristic

$$P(I) = \eta_D(T)[I - I_{th}(T)],$$

with account taken of the temperature dependences of the differential efficiency η_D and threshold current and the above estimates of the active region overheating, demonstrated that the sublinearity of the light–current curve in the "long" (L = 640 μm) laser is virtually completely determined by the active region overheating, i.e., by a decrease in the internal quantum efficiency and an increase in the threshold current. We attribute this circumstance to an increase in the Auger recombination rate with temperature. In the "short" (L = 140 μm) laser, the contribution of the active region overheating is not the key factor, since it accounts for only 50% of the experimentally observed sublinearity. In short-cavity lasers, the increase in the threshold concentration because of the enhanced output loss gives rise to a nonthermal mechanism of internal losses—intraband absorption in the valence band. As shown in our previous studies [9], this effect reduces the differential quantum efficiency and results in this parameter becoming not only temperature- but also current-dependent.

3.3. Single-Mode Emission Power

Single-mode lasing is easily achieved in short-cavity lasers owing to the large intermode distance. Therefore, we restricted our study to a laser with L = 140 μm and w = 20 μm, in which single- and quasi-single-mode lasing was obtained at currents $I = 17I_{th}$(77 K) and $I = 6I_{th}$ (100 K). Figure 4 shows the CW emission power and the "spectral purity," characterized by the dominant mode power to total emission power ratio, as functions of current at T = 77 and 100 K. At these temperatures, the maximum emission power was as high as 19.7 and

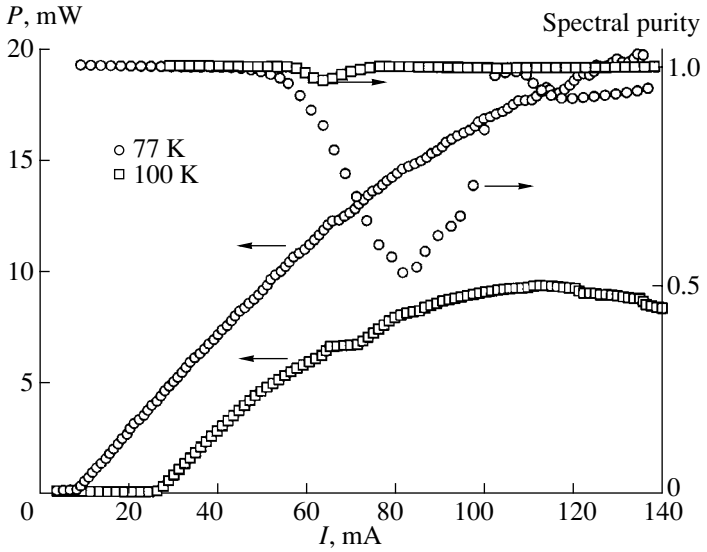

Fig. 4. Light–current characteristic and dependence of the spectral purity on laser current in CW operation. $w = 20$ μm, $L = 140$ μm.

9.3 mW, with a spectral purity of 0.95 and 1, respectively. The spectral modes shifted with current to shorter wavelengths, as described in [11].

The heating of the active region shifts the gain contour to longer wavelengths. On the other hand, the proximity of the band gap and spin–orbit splitting energies leads to enhanced internal loss above the generation threshold [9], with the corresponding upwards shift of the Fermi level and a shift of the gain contour to shorter wavelengths. The shift to shorter wavelengths, constituting less than ~10 cm^{-1} (1.2 meV) [9], is usually smaller than the shift to longer wavelengths, induced by heating. Therefore, with increasing current, generation hopping occurs over the intermode distance to a longer-wavelength mode. This process affects the dependence of the spectral purity on the current at $T = 77$ K: the spectrum is of the single-mode type with spectral purity equal to unity at $I = (1–6)I_{th}$, consists of two main modes at $I = (6–13)I_{th}$, and is dominated by the long-wavelength mode at $I = (13–17)I_{th}$ with the spectral purity again approaching unity.

The light–current characteristic $P(I)$ is similar to that of a wide-contact laser with the same cavity length: the curve levels off at $I \approx 20I_{th}$. In contrast to the wide-contact laser, the lasers with $w = 20$ μm show better stability in the CW mode, owing to the lower operation current and the correspondingly better heat removal conditions.

4. CONCLUSION

The use of InGaAsSb/InAsSbP DHS grown by LPE on (111) *n*-InAs substrates and the Gd doping of the active region allowed the fabrication of lasers with a multimode emission power of 1.6 W in pulse operation ($I = 9.5$ A, $\tau = 30$ μs, $f = 500$ Hz) and 160 mW in the CW case ($I = 1$ A, 77 K). The maximum power of single-mode lasing is as high as 18.7 and 9.3 mW (at 77 and 100 K); to the authors' knowledge, these are record values for lasers operating in the $\lambda = 3$ μm spectral range. The internal quantum efficiency is 74%, which coincides with the theoretical value limited by Auger recombination. The light–current characteristics of long-cavity lasers are sublinear owing to the active region heating, whereas in short-cavity lasers (L = 140–300 μm) the power is mainly limited by internal losses.

ACKNOWLEDGMENTS

This study was supported by the Ministry of Science of the Russian Federation, the Intercollegiate Scientific and Technological Program "Optics: Laser Physics" (project no. 4.14) and by ISTC (project no. 2044-R).

REFERENCES

1. T. N. Danilova, A. N. Imenkov, V. V. Sherstnev, and Yu. P. Yakovlev, Fiz. Tekh. Poluprovodn. (St. Petersburg) **34** (11), 1396 (2000) [Semiconductors **34**, 1343 (2000)].
2. H. K. Choi, G. W. Turner, and M. J. Manfra, Electron. Lett. **32** (14), 1296 (1996).
3. W. W. Bewley, H. Lee, I. Vurgaftman, *et al.*, Appl. Phys. Lett. **76** (3), 256 (2000).
4. J. Faist, F. Capasso, D. L. Sivco, *et al.*, Appl. Phys. Lett. **72** (6), 680 (1998).
5. A. Rybaltowski, Y. Xiao, D. Wu, *et al.*, Appl. Phys. Lett. **71** (17), 2430 (1997).
6. B. Lane, D. Wu, A. Rybaltowski, *et al.*, Appl. Phys. Lett. **70** (4), 443 (1997).

7. K. Oe and K. Sugiyama, Appl. Phys. Lett. **33**, 449 (1978).
8. M. Aydaraliev, N. V. Zotova, S. A. Karandashev, *et al.*, Fiz. Tekh. Poluprovodn. (St. Petersburg) **33** (2), 233 (1999) [Semiconductors **33**, 200 (1999)].
9. M. Aydaraliev, N. V. Zotova, S. A. Karandashev, *et al.*, Fiz. Tekh. Poluprovodn. (St. Petersburg) **33** (6), 759 (1999) [Semiconductors **33**, 700 (1999)].
10. M. Aydaraliev, N. V. Zotova, S. A. Karandashev, *et al.*, Fiz. Tekh. Poluprovodn. (St. Petersburg) **34** (4), 504 (2000) [Semiconductors **34**, 488 (2000)].
11. M. Aydaraliev, T. Beyer, N. V. Zotova, *et al.*, Fiz. Tekh. Poluprovodn. (St. Petersburg) **34** (7), 881 (2000) [Semiconductors **34**, 848 (2000)].
12. N. V. Zotova, S. A. Karandashev, B. A. Matveev, *et al.*, Fiz. Tekh. Poluprovodn. (St. Petersburg) **33** (8), 1010 (1999) [Semiconductors **33**, 920 (1999)].
13. M. Aydaraliev, Author's Abstract of Candidate's Dissertation (Fiz.-Tekh. Inst. im. A. F. Ioffe Ross. Akad. Nauk, Leningrad, 1991).

Translated by D. Mashovets

Semiconductors, Vol. 35, No. 10, 2001, pp. 1213–1221. Translated from Fizika i Tekhnika Poluprovodnikov, Vol. 35, No. 10, 2001, pp. 1266–1274.

PHYSICS OF SEMICONDUCTOR DEVICES

Fabry–Perot *a*-Si:H/*a*-SiO_x:H Microcavities with an Erbium-Doped *a*-Si:H Active Layer

V. G. Golubev[1], A. A. Dukin[1]*, A. V. Medvedev[1], A. B. Pevtsov[1], A. V. Sel'kin[1,2], and N. A. Feoktistov[1]

[1] *Ioffe Physicotechnical Institute, Russian Academy of Sciences, Politekhnicheskaya ul. 26, St. Petersburg, 194021 Russia*

** e-mail: dookin@gvg.ioffe.rssi.ru*

[2] *Centro de Investigaciones en Dispositivos Semiconductores, Instituto de Ciencias, BUAP, Puebla 72570, Pue. Mexico*

Submitted March 19, 2001; accepted for publication April 2, 2001

Abstract—Fabry–Perot microcavities tuned to a wavelength of 1.5 μm have been fabricated by means of plasma-enhanced chemical-vapor deposition on the basis of *a*-Si:H and *a*-SiO_x:H. Distributed Bragg reflectors (DBRs) and the active layer were grown in a single technological cycle. The half-wave active layer was doped with erbium in the course of growth from a metal-organic compound. The high optical contrast enabled a high microcavity quality factor (Q = 355) with only three DBR periods. The intensity of erbium photoluminescence (PL) from the microcavity is two orders of magnitude higher than that of erbium emission from an identical *a*-Si:H layer without DBR. Transmission, reflection, and PL spectra are analyzed. It is found that the spectral shape of the line of erbium PL (transition $^4I_{13/2} \longrightarrow {}^4I_{15/2}$) from the microcavity virtually coincides with the shape of the resonance peak of its transmission spectrum. Theoretical calculations have been performed providing a comprehensive description of the observed experimental spectra. © *2001 MAIK "Nauka/Interperiodica"*.

1. INTRODUCTION

Hydrogenated amorphous silicon (*a*-Si:H) is widely used in semiconductor electronics [1]. There exists a low-cost well-developed technology of fabrication of multilayer thin-film structures of intrinsic and doped *a*-Si:H. The possibility has been demonstrated of creating light-emitting diodes (LEDs) that are based on *a*-Si:H and other materials of this kind (*a*-Si:C:H, *a*-Si:N:H, *a*-Si:O:H, and *a*-C:H) and operate in the visible range [2, 3]. However, the brightness achieved in these devices is insufficient for their wide practical application. Of interest, therefore, is the use of *a*-Si:H in light-emitting devices with a Fabry–Perot microcavity, which could substantially raise the emission intensity [4]. In addition, the properties of *a*-Si:H make this material promising for creating high-efficiency microcavities (MC) for the infrared region of the spectrum. The optical contrast (ratio of refractive indices) of *a*-Si:H and hydrogenated amorphous silicon saturated with oxygen (*a*-SiO_x:H) greatly exceeds that in III–V semiconductors widely used for creating microcavity structures [4]. This allows the fabrication of mirrors (distributed Bragg reflectors, DBR) having a high reflectance for a much smaller number of layers in the periodic structure of each mirror. A DBR based on *a*-Si:H and *a*-SiO_x:H comprises several pairs of layers (*a*-Si:H/*a*-SiO_x:H), each having an optical thickness equal to a quarter of the resonance wavelength. These mirrors have a much wider stop band (photonic gap) than similar III–V mirrors. The high reflectance makes readily achievable the fabrication of MCs with a high quality factor, exhibiting a substantial gain of the spontaneous emission and narrow transmission band at the resonance frequency. The high difference of the refractive indices opens up the possibility of tuning the resonance frequency of an *a*-Si:H/*a*-SiO_x:H MC over a wide range (over the entire photonic gap) by only varying the active layer thickness, with the DBR layer thicknesses remaining unchanged.

The optical properties of thin-film Si/SiO_2 MCs with an active layer of SiO_2 doped with Er by ion implantation were studied in [5–7]. The trivalent erbium ion Er^{3+} was chosen as an emitting center, since the radiative optical transition in the inner 4*f* shell ($^4I_{13/2} \longrightarrow {}^4I_{15/2}$) gives rise to a narrow luminescence band at $\lambda \approx 1.53$ μm, corresponding to minimum attenuation and dispersion in quartz light guides. The strong interaction of Er^{3+} ions with the resonance mode in a Si/SiO_2 microcavity with an Er_2O_3 active layer was considered in [8, 9]. In this study, the active layer material is *a*-Si:H. The optical properties of the *a*-Si:H/*a*-SiO_x:H MC enable a high gain of spontaneous emission. In Er-doped *a*-Si:H, the intensity of room temperature photoluminescence (PL) at $\lambda = 1.53$ μm is higher, the temperature quenching of PL is weaker, and the radiative lifetime of excited Er^{3+} ions is shorter than that in crystalline silicon [10, 11]. Room-temperature electroluminescence has also been observed in barrier (Schottky) structures based on Er-doped *a*-Si:H [12]. The technology of *a*-Si:H layer deposition also enables the growth of active *p–n* and *p–i–n* structures necessary

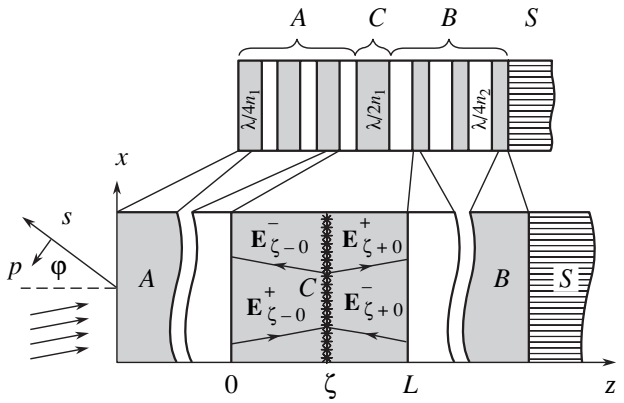

Fig. 1. Schematic diagram of an *a*-Si:H/*a*-SiO_x:H microcavity comprising two quarter-wave DBRs (each with 3 periods)—the (*A*) left- and (*B*) right-hand, and (*C*) a half-wave active layer in between; *S* is the substrate. An infinitely thin layer of singular currents is shown at $z = \zeta$ ($0 < z < L$), emitting two plane waves with amplitudes $\mathbf{E}^{-}_{\zeta-0}$ and $\mathbf{E}^{+}_{\zeta+0}$, which have, on being reflected from the DBR, the amplitudes $\mathbf{E}^{+}_{\zeta-0}$ and $\mathbf{E}^{-}_{\zeta+0}$. *p* and *s* denote the polarization of light; φ is the angle of light emergence.

for creating LEDs. The compatibility of the technology of deposition of thin *a*-Si:H layers with the conventional silicon integrated-circuit technology is one more reason for studying the possibility of using *a*-Si:H in light-emitting microcavity structures. The preliminary results of the present study were reported in [13].

2. EXPERIMENT

Several MCs with different numbers of layers in the DBR and active layer thicknesses were fabricated. The DBR and the active layer were grown in an automated installation for plasma-enhanced chemical-vapor deposition (PECVD) in a single technological cycle without exposure to air between successive stages of growth of separate layers constituting a structure [3, 14]. *a*-Si:H layers were deposited from a 10% mixture of silane with argon. To deposit *a*-SiO_x:H, oxygen was added to the gas mixture (up to 10%). Other parameters of the PECVD process were as follows: working pressure 0.1–0.2 Torr, rf power 0.03–0.1 W/cm^2, substrate temperature 200°C, gas mixture flow rate 5–10 sccm. The average rate of MC-layer growth was no higher than 0.2 nm/s. The thickness, optical properties, and growth rate of a film were directly monitored by means of *in situ* interferometry. In the course of growth, the *a*-Si:H active layer was doped with Er from a specially synthesized fluorine-containing metal-organic complex $Er(HFA)_3 \cdot DME$ (HFA = $CF_3C(O)CHC(O)CF_3$, DME = $CH_3OCH_2CH_2OCH_3$) [15, 16]. This volatile and rather thermally stable compound has a low sublimation temperature and shows a noticeable vapor pressure at 90–100°C in a forevacuum. Its saturated vapor pressure is 124 Pa at 127°C. This allows this compound to be used for doping with Er in standard low-temperature (<300°C) PECVD. A powdered organometallic compound was placed in a stainless steel container near the glow discharge region. The rate of sublimation could be varied by heating the powder in the temperature range 20–100°C. This doping method allows control over the Er concentration profile across the active layer thickness. In the present study, the Er distribution across the *a*-Si:H active layer thickness was uniform. The Er concentration was found by secondary-ion mass spectrometry to be 10^{19} cm^{-3}.

The microcavities were fabricated in such a way that the resonance wavelength coincided with the emission wavelength $\lambda = 1.53$ μm corresponding to the transition $^4I_{13/2} \longrightarrow {}^4I_{15/2}$ in Er^{3+} ions in *a*-Si:H. All MCs were symmetric; i.e., the number of layers in the left- and right-hand DBRs were the same. The structure of an MC is shown schematically in Fig. 1. The left- (*A*) and right-hand (*B*) reflectors each comprise three pairs (periods) of quarter-wave *a*-Si:H and *a*-SiO_x:H layers (*a*-Si:H: $\lambda/4n_1 \approx 110$ nm; *a*-SiO_x:H: $\lambda/4n_2 \approx 260$ nm; respective refractive indices at $\lambda = 1.53$ μm: $n_1 = 3.46$ and $n_2 = 1.46$). The half-wave active layer of Er-doped *a*-Si:H, *a*-Si(Er):H is $\lambda/2n_1 \approx 220$ nm thick. The refractive index of *a*-SiO_x:H was found by interferometry during film growth and verified independently by ellipsometry. The microcavities were fabricated with varied active layer thickness to ensure emission wavelength tuning within the natural spectrum of erbium emission in *a*-Si:H.

The transmission, reflection, and PL spectra were measured with a computerized grating monochromator equipped with a Hamamatsu InGaAs photodiode as a radiation detector. The PL of Er^{3+} ions was excited by the emission line of the Kr^+ laser with wavelength $\lambda_{ex} = 647.1$ nm (≤40 mW). The use of a Kr^+ laser minimized the energy loss for bandgap absorption in *a*-Si:H DBR layers at the excitation wavelength.

3. RESULTS AND DISCUSSION

3.1. Transmission and Reflection Spectra of Microcavities

Figure 2 shows the reflection and transmission spectra of an MC with 3 periods in DBR, measured under a normal incidence of light. The stop band at wavelengths $\lambda > 1270$ nm corresponds to the photonic gap. The low-wavelength edge of the spectrum is limited by the sensitivity of the InGaAs photodiode. The sharp peaks of transmission and reflection at $\lambda \approx 1.53$ μm correspond to the resonance mode of MC. It should be noted that the sum of transmittance and reflectance is close to unity in the photonic band gap. This indicates that diffuse scattering of light in the structure is negligible. As can be seen from the figure (inset), the maximum and minimum, respectively, of the resonance transmission

and reflection peaks lie at the same wavelength λ = 1534 nm. In the range of the resonance peaks, the sum of reflectance and transmittance is also approximately unity, indicating the absence of significant absorption by the material of the active layer and DBR at this wavelength.

To analyze the experimental data obtained, the reflection and transmission spectra of MCs were calculated theoretically using the Airy formulas [17]. This approach is equivalent to the commonly employed transfer matrix method but prevents round-off error accumulation. Describing each DBR by a single matrix of transmission and reflection coefficients, we can derive the following formulas for the amplitude transmission and reflection coefficients for the entire MC:

$$t = t_{AA}\Phi t_{BB}t_{SV}/D, \quad (1)$$

$$r = r_A + t_{AA}\tilde{t}_{AA}\Phi^2 r_B/D, \quad (2)$$

where $D = 1 - \tilde{r}_A r_B\Phi^2$ is the interference denominator; $\tilde{r}_A$ and r_B are the amplitude reflection coefficients for light incident from the active layer side for, respectively, DBRs *A* and *B* (Fig. 1); t_{AA} and t_{BB} are the amplitude transmission coefficients of DBRs *A* and *B* for light incident on the microcavity surface; t_{SV} is the amplitude transmission coefficient of the boundary between the substrate and the ambience with dielectric constant ε_V; and $\tilde{t}_{AA}$ is the amplitude transmission coefficient of DBR *A* for light emerging from the active layer. $\Phi = \exp(ik_0 n_z L)$ defines an increase in the phase and a decrease in the amplitude of the light wave passing through an active layer of thickness *L*; $k_0 = \omega/c$, $n_z = \sqrt{\varepsilon - n_x^2}$, $n_x = \sqrt{\varepsilon_V}\sin\varphi$; φ is the radiation emergence angle; and ε is the dielectric constant of the active layer. The tilde indicates that light propagates in a direction opposite to the *z*-axis.

Formulas (1) and (2) have clear physical meaning. When the light wave passes through an MC, it first passes through DBR *A* (t_{AA}) and the active layer (phase factor Φ), then being reflected from DBR *B*. Owing to the multiple transmission through the active layer and reflection from the DBR, the denominator *D* appears describing the interference in this layer. Light emerges from the active layer through DBR *B* (t_{BB}) and then passes through the interface between the substrate and the ambient (t_{SV}). Formula (2) can be considered in a similar way. The reflected light is constituted by light reflected directly from DBR *A* (first term r_A) and light that passes into the MC and is reflected from DBR *B* (second term). In the second case, light first passes through DBR *A* (t_{AA}) and then through the active layer (phase factor Φ), is reflected from DBR *B* (r_B), and again passes through the active layer (Φ). The interference in the active layer gives rise to the denominator *D*.

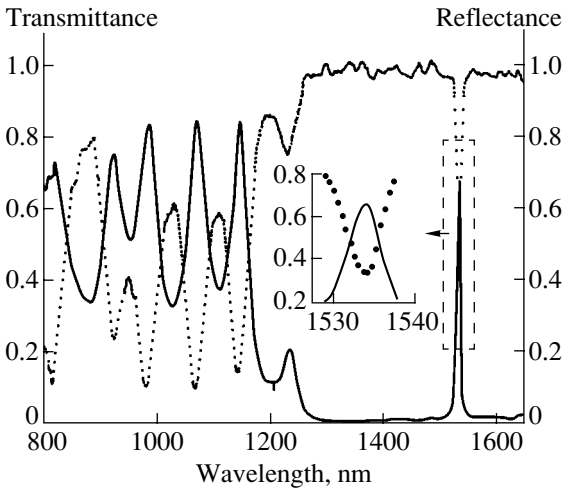

Fig. 2. Transmittance (solid line) and reflectance (dotted line) spectra for *a*-Si:H/*a*-SiO$_x$:H microcavity with 3-period DBR. Inset: resonance peaks.

The light reemerges from the active layer through DBR *A* ($\tilde{t}_{AA}$).

In the photonic gap region, the reflection energy coefficient for the DBR is virtually constant, but the phase varies nearly linearly with frequency $\tilde{r}_A = \pm\sqrt{R_A}\exp[i\alpha_A(\omega - \bar{\omega}_A)]$, $r_B = \pm\sqrt{R_B}\exp[i\alpha_B(\omega - \bar{\omega}_B)]$ [18]. Here, R_A and R_B are the reflection energy coefficients; α_A and α_B are coefficients in the linear frequency dependence of the phase in reflection from the DBR; and $\bar{\omega}_A$ and $\bar{\omega}_B$ are the center frequencies of the photonic gap for DBR *A* and *B*, respectively. The phase change in reflection from a DBR is due to the light wave penetrating into the DBR to a certain depth, with the active layer thickness effectively increasing on the side of this DBR by $l = \alpha c/2\sqrt{\varepsilon}$ ($\alpha = \alpha_A, \alpha_B$; *c* is the speed of light in vacuum). The penetration depth is inversely proportional to the difference of the refractive indices $l = \bar{\lambda}\, n_1 n_2/4(n_1 - n_2)\varepsilon$ ($n_1 > n_2$, $\varphi = 0$, $\bar{\lambda} = 2\pi c/\bar{\omega}$) [19]. The reflection phase at the center frequency of the photonic gap is zero if the active layer has a larger refractive index $\sqrt{\varepsilon} = n_1$ (as in the given case) and π if the active layer is characterized by smaller refractive index $\sqrt{\varepsilon} = n_2$ [18]. The shape and position of resonance peaks is mainly determined by the denominator *D*. Therefore, the transmission and reflection lines have a Lorentzian shape with extrema at the resonance frequency

$$\omega_r = (2\pi N + \alpha_A\bar{\omega}_A + \alpha_B\bar{\omega}_B)/\left[2\frac{L}{c}\mathrm{Re}(n_z) + \alpha_A + \alpha_B\right] \quad (3)$$

and full width at half-maximum (FWHM)

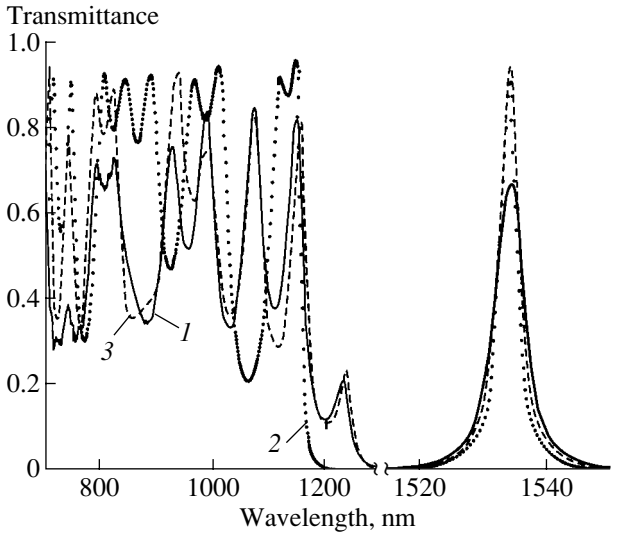

Fig. 3. Transmittance spectra of a microcavity in the region of the resonance peak and beyond the short-wavelength edge of the photonic band gap ($\lambda < 1270$ nm). Each DBR in the microcavity has 3 periods. (*1*) Experimental spectrum, (*2*) spectrum calculated theoretically, and (*3*) theoretical spectrum for a microcavity in which the DBR layer thicknesses are chosen so that the interference pattern beyond the short-wavelength edge of the photonic gap is as close as possible to the interference pattern of the experimental spectrum.

$$\Gamma = \frac{(1 - \sqrt{R_A R_B} F^2)}{\sqrt[4]{R_A R_B} F} \frac{2}{\gamma}, \qquad (4)$$

where $\gamma = \alpha_A + \alpha_B + 2L\,\mathrm{Re}(n_z)/c$, and $F = |\Phi(\omega_r)|$ is the factor characterizing the attenuation of the wave amplitude after a single transmission through the active layer. This factor accounts for the background absorption at the resonance frequency within the active layer, provided that $\Gamma L\,\mathrm{Im}(n_z)/c \ll 1$, which is virtually always the case. The condition for applicability of formulas (3) and (4) is that the quantity $(1 - R)$ for the DBR varies only slightly across the resonance peak and the product $\Gamma\gamma$ is small ($\Gamma\gamma \ll 1$ is the condition for the Lorentzian shape of the line). The experimental resonance transmission spectra are close to those calculated theoretically (Fig. 3).

It should be noted that the phenomena of propagation and emission of light in a periodic structure of Fabry–Perot MC with DBR are actually related to properties of a one-dimensional (1D) photonic crystal containing a planar defect. In this case, the eigenmodes of the MC are photonic modes localized by the defect. By the example of such a 1D photonic crystal, we can gain an understanding of the most general, fundamental properties of photonic crystals, also valid for 3D periodic structures with a period on the order of the light wavelength. In contrast to 2D and 3D photonic crystals, the system considered in this study is much simpler and more controllable as regards both the adequate theoretical description and practical application.

Let us now consider the spectral region outside the photonic gap. Beyond its short-wavelength edge ($\lambda < 1270$ nm), a complex interference pattern appears in the MC reflection and transmission spectra (Figs. 2, 3). The transmission and reflection spectra of the DBR also have a complex structure with multiple peaks outside the photonic gap. The interference pattern in the reflection spectrum is a mirror reflection of the pattern in the transmission spectrum (Fig. 2) since the absorption of *a*-Si:H is low in this spectral region (only a very strong absorption in the DBR layers could disturb this similarity). A spectrum calculated theoretically for an ideal MC (Fig. 3, curve *2*) has a peak structure in this region markedly different from that in the experimental spectrum (curve *1*). In addition, one more minor peak is observed in the experimental spectrum at $\lambda = 1240$ nm at the edge of the photonic gap.

During growth, layer thicknesses deviate from the prescribed values. By varying within a narrow range the thicknesses of the DBR layers and the active layer in performing the calculation, we could achieve a satisfactory agreement between the theoretical and experimental spectra (Fig. 3, curves *1* and *3*), including the general appearance of the interference pattern, and the positions of the photonic gap and the resonance peak. Fitting the calculated curves to the experimental data can give information about the scatter of layer thicknesses in the DBR. This scatter affects the resonance peak only slightly, leading to only a minor decrease in the DBR reflectance and a slight change in the phase of the reflected signal, with the mean frequency of the photonic gap shifted. As a result, the resonance peak is shifted as a whole and is broadened somewhat. Therefore, despite the significant change in the shape of the interference bands, compared with the case of an ideal MC, the width of the transmission peak increases by no more than 16%. A minor peak at $\lambda = 1240$ nm (Fig. 3) at the photonic gap edge is not a second resonance peak, but the result of the shift of gap edges for two DBRs with respect to each other. It corresponds to the first transmission maximum beyond the edge of the photonic gap for a single DBR, lying within the photonic gap of the other DBR. Thus, the deviation of DBR layer thicknesses exerts a very strong influence on the spectrum shape beyond the photonic gap edge and a relatively weak influence on the resonance peak. In contrast, a change in the active layer thickness shifts the resonance peak very strongly and affects only slightly the interference pattern beyond the photonic gap edge. This occurs because the phase of the wave reflected from the DBR varies with frequency outside the photonic gap more rapidly than the phase change $\arg(\Phi)$ does across the active layer thickness.

Thus, our theoretical consideration allows a comprehensive description of the MC transmission and reflection spectra observed.

The analysis of the resonance peaks can yield the MC quality factor

$$Q = \frac{\omega_r}{\Gamma} = \frac{\sqrt[4]{R_A R_B}F}{1 - \sqrt{R_A R_B}F^2}\frac{\gamma\omega_r}{2}. \quad (5)$$

Formula (5) also accounts, through the parameter γ, for the spectral change in the DBR reflectance phase and shows that the correction for the phase shift may markedly increase the calculated quality factor. In the case under study, this accounts for the experimentally observed MC quality factors. For an MC with each DBR having two periods, the maximum experimentally observed quality factor $Q = 97$. The quality factor calculated taking into account the phase shifts (5), $Q = 113$, which is 1.7 times that found without account of the shifts ($Q = 68$).

To demonstrate the possibility of achieving a high quality factor in a-Si:H/a-SiO$_x$:H MCs, several samples with different numbers of DBR periods were fabricated. Figure 4 compares the results of a theoretical calculation of the quality factor (points *1*) and experimental values for different samples (points *2*). The quality factor was determined experimentally from the FWHM ($\Delta\lambda$) of the resonance peak in the transmission spectrum as $Q = \lambda_r/\Delta\lambda$ (λ_r is the resonance wavelength). The theoretical quality factor of an a-Si:H/a-SiO$_x$:H MC grows exponentially with an increasing number of periods. The increase in the quality factor lowers the threshold gain of the active medium, necessary for the onset of lasing. Owing to the high optical contrast, it is possible to obtain the rather high quality factor ($Q \sim 1000$), necessary for vertical cavity surface-emitting lasers, even at a small number of periods. Thus, we could markedly improve the MC quality factor by selecting materials and optimizing the layer growth technology.

The inset in Fig. 4 presents the experimental (solid line) and a theoretical (dashed line) transmission spectra of an a-Si:H/a-SiO$_x$:H MC with DBRs having three periods each. The transmission peak width in the experimental spectrum is 4.3 nm, which gives an estimate $Q = 355$ for the quality factor of the grown structure.

For comparison, the same figure presents a theoretically calculated quality factor for a GaAs/AlAs MC (points *3*). The refractive indices of the constituents of this MC at $\lambda = 886$ nm are as follows: $n_1 = 3.55$ for GaAs and $n_2 = 3.01$ for AlAs. Owing to the higher optical contrast at the same number of periods in the DBR, the quality factor of an a-Si:H/a-SiO$_x$:H MC exceeds by 1–2 orders of magnitude that of a GaAs/AlAs MC, and this difference becomes more pronounced with increasing number of periods. An identical reflectance is achieved at a number of a-Si:H/a-SiO$_x$:H DBR periods five times smaller than that in the GaAs/AlAs DBR. Therefore, with the use of a-Si:H/a-SiO$_x$:H, it is easier to fabricate the DBR with a high reflectance of ~99.8% necessary for creating vertical cavity surface-emitting lasers; with the smaller thickness of the a-Si:H/a-SiO$_x$:H DBR

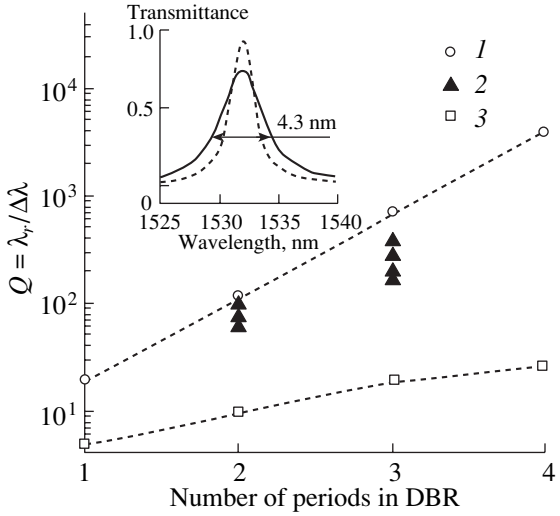

Fig. 4. Quality factor of a symmetrical microcavity vs. the number of periods in the DBR. (*1*) Theoretical calculation for an a-Si:H/a-SiO$_x$:H MC, (*2*) experimental values for different a-Si:H/a-SiO$_x$:H MCs, and (*3*) theoretical calculation for a GaAs/AlAs MC. The theoretical points are connected by lines for clarity. Inset: Experimental (solid line) and theoretically calculated (dashed line) resonance peaks in transmission spectra of an a-Si:H/a-SiO$_x$:H microcavity with 3-period DBRs.

leading to lower diffraction loss. Another major advantage of the a-Si:H/a-SiO$_x$:H MC is the wider photonic gap, determined only by the optical contrast and independent of the number of layers in the DBR [20]. The relative width of the photonic gap, equal to the ratio of the gap width ($\Delta\bar{\omega}$) to the center frequency ($\bar{\omega}$), is 0.5 for the a-Si:H/a-SiO$_x$:H DBR and 0.1 for the GaAs/AlAs DBR. The large width of the photonic gap leads to a wide angular range in which the reflectance at the mean frequency is close to unity and a narrower region with low reflectance, through which the useless leakage of radiation from the MC occurs. Therefore, it is advantageous to use a-Si:H/a-SiO$_x$:H for creating MC LEDs.

One more advantage of the a-Si:H/a-SiO$_x$:H MC is that the resonance wavelength shows a much stronger dependence on the active layer thickness [as follows from formula (3)]. As a result, the resonance frequency is readily tuned over the entire wide photonic gap by varying the active layer thickness.

3.2. PL Spectra

To demonstrate the possibility of tuning the emission from Er^{3+} ions in a MC, several MCs were fabricated with different active layer thicknesses. Figure 5 shows spectra of the erbium PL from these MCs (the peaks are enumerated). In each microcavity, the DBRs have three periods. All the spectra were measured at room temperature in an experimental arrangement with

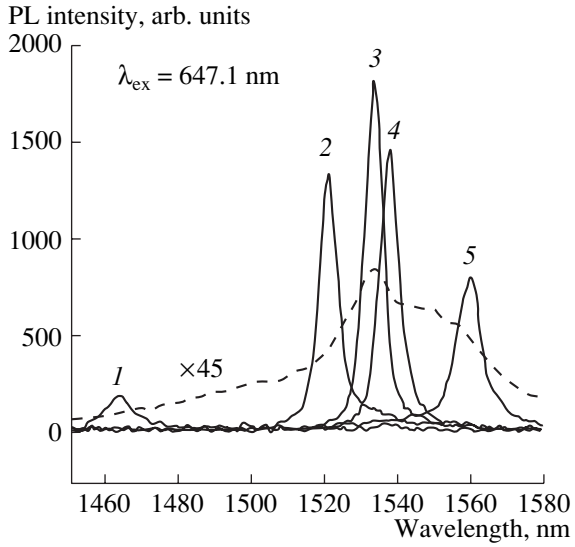

Fig. 5. Erbium PL spectra at room temperature. Peaks (*1*–*5*) are the spectra of *a*-Si:H/*a*-SiO_x:H microcavities (3-period DBRs) with different *a*-Si(Er):H active layer thicknesses. Dashed line represents PL spectrum of *a*-Si(Er):H film on quartz substrate (magnification 45).

emission propagating normal to the sample surface. For comparison, a PL spectrum of an Er-doped *a*-Si:H film is presented of thickness approximately equal to that of the active layer in the MC. Changing the active layer thickness shifts the resonance PL peak. The spectral position of the emission peak can be used to calculate the active layer thickness for each MC, varying between 204 and 228 nm. When the peak is shifted, its amplitude changes in such a way that, on the whole, it reproduces the shape of the Er^{3+} emission spectrum in *a*-Si:H. Owing to the resonance effect, the PL intensity increases by 2 orders of magnitude, with the FWHM of the line decreasing three- to fourfold. The PL line becomes simple and symmetrical, compared with the complex (Stark) inhomogeneously broadened Er emission line in *a*-Si:H, showing two peaks. The external quantum efficiency of PL from MC, found by comparison with the emission of a commercial InGaAs structure with known efficiency under the same excitation conditions, was no less than 0.1%.

Changes in the spontaneous emission from Er^{3+} ions in MCs are entirely effected by the interaction of the ions in the resonance optical mode of the MC. We calculated the PL spectra of MCs by the previously developed method [21]. In doing so, we used the classical theory of the electromagnetic field, yielding for spontaneous emission results completely coinciding with those obtained by means of the quantum theory [22]. Figure 1 shows schematically the propagation of waves in the active layer of an MC. An infinitely thin layer situated at $z = \zeta$ inside the active layer ($0 < z < L$) emits two outgoing plane waves with amplitudes $\mathbf{E}^-_{\zeta-0}$ and $\mathbf{E}^+_{\zeta+0}$, related via the boundary conditions to the amplitudes $\mathbf{E}^+_{\zeta-0}$ and $\mathbf{E}^-_{\zeta+0}$ of two incoming waves reflected from the DBR [21]. Direct integration of the Maxwell equations allows the amplitude of the field at the outer boundary of the left-hand DBR *A* to be expressed in terms of induced singular polarization currents. The integration of the bilinear combination of amplitudes over the active layer thickness and the statistical averaging of the integration result over an ensemble of realizations of a random current yield the following expression for the intensity *I* of emission in the external medium (formula for the *p* polarization is given):

$$I(\omega) \propto I_0(\omega)\left|\frac{\tilde{t}_{AA}\Phi}{D\varepsilon\cos\varphi}\right|^2 \times \{(|n_z|^2 + n_x^2)(I_1 + |r_B|^2 I_2) + 2(|n_z|^2 - n_x^2)|r_B| I_3\}, \quad (6)$$

where $I_0(\omega)$ is the internal spectral density of emission in an infinite medium with dielectric constant ε of the active layer, $I_1 = [\exp(\kappa L) - 1]/\kappa$, $I_2 = [1 - \exp(-\kappa L)]/\kappa$, $I_3 = \sin(qL)\cos(\Delta_B + qL)/q$, $\Delta_B = \arg r_B$, $\kappa = 2k_0\mathrm{Im}(n_z)$, and $q = k_0\mathrm{Re}(n_z)$. I_1 is determined by the contribution of waves $\mathbf{E}^-_{\zeta-0}$ emitted by the random currents directly toward the DBR *A*. I_2 accounts for waves $\mathbf{E}^+_{\zeta+0}$, which were originally emitted toward DBR *B* and then changed their propagation direction after a single reflection from the DBR. I_3 characterizes the mutual interference of waves $\mathbf{E}^+$ and $\mathbf{E}^-$. The remaining quantities were defined previously. The shape and position of the resonance PL peak are mainly determined by the resonance denominator *D* if the internal spectral emission density $I_0(\omega)$ varies only slightly across the resonance peak width. In our experiment, this condition was satisfied (as can be seen from Fig. 5). In this case, the resonance PL line also has a purely Lorentzian shape with resonance frequency (3) and width (4), and its shape virtually coincides with that of the transmission peak. In contrast to the amplitudes of the transmission and reflection peaks, that of the emission peak grows exponentially with increasing reflectance of the mirrors. Mathematically, this follows from the fact that the numerator of formula (6) for the emission intensity contains a single small parameter ($\tilde{t}_{AA}$), and formula (1) for the transmission, two small parameters (t_{AA} and t_{BB}). Figures 6a and 6b compare the shapes of resonance transmission and PL peaks, measured experimentally (solid lines) and calculated theoretically (dashed lines). The PL spectra are normalized to the same maximum value; the transmission spectra are given in absolute values. An MC with a two-period DBR with a small quality factor ($Q = 97$) and a relatively broad resonance line ($\Delta\lambda = 15.7$ nm) was taken for comparison. This was done to reduce the relative line broadening because of the finite aperture of spectral measurements and layer thickness scatter. The resonance peaks of transmission

and PL, found in the experiment, are somewhat broader than those calculated theoretically, which can be attributed to variation of the active layer thickness in the illuminated part of the sample. However, the positions and shapes of the PL and transmission lines are, on the whole, close, as follows from the theoretical analysis. Thus, spontaneous emission in the MC is totally controlled by the resonance optical mode.

3.3. Gain of Spontaneous Emission

It should be noted that formula (6) in fact defines the spectral gain of spontaneous emission from the active layer of MC as compared with the internal spectral density of emission $I_0(\omega)$. The maximum gain of the spontaneous emission is observed at the resonance frequency. For emission emerging along the normal to the surface, let us introduce a coefficient G_{MC} characterizing the emission intensity gain at the resonance frequency ω_r, defined as the intensity ratio of the emission from MC to the emission from the active layer confined, instead of by DBRs, between two semi-infinite media with refractive indices coinciding with that of the active layer:

$$G_{MC} = |\tilde{t}_{AA}|^2 \frac{1 + R_B F^2 + 2\sqrt{R_B} Y_{MC}}{(1 - \sqrt{R_A R_B} F^2)^2}, \quad (7)$$

where

$$Y_{MC} = \frac{2L\kappa(\omega_r)\sin(\nu/2)\cos(\mu/2)}{(1 - F^{-2})(2\pi N - \nu)}, \quad (8)$$

N is an integer approximately equal to the number of half-waves at the resonance frequency $\omega_r = 2\pi c/\lambda_r$ fitting into the active layer thickness, $N \approx 2L\,\mathrm{Re}(n_z)/\lambda_r$, $\nu = \omega_r(\alpha_A + \alpha_B) - (\alpha_A\bar{\omega}_A + \alpha_B\bar{\omega}_B)$; and $\mu = \omega_r(\alpha_A - \alpha_B) - (\alpha_A\bar{\omega}_A - \alpha_B\bar{\omega}_B)$. If $\alpha_A \approx \alpha_B \approx \alpha$ and $\bar{\omega}_A \approx \bar{\omega}_B \approx \omega_r$, then $\nu \approx \mu \approx 0$. At negligibly small absorption in the DBR and the active layer, $|\tilde{t}_{AA}|^2 = (1 - R_A)\mathrm{Re}\sqrt{\varepsilon}/\mathrm{Re}\sqrt{\varepsilon_V}$.

In practice, it is convenient to compare PL from an MC and a film with thickness equal to that of the active layer, deposited onto the same substrate as the MC structure. A film with a high refractive index acts as a low-quality-factor MC. By analogy with definition (7), the intensity gain of emission from a film having a thickness equal to that of the active layer is written as

$$G_{\mathrm{film}} = |\tilde{t}_1|^2 \frac{1 + R_2 F^2 + 2\sqrt{R_2} Y_{\mathrm{film}}}{(1 - \sqrt{R_1 R_2} F^2)^2 + 2\sqrt{R_1 R_2} F^2 (1 - \cos\nu)}, \quad (9)$$

where $\tilde{t}_1$ is the amplitude transmission coefficient of the outer boundary of the film for a wave propagating into the ambient and R_1 and R_2 are the reflection energy coefficients for the outer and inner boundaries of the film, respectively, readily calculated analytically by means of Fresnel's formulas,

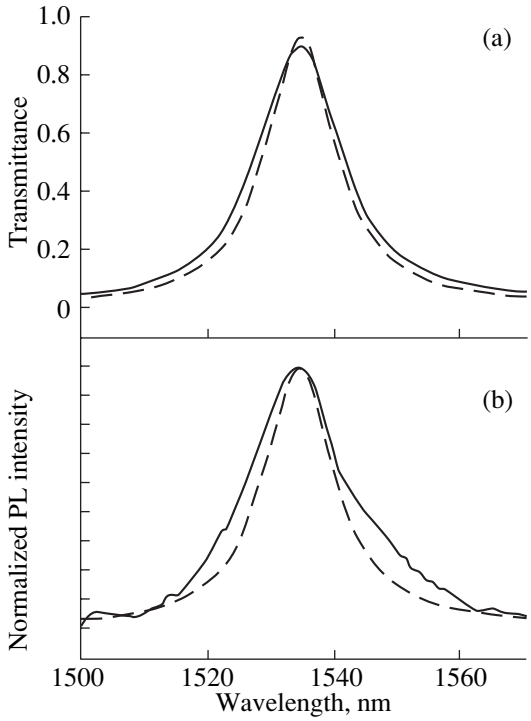

Fig. 6. Resonance peaks in (a) transmission and (b) PL spectra. Solid line represents experiment, dashed line corresponds to theoretical calculation. Transmission spectra are given in absolute values, PL spectra are normalized to the peak value. Each DBR in the microcavity has two periods.

$$Y_{\mathrm{film}} = \frac{L\kappa(\omega_r)\sin\nu}{(2\pi N - \nu)(1 - F^{-2})}. \quad (10)$$

At negligibly small absorption in the film, $|\tilde{t}_1|^2 = (1 - R_1)\mathrm{Re}\sqrt{\varepsilon}/\mathrm{Re}\sqrt{\varepsilon_V}$.

The fact that formula (9) has a form different from that of (7) is due to the different phase shifts in reflection from the film boundaries, compared with that from the DBR. The experimentally measured intensity gain of the PL from the MC, compared with that from the film, is equal to the ratio of gains for the MC and the film: G_{MC}/G_{film}.

For our samples, the theoretically calculated gain of the PL from an MC (in which each DBR has three periods), related to that of the film, $G_{MC}/G_{\mathrm{film}} = 150$ (peak width $\Delta\lambda = 2.3$ nm), is of the same order of magnitude as that found in the experiment, $G_{MC}/G_{\mathrm{film}} = 100$ ($\Delta\lambda = 5.7$ nm). The difference can be attributed to the broadening of the PL peak and a decrease in its amplitude because of the heterogeneity of the active layer and the finite PL spectrum measurement aperture. In addition, the excitation efficiencies of the emission spectra may differ somewhat because of the dissimilar conditions of transmission of the exciting light through the outer surface of the film and the outer DBR.

In contrast to the formulas reported in [6, 23], valid only for point emitters or sheets of oriented dipoles, formulas (6) and (7) describe the emission from the entire active layer with a uniform distribution of emitters across the thickness and an average isotropic emission of an ensemble of sources in a bulk material without DBR. It follows from formula (7) that for an ideal MC, in which the resonance frequency and center frequencies of the photonic gaps of the DBRs coincide, $\omega_r = \bar{\omega}_A = \bar{\omega}_B$, and in which there is no absorption in the active layer or the DBR, the condition $N = 2L\sqrt{\varepsilon}/\lambda_r$ is strictly fulfilled and

$$G_{MC} = \sqrt{\frac{\varepsilon}{\varepsilon_V}}\frac{(1-R_A)(1+R_B)}{(1-\sqrt{R_A R_B})^2}. \quad (11)$$

In this case, the maximum gain at the resonance frequency, G_{MC}, is independent of the active layer thickness or phase change in reflection from a DBR. For such an MC, we have, provided that the DBRs have the same reflectance ($R_A = R_B$), $Q = \gamma\omega_r\sqrt{G_{MC}^2(\varepsilon_V/\varepsilon) - 1}/4$. If $G_{MC}^2 \gg 1$, then the gain is directly proportional to the quality factor. Thus, the high quality factor, readily achievable in *a*-Si:H/*a*-SiO_x:H MCs with a small number of layers in the DBR owing to the high optical contrast, directly leads to a high gain necessary for creating high-efficiency emitting devices.

It should be noted that, because of the high optical contrast, the penetration depth of the electromagnetic wave into the *a*-Si:H/*a*-SiO_x:H DBR is many times smaller than that in the case of the GaAs/AlAs DBR. This leads to an effective decrease in the photon path length in the *a*-Si:H/*a*-SiO_x:H MC between successive reflections in the DBR. The effective decrease in the MC length leads to shorter photon lifetime and resonance line broadening. Therefore, at equal DBR reflectances, the resonance peak width in the *a*-Si:H/*a*-SiO_x:H MC is several times that in the GaAs/AlAs MC, and, consequently, the frequency band of signal modulation is broader and the data transfer rate is higher. The gain of the spontaneous emission in an ideal MC depends only on the DBR reflectance. Therefore, for the same gain, the spectral band in which the *a*-Si:H/*a*-SiO_x:H exhibits amplification will also be several times broader.

4. CONCLUSION

The PECVD technique was applied to grow in a single technological cycle planar *a*-Si:H/*a*-SiO_x:H Fabry–Perot microcavities. The half-wave *a*-Si:H active layer was doped with erbium from a metal-organic compound in the course of growth. The DBRs comprised alternating quarter-wave layers of *a*-Si:H and *a*-SiO_x:H. Symmetrical microcavities with two- and three-period DBRs were tuned to the resonance wavelength of 1.53 μm corresponding to the intracenter ($^4I_{13/2} \longrightarrow {}^4I_{15/2}$) emission from Er^{3+} ions in *a*-Si:H. Owing to the high optical contrast between *a*-Si:H and *a*-SiO_x:H (the ratio of the refractive indices is 2.40), a high quality factor of the microcavity was achieved ($Q = 355$) even with three-period DBRs, and the erbium PL was enhanced by two orders of magnitude as compared with a film of erbium-doped *a*-Si:H on a quartz substrate.

The transmission and reflection spectra of the microcavities were studied experimentally and analyzed theoretically. A theoretical calculation allowed a comprehensive description of the experimental transmission and reflection spectra, including the resonance peak, photonic gap, and interference peaks beyond its edge. It was found that the interference pattern beyond the photonic band-gap edges is mainly determined by the DBR layer thicknesses and depends only slightly on the active layer thickness. An analysis of the interference pattern beyond the short-wavelength edge of the photonic gap enabled an estimate of the scatter of DBR layer thicknesses to be made.

The method of amplitudes of the field created by stochastic polarization currents was applied to calculate the spectrum of PL from Er^{3+} ions in the active layer of the microcavity. It is shown theoretically and confirmed experimentally that the shape of the resonance PL peak is completely determined by the shape of the resonance peak in the transmission spectrum.

ACKNOWLEDGMENTS

This study was supported in part by the Ministry of Science of the Russian Federation (program “Physics of Solid-State Nanostructures, project no. 99-1107) and TIMOC (project no. ERB IC15 CT98 0819).

REFERENCES

1. *Amorphous and Heterogeneous Silicon Thin Films–2000*, Ed. by R. W. Collins, H. M. Branz, S. Cuha, H. Okamoto, and M. Stutzmann (Materials Research Society, Warrendale, 2000); Mater. Res. Soc. Symp. Proc. **609** (2000).
2. S. M. Paasche, T. Toyama, H. Okamoto, and Y. Hamakawa, IEEE Trans. Electron Devices **36**, 2895 (1989).
3. A. B. Pevtsov, A. V. Zherzdev, N. A. Feoktistov, *et al.*, Int. J. Electron. **78**, 289 (1995).
4. *Semiconductor Quantum Optoelectronics: from Quantum Physics to Smart Devices: Proceedings of the 50th Scottish Universities Summer School in Physics, St. Andrews, 1998*, Ed. by A. Miller, M. Ebrahimzadeh, and D. M. Finlayson (Inst. of Physics Publ., Bristol, 1999).
5. E. F. Schubert, A. M. Vredenberg, N. E. J. Hunt, *et al.*, Appl. Phys. Lett. **61**, 1381 (1992).
6. A. M. Vredenberg, N. E. J. Hunt, E. F. Schubert, *et al.*, Phys. Rev. Lett. **71**, 517 (1993).

7. E. F. Schubert, N. E. J. Hunt, A. M. Vredenberg, *et al.*, Appl. Phys. Lett. **63**, 2603 (1993).
8. M. Lipson, T. D. Chen, D. R. Lim, *et al.*, J. Lumin. **87–89**, 323 (2000).
9. M. Lipson and L. C. Kimerling, Appl. Phys. Lett. **77**, 1150 (2000).
10. M. S. Bresler, O. B. Gusev, V. Kh. Kudoyarova, *et al.*, Appl. Phys. Lett. **67**, 3599 (1995).
11. J. H. Shin, R. Serna, G. N. Hoven, *et al.*, Appl. Phys. Lett. **68**, 997 (1996).
12. M. S. Bresler, O. B. Gusev, P. E. Pak, *et al.*, Fiz. Tekh. Poluprovodn. (St. Petersburg) **33**, 671 (1999) [Semiconductors **33**, 622 (1999)].
13. A. A. Dukin, N. A. Feoktistov, V. G. Golubev, *et al.*, Appl. Phys. Lett. **77**, 3009 (2000).
14. N. A. Feoktistov, N. L. Ivanova, L. E. Morozova, *et al.*, Mater. Res. Soc. Symp. Proc. **420**, 189 (1996).
15. V. B. Voronkov, V. G. Golubev, N. I. Gorshkov, *et al.*, Fiz. Tverd. Tela (St. Petersburg) **40**, 1433 (1998) [Phys. Solid State **40**, 1301 (1998)].
16. N. A. Feoktistov, V. G. Golubev, A. V. Medvedev, and A. B. Pevtsov, Mater. Res. Soc. Symp. Proc. **507**, 255 (1998).
17. A. Yariv and P. Yeh, *Optical Waves in Crystals* (Wiley, New York, 1984; Mir, Moscow, 1987).
18. G. Panzarini, L. C. Andreani, A. Armitage, *et al.*, Fiz. Tverd. Tela (St. Petersburg) **41**, 1337 (1999) [Phys. Solid State **41**, 1223 (1999)].
19. R. Ram, D. Babic, R. York, and J. Bowers, IEEE J. Quantum Electron. **31**, 399 (1995).
20. P. Yeh, *Optical Waves in Layered Media* (Wiley, New York, 1988).
21. V. G. Golubev, A. V. Medvedev, A. B. Pevtsov, *et al.*, Fiz. Tverd. Tela (St. Petersburg) **41**, 153 (1999) [Phys. Solid State **41**, 137 (1999)].
22. Y. Xu, R. K. Lee, and A. Yariv, Phys. Rev. A **61**, 33807 (2000).
23. *Confined Electrons and Photons: New Physics and Applications*, Ed. by E. Burstein and C. Weisbuch (Plenum, New York, 1995); NATO ASI Ser., Ser. B **340** (1995).

Translated by M. Tagirdzhanov